NASA Technical Memorandum 81676

Microstructure of Al2O3 Scales Formed on NiCrAl Alloys

James Leo Smialek
Lewis Research Center
Cleveland, Ohio

January 1981

NASA

Table of Contents

INTRODUCTION

Study of the microstructure of Al_2O_3 scales formed on high temperature alloys has become a more intense field of research over the last 15 years. This is in large part due to the availability of scanning electron microscopes to most laboratories, by which magnification of 10,000X can be achieved routinely High magnifications are required to study scale features, since the total scale thicknesses generally attained are less than 5-10 μm. The driving force behind the SEM scale studies has been the development of oxidation resistant Ni,Co,Fe-Al alloys, which depend on the production of a stable adherent α-Al_2O_3 scale for their performance in oxidizing atmospheres at high temperature.

The use of transmission electron microscopy for studying Al_2O_3 scales has been much less extensive due, most probably, to experimental difficulties in thin foil preparation and unavailability of ion thinning procedures. Most of the TEM studies of Al_2O_3 scales have been limited to low temperature/short time transient oxidation which produced electron transparent scales. The internal structure of mature Al_2O_3 scales has not been studied at all. Furthermore, the transient oxidation studies were directed towards phase identification by electron diffraction and gross scale variations over alloy grain boundaries; thus, even in the transient scales little information on the fine structure exists.

The following literature survey will briefly review the structural studies of α-Al_2O_3 scales. In addition to the limited TEM studies, the SEM works will also be discussed. Special attention will be given to the importance of the observed scale structures to the development of oxide adherence theories as well as the need for TEM to confirm additional features at submicron-level resolutions required by these theories.

A) SEM Studies

Much of the pioneering work on the structure of Al_2O_3 scales was done by Pettit and co-workers on FeCrAl, NiCrAl, CoCrAl, and Pt-Al alloys. The vacancy sink mechanism put forth by Tien and Pettit related oxide adherence to the prevention of voids at the oxide-metal interface.[1] FeCrAl alloys with Y or Sc additions were found to form internal oxide protrusions which were thought to provide surfaces which served as vacancy sinks. Pure FeCrAl on the other hand formed voids at the oxide-metal interface, presumably as a Kirkendall effect caused by the selective oxidation of aluminum. A dispersion of Al_2O_3 particles was also found to prevent voids and oxide spalling in the absence of Y or Sc. This is consistent with the requirement of additional surfaces to remove vacancies. The Al_2O_3 scales were found to grow by inward oxygen diffusion on all the alloys. The scale on the pure FeCrAl had a duplex structure with fine grains at the gas surface and coarse grains near the metal. The gas surface appeared to be dimpled or porous and had many oxide whiskers. The scale was also wrinkled in the areas where

the interface voids were. Voids were also observed to be present in the underside of the oxide at these regions. The scales on the doped alloys were flat, showed no voids at the oxide-metal or gas surfaces, and had $YAlO_3$ formation for alloys with 0.1%Y or greater. Alloys with 0.01Y formed no Y oxides, but were still adherent. It was therefore proposed that Y-vacancy complexes were also useful in preventing void formation and spalling and that internal oxide penetration (pegging) was not required for adherence.

In an extensive work on NiCrAl and CoCrAl alloys, Giggins and Pettit found essentially the same features previously reported for the FeCrAl alloys.[2] However, some additional experiments further complicated the understanding of oxide adherence mechanisms. It was found that electropolished samples of undoped NiCrAl did not form interface voids during oxidation, but the Al_2O_3 scales still spalled profusely. This indicated that voids are not necessary to cause spalling, and the generality of the vacancy sink mechanism was accordingly limited. Also, in compressively stressed Y-doped specimens the oxide was still found to be quite adherent. This indicated that adherence was not primarily due to the lack of internal stress in the oxide, as suggested by the growth stress model to be discussed later. The final conclusion was that the oxide-metal bond was enhanced by a "micropegging" mechanism due to Y additions.

Some additional interesting Al_2O_3 structures were observed on Pt-Al alloys by Felten and Pettit.[3] In a Pt-6%Al alloy different Al_2O_3 morphologies were found over the Pt_2Al and Pt_5Al_3 phases.

The initial scale on the Pt_2Al phase imaged polishing marks on the metal, whereas the Pt_5Al_3 phase showed no polishing marks after oxidation. This suggested that the Pt_2Al scale was growing inward, whereas the Pt_5Al_3 scale was growing outward. The Pt_2Al oxide was very thick at oxide grain boundaries and thin over the interior of the oxide grain. Supplementary TEM studies confirmed this and also documented some preferred orientation during initial oxidation. The Pt_5Al_3 oxide phase was essentially a single crystal made up of highly oriented subgrains during initial oxidation. This eventually transformed into a polycrystalline oxide, with a grain size finer than that in the Pt_2Al oxide. At long oxidation times the scales exhibited a columnar structure. An irregular oxide-metal interface morphology also developed where alloy protrusions existed in the underside of the scale. This rough interface or a good Pt-Al_2O_3 chemical bond was believed to account for excellent oxide adhesion in cyclic oxidation tests.

Golightly, Stott, and Wood have explained the adhesion of Y-doped FeCrAl as due to the minimization of growth stress in the scale.[4] The undoped FeCrAl exhibited oxides which were severely wrinkled and detached from the metal, whereas Y-doped alloys produced flat scales in good contact with the metal. Oxide penetration into the alloy was observed in an 0.82%Y alloy, but not for an 0.023%Y alloy. Since adhesion was good for both compositions, the effect of mechanical attachment due to the oxide intrusion was dismissed. The occurrence of interface voids in the undoped FeCrAl were explained

as the result of lateral growth of the oxide. This lateral growth was believed to result from the short-circuit outward diffusion of aluminum in addition to the primary transport mechanism of inward oxygen grain boundary diffusion. Dislocations in the oxide were felt to be the most likely candidate for these short-circuit paths which could then be blocked by the segregation of Y atoms at the cores.

In a more detailed study by the same authors, the equiaxed scale structure of the undoped FeCrAl was explained as a result of outward aluminum diffusion and growth stresses.[5] With increasing amounts of Y, the equiaxed structure became more of a duplex structure with columnar grains at the oxide-metal interface. Cusped surfaces of oxide grains, where additional material was present near oxide grain boundaries (at both the gas and metal surfaces) was believed to be due to plastic flow of the oxide. This was caused by growth stresses resulting from oxide formation in the vicinity of oxide grain boundaries.

Alam, Whittle, and Stringer, and Whittle and Stringer have explained the adherence effects of rare-earth additives according to a third mechanism -- that of oxide pegging.[6,7,8] While the growth stress and vacancy sink models may also apply to some degree, they believed that the greatest adherence is achieved when a finely dispersed assemblage of oxide intrusions is developed. They have enhanced adherence by a pre-oxidation treatment of Hf-doped CoCrAl alloys in order to internally oxidize the Hf to a very fine HfO_2

dispersion. Upon subsequent oxidation the HfO_2 particles presented rapid paths for oxygen penetration, and Al_2O_3 oxide intrusions formed on the underside of the Al_2O_3 scale.

The foregoing has outlined briefly the tenents of the three prominent Al_2O_3 adherence mechanisms: vacancy sink, growth stress, and pegging. As yet, no one argument has been accepted unequivocally by the oxidation community. The oxide structures as revealed by SEM have been an important source of information for these theories. Some features which can be revealed only by TEM could support these theories, such as the preferential precipitation of vacancy dislocation loops in doped alloys or a large number of dislocations in the Al_2O_3 scale serving as short-circuit paths for aluminum. Although the major objective of the present work is not to develop an oxide adherence model, the TEM studies do afford information useful to these theories of adherence.

B) TEM Studies

Transmission microscopy studies of Al_2O_3 films on aluminum date back as early as 1934, as briefly reviewed by Phelps, Gulbransen, and Hickman in 1946.[9] Basically, what was found in these studies was that small submicron crystallites of γ-Al_2O_3 or α-Al_2O_3 were formed by low temperature ($\sim 500^{o}C$) short time (5 minute) oxidation exposures. More recently Scamans and Butler studied oxidation of aluminum and found that above $475^{o}C$ crystallites of γ-Al_2O_3 nucleated beneath an amorphous oxide layer after an incubation period when no crystals were observed.[10] The crystals were in the

750-1000 Å size region and were highly oriented, but did not exhibit any unique orientation relationship with the metal substrate.

Thin scales formed on Ni-Al alloys were studied by electron diffraction by Nazarova in 1964.[11] He found a predominance of γ-Al_2O_3 for alloys greater than 33 w/o Al in the range of 540-860°C. For lower concentrations, NiO and $NiAl_2O_4$ predominated. Wood and Chattopadhyay studied the 600°C transient oxidation of Ni-Al alloys containing from 2-23% Al.[12] They found non-uniform scale structures consisting of dispersed NiO crystallites with an underlying "healing" layer of γ-Al_2O_3 and a $NiAl_2O_4$ reaction layer.

Similar results were observed by Kear, Pettit, Fornwalt, and Lemaire for Ni-15Cr-6Al oxidized at 1000°C.[13] After one minute of oxidation, dispersed crystallites of NiO (>50 Å dia.) were observed with an underlayer of α-Cr_2O_3 (>50 Å dia.) and a major intermediate layer of $NiAl_2O_4$ (<50 A dia.). After five minutes crystallite growth occurred and some degree of crystallographic texture was observed. After 40 minutes randomly oriented grains of a α-Al_2O_3 were found in a random α-Cr_2O_3 underlayer with both having a 2000 Å grain size. Further oxidation to 20 hours produced only a stable α-Al_2O_3 scale as observed by X-ray diffraction. Koch and Romeo studied a Ni-10Cr-13Al alloy oxidized at 900°C for 16 hours and found highly oriented $NiAl_2O_4$ and $NiCr_2O_4$ oxides.[14]

Thus the state of the TEM observations is such that the stable α-Al_2O_3 scales have never been studied. The purpose of the present study is therefore to begin to "fill the gap" in the knowledge of

the substructures of Al_2O_3 scales by investigating mature stable α-Al_2O_3 as well as the fine structure in transient scales.

Special attention is given in this work to features (or the lack of such features) which have significance to oxide adherence theories. However, a great deal of emphasis is also placed on other prominent features which are of importance to a fundamental understanding of Al_2O_3 scale structures and growth processes. The scope of the work entails a detailed look at scales formed on undoped Ni-15Cr-13Al oxidized at 1100°C from 0.1 to 20 hours. Scale variations through the thickness were studied by successive ion thinning of a single specimen or by producing multiple specimens at various levels in the scale. A concerted effort was made to discuss the Al_2O_3 scale structures in terms of bulk α-Al_2O_3 properties.

EXPERIMENTAL PROCEDURE

Button melts of Ni-15Cr-13Al alloys were made by non-consumable tungsten arc melting in a copper-cooled mold. The approximate casting dimensions were 1 x 2 x 10cm. Melt charge materials were all 99.99% pure. The compositions determined by wet chemistry are as follows: (weight percent)

Ni	Cr	Al	X
bal	15.0	12.6	
bal	14.8	12.7	0.47 Y
bal	15.3	12.8	0.50 Zr

The castings exhibited a two-phase structure of ∿25 μm wide β-NiAl primary dendrites in a γ/γ' Ni(SS)/Ni_3Al matrix. The γ' particles exhibited the classic (100) cuboidal morphology as revealed by dark field imaging with superlattice reflections. The γ' particle size was ∿500 Å and did not change with thermal treatments at 1100°C; thus the γ' was apparently taken into solution and re-precipitated after each exposure.

Specimens for oxidation studies were produced by taking 0.6 mm thick slices, electrodischarge machining 3 mm dia. discs from the slices and manually sanding the discs to 0.25 mm thickness. The discs were metallographically polished with 3 μm diamond and 0.5 μm chromic oxide, and ultrasonically cleaned in detergent, then in ethanol. Oxidation was performed in FeCrAl cups that were pre-oxidized to form a thick α-Al_2O_3 coating. The cups were pre-heated,

the specimens inserted, and the assembly quickly lowered into a resistance furnace maintained at 1100±3°C. Oxidation times were 0.1, 1, and 20 hours.

Thin foils of specimens exposed for 0.1 hour were produced by careful 600 grit sanding of one side of the disc to a 125 μm thickness, electropolishing from this same side only, until transparent to high intensity light, and ion thinning the remaining oxide film. Electropolishing was accomplished at 35V and 10mA in a 5-17-78 perchoric acid/acetic acid/butylcellosolve solution at 3°C. Ion thinning was performed at 5kV, with a 10-15° angle of incidence. Scales formed on the pure NiCrAl for 1 and 20 hours spalled cleanly at the oxide-metal interface and could be ion thinned directly. The 20 hour scale was ion thinned for varying durations from the top or bottom side to produce foils at different levels in the scale. Thus, all thin foils studied were produced in the plane of oxidation. The foils were examined in a JEOL 7A microscope operating at 100kV. The limits of the specimen stage were ±20° of tilt and ±180° of rotation about the specimen axis.

RESULTS AND DISCUSSION

Chapter I. Morphology of Transient Oxide Scales

A) Pure Ni-15Cr-13Al

1) Metal Structures

a) γ/γ' dislocation structures at the Al_2O_3 oxide-metal interface.

A large transparent area of γ/γ' produced by electrpolishing and ion thinning is shown in Figure 1. The γ/γ' area is relatively uniform in thickness. The β regions, however, show scattered holes, $\sim$2-3 μm in diameter. These holes are interpreted as voids in the metal caused by selective oxidation of Al. The void size is comparable to the 1-2 μm voids formed in Ni-42 a/o Al after 0.075 hr oxidation at 1100°C.[15]

The entire γ/γ' region of Figure 1 contained a "cross-hatched" array of parallel dislocations. This is shown more clearly in Figure 2. The arrays consisted of two mutually perpendicular sets aligned along <110>, as will be shown later. Oxide grains (marked "X") are also present throughout the γ/γ' region. Thus, a layered structure of oxide grains and dislocations in γ/γ' exists here. This oxide + metal structure therefore represents the interface structure where oxide grains are bonded to the metal substrate. The dislocation arrays show a periodic spacing of $\sim$0.2 μm. Details of the interface structure in a similar region are shown in Figure 3. Here the periodic dislocation array can, in some cases, be seen as periodic clusters of dislocations (marked "C"). The oxide grain

size varied from ∿0.05 to 0.10 μm, and is on the order of the spacing of the periodic clusters. This correlation suggests a possible pinning effect of oxide grain boundaries on dislocations in the metal. The intimacy of the oxide-metal bond is illustrated by areas showing a sharp oxide-metal interface ("M-X") and interfacial dislocations ("I") produced by some crystallographic disregistry at the plane of contact. The intense "salt and pepper" contrast apparent in Figure 3b is damage in the γ/γ' due to ion thinning.

The projected dislocation line directions are seen to be within $\sim 2^{o}$ of [110] and [$\bar{1}$10] in Figure 4. Because the dislocation projected lengths, L, are quite long, 3-13 μm, it is expected that they lie nearly parallel to the oxidized surface, and that the true line directions, $\hat{u}$, are also [110] and [$\bar{1}$10]. The dislocations were calculated to indeed be only about $1\text{-}5^{o}$ to the plane of oxidation from $\sin \Theta = t/L$, where the foil thickness, t, was estimated to be 1500 $\overset{o}{A}$.

Based on this information a simplified account of the dislocation structures can be proposed. The high degree of orientation indicates that the lines are either pure edge or pure screw in nature. The Burgers vectors were not determined because of the complicating effects of the oxide layer on dislocation images. The stress induced in the metal from oxide growth stresses during oxidation or thermal expansion differences during cooling are a maximum at the oxide-metal interface and decrease in towards the

midsection of the metal substrate. This stress gradient causes a shear stress which is a maximum in the plane of oxidation. In this sample the plane of oxidation was $(\bar{1}05)$, or 10^{o} from (001). If $\vec{b}$ is assumed to lie in this plane of maximum shear stress, then it must be 1/2 <110> for perfect pure screw or pure edge dislocations. An orthogonal array of pure screw dislocations results in a pure twist boundary. This configuration could not result from the bi-axial stress state at the oxide-metal interface. An orthogonal array of pure edge dislocations, however, can produce a biaxial expansion in the plane of the array. This is consistent with the expected stress state of biaxial tension in the metal at the oxide-metal interface.[4,16]

The existence of an (001) slip plane is contrary to the {111} slip planes normally observed for FCC materials. However, the stress state at the oxidized surface is dramatically different from that in a conventional uniaxial mechanical test specimen. During oxidation the stress is applied directly to the plane of maximum deformation with a Schmid factor near unity. However, in a uni-axial tension or compression test, the stress is applied at some angle to the plane of maximum shear, and the maximum Schmid factor is limited to 0.5 or less. Furthermore, a recent study has shown that <110> slip on {001} planes for FCC Ni, Cu, and Ag single crystals deformed in tension.[17]

The dislocation density of Figure 4 was calculated to be $10^{10} cm^{-2}$ by the method of Ham.[18] (The foil thickness was estimated

to be $\sim 4\xi_g$, $\bar{g} = (200)$.) This value is between those for a well annealed metal, $10^8 cm^{-2}$, and a heavily cold worked metal, $10^{12} cm^{-2}$.

The diffraction pattern of Figure 4c includes a number of reflections from the oxide grains as well as from the metal structure. There is no clear epitaxial relationship between the oxide and metal, nor is there a preferred orientation of the various oxide grains in this area. The oxide reflections were indexed as primarily α-Al_2O_3 with some possible α-Cr_2O_3 reflections. In another area a single crystal pattern was obtained for a large α-Al_2O_3 grain and metal, Figure 5. Some planes were found to be parallel: $(013)_\gamma \parallel (0\bar{1}11)_\alpha$ and $(\bar{1}\bar{3}1)_\gamma \parallel (0\bar{1}12)_\alpha$. However, in general, there was no compelling evidence for a strong epitaxial effect.

The oxide structure in the pitted areas of the β-NiAl phase was thin enough to show some structural features, Figure 6. No distinct grain boundaries are evident, but there are delineations of various thicknesses in an undulating pattern. This morphology agrees with the very porous structure observed for Al_2O_3 areas directly above oxidation-induced voids in NiAl.[15] The diffraction pattern was identified as primarily α-Al_2O_3. A rectangular array of spots suggested the possibility of a single crystal or preferred orientation pattern for the oxide. Indexing as a $[2\bar{1}\bar{1}2]$ Al_2O_3 pattern was possible, although the certainty of any indexing scheme based on large $|\bar{g}|$ values of marginal intensity is questionable. It is noteworthy that the $(0\bar{5}\bar{3}0)$ reflections show a rotational variation of $\sim 4^o$. This may have some relation to the Al_2O_3

scales to be discussed later, which have preferred orientations with some rotational variations from subgrain to subgrain in the oxide.

b) γ/γ' dislocation structures beneath the oxide-metal interface. Metal structures were also observed in areas where no oxide remained after specimen preparation. Dislocation structures reminiscent of the long <110> lines found in the plane of oxidation were found beneath the interface. In addition, networks of dislocations in subgrain arrays were also observed. The distance beneath the plane of oxidation for these structures was estimated to be between 1-5 μm, but could not be determined by any straightforward technique.

Typical dislocation arrangements are shown in Figures 7a, b, and c. The low angle grain boundary networks (marked "A") consist of jagged dislocations lines. Each segment direction shows approximate parallelism to segments in neighboring dislocations. Thus, a definite crystallographic direction is assumed by the dislocation segments. The average γ' particle width was determined from the $(010)_{\gamma'}$ dark field micrograph of Figure 7d to be 270 ± 70 Å. Referring to Figure 7a, this dimension is characteristic of the smaller segments of the low angle boundary dislocations. It is thus believed that these dislocations dodge the hard γ' particles and remain in the relatively soft γ areas between particles. Longer segments may then extend between two or more particles whose faces share a common plane. The γ' particles in Figure 7d show no

evidence of dislocations cutting particles, which is further evidence that the dislocations lie between particles.

At some distance from these jagged dislocation arrays, longer straight dislocation segments are present (marked "B" in Figures 7a, b, and c). Their projected directions were about 40^{o} from [010] and thus, can be easily described as <110> lines at 45^{o} to [010], but at some inclination to the plane perpendicular to the beam. In Figures 7b and 7c the long dislocation structures can be seen to gradually "merge" into the low angle boundary arrays. Thus, a relationship of the long <110> dislocations found directly at the oxide-metal interface and the segmented dislocations in the low angle boundaries beneath the interface is strongly suggested. It is proposed that the low angle boundaries resulted from thermally activated climb of prior <110> dislocation arrays.

The previously discussed long dislocations at the oxide-metal interface represent an unrecovered structure produced by oxidation growth stresses. Thus, a decrease in dislocation density of the long <110> lines occurs as a function of distance below the oxide-metal interface. This is consistent with a decay of the oxidation growth stresses from the oxide-metal interface into the metal interior.

c) β structures beneath the oxide-metal interface. No areas of β-NiAl were found that were still in contact with the oxide, and as a result the β structure at the immediate oxide-metal interface was

not studied. However, β structures were observed at some slight distance beneath the scale. The major effect was compositional in nature. Aluminum depletion caused by selective oxidation resulted in the formation of the lower aluminum phase γ'-Ni_3Al. Because of the planar front of oxidation the γ' formed as a layer of numerous subgrains on top of the parent β phase. The γ' subgrains were often coherent with the β and showed a definite crystallographic relationship with β. Typical γ' structures resulting from the aluminum depletion of β are shown in Figure 8. Voids (Figure 1a) on the order of 3 μm diameter were produced in the original β phase as the result of selective oxidation of aluminum. Since voids of this size were previously identified as interface voids in the oxidation of NiAl, it is concluded that this foil plane is less than 3 μm beneath the oxide-metal interface. On a finer scale, Figure 8b, this region is seen to consist of a mosaic of grains or subgrains, identified as γ' by electron diffraction. The subgrain size varied from 0.5 to 3 μm, with an average of 2 μm. Antiphase domain boundaries (APB in 8b) presumably resulted from the growth and impingement of multiple γ' nuclei. Wide thickness contours were also common ("C" in 8b and 8c) which indicate a relatively flat interface topography, such as a layered structure. The convoluted shape of these contours favors an interpretation of them as growth APB's as opposed to the more regular structure of simple grain boundary fringes.

An example of a layered $\gamma' + \beta$ structure is shown in Figure 9. The extent of the γ' subgrain (1 μm) is outlined by the thickness fringes (arrow) formed by the γ'-β interface inclined to the plane of the foil. The areas corresponding to β only, layered $\beta + \gamma'$, and γ' only are labeled in Figure 9b. The β structure shows a fine periodic structure ("cross-hatching" or "tweed") to be discussed later. The $\beta + \gamma'$ layered structure has produced a series of Moire' patterns resulting from near-alignment of the Bragg planes in the two phases. The γ' region contains a large annealing twin, fine α-Cr from the parent β, and fine cuboids of γ' electropolishing debris from other areas.

The diffraction pattern obtained from the γ' area only is shown in Figure 10a and b. The twin plane was the usual {111} for FCC materials. Matrix and twin patterns were separated by dark field imaging (see Figure 9c for $\bar{g} = (11\bar{1})\gamma'$, matrix reflection). The diffraction pattern for the β phase is shown in Figure 10c and d. The indexed pattern has identified a number of satellite spots in <100> directions. These resulted from the intersection of <110> rel rods with the Ewald sphere for a [100] zone.[19] (The origin of these rel rods will be discussed later.) Extra streaked spots (not identified) probably resulted from rel rods from a nearby zone.

A superimposed pattern from the γ' matrix is shown in Figure 10d. (10a and 10c were obtained at the same foil tilt, and the (220) and (111) γ' relfections were recorded in the β pattern.)

Thus, the orientation relationship between γ' and β defined by the diffraction patterns is:

$$(100)_\beta \parallel (1\bar{1}0)_{\gamma'}$$

$$(01\bar{1})_\beta \parallel (11\bar{1})_{\gamma'}$$

The specific lattice strains and rotations required to produce the γ' cell with the above orientation can be best described by examining the unit cells of both structures, shown in Figure 11. X-ray diffraction lattice parameter was found to be 2.860 ± 0.002 Å for the ordered BCC NiAl cell. With this internal standard, a_o was found to be $3.594 \pm .005$ Å for the ordered FCC Ni_3Al cell. The γ' cell can be described as a 0.45 Å contraction along $[110]_\beta$ and $[\bar{1}10]_\beta$, and a 0.73 Å elongation along $[00\bar{1}]\beta$. At perfect stoichiometry the aluminum atoms occupy all of the sites at the cube corners. As aluminum is depleted, nickel atoms occupy aluminum sites in a random substitutional manner.[20] The stoichiometric Ni_3Al cell is produced when half of the NiAl cube corners are occupied by nickel atoms and by the lattice distortions just described.

Stereographic projections of the idealized cell orientations of Figure 11 are shown in Figure 12. No parallelism of close packed $\{110\}_\beta$ and $\{111\}_{\gamma'}$ planes has been produced by lattice distortions alone. However, rotating γ' by $\theta = 9.7^\circ$ about the $[100]_\beta$ brings $(11\bar{1})_{\gamma'} \parallel (01\bar{1})_\beta$. (See θ in Figure 11.) This is equivalent to the Nishiyama-Wasserman (N-W) BCC-FCC relationship.[21]

This is also identical to the relationship found in Figure 10 for NiAl-Ni_3Al. Since exact zone axis orientations were not obtained for Figure 10, it also is possible that $[111]_\beta \parallel [101]_{\gamma'}$ (by further rotating $\varphi = 5.3^o$ in Figure 12). This corresponds to the Kurdjumov-Sachs (K-S) relations. The following table lists the two orientation relationships for the BCC $\leftrightarrow$ FCC transformation:[21]

Kurdjumov-Sachs		Nishiyama-Wasserman	
$(01\bar{1})_{BCC}$	$(11\bar{1})_{FCC}$	$(01\bar{1})_{BCC}$	$(11\bar{1})_{FCC}$
$[111]_{BCC}$	$[101]_{FCC}$	$[100]_{BCC}$	$[1\bar{1}0]_{FCC}$

It should be noted that the θ rotation causes misalignment of several previously parallel $\{110\}_{\gamma'}$ and $\{100\}_\beta$ planes. However, none of these disrupted pairs consisted of two close-packed planes. The energetically preferred situation is to produce the highest degree of atom correspondence, i.e., aligned close-packed planes and directions. Thus, the N-W or K-S relationships should prevail.

The superimposed atom positions of the $(100)_\beta$ and $(1\bar{1}0)_{\gamma'}$ planes (i.e., the foil plane) are shown in Figure 13. No significant site coincidence has resulted from the N-W rotation, θ. However, the parallel close packed planes show agreement in d-spacing; d $(01\bar{1})_\beta$ = 2.022A, d $(11\bar{1})_{\gamma'}$ = 2.075A. The Moire' pattern arising from the near alignment of these overlapping Bragg planes of similar spacing can be described as phase interference patterns of spacing $|\frac{1}{\Delta \vec{g}}|$ and oriented normal to $\Delta \vec{g}$.[22] From Figure 9c, $\Delta \vec{g} = \vec{g}(01\bar{1})_\beta - \vec{g}(11\bar{1})_{\gamma'}$ or 80 ± 5 A. The measured Moire' spacing

from Figure 9c was 86 Å, which is good agreement with the predicted value.

The tweed or cross-hatched β-NiAl structure referred to previously will now be discussed. Figure 14 shows a very fine modulated structure having a 30-60 Å periodicity parallel to (011) and (01$\bar{1}$). Diffuse patches (P) also show 60-100 Å modulations parallel to (010) and (001). The diffraction pattern in Figure 14b shows both [01$\bar{1}$] and [011] streaking as well as what appear to be satellite spots oriented along [002] and [020] directions in reciprocal space.

These diffraction effects have been observed for other β-phase alloys and were recently examined in detail for quenched Cu-Zn.[19,23] It was concluded that the diffuse intensity resulted from all variants of <110> rel rods in reciprocal space. Thus, for a perfect zone axis orientation, the diffuse streaking was indeed along <110> directions. However, at some small angle from ideal Bragg conditions, the Ewald sphere intersected rel rods from other <110> directions not in the zone plane. For the case of a [100] zone, it was found that the rel rods produced satellite spots displaced along <100> directions in reciprocal space. This is exactly what is shown in Figure 14c. It was also reported that as $\vec{s}$ increased, the spacing of the satellites increased. This effect is apparent in Figure 14c.

The origin of the rel rods for Cu-Zn was concluded to be a low frequency phonon wave in {110} planes along <110> directions. The phonon wave derives directly from the inherent lattice instability of β-phase alloys in these directions. The likely association of this phonon wave with the atomic shuffling required to generate martensitic structures was also mentioned. Since the observation of diffuse scattering effects had been identified as a premartensitic effect, it may be surmised that the phonon wave is a precursor to the martensitic transformation. Some regions indeed showed martensite plates in the βNiAl phase in the present study.

Satellite spots were also observed in aged Cu-Zn alloys as a result of spinodal decomposition.[23] Again the intensity maxima were displaced with respect to the fundamental reflections; however, the degree of displacement did not vary with $\vec{s}$, nor did <110> streaking result when $\vec{s} = 0$, as occurred in the NiAl. Also, <100> cross-hatching was observed as the distinctive structural characteristic of the spinodal transformation. Thus, the diffraction effects in the present study were consistent with the phonon instability phenomenon, while the modulated structure (along <100> in Figures 9c and 14b) was indicative of spinodal decomposition. It appears that both the phonon and spinodal phenomena may occur simultaneously in β-NiAl.

2) Oxide Structures

a) Random Al_2O_3 scales. An area of scale was found where the metal substrate had been completely electropolished. The structure, after

eight minutes of ion thinning is shown in Figure 15. The scale shows widely varying thickness from grain to grain. Some grains, marked (G), were quite electron transparent, but in general the scale was too thick to give good diffraction contrast and resolution. A large amount of porosity, marked (P), is evident. The mean void diameter was found to be 430 ± 130 Å (1σ). After complete ion thinning, ring patterns were obtained in electron diffraction, Figure 16. The even distribution of diffraction spots is clear evidence for the random orientation of these oxide grains. The d-values from the indexed pattern are shown in Table I. All but two of the inner α-Al_2O_3 lines were present; there were no unexpected absences that may have indicated a preferred growth direction. The overall structure of the random α-Al_2O_3 grains after ion thinning was completed (90 minutes), is shown in Figure 17. Here the average grain size was 0.14 ± 0.03 μm. The voids had varied shapes, from equiaxed to tubular. In the grain indicated in Figure 17a, some of the tubular voids can be seen by stereoviewing to be oriented at various angles to the plane of oxidation. In general, stereopairs showed the voids to be distributed throughout the foil thickness. The average void size was 100 ± 60 Å. Large variations in void size are apparent from Figure 17; however, few voids approach the 430 Å average void size found after eight minutes of ion thinning. It is concluded that many of the large voids initially present in the scale have been removed by ion thinning. It is believed that the

large voids existed at the oxide-gas surface as was the case for thicker oxides formed on NiCrAl alloys.

The average void diameter is plotted as a function of ion thinning time in Figure 18. This trend confirmed the premise that a gradient in the void size existed from the outer layer of the scale. The void size at 90 minutes of ion thinning represents a true average for all voids present. However, when the scale was thicker, the fine voids were not observable, and the average values at short ion thinning times were biased towards the larger voids. The criterion for visibility of voids in thick foils ($>5\xi_g$) is that they are $>0.5\xi_g$.[22] This is shown on Figure 18 for $\vec{g} = (11\bar{2}0)$. This explains why voids smaller than $\sim$300 Å were not observed when the scale was thick.

The thickness at which the small voids should be invisible is $\sim$3300 Å. The total oxide thickness at 0.1 hr was calculated from k_p (1100°C) = $0.002\frac{(mg/cm^2)^2}{hr}$ oxygen (Ref. 15) to be $\sim$750 Å. This is clearly too small a value to mask normal contrast effects from small voids or any other feature. Errors in this calculation due to incorrect k_p, measured time or temperature, or variations in oxide thickness are unlikely to account for more than a factor of two error in the thickness calculation. A high degree of surface porosity may contribute to a thicker oxide for a given weight gain of oxygen gas, but again it is difficult to rationalize such a large discrepancy. The thickness after ion thinning was estimated

to be ~400 Å from stereopair measurements of a number of grain boundaries. This appears to be reasonable considering the lack of thickness fringes and the lack of overlapping grains.

The small grain size precluded any controlled tilting in diffraction mode in order to obtain two-beam conditions for optimum contrast. Elastic strain contrast features were commonly observed, however, simply by examining a large number of grains over a range of specimen tilt. The lineal feature, "A", in Figure 19a is probably a dislocation. It appears to bisect the grain and weave around two voids in the grain, due to elastic interaction with the voids.

In other grains the elastic strain contrast cannot be resolutely termed dislocations, but does indeed appear to be associated with the pores (see "B" in Figure 19). One account for the strain contrast is the alteration of internal stresses at the free surface of a void. An alternative way of discussing the origin of strain contrast around small voids is from surface energy stresses. The work done in adding material to a curved surface is $\Delta P dV$, where ΔP is the pressure or stress difference from the interior of the material to the external pressure, and dV is the incremental volume change. This is equal to the increase in total surface energy of the system given by γdA, where γ is surface energy and dA is the incremental increase in area. Substitution of the geometric relations for a sphere leads to the Laplace equation:[24]

$$P - P_r = \frac{2\gamma}{r_i} \qquad \text{(Eqn. 1)}$$

where P is the pressure or stress resulting in the solid, P_r is the external pressure, and r_i is the radius of curvature of a particle. Concave surfaces may be dealt with by using negative radii. This relation is equivalent to the derivation by Kuczynski based entirely on balancing the forces of surface energy and the opposing reaction stresses at static equilibrium.[25] Thus, the surface energy stresses are seen to always act in the direction that decreased the surface area. In the case of a small particle an internal compressive stress is generated, while in the case of a small cavity an internal tensile stress results in the adjacent material.

The Laplace equation was applied to the case of voids in the Al_2O_3 scales. The pressure in the void was found to be negligible ($<<1$ atm = 0.1 MPa) based on equilibrium vapor pressures calculations for Al_2O_3.[26] The surface energy of Al_2O_3 at 1100°C was estimated from $\gamma = 1.4 - 2.32\times10^{-4}T(^{o}K)$ Joules/m^2 in Ref. 27 to be 1.081 Joules/m^2. The resultant tensile stresses acting on the surface of the voids is shown as the dashed line in Figure 20 for various void sizes. It can be seen that stresses well above 100 MPa are generated for voids with radii less than 200 Å.

The potential for plastic deformation by these stresses is now considered. Extrapolated strength values for single crystal Al_2O_3 at 1100°C are ≈100 MPa.[28] These values are seen to be in the range

for those calculated for the voids. However, the published values represent stresses required for dislocation motion and multiplication. In general, there are few dislocations in the oxide available for motion , thus the surface energy stresses cannot operate in this mode of plastic deformation.

The diminution of surface energy stresses with distance from the void was treated in order to assess the effective range of the surface stresses. The void was treated as a thick-walled sphere with a pressure differential between the internal and external surfaces. The variation of stress with distance from the center of the cavity, r, is given by:[29]

$$\sigma_r = \frac{\sigma_e (r_e)^3 (r^3 - r_i^3) + \sigma_i (r_i^3) (r_e^3 - r^3)}{r^3 (r_i^3 - r_e^3)} \qquad \text{(Eqn. 2)}$$

where the subscripts "e" refer to external, and "i" refer to internal. Since $r_e >> r > r_i$, this relation can be simplified to:

$$\sigma_r = -\sigma_e - (\frac{r_i}{r})^3 (\sigma_i - \sigma_e) \qquad \text{(Eqn. 3)}$$

Since σ_e = 1 atm = 0.101 MPa, $\sigma_i >> \sigma_e$, and $\sigma_r \approx -(\frac{r_i}{r})^3 \sigma_i$ for the important values of r. Note that positive σ_i was defined as an internal pressure, so that the tensile stress acting on the void surface produced by surface energy is here treated as a negative "pressure". The resultant stresses, σ_r, are thus always positive tensile stresses according to the usual convention. The surface energy stresses thus decay rapidly as $\frac{1}{r^3}$. The decay curves for a

number of void radii are shown in Figure 20 as solid lines.

The total elastic strain energy around a void was also calculated in order to assess the likelihood of nucleating a dislocation. The strain energy per unit volume is given by:[30]

$$\frac{dE}{dV} = \frac{1/2\ \sigma_r^2}{K} \qquad \text{(Eqn. 4)}$$

where σ_r is the hydrostatic stress, given by Eqn. 3 for void surface energy stresses, and K is the bulk modulus for Al_2O_3 at 1100°C (2.258×10^{11} Pa).[31] Integrating with respect to volume yields:

$$E_r = \frac{8}{3}\ \frac{\pi\gamma^2}{K}\ (r_i)\ \left(1 - \left(\frac{r_i}{r}\right)^3\right) \qquad \text{(Eqn. 5a)}$$

$$\therefore E_r = 4.34 \times 10^{-21}\ r_i\ (\text{Joule/A}^{\circ}) \qquad \text{(Eqn. 5b)}$$

For a 50 A° void radius the strain energy over a large field (r) is 2.17×10^{-19} Joule.

The strain energy per unit length for an edge dislocation is given by:[32]

$$E_{\perp} = \frac{G\ b^2\ \ln r_G/r_o}{4\pi\ (1-\nu)} \qquad \text{(Eqn. 6a)}$$

where G is the shear modulus (1.374×10^{11} Pa for Al_2O_3 at 1100°C), ν is Poisson's ratio (0.243), r_G is the radius of the grains ($\sim$500 A°) and r_o is the dislocation core ($\sim$10 A°). For a dislocation loop of radius r , the elastic strain energy is given by:

$$E_{\perp} = (12.792 \times 10^{-19}) \text{ Joule/A}^{o} \cdot 2\pi r_L \qquad \text{(Eqn. 6b)}$$

Thus, for a loop twice the average radius of the voids, the dislocation strain energy is 8.0×10^{-16} Joule. Since this is three orders of magnitude greater than the elastic strain energy around the voids, it is unlikely that the voids can nucleate a dislocation. This is the case for any void in the size range found, for:

$$\frac{E_{\perp}}{E_r} = 1.85 \times 10^{3} \frac{r_L}{r_i}, \text{ and } \frac{r_L}{r_i} > 1 \qquad \text{(Eqn. 8)}$$

Based on the above energetic considerations, the surface energy stresses were found to be large enough to cause dislocation motion of pre-existing dislocations and to produce elastic strain energy about three orders of magnitude too small to nucleate a dislocation. The latter is consistent with the low dislocation density observed experimentally.

b) Oriented Al_2O_3 scales. Much of the oxide scale observed on pure NiCrAl was notably different than the distinct randomly oriented Al_2O_3 grains just discussed. Some degree of preferred orientation of these new areas was always observed. Individual grains were seldom resolved, and the structure appeared to be that of fine slightly misoriented subgrains.

The degree of preferred orientation is shown in Figure 21. While the major diffraction spots were found to fit an [0001] Al_2O_3 zone, numerous other spots of random orientation were also

present. The $\{30\bar{3}0\}$ spots were arcs of $\sim 7^{o}$, thus some rotational variation of the [0001] subgrains was also present. This [0001] pattern was obtained with the plane of oxidation tilted 17^{o} about $[03\bar{3}0]$. Thus, the actual plane of oxidation was not a low index plane. Coincident oxide and metal diffraction patterns were unobtainable because thin metal was not present in these areas. Thus, possible epitaxial relationships with the metal could not be determined.

The structure of the oriented oxide is shown in Figure 22. The absence of distinct grain boundaries is evident in Figure 22a. A high density of fine 100 ± 40 Å voids is also present, similar to the voids found in the random Al_2O_3. Other areas in the oriented oxide had average void sizes of 130 ± 55 Å and 100 ± 65 Å. Colonies of distorted Moire´ patterns are also present in Figure 22b (arrows). Since the occurrence of Moire´ patterns indicates a layered structure,[22] the colonies suggest a layered grain or subgrain arrangement. In Figure 22b, distinct grains can indeed be seen to be associated with the Moire´ patterns. The subgrain size was measured from the size of Moire´ colonies in various areas to be 0.094 μm + 0.033 μm. The subject of oriented oxide and Moire´ patterns will be treated thoroughly for the NiCrAl+Y and NiCrAl+Zr alloys, where more detail was observed.

B) Ni-15Cr-13Al + 0.5Y

1) Metal Structures

The structures observed in the NiCrAl + 0.5Y substrate after 0.1 hr oxidation at 1100°C were in general similar to those found after oxidizing the pure alloy. Some differences in detail may be noted between the two alloys. However, due to the diverse structural features found on any one particular sample, it is not immediately possible to ascribe these differences to a compositional effect alone.

a) γ/γ' structures at the oxide-metal interface. Overlapping γ/γ' metal and random Al_2O_3 oxide areas were found in this Y-doped alloy, as they were for the pure NiCrAl. An example of such a structure is shown in Figure 23. Clearly, in Figure 23a, a mosaic of fine grain oxide is present in the right half of the micrograph. Towards the left, there are faint dislocation images, D, (many beam conditions) in the γ/γ', reminiscent of the bi-directional arrays found in the pure NiCrAl. In Figure 23b the dislocations in the same area have stronger contrast (nearly 2-beam conditions) and a zig-zag nature is apparent. The segments of the dislocations are on the order of the grain size of the oxide, i.e., 0.1-0.2 μm. In Figure 24 the oxide-metal interface is shown in more detail, where a patch of metal remains in contact with the oxide at the interface (I). The spotty nature of the metal is believed to be damage from ion thinning. A scattering of inter- and intragranular porosity (P) is apparent in the oxide in both Figure 24 and Figure 23a.

Zone axis diffraction patterns obtained near the orientation of Figure 23a and b are shown in Figure 25a and b, respectively. The patterns were identified as γ-Ni (spots) and α-Al_2O_3 (rings). The single crystal metal pattern shows no γ' superlattice spots; thus, the original Ni_3Al phase has been decomposed by aluminum loss during oxidation. The rotational smearing of the spots in Figure 25b is another indication of lattice distortion due to stresses caused by oxidation. The ring patterns were unequivocally α-Al_2O_3. There is very little evidence in either pattern for preferred orientations of the oxide grains.

In an area immediately adjacent to that in Figure 23, a complex tangle of dislocations was observed, again in the depleted γ/γ' phase (Figure 26). The dislocation density was estimated to be $\sim 2 \times 10^{10} cm^{-2}$ (the same as for pure NiCrAl). An attempt was made to study the line direction of the dislocations. While some evidence for <110> alignment was obtained, the wide variation in the direction of the segments precluded a more substantive determination.

b) β-NiAl structures at the oxide-metal interface. The oxidized β-NiAl phase showed some features similar to those in the pure NiCrAl alloy. Basically, γ'-Ni_3Al subgrains formed as a result of aluminum depletion during oxidation. In Figure 27b, a large 1 μm γ' subgrain has been imaged, as well as $\sim$0.1 μm oxide grains. Dislocations can be seen in the interior of the subgrain. Diffraction has shown the presence of both random and oriented sesquioxide. (The oxide structures will be discussed in the next section.) Here it

was found that $[1\bar{2}\bar{1}0]$ α-$(Al,Cr)_2O_3$ || [110] γ'-Ni_3Al , i.e., both close packed directions were parallel. Also $d_{(30\bar{3}0)\alpha}$ = 1.408 Å $\simeq$ $d_{(220)\gamma}$ = 1.273 Å. Thus, the possibility of some epitaxial relationship is acknowledged.

Another example of the γ' subgrain structure is given in Figure 28. A number of layered γ' subgrains are present as well as areas of β NiAl. The β-NiAl areas were identified from dark field (Figure 28b, $\bar{g} = (200)_\beta$). Oxide grains with random orientations were also identified. The NiAl areas showed striations which gave rise to rel rods in diffraction perpendicular to the plane of the striations (Figure 28c). The identification of both oxide and metal phases proves that the oxide-metal interface structures are again represented here. It appears that both random and oriented oxide phases may be in contact with the oxidized β phase. Random oxide has also been observed in contact with the γ/γ' phase in both pure and Y-doped material.

2) Oriented Oxide Structures

a) Phase identification and epitaxy. The structure of the oriented oxide on the NiCrAl + 0.5Y alloy was characterized by small colonies of Moire' patterns and lineal precipitate-like features. Since the treatment of these structures is based substantially on the analysis of the diffraction patterns, this section will begin with a discussion of phase identification.

The possible stable oxides which are commonly found on NiCrAl alloys are the NiO monoxide, $Ni(Al,Cr)_2O_4$ spinels, and the

α-$(Al,Cr)_2O_3$ sesquioxides.[12,13,14] The major oxide formed at 1100°C on alloys near the composition used in this study is α-Al_2O_3, with small amounts of $NiAl_2O_4$ increasing slightly with time. However, at very short times all the oxides may be found as transient oxides before steady state kinetics are achieved. In order to systematically separate the possible diffraction patterns, it is illustrative to first consider the three crystal structures. All three oxide types have been described as nearly close-packed anion structures with different cation sublattices. Thus, for mixed oriented oxide structures, it would be expected that the anion lattices match crystallographically.

NiO and spinel can be described as FCC arrangements of oxygen atoms, with {111} and <110> as the close packed planes and directions. For a mixed oxide with continuity of the oxygen lattice, the following orientation relationships would be expected for NiO (N), $NiAl_2O_4$ (S), and α-Al_2O_3 (α):

$$\{0001\}_\alpha \parallel \{111\}_S \parallel \{111\}_N$$

$$\langle 10\bar{1}0\rangle_\alpha \parallel \langle 110\rangle_S \parallel \langle 110\rangle_N$$

A diffraction pattern for the oriented scale formed on NiCrAl + 0.5Y is shown in Figure 29a. The schematic pattern in 29b shows the basal zone of Al_2O_3 as well as [111] zones for NiO and $NiAl_2O_4$. Indexing of the patterns was performed by considering the d-spacings of all possible oxides (Appendix A). The spot pattern was found to be an [0001] Al_2O_3 pattern. The arc pattern, nearly coincident with

the spot pattern, was indexed as [0001] α-$(Al,Cr)_2O_3$. The lattice parameter of the arc pattern, a = 4.84 Å, is between that for pure Al_2O_3 (4.758 Å) and pure Cr_2O_3 (4.954 Å). The inner arc pattern was found to be [$\bar{1}$11] spinel with a_o = 8.25 Å, as compared to 8.048 Å for pure $NiAl_2O_4$. No possible indexing scheme allowed for the existence of NiO. The rotational variation in the arc patterns was 15°.

The pattern for a similar area was obtained for the plane of oxidation (Figure 30). Here reflections from the [0001] zone of α-$(Al,Cr)_2O_3$ were still observed. The spinel pattern has become primarily [$\bar{1}$12]. This spinel zone possesses good correspondence of interplanar spacing and crystallographic directions with the sesquioxide pattern. The occurrence of ($\bar{1}1\bar{1}$) spinel spots eliminated the possibility of NiO or a different chemistry of sesquioxide as the second pattern. Both patterns are thus consistent as oriented sesquioxide + spinel with a fair degree of crystallographic alignment. The spot pattern in Figure 29a indicates the presence of some large grains.

The degree of preferred orientation suggests that the oxide has grown epitaxially from the metal surface. Unfortunately, most oxide areas exhibiting preferred orientation did not have suitable thin metal areas in proximity. Thus, epitaxial relationships were not studied extensively. It was occasionally possible, however, to obtain superimposed metal and oriented oxide diffraction patterns, as shown in Figure 31a. The intense spot pattern was a [$\bar{1}$11] zone

of γ'-Ni_3Al. The diffuse arcs were indexed as an [0001] zone of α-$(Al,Cr)_2O_3$ ($a = 4.83$ Å), and the spots lying on the arcs were indexed as an [0001] zone of pure α-Al_2O_3 ($a = 4.758$). A nearby area produced the pattern in 31b, again being a $[\bar{1}11]$ zone of γ' with a corresponding oxide arc pattern. The d-spacings of the arc pattern were high for the oxides in Appendix A. The closest fit was for NiO with $a_o = 4.214$ Å (compared to 4.177). On the basis of this limited amount of data, the following epitaxial relationships were found.

$$(\bar{1}11)\gamma' \;||\; (0001)Al_2O_3 \text{ or } (\bar{1}11)NiO$$

$$\langle 110\rangle\gamma' \;||\; \langle 10\bar{1}0\rangle Al_2O_3 \text{ or } \langle 110\rangle NiO$$

Again close packed planes and directions were found to be correlated, now between metal and oxide crystals. This is to be expected for Ni_3Al and NiO, where both metal sublattices are FCC. Similar orientation relationships were found for in-situ oxidation of Ni at 600°C, but not exclusively.[33] It is believed that the orientation of subsequent Al_2O_3 layers is derived from anion lattice matching with the initial epitaxial NiO scale.

b) Moire' patterns and precipitates. The arrangement of Moire' colonies in the oriented $(Al,Cr)_2O_3$ scale formed on NiCrAl+Y is shown in Figure 32. In general, small 750 Å "subgrains" of Moire' patterns were dispersed throughout the scale. However, in some cases numerous subgrains were clustered into large 0.4 μm grains as shown in Figure 32c.

Moire' patterns are produced by phase contrast produced by the interaction of two nearly coincident diffracted beams. This commonly occurs for a layered arrangement of two crystals having slightly different Bragg plane spacings (parallel Moire') or orientations (rotational Moire'). The resultant Moire' pattern is a set of parallel fringes whose spacing is $\frac{1}{\Delta\bar{g}}$ and whose direction is perpendicular to $\Delta\bar{g}$.[22] The diffraction patterns of the previous section have shown that certain Al_2O_3 and $NiAl_2O_4$ planes are nearly coincident. Thus, it is concluded that the Moire' patterns arose from a layered arrangement of Al_2O_3 and $NiAl_2O_4$ subgrains.

The spacing of the Moire' patterns were thus calculated from $1/\Delta\bar{g}$ from the diffraction patterns for parallel Bragg planes of Al_2O_3 and $NiAl_2O_4$. For exactly parallel $\bar{g} = (30\bar{3}0)Al_2O_3$ and $(440)NiAl_2O_4$, $1/\Delta\bar{g} = 33$ Å. Since considerable rotational variations in oxide orientation were observed ($\sim 15^{\circ}$), it is possible to have rotational Moire' patterns as well. For example, $(30\bar{3}0)Al_2O_3$ and $(440)NiAl_2O_4$ planes rotated 4° with respect to each other would produce a Moire' pattern with a 17 Å spacing. (Larger rotational mismatches are clearly possible, but these would produce Moire' spacings increasingly more difficult to resolve.)

The actual Moire' spacings were measured from Figure 32c, where $\Delta\bar{g} = \bar{g}(440)_S - \bar{g}(30\bar{3}0)_\alpha$. The spacings ranged from ~20-30 Å, with an average spacing of 24 ± 4 Å. Similarly, spacings measured from Figure 34c ranged from ~15-50 Å, with an average of 26 ± 7 Å. The Moire' spacing in Figure 32b was 21 Å. These values are in

accordance with those previously calculated from the appropriate $\frac{1}{\Delta \bar{g}}$ obtained from the diffraction patterns ($\leq$33 Å).

An additional feature was often observed in the oriented Al_2O_3 scale formed on NiCrAl+Y. Fine 50 Å wide plates (P) or blades were nearly aligned with <10$\bar{1}$0> directions in Figure 33. In Figure 34a, similar lineal <10$\bar{1}$0> aligned features were observed, although they were less distinct. This area also contained a high density of the Moire´ colonies previously discussed, as shown in the dark field companion micrograph, Figure 34b. It is therefore reasonable to expect that both the Moire´ structure and plates represent two forms of the secondary $NiAl_2O_4$ phase -- one as a layered structure, the other as a Widmanstatten precipitate. Recently, precipitate structures in oxides has been reviewed.[34] Although the specific case of spinel precipitates in sesquioxides was not treated, it was generally true that precipitate morphologies resulted from a tendency to maintain coherency with the close-packed anion structure of the parent phase. Thus, for $NiAl_2O_4$ in Al_2O_3, the parallelism of close-packed planes and directions would be preserved for small coherent precipitates. Since the diffraction patterns from the area of Figure 34 exhibited these same close-packed orientation relationships (see Figure 29), it is reasonable to interpret the plates as spinel precipitates.

One final structure observed in the regions of the oriented Al_2O_3 scale needs to be mentioned, that of large α-Al_2O_3 grains. Here the average grain diameter was 0.200 $\pm$ 0.068 µm, or about

three times the usual grain size of Al_2O_3 in the oriented oxide regions. The typical structure is shown in Figure 35. The large grains are heavily decorated with intergranular porosity (I.P.) and are peppered with dispersed porosity (D.P.) inside each grain. The dispersed porosity was 89 ± 35 Å on the average, and was found to be somewhat faceted and to lie within the grain volume by stereomicroscopy. By comparison the voids in the finer grained areas of the oriented oxide were also faceted and 110 ± 60 Å in diameter. The large grains commonly had orientations similar to each other as well as to the finer grained oriented scale. Apparently grain growth of the oriented oxide occurred at varying rates in different areas of the scale.

The porosity in the regions of random Al_2O_3 was for the most part intergranular, Figure 36. This form of porosity closely resembles the long channels of porosity in the large grained oriented scale (Figure 35). In summary, three types of porosity were observed in the Y-doped NiCrAl: (1) tubular intergranular porosity in both random and oriented scales (Figures 23, 24, 35 and 36); (2) faceted intergranular voids in the oriented oxide (Figures 32b and 34a); and (3) dispersed porosity in large oriented grains (Figure 35).

Other fine features were occasionally observed in the random Al_2O_3 scale, as shown in Figure 37. These may be aligned spinel precipitates or mechanical microtwins.

3) Transition Between Oriented and Random Oxide Structures

Some areas exhibited features common to both the random and oriented Al_2O_3 scale. Diffraction patterns identified the light grains in the top of Figure 38 as randomly oriented Al_2O_3 grains. Towards the thicker area of the foil (lower half of Figure 38), colonies of Moire' patterns are clearly visible (M). It is believed that the Moire' structures are representative of the oriented α-$(Al,Cr)_2O_3$ + $Ni(Al,Cr)_2O_4$ structures previously discussed. Since the Moire' colonies are only present in the thicker areas, it indicates that the oriented scale is positioned as a layer on the surface of the random oxide. This interpretation is compositionally consistent with the accepted interpretations of transient oxidation. That is, the first oxides to form contain all the elements of the alloy (Ni, Cr, and Al). Further oxidation allows a continuous scale of the oxide having the lowest free energy of formation, α-(Al_2O_3). Thus it appears that the oriented α-$(Al,Cr)_2O_3$ + $Ni(Al,Cr)_2O_4$ was the first oxide to form, and pure Al_2O_3 formed beneath this layer by subsequent inward oxygen diffusion.

C) Ni-15Cr-13Al + 0.5Zr

1) Oriented Spinel Scale, General Structure

The structures studied on the Zr-doped alloy were limited to the oxides only. The scales studied were of the spinel structure, were always in a preferred orientation, and exhibited very fine features -- such as precipitates, Moire' patterns, and antiphase domain boundaries. Porosity in the scale was also prevalent, as

it was in the pure and Y-doped NiCrAl.

An overview of one area of the oxide formed is shown in Figure 39. No ion thinning of the scale had been performed at this point. The scale is seen to be very non-uniform in thickness. The preferential oxidation of the alloy grain boundaries is indicated by the arrows.

The preferred orientation of the scale was evident from the single crystal diffraction patterns shown in Figure 40. The as-oxidized scale was somewhat thick for electron diffraction, but did show the hexagonal symmetry of an [0001] zone expected for a corundum-type structure (Figure 40a). After 10 minutes of ion thinning the $\{30\bar{3}0\}_\alpha$ reflections appeared to remain, but the symmetry now indicated the $[\bar{1}11]$ zone of cubic structures (Figure 40b). The $[\bar{1}12]$ zone in Figure 40c is further evidence of the cubic structure. The results indicate that $d_{\{30\bar{3}0\}_\alpha}$ (rhombohedral) $\equiv d_{\{440\}}$ (cubic), and that ion thinning has thus exposed a γ-Al_2O_3 spinel oxide near the midsection of the scale.

From Appendix A, $d_{\{440\}_\gamma} = 1.398$ Å. This is the same as $d_{(30\bar{3}0)_A} = 1.395$ Å found for the α-$(Al,Cr)_2O_3$ formed on NiCrAl+Y (section IB). These values were the most consistent with the camera constant of the microscope, although a gold film calibration was not obtained on this specimen. It is acknowledged that other stoichiometries of the rhombohedral and cubic oxides could be invoked to give $d_{\{30\bar{3}0\}}$ rhombohedral $= d_{\{440\}}$ cubic. For example, $d_{\{440\}}$ of pure $NiAl_2O_4 = 1.423$ Å would match $d_{\{30\bar{3}0\}}$ of a Cr-rich

sesquioxide, α-$(Cr,Al)_2O_3$. SEM-EDS spectra obtained on the cubic oxide did not show Ni/Al intensity ratios higher than those for the oriented α-$(Al,Cr)_2O_3$ scales. It is concluded that an aluminum-rich cubic oxide, i.e., γ-Al_2O_3 pseudo-spinel, was the major oxide after removing the outer layer by ion thinning.

Secondary arcs were observed in both Figures 40a and 40b parallel and adjacent to the $\{30\bar{3}0\}_\alpha$ and $\{440\}_\gamma$ reflections, respectively. The d-spacing was 1.452 $\mathring{A}$ as obtained for d{440} of the oriented $Ni(Al,Cr)_2O_4$ found on NiCrAl+Y. (The {220} spinel reflection was not observed because of the low intensity of the pattern.) These arcs disappeared after 20 minutes of ion thinning, leaving γ-Al_2O_3 as the primary oxide. The following summarizes the orientation relationships found in the oriented oxides on NiCrAl+Zr:

1) $d\{440\}Ni(Al,Cr)_2O_4 = d\{440\}\ \gamma\text{-}Al_2O_3 = d\{30\bar{3}0\}_\alpha (Al,Cr)_2O_3$

   (a_o = 8.21 $\mathring{A}$) (a_o = 7.908 $\mathring{A}$) (a_o = 4.832 $\mathring{A}$)

2) $\{\bar{1}11\}_\gamma \parallel \{\bar{1}11\}_s \parallel \{0001\}_\alpha$

3) $\langle 110\rangle_\gamma \parallel \langle 110\rangle_s \parallel \langle 10\bar{1}0\rangle_\alpha$

This is similar to the parallelism of close packed oxygen planes and directions found for $(Al,Cr)_2O_3$ and $Ni(Al,Cr)_2O_4$ scales formed on NiCrAl+Y.

Similar orientation relationships have been recorded for a Ni-10Cr-14Al (w/o) alloy oxidized 24 hours at 900°C (Koch & Romeo).[14] However, the diffraction patterns were analyzed only as

ring patterns, and no discussion was made of the symmetry or orientation of the pattern. An analysis of the pattern is given in Figure 40d. It is immediately clear that two [$\bar{1}11$] cubic patterns exist and that a [0001] rhombohedral zone is superimposed on them. Koch & Romeo indexed the outer arc #8 of the doublets as {440} $NiAl_2O_4$ (1.423 Å) and the inner arc #7 as {440} $NiCr_2O_4$ (1.471 Å). The reflections labeled #3 were indexed as {311} $NiAl_2O_4$ (2.427 Å) But such reflections do not possess hexagonal symmetry, nor do they belong in a [$\bar{1}11$] cubic zone. It is more compelling to discuss these reflections as the {$11\bar{2}0$}, d = 2.471 Å, of an [0001] hexagonal pattern. This is shown in the schematic; the hexagonal pattern fits the d-spacings of α-$(Cr,Al)_2O_3$ sesquioxide, a = 4.942 Å. Measurement of d-spacings from the reproduced photo of the diffraction pattern showed a large variation for #3 reflections. It is thus believed that the discrepancy between published (2.42 Å) and proposed (2.47 Å) spacings may not be real.

It is interesting to point out the similarities between this pattern obtained by 900°C oxidation with those obtained after 1100°C oxidation (Figures 40a and b). In both cases a doublet of the {440} spinel reflection occurred and in both cases d {440} spinel ≡ d {$30\bar{3}0$} hexagonal. The schematics in Figure 40a and b were superimposed in Figure 40e. Comparison with the schematic of Figure 40d shows the striking similarities of the 900°C and 1100°C oxides. The 1100°C scales required ion thinning to reveal all the cubic phases, and the oxides appeared to be more aluminum-rich.

Oxide orientations on the NiCrAl+Zr alloy were found to be primarily of one zone over the entire metal dendrite (as replicated by oxidation). Other metal dendrites were found to have different oxide orientations formed over them. In accord with the data found for the Y-doped alloy, epitaxial oxide-metal relationships appear to be the cause of the preferred oxide orientation found here. The lack of any thin metal areas precluded study of the specific epitaxial relationships involved.

The oxide structures to be discussed below were from two adjacent metal dendrites. One general oxide orientation had $(011)\gamma\text{-}Al_2O_3$ near the plane of oxidation; the other was near $(\bar{1}12)$. Both areas had many common structural features such as fine precipitates and Moire' fringes. However, features peculiar to the [011] orientation were regular arrays of superlattice reflections and large irregular domains. The basic structure of both orientations is typified by that in Figure 41. The structure appears to be quite similar to the oriented oxide found on the Y-doped alloy. Colonies of distorted Moire' patterns or strain contours 0.15 ± 0.07 μm diameter are revealed in dark field (Figure 41b). A dispersion of 200 ± 100 Å voids is also present. The colonies are believed to represent small subgrains of large areas having substantially the same orientation.

2) Defect Spinel ($\gamma\text{-}Al_2O_3$)

The array of superlattice spots for the area of scale having an [011] spinel orientation is shown in Figure 42. The schematic

identifies two subcells in reciprocal space which account for all the extra spots: set 1 consists of 1/2 $\bar{g}$ $(11\bar{1})$, 1/3 $\bar{g}$ $(3\bar{1}1)$; set 2 consists of 1/2 $\bar{g}$ $(1\bar{1}1)$, 1/3 $\bar{g}$ $(31\bar{1})$. It is expected that each superlattice cell represents one of several possible variants arising from the four {111} planes and the twelve {311} planes in a cubic material.

Ordered spinel structures have previously been observed in $MgAl_2O_4$ spinel, as reviewed by Heuer and Mitchell.[34] The structure known as δ_2 was described as a periodic disruption of the normal spinel ordering with an array of APB's. An enlarged unit cell resulted such that $a_\delta = 3/2\ a_o$, $b_\delta = 2a_o$, $c_\delta = a_o$. This phase has been described as a transitional phase towards α-Al_2O_3 formation. An attempt was made to determine what (hkl) planes in the δ_2 structure would give rise to 1/2 $\bar{g}$ {111} and 1/3 $\bar{g}$ {311} spinel reflections. The following indices were obtained by the transformation:

(hkl) Spinel	$(hkl)\delta_2$
1/2 (111)	(3/4, 1, 1/2)
1/3 (311)	(3/2, 2/3, 1/3)
1/3 (131)	(1/2, 2/3, 1/3)
1/3 (113)	(1/2, 2/3, 1)

None of the $(hkl)\delta_2$ were completely integral, which implied that a larger unit cell would be required to give reflections at 1/2 $\bar{g}$ (111) and 1/3 $\bar{g}$ (311).

Antiphase domain boundaries (APB) were commonly observed within the subgrains of the [011] oriented spinel, Figure 43. The average domain size was 170 ± 60 Å. Some degree of linearity and parallelism of the APB's was apparent and suggests a crystallographic relationship with the lattice. The directions of the APB's were plotted in Figure 44. Although some grouping of the directions existed, no specific set of low indice directions was apparent. It is important to point out that the APB's were imaged with normal allowed spinel reflections (i.e., $(1\bar{1}1)$ and $(3\bar{1}1)$). The domains thus represent regions of order which grew epitaxially from a parent substrate phase with a less ordered structure, probably based on NiO. It is not believed that the APB's arose from domains of the weak superlattice structure shown in Figure 42.

3) Precipitation and Fine Moire´ Patterns in γ-Al_2O_3 Spinel

In addition to the APB's, fine plate-like precipitates were observed in the [011] oriented spinel. It was generally necessary to use precision dark field to resolve these features, because bright field images were confused by strain contrast or distorted Moire´ patterns as in Figure 41. Three orientations of 12 Å wide blades (viewed end-on) are exhibited in Figure 45a. The right half of the micrograph also exhibits APB's. In Figure 45b, 150 Å wide blades (B) can be seen as well as 10 Å wide blades viewed edge-on.

The directions of these features from five colonies or subgrains were plotted in a stereographic projection, Figure 46. All of the projected directions fell into three groupings. Two of the groupings

near [$\bar{2}\bar{1}$1] and [2$\bar{1}$1], were parallel to the projections of the close-packed [$\bar{1}$01] and [101] directions on a [011] zone. The third grouping is not parallel to any crystallographic directions but is 90 ± 5° from the ($\bar{3}\bar{1}$1) pole and may thus represent blades lying in the ($\bar{3}\bar{1}$1) plane. In fact, the other two directions can be viewed as planar defects lying in ($\bar{1}\bar{1}$1) and (1$\bar{1}$1) planes.

The structure in the [$\bar{1}$12] oriented spinel scale over an adjoining metal dendrite will now be discussed. Features similar to the fine precipitates in the [011] oriented spinel were common. A dense concentration of parallel blade-like precipitates (viewed edge-on) is shown in Figure 47. Small blade-like clusters of Moire´ frings are seen to be parallel to the precipitate directions. In some areas the Moire´ fringes are adjacent to and nearly distinguishable from the precipitates. The directions of both are shown in Figure 48. The major directions obtained from Figure 47 (large triangles) are close to projections of <110> directions on a [$\bar{1}$12] zone. Directions obtained from other areas, shown as small triangles, were also found to be parallel to <110> projections. Features from other areas, however, were parallel to [311].

The blades were not wide enough to intersect the foil surface along their entire length. (If the habit plane is assumed to be {111}, as if often the case for precipitation in bulk spinels, then the intersection of the habit plane with the foil surface can be determined. These are shown as "X" in Figure 48. The blade orientations are thus closer to projected <110> directions than to {111} intersections with the foil.)

The bulk of the data is thus consistent with a blade morphology aligned along <110> directions and lying on {111} habit planes. This is shown schematically in Figure 49. The primary variants observed in Figure 47 were $(111)[0\bar{1}1]$ and $(\bar{1}\bar{1}1)[101]$, which are sketched as the dotted blades. The additional variants, all on $(\bar{1}11)$, represent the blade-like clusters of fine Moire' fringes also present in Figure 47. The habit plane shown here is near the foil plane and is thus well suited for phase interference caused by layered structures (i.e., Moire' fringes).

Since Moire' fringes are perpendicular to $\Delta\bar{g}$ and their spacing equal to $|\frac{1}{\Delta\bar{g}}|$, it was possible to identify the reflections producing the fringes, given as $\bar{g}$ = (220) in Figure 47. This exercise gave the results shown in Table II and thus identified the $\Delta\bar{g}$ giving rise to each orientation of fringes. Attempts were then made to identify the extra reflections as the superlattice reflections found in the [011] area of the scale (1/2 {111} and 1/3 {311}). However, it was not possible to produce the required $\Delta\bar{g}$ by a hypothetical array of the superlattice reflections. Nor could the necessary $\Delta\bar{g}$ be obtained by reflections from a hypothetical coherent α-Al_2O_3 structure. Thus, no structural information on the nature of the precipitates was obtained. It is clear that a very fine precipitate has formed from γ-Al_2O_3 and probably represents some precursor to the α-Al_2O_3 present in other layers.

4) Void Morphology

Faceted voids were also a common feature to the scale formed on the NiCrAl+Zr alloy. A high concentration of voids is shown in

Figure 50. Some association with subgrain boundaries is observed (arrows), but in general the voids are randomly distributed. Average void diameter here was found to be 200 ± 100 Å, approximately twice that in the oriented Al_2O_3 found on NiCrAl+Y.

The edge directions of the voids are shown in Figure 51. They show a remarkable correspondence to the directions found for the aligned precipitates in this area, Figure 48. Again alignment is found along the projections of $[0\bar{1}1]$, [101], and [110]. Following the same crystallographic arguments, it can be postulated that the void faces also lie on {111} planes. The other void edge direction, [311], was also found for precipitates. The coincidence suggests that these surfaces are energetically favorable for both void and oxide precipitation, and perhaps that precipitation is a precursor or cause of void nucleation.

D) Discussion of Transient Scales

1) Summary of Oxide Morphologies

To discuss the myriad of oxide structures formed, it is essential to first review the major features of the scales. Differences between adherent and non-adherent scales should be pointed out, since structure may be relevant to oxide adherence mechanisms.

The grain sizes for the random Al_2O_3 scales formed on pure and Y-doped NiCrAl were not significantly different (TableIII). The subgrain size of the oriented scales (estimated from dark field imaging and the size of the distorted Moire´ pattern colonies) also did not vary significantly from one alloy to another. The Y-doped alloy did exhibit some unusually large 0.2 μm Al_2O_3 oriented grains

in a limited area. Also the various Moire' colonies of the oriented oxide were often grouped in 0.5 μm clusters of nearly identical orientation. However, the grains and subgrain sizes taken as a whole fell in the range of 0.05 to 0.15 μm. Thus, no distinction existed between grain sizes of adherent and non-adherent scales.

The void sizes of the random Al_2O_3 scales on the Y-doped alloy was slightly less than that on the pure NiCrAl. The void size of the oriented scale on the Zr-doped alloy was ~10 (75 Å) greater than those on the pure and Y-doped alloys. Thus, no trend in void size with oxide adherence existed. The large 430 Å voids noted in the random Al_2O_3 on the pure alloy were located in the gas-oxide surface layer only and did not exist after ion thinning. Large voids in the surface layer of the scales probably existed for the other alloys as well, prior to ion thinning. The average void sizes of all the thinned scales were grouped in the range of 60-200 Å. There was a trend for the more faceted porosity to exist in the oriented scale as opposed to spherical and cylindrical voids in the random scale. There was also a tendency for the voids in both oriented and random scales on the Y-doped alloy to be intergranular and cylindrical as opposed to dispersed equiaxed porosity.

The finer structures observed in the oriented scales are listed in Table IV. All three alloys contained areas where colonies of distorted Moire' patterns existed. The Zr-doped alloy contained fine aligned Moire' patterns and large APB's resulting from growth and impingement of domains of γ-Al_2O_3. Both the Y-doped and Zr-doped alloys contained needle-like precipitates parallel to the

close-packed anion directions of the oxides. The structures are shown schematically in Figure 52. The foils were not prepared systematically from various levels through the thickness; thus, it was not possible to construct an unqualified full cross-section. However, it was found that areas of randomly oriented Al_2O_3 grains were definitely in contact with metal, thus establishing that in some areas random Al_2O_3 was the inner scale. Some areas on the pure NiCrAl were known to be α-Al_2O_3 through the entire oxide thickness because the scale structure was monitored intermittently during ion thinning.

2) Comparison to Previous Work

a) Phase identifications and orientations. It is useful to compare the various phases formed here with those observed during transient oxidation of Ni-15Cr-6Al at 1000°C, Figure 52b (Kear, et al).[13] The sequence of transient oxidation was described as NiO and spinel nucleation, then Cr_2O_3 internal oxidation and formation of a continuous inner layer, and finally the formation of a continuous rate-controlling Al_2O_3 inner layer. The occurrence of substantial amounts of NiO and Cr_2O_3 was due to the lower aluminum content and lower temperature of oxidation used by Kear. Both of these latter factors lessened the flux of aluminum to the interface and precluded the formation of an Al_2O_3 film.

It is especially interesting that Kear was able to find distinct layers of outer oriented spinel and inner random Cr_2O_3. Applying this sequence to the present Ni-15Cr-13Al alloys at 1100°C, the oriented spinels are seen to represent outer layers which then give

way to inward growing oriented α-$(Al,Cr)_2O_3$ layers, and finally random α-Al_2O_3. It was found that this full sequence is not followed in all areas of the scale, but that some metal grains have oxidized primarily to oriented $(Al,Cr)_2O_3$, while others have formed only random Al_2O_3. The occurrence of different oxidation sequences for different areas on the same specimen is probably related to different grain orientations or phases in the metal, however, the details of such effects could not be studied. Random α-Al_2O_3 was often found on γ/γ' metal grains but no statement can be made regarding the substrate variation of the oriented oxide.

These variations with position on the alloy made it difficult to conclude any definite effects caused by Y or Zr additions. Yet, there does seem to be a trend toward more amounts of oriented oxide, especially spinel, for the doped alloys. The adherence effect of Zr was greater than that of Y, due to the poor distribution of Y throughout the alloy. It is thus suggested that preferred orientation resulting from a strong epitaxial effect may be related to oxide adherence.

The scales formed by 24-hour oxidation at 900°C of a Ni-10Cr-13Al alloy (by weight) were studied by TEM.[14] The diffraction pattern of the oxide clearly showed an orientation effect, but they did not discuss it. Therefore, an analysis of the pattern was made in Section IC. The oxide was found to be superimposed $[\bar{1}11]$ $Ni(Al,Cr)_2O_4$, $[\bar{1}11]$ NiO, and [0001] α-$(Cr,Al)_2O_3$ zones (see Figure 40d, Section C). As in the alloy studied by Kear at 1000°C, these oxide constituents represented lower % aluminum phases than

those observed at 1100°C in the present study. The 900°C oxide required no ion thinning to clearly reveal the superimposed cubic and hexagonal textured diffraction patterns. This reinforces the notion that preferred orientation is a manifestation of epitaxial effects which prevail at low temperatures and short times.

The intimacy of the various oxide phases is suggested by the coincidence of d($30\bar{3}0$) α-$(Cr,Al)_2O_3$ and d(440) $NiAl_2O_4$ (1.423 Å) for the 900°C scale. Thus, the stoichiometry of the phases seems to have been adjusted to allow precipitation or growth of a new oxide structure with the same anion spacing of the parent phase. This same phenomenon was found for d($30\bar{3}0$) α-$(Al,Cr)_2O_3$ and d(440) γ-Al_2O_3 (1.395 Å) of the scale formed on Ni-15Cr-13Al + 0.5 Zr at 1100°C in this study.

It is informative to examine the close-packed oxygen planes of the α-Al_2O_3, $NiAl_2O_4$, and γ-Al_2O_3 structures and relate them to the tendency for coherency between adjacent structures. Figure 53 shows the close-packed oxygen planes for all three structures as well as the aluminum atoms in the plane immediately above. Direct superposition of the α-Al_2O_3 structure upon the $NiAl_2O_4$ layer produces a one-to-one correspondence between the oxygen atoms and 6 out of 12 for the aluminum atoms. A similar situation arises for the γ-Al_2O_3 structure, except that here only a fraction, 8/9, of the spinel cation sites are randomly occupied.

The crystallographic reasons for the formation of oriented layers of subgrains or Widmanstätten precipitates can be seen from the similarity of these atom planes. The Moire´ fringes and fine

precipitates in the γ-Al_2O_3 scale can be viewed as arising from special ordering of the aluminum atoms on preferred sites. Another possibility is occasional changes in the stacking sequence from ABCABC (cubic) to ABAB (hexagonal). The existence of weak superlattice spots supports the premise that ordering has occurred.

The existence of γ-Al_2O_3 on the Zr-doped NiCrAl is at odds with the phases observed on the pure and Y-doped NiCrAl at 1100°C and on the pure NiCrAl alloys at 1000° and 900°C.[13,14] A review of the literature on the oxidation of Ni-Al Alloys has shown that γ-Al_2O_3 does form, but only at temperatures below ~900°C. A summary of all oxide phases observed is shown in Figure 54. Regimes of oxide types were classified in the oxide map in Figure 54b based on the data of Figure 54a. It is seen that α-Al_2O_3 is favored as an exclusive external scale at high temperatures and alloy aluminum content. γ-Al_2O_3 is present in combination with other phases over much of the binary system between ~475-850°C. Thus, the γ-Al_2O_3 found in the present study may represent a low temperature oxide formed during heating. The eventual transformation to the stable α-Al_2O_3 can be approximated from a kinetic study of the decomposition of bulk γ-Al_2O_3.[35] It was reported that α-Al_2O_3 formed at the rate of 2.62×10^{-3} $\frac{\text{molefraction}}{\text{minute}}$ at 1100°C. Thus, less than 1.6% of the original γ would have transformed after the 0.1 hr exposure at 1100°C.

b) TEM structures. The fine structures (Moire's and precipitates) were not dealt with in the prior studies by Kear or Koch.[13,14] Magnifications of published micrographs were usually ≤45,000X as

compared to 100,000 to 400,000X used here to document features $\lesssim$100 Å. Also, the orientation relationships between the layers of oriented spinel and Cr_2O_3 were not studied. Thus, it is likely that the detailed morphologies of Ni-15Cr-6Al at 1000°C and Ni-10Cr-13Al at 900°C are closely related to those observed here for Ni-15Cr-13Al at 1100°C. Since finer grain sizes were reported for 1000°C, the task of studying the fine structure inside these grains could be prohibitively difficult. The structure shown by Koch and Romeo for 900°C did contain indications of aligned features at 150,000X, but they were not discussed.[14]

In general it can be stated that the occurrence of Moire' patterns, APB's, and precipitates has been related here to compositional transitions from one oxide layer to another. For example, the large Moire' fringes in the Y-doped alloy were caused by layered subgrains of oriented spinel and sesquioxide. Also, the $\langle 10\bar{1}0 \rangle$ precipitates in Al_2O_3 were interpreted as plates of spinel. Similarly, the $\langle 110 \rangle$ precipitates and fine Moire' fringe patterns in γ-Al_2O_3 on the Zr-doped alloy were interpreted as a transition phase towards α-Al_2O_3. Thus, an intimate relationship was apparent between oriented spinel and sesquioxide scales.

Conversely, the random α-Al_2O_3 scales contained few precipitates and, by definition, had no crystallographic relationship with prior scales or the metal substrate in contact with them. It appears that a discontinuity in oxidation mechanism exists between transient oxidation (oriented oxides with fine transitional features) and steady-state oxidation (random α-Al_2O_3). Possible explanations of

the loss of epitaxy will be put forth in the next section.

c) Epitaxy. Epitaxial oxide nucleation effects have typically been discussed as an effort by the oxide to reduce the interfacial surface energy by matching the metal structure as closely as possible. That is, the cation structure of the substrate surface plane is imitated by the cation structure of the oxide. With further scale growth, the interfacial stresses are increased due to differences in the specific volume of the oxide and metal substrate per mole of metal cation. Eventually, the accumulated strain energy will force loss of coherency, the possible loss of a preferred oxide orientation, and the nucleation of randomly oriented polycrystalline oxide.[36]

Some additional important insights on the prerequisites for epitaxial oxide nucleation were gained by in situ TEM studies of titanium oxidation.[37] They found that a metal surface, cold worked from mechanical polishing, or a surface with a contamination film left from rinsing, formed a polycrystalline oxide directly upon heating. The high angle grain boundaries of the polycrystalline oxide allowed grain boundary diffusion of oxygen to occur and a tenfold increase in oxidation rate over that of the perfectly oriented oxide.

The specimens in the present study were mechanically polished (not electropolished). Also, a considerable level of growth stress existed as evidenced from the generation of dislocations in the metal. From the above discussions these factors would tend to produce a polycrystalline oxide, either as-nucleated or after some

growth of an epitaxial scale. The polycrystalline alumina found adjacent to the γ/γ' metal surface represented the freshest oxide formed (for an inward growing scale). The oxide in these inner areas may have changed from an original epitaxial outer scale due to buildup of growth stresses and loss of coherency. But in some areas the scale was random polycrystalline alumina through the entire scale. This may have been caused directly by the cold worked surface.

Oriented cubic spinel-type oxides have been observed on a Fe-28 w/o Cr alloy[38] and pure aluminum.[10] The cubic oxides formed oriented rhombohedral oxides at lower temperatures and pressures for the Fe-Cr alloy. The orientations of the cubic oxides were clearly shown to derive from an epitaxial relationship with the cubic metal, and it was suggested that this was the driving force which favored cubic oxides over the thermodynamically stable rhombohedral oxides. Such an argument is attractive for γ-Al_2O_3 formation on pure aluminum: the possible oxides contain only cations of Al. However, in the case of Fe and Ni alloys, it can also be argued that the cubic spinel and γ oxides involved both a structural and a <u>compositional</u> transition with time:

$$\text{e.g.,} \qquad NiO \rightarrow NiAl_2O_4 \rightarrow \gamma\text{-}Al_2O_3 \rightarrow \alpha\text{-}Al_2O_3$$

While low temperature epitaxy and cubic oxide structures are related, it is not clear that epitaxy alone is the cause of the cubic oxides.

3) Implications on Oxidation Theories

a) Growth stress, vacancy sinks, and adherence. It would appear from the above discussion that the production of a highly textured oxide with few grain boundaries could reduce the oxidation rate. Thinner scales have less growth stress and in many instances less tendency to spall on cooling. Y and Zr additions do appear to increase the amount of oriented oxide, at least at short oxidation times. And small Y, Zr, and Hf additions have been found to decrease the oxidation rate slightly.[6,39] Whether this reduction in k_p (~40-60%) could significantly reduce growth stresses and prevent spalling is questionable. Indeed an experiment with electropolished pure NiCrAl showed a dramatic decrease in oxide buckling (and growth stress), but nonetheless spalled profusely.[2] The texture, if any, of the oxide was not studied, and it may still have been random polycrystalline α-Al_2O_3. A systematic study of oxide textures on controlled orientations of NiCrAl surface planes for various surface conditions would be required to make a definitive statement regarding the epitaxy-growth stress-adherence relationship.

The similarity of underlying metal structures for both the pure and Y-doped alloy is not consistent with a vacancy sink mechanism of oxide adherence.[1] Numerous dislocations existed at the oxide-metal interface of both materials and should be available as excellent conduits for vacancy diffusion. No micro-distribution of internal Y-oxides or intermetallics was apparent as possible vacancy sinks. No evidence of vacancy loops in either alloy was observed.

The proposed submicroscopic Y-vacancy complex as a mechanism of void prevention[1] is not supported by the present work.

Chapter II. Morphology of Mature Al_2O_3 Scales

It has been shown that the 0.1 hr scales possessed a multitude of structures. Oriented $Ni(Al,Cr)_2O_4$ spinel and $(Al,Cr)_2O_3$ corundum structures represented early epitaxial films. The inward growing scale then formed randomly oriented α-Al_2O_3 which was observed in contact with the metal. This random α-Al_2O_3 scale persists with further oxidation during which coarsening of the void and grain structure occurs. Variation in the void size and amount with depth in the scale exists. Numerous low angle grain boundaries in areas of preferred orientation also develop in the 20 hr scale. The description of these features comprises the results of this chapter. The remainder discusses proposed models of void formation, diffusion and deformation processes in Al_2O_3 scales.

A) 1 Hr Scale Formed on Pure Ni-15Cr-13Al at 1100°C

1) Differentiation of Scales Formed Over γ/γ' and β Metal Phases

Very low magnification TEM of the scale revealed a definite imaging of the alloy microstructure, Figure 55. The oxide over β-NiAl dendrites could be differentiated from the oxide over the γ/γ' phase. Dark oxide nodules were present over the entire foil and exhibited a definite linear alignment (arrows). This agreed with SEM observations which showed thicker oxide growths over scratches left from polishing.

The micrographs in Figure 56 show the three large scale features of oxide over β, γ/γ', and scratch nodules. Selected area

diffraction patterns were obtained over the areas marked "A" to "E", some of which are shown in Figure 57. Patterns from all five areas were indexed as randomly oriented α-Al_2O_3. The camera constants used to index patterns from areas over adjacent β and γ/γ' areas ("A" and "B" in Figure 56b) were identical within the accuracy of determination (0.2%). This indicated that the oxides over β and γ/γ' phases possessed the same lattice parameters and stoichiometry. A gold film internal standard used on the random α-Al_2O_3 scale formed at 0.1 hr had previousiy shown that scale to be pure Al_2O_3. It is therefore believed that the 1 hr scale is also pure Al_2O_3. The diffraction patterns from areas "C", "D", and "E" also indicated only a 0.6% difference in lattice parameters. (Note that the difference in lattice parameters and d-spacings between pure α-Al_2O_3 and pure α-Cr_2O_3 is much higher and is equivalent to 4.8%, Appendix A.) These differences in scale structures and thicknesses thus represent differences in Al_2O_3 transport rates (presumably oxygen grain boundary diffusion) with no detectable change in crystal structure or composition.

Some slight differences in grain structure between the γ/γ' and β oxide can be seen in Figure 58. The γ/γ' scale has less distorted grains than the β scale. This indicates less internal stress in the oxide over the γ/γ' phase. Furthermore, the γ/γ' scale has a finer grain size than the β scale, i.e., 0.10 ± 0.05 μm compared to 0.17 ± 0.05 μm. This can be seen graphically in the grain size distribution curves of Figure 59, obtained from measurements of grain diameters in Figure 58. While appreciable overlap

exists, the grain size differential is significant. Grain size measurements of the areas in Figure 56a yielded an average diameter of 0.12 ± 0.04 μm for the light γ/γ' scale and 0.19 ± 0.06 μm for the dark β scale. This is in agreement with the aforementioned trend.

It should be pointed out that such distinct structural differences cannot always be observed. The grain size and amount of distortion also varies with position through the thickness of the scale. Since this position was not a controlled variable, an accurate representation of true scale differences was not always apparent. Grain size distributions were obtained at various other locations in the foil, without regard to γ/γ' or β scales, and are shown in Figure 60. The curves did not fall into two distinct groupings as might be suggested by Figure 59. Also, no areas studied showed quite the fine grain size of area "B" in Figures 56b and 58a. This affirms the need to be cautious in generalizing the overall scale morphology from studies of only a few areas.

2) Porosity

As in the scales formed at 0.1 hr, the 1 hr scales contained numerous areas containing intragranular (entrapped) porosity. The typical microstructure of such an area is shown in Figure 61. Stereoviewing reveals the dispersion of voids located with individual oxide grains. Often a decrease in void size with depth into the foil can be discerned. (The fine grains are located towards the bottom of the foil.) The correlation of void size and position is

shown in Figure 62 for the voids located in the grains marked "1" and "2". (The vertical position of the voids was determined by standard stereographic measurements.)[88] A linear regression fit to the data resulted in the straight line equation with a regression coefficient, r, of 0.72:

$$vs = 390 - 0.25\ y$$

where, vs = void diameter ($\mathring{A}$)

and, y = position in foil ($\mathring{A}$)

This gradation in void size was also evident in the thick regions of the foil, away from the ion thinning hole, Figure 63. The structure is somewhat complicated by the image of overlapping grains. However, stereoviewing did confirm that the large voids, (L), are located within grains at the top of the foil and that the finer voids, (F), are intragranular and located within the next layer of grains. This gradation in void size is consistent with the profile presented in Figure 62. The distribution of void sizes measured from various micrographs is shown in Figure 64. The peak distributions lie between 100-200 $\mathring{A}$, although each area contained some voids over 500 $\mathring{A}$. The macrovoids of Figure 63 are shown as a separate population; the peak distribution here was at 500 $\mathring{A}$, with some voids as large as 1000 $\mathring{A}$.

A summary of the average grain and void sizes measured from eight micrographs at 100,000X is given in Table V. The overall average grain size was 0.18 ± 0.07 μm, and the overall average void size was 150 ± 90 $\mathring{A}$. The ratio of average void size to average grain size was about 1:10. No correlation of void size with grain

size was observed.

3) Strain

Often highly irregular bend contours were apparent which indicated the presence of internal stress in the scale (arrows in Figures 63 and 65). Occasionally more distinct strain features were observed, as in the large central grain of Figure 66. While not totally unambiguous, these defects appear to be groups of two or three dislocations viewed edge-on. Optimum imaging of dislocation structures was made difficult by the fine grain size and the inability to tilt, in a controlled manner, to proper two-beam diffracting conditions. Surveys of a large number of grains imaged under some random orientation did reveal a number of grains that contained strain contrast resembling dislocations, as did the random Al_2O_3 scale formed at 0.1 hr in Section IA. Some such linear defects are shown in Figure 67. The features indicated by the arrows were distinguished from bend contours by tilting a few degrees. The bend contour configurations moved considerably, while the defect features remained stationary. Other strongly diffracting grains (lower left of micrograph) clearly contained no such defect features.

B) 20-Hour Scale Formed on Pure Ni-15Cr-13Al at 1100°C

The structure of the 20-hour scale exhibited a number of features common to the random α-Al_2O_3 scales formed at 0.1 and 1 hour: dispersed porosity, overall random scale orientation, decreasing void size with depth below the scale surface, and precipitates associated with fine porosity. Some additional features were

also observed which are of interest: whisker formation at the gas surface, isolated dislocations in some percentage of the grains, dislocation arrays in low angle subgrain boundaries, and a definite crystallographic alignment of clusters of 20 or more subgrains. The changes in oxide structure with position in the scale and the subgrain structures will be presented separately in the following two parts.

1) Structural Variation Throughout the Scale Thickness

The specimens produced by selective ion thinning of the 1.0 μm thick spalled scale were estimated to be 0.17, 0.50, and 0.73 μm beneath the gas surface. Because of the uneven topography of the scale, each specimen contained some areas more typical of other levels, giving rise to a wide spectrum of structures for each foil. Examination of a large number of areas permitted the representative average structure for each specimen to be constructed and the true variation with position in the scale to be determined.

a) Near the gas-oxide interface. The structure of the oxide foil produced 0.17 μm beneath the gas surface is represented in Figures 68-69. An area at the immediate oxide-gas interface was identified by the appearance of 0.5 μm wide X 3 μm long whiskers which grew out into the gas, Figure 68a. The surface of the oxide is covered with large pores, 0.13 ± 0.07 μm wide on the average. Since the whiskers were intact only at thick areas of the specimen, the detailed structure at the base of the whiskers was not visible. However, some correlation between pores and whiskers appears possible from

Figure 68a, (arrows). A segment of one is shown in Figure 68b. A faint band of reduced electron abosrption can be discerned parallel to the major growth axis. It is suggestive of the hollow channels recently observed in TEM studies of Fe_2O_3 whiskers grown on pure Fe.[44] These limited results suggest that whisker formation and growth may be associated with fast aluminum surface diffusion on the pore surface in the scale as well as in the channel inside the whisker.

The more common features of the 0.17 μm level foil are shown in Figure 69. The voids are somewhat smaller than in the area of Figure 68a; i.e., less than 0.1 μm compared to 0.13 μm. Smaller voids, 500 Å, developed a faceted surface.

Many of the voids were connected to a nearby grain boundary by a single dislocation, D, lying parallel to the plane of oxidation. This is consistent with a low energy configureation of dislocations often found in bulk polycrystalline material.[45,46] Double lobes of strain contrast probably indicated some stage of void nucleation, such as a vacancy dislocation loop. Dark 200 Å precipitates, P, were often located at the surfaces of grain boundaries or microvoids. Dislocation arrays or Moire´ patterns were also observed to divide grains into two slightly misoriented subgrains (S.G.).

b) Near the scale midsection. The structure of a foil produced at the 0.50 μm level by equal ion thinning from both sides is represented in Figures 70-79. The features of this specimen showed characteristics of the gas-oxide, midsection, and metal-oxide levels.

A highly porous region, Figure 70a, illustrates that nearly every grain contains a large void. The porosity in this area was estimated to be 0.045 by point counting. The same area at higher magnification shows many of the macrovoids are covered with fine 50-100 Å crystallites. Although the size is consistent with the dark precipitates in Figure 69, these are more electron transparent.

A high density of crystallites layered over α-Al_2O_3, and the corresponding spot + ring diffraction pattern, are shown in Figure 71. The analysis in Table VI fitted the spot pattern to α-Al_2O_3 and the ring pattern to an FCC structure (metal) with a_o = 3.595 Å. The best candidate metal fits would be Cu (a_o = 3.615 Å) from ion beam sputter deposition from the copper specimen grid, or Ni(Cr), $Ni(Cr)_3Al$ (a_o (max) 3.565 Å) from some decomposition process of a prior $NiO/NiAl_2O_4$ transient oxide. Verification of copper contamination was obtained by STEM analysis of "clean" grains and grains covered with crystallites. No Ni intensity was obtained in either area, while the Cu peak was more than doubled.

The structure which most accurately represents the scale midsection is shown in Figure 72. The average grain size here is 0.49 μm as compared to 0.35 μm in Figure 69 or 0.31 μm in Figure 70a. Also, a dispersion of fine 100-300 Å voids is present rather than the large voids located in the center of grains. The vertical position of the voids can be seen in the stereopair of Figure 73; no specific arrangement, such as vertical columns of voids, is apparent.

The finer structure of the porosity in areas A, B, and C of Figure 72 is shown in the enlargements in Figure 74. Many of the voids have dark, spherical precipitates (P) associated with them. Some of the larger voids (V) also have a mottled structure, as though the void were not completely empty, but contained an open lattice - work of oxide. It is believed that the precipitates and mottled structure may be due to decomposition of transient $NiAl_2O_4$ or γ-Al_2O_3 oxides into more dense α-Al_2O_3. The volume contraction associated with such a reaction ($\sim$7%) could give rise to void nucleation. However, the total amount of porosity, especially the large voids at the gas surface, will require an additional source of vacancies to be satisfactorily explained. This matter will be discussed more completely in Part IID.

These basic structures (fine voids plus associated dislocations and precipitates) were found adjacent to an area showing additional features of interest, Figure 75. The upper left of the micrograph shows a thicker region which is populated with clusters of strain contours. Such features probably resulted from coherency strains associated with a fine grained α-Al_2O_3 layer superimposed on the larger grains of the scale midsection. (The strained areas were not observed in thin portions of the foil.)

The occurrence of isolated dislocations and their loose relationship with dislocation arrays in subgrain boundaries is shown in Figure 76. The occurrence of individual dislocations was definitely not a characteristic of most grains. This point is difficult to quantify exactly without a systematic check of

hundreds of grains imaged under at least two different operating reflections. Nevertheless, some attempt was made to determine the average number of dislocations occurring in a grain. This was accomplished by examining many micrographs totalling 476 grains. The results are shown below:

Grains with no dislocations	416
Grains with some dislocations	60
#/Grain for those having them	2.9 ± 2.7
#/Grain overall	0.36 ± 1.41

(Dislocations in low angle boundaries were not counted.) Such estimates of dislocation frequency are biased downwards by not imaging the grains under optimum conditions, but they are also biased upwards by selectively photographing areas showing definite features, such as dislocations. It is concluded that there exist less than one dislocation per grain on the average.

Low magnification micrographs of relatively featureless grains over many microns are presented in Figures 77 and 78. It is believed that these pore-free regions are representative of the structure near to the oxide-metal interface. The few pores that do exist are located at grain boundaries rather than dispersed throughout the grain interiors. Figure 78 also shows an interesting gradation in grain size from the center of the micrograph, X, to the darker (thicker) edges. This is shown graphically in Figure 79, where grain size is plotted against radial distance from X. The average grain size decreased from ~0.6 μm to 0.3 μm. This can partially be explained by the variation in grain size with level in

the scale by assuming that the fine grains in the thick region belong to the oxide-gas layer. However, the absence of any intragranular porosity over this wide spectrum of grain size (position beneath the scale surface) indicates that considerable variability in the extent of porosity can exist.

c) Near the oxide-metal interface. Lastly, some features from the foil produced near the oxide-metal interface (0.72 μm beneath the oxide-gas surface) are presented. Figure 80 shows a high density of voids, many of which are faceted and have dark precipitates. A few grains were also observed to have individual dislocations, Figure 81. Many areas were dislocation- and void-free; these will be described in a later part on subgrain structure.

d) Summary of structural variations through the scale. Table VII lists all the grain and void size statistics obtained by TEM from the three levels in the scale. Values at the immediate gas-oxide and oxide-metal interface were also obtained by SEM analysis of the spalled oxide. The average grain and void size obtained from individual micrographs is listed along with the standard error, s, and number, N, of measurements. The weighted mean and the pooled standard error are also shown for each level.

The plot of this data in Figure 82 shows the very definite increase in grain size and decrease in void size with depth in the scale. There is considerable variation from micrograph to micrograph, partially due to variations in actual depth position of a given thin foil. However, the average values show a statistically meaningful trend. The mean grain size at the gas surface (0.3 μm)

is thus concluded to be one-half of that at the metal surface (0.6 μm). Conversely, the mean macrovoid size at the gas surface (0.13 μm or 1300 Å) is concluded to be greater than ten times the macrovoid size near the metal surface (0.01 μm or 100 Å).

Often the larger grain sizes obtained for a given depth were associated with smaller void sizes, and conversely. This suggested that a void size-grain size relationship held, regardless of the uncertainty in the depth position of a given micrograph. This correlation is shown in Figure 83. Here the macrovoids cluster at the smaller grain size values; the microvoids are clustered at the larger grain size. The overall mean values (circles) supports this trend of the individual means (dots).

The overall amount of porosity was also observed to decrease as the oxide-metal interface was approached. An indication of the amount of porosity was obtained by point counting. (This technique gives actual volume percent in a strictly planar analysis, but will tend to overestimate for fine particle or voids dispersed through the thickness of thin foil TEM specimens.) The qualitative trend is shown in Figure 84, where void fraction has been plotted as though a two-dimensional analysis was performed. The trend to essentially zero porosity at the oxide-metal interface is nonetheless clear.

The reconstitution of all the features discussed above into a schematic cross-section of the 20 hr scale is shown in Figure 85. The information reflected by the schematic is:

- o increase in grain size with depth
- o decrease in void size with depth
- o decrease in total amount of porosity with depth
- o dislocations associated with voids and grain boundaries
- o subgrain boundaries bisecting many grains
- o variability of grain and void size for any lateral section

2) Subgrains Clusters and Preferred Orientations

a) Subgrains near the oxide-gas surface. Examples of subgrain structure found in the foil produced 0.17 μm from the gas surface are shown in Figures 86-89.* The subgrain boundary A-B in Figure 86 cuts a typical α-Al_2O_3 grain in two. A number of single dislocations (arrows) extend into the grain interior. The slight misorientation of the subgrain halves gives rise to phase contrast in the form of Moire´ fringes, Figure 87. In region "A" two orthogonal sets of fringes can be resolved, with spacings of 15 and 24 Å. The spacings predicted from the diffraction pattern, i.e., $\frac{1}{\Delta\bar{g}}$ or $\frac{d_{hkl}}{0}$, were 16 Å and 25 Å, respectively.

The treatment of the Moire´ pattern is shown in Figure 88. The direction of the Moire´ fringes ($\bar{M}$) can be seen to be nearly perpendicular to the spot splitting, i.e., $\Delta\bar{g}$, in agreement with the theory of fringe patterns. The $\Delta\bar{g}$ vectors are rotational in nature as seen by the direction of the $(30\bar{3}0)$ and (0006) spot splitting. The results indicate that the Moire´ fringes were produced by a 4.9^o rotation of the $(30\bar{3}0)$ planes and a 5.0^o rotation of the (0006)

*(These photomicrographs were obtained by Professor Linus Ogbuji of the University of Florida at CWRU on a Siemens 102 microscope operating at 125 kV.)

plane about a [1$\bar{2}$10] axis.

A coarser periodic structure with a 100 Å spacing can also be seen along the entire subgrain boundary, Figure 87. These bands are associated with nodes in the 15 Å spaced set of fringes of region "A". It is suggested that the regular array of Moire´ fringes is disrupted at these nodes by subgrain boundary dislocations. The lower portion of the boundary, area "B", shows a single set of 20 Å fringes which are roughly parallel to the 25 Å fringes in area "A". This single set is produced with another subgrain in an area below the micrograph.

An additional subgrain "Y" can be seen to adjoin the original subgrains "X" and "Z" in Figure 89a. The projection of the triple point boundary between all three subgrains, indicated by T-T´, exhibits a discontinuity in the large 100 Å bands. The subgrain boundary between "Y" and "Z" contains two sets of fringes spaced 14 and 30 Å; the 14 Å set is continuous across the triple point and is the same set seen in bright field for the X-Z subgrain boundary.

b) Subgrains in the midsection of the scale. The structure and degree of misorientation is now examined for a number of clustered subgrains in a foil produced at 0.5 μm from the oxide-gas surface. However, it is informative to first examine the orientation of a large number of grains. The diffraction pattern in Figure 90 was obtained for approximately 300 grains. It shows a reasonably uniform distribution of spots; as such, no preferred orientation would be expected. Analysis of the ring pattern as α-Al_2O_3, Table VIII, allowed for no substantial amounts of other phases such

as γ-Al_2O_3, α-Cr_2O_3, or $NiAl_2O_4$.

However, on a finer level, substantial numbers of grains showed similar orientations. The array in Figure 91 has at least 19 subgrains whose orientations, normal to the plane of oxidation, were close to $[10\bar{1}\bar{1}]$. (Grain "D" possessed a $[21\bar{3}\bar{1}]$ orientation and therefore was not part of the cluster.) Diffraction patterns bearing out this fact are shown in Figure 92 for areas A, B, C, and F. Pertinent data describing the individual patterns are given in Table IX. A number of subgrains were usually sampled at once because the subgrain size was less than that of the selector aperture. This gave rise to some "rotated" diffraction spots due to the slight misorientation of subgrain to subgrain, e.g., $1\text{-}5^{o}$.

The near $[10\bar{1}\bar{1}]$ patterns of Table IX were all obtained within a $\sim 10^{o}$ range of specimen tilt. The $[10\bar{1}\bar{1}]$ poles of these and other subgrains were plotted on an expanded Wulff net with the plane of oxidation (foil normal) as the center, Figure 93a. The $[10\bar{1}\bar{1}]$ directions clustered in an 18^{o} overall range. The range of subgrain rotations, Figure 93b, was generally less than 6^{o}. (These ranges are meant to give a semi-quantitative indication of the actual subgrain misorientations. The precise method of obtaining two exact zone axes for each subgrain and plotting foil normals on a standard stereographic projection was not feasible for these small grain sizes and the limited flexibility of the microscope tilt stage.)

The following four examples of subgrain structures from Figure 91 are now discussed in terms of dislocation arrays or Moire'

patterns. The analysis makes use of the relationships between crystal rotation and Moire' fringe or dislocation array spacings for a simple tilt boundary (bottom of Table X). The direction of a rotational Moire' pattern should be perpendicular to $\Delta\bar{g}$ of the operating reflections from the two subgrains. In Figure 94 a Moire' pattern (M) is shown at the C2-C3 boundary. It is also shown to be perpendicular to $\Delta\bar{g}$. From Table X, the Moire' fringe spacing predicted for an observed rotational angle in diffraction of $\theta = 2.3^{o}$ is 58 Å and is in good agreement with the observed value of 62 Å. The predicted value for a dislocation array is 118 Å. The data is therefore consistent with interpretation as a Moire' pattern. Individual dislocations are present in this micrograph, i.e., at the C1-C2 boundary, within C2, and at a boundary inside C3 (arrows).

In Figure 95 a closely spaced array of what appears to be end-on dislocations is present at the A4-B5 subgrain boundary (arrow). The spacing and rotational measurements in Table X are consistent with analysis as a Moire' pattern, i.e., 91 Å $\gtrsim$ 124 Å or $1.0^{o} \gtrsim 1.4^{o}$ for the measured and calculated values. The fringe pattern in Figure 96 at the A3-B5 and A4-B5 boundary supports the interpretation as a Moire' pattern.

The loosely spaced dislocation array at the A2-A3 boundary, Figure 96, is not regularly spaced and interpretation as a Moire' pattern does not appear to be possible. Indeed the data in Table X are consistent with analysis as a dislocation array, i.e., 216 Å $\gtrsim$ 248 Å or $1.1^{o} \gtrsim 1.3^{o}$ measured and calculated values.

The F3-F4 array in Figure 97 is a Moire' pattern as indicated both by the perpendicularity of $\Delta\bar{g}$ and $\bar{M}$ and the agreement in measured and calculated spacing (50 Å $\approx$ 47 Å) and rotation ($2.1^{o} \approx 2.0^{o}$). It is thus clear that many of the subgrain boundaries are imaged as Moire' patterns rather than dislocation arrays. The image ambiguity between Moire' patterns and a regular array of dislocations has been discussed for an interface perpendicular to the electron beam.[47] This study concluded that the overlapping strain fields of a closely spaced dislocation array produced a line pattern essentially equivalent to a Moire' pattern if the spacing were $\leq 0.3\xi g$. From the last column in Table X it is clear that all the patterns analyzed contained $D \leq 0.3\xi g$. The successful analysis of three boundaries as Moire' patterns can not preclude the presence of dislocations at these boundaries, but does indicate that the individual fringe lines are not to be confused with individual dislocations. The resolution of individual dislocations at the subgrain boundaries described in Figures 94 and 96 suggests that individual dislocations may be present in many of the boundaries, even though imaging of the boundaries produced a Moire' pattern.

The rare case of dislocations not associated with a subgrain boundary is exemplified by Figure 98. Two inclined dislocations are shown along with dot contrast, possibly end-on dislocations. Fringed contrast at a planar void or dislocation loop is also evident (arrows).

This specimen was examined in other areas to confirm the prevalence of clusters of oriented subgrains. Without too much difficulty an area on the order of 10-15 grains wide (∿7 μm) was found to have a $[10\bar{1}\bar{1}]$ orientation as before. A sampling of four subgrains showed that the position of $[10\bar{1}\bar{1}]$ varied on the order of 5^{o} from subgrain to subgrain; and the rotational variation of poles in the $[10\bar{1}\bar{1}]$ pattern about the $[10\bar{1}\bar{1}]$ axis was ∿8°. These variations are similar to those presented in Figure 93. The important finding here is that clusters of $[10\bar{1}\bar{1}]$ subgrains appear to be a common structure in the mature scale.

c) Subgrains near the oxide-metal surface. Subgrain structure in the foil produced 0.72 μm from the gas surface was also observed. A 4 μm wide cluster of ∿20 subgrains having a $[20\bar{2}1]$ orientation is shown in Figure 99. The specific subgrain boundaries indicated by the arrows were examined by diffraction. The pattern for region "A" including six subgrains indicates a rotational variation of 5.5^{o}. The fine structure of the subgrains in regions "A" and "B", Figure 100, were again found to consist of finely spaced Moiré fringes (100 and 60 Å, respectively). The angular mismatch of the subgrains in region "B" was calculated to be 2.3^{o} from the relation $D=\frac{d_{hkl}}{\theta}$. These spacings and boundary angles are similar to those observed in the foil produced at the midsection. The major difference here is that a $[20\bar{2}1]$ orientation was observed rather than $[10\bar{1}\bar{1}]$. The separation of $\langle 20\bar{2}1\rangle$ and $\langle 10\bar{1}1\rangle$ directions can be as close as 19.4^{o} (e.g., $[20\bar{2}1]$ and $[10\bar{1}1]$, specifically). The reported observation of $[20\bar{2}1]$ and $[10\bar{1}\bar{1}]$ clusters could thus

represent a tendency towards the same overall texture if some latitude in the degree of orientation is allowed for. (Recall that the zone directions were $\sim$5-15^{o} from the foil normal, so that the exact scale orientation was probably a high index direction or a range of directions.)

The subgrain structures shown in Figure 101 were not typical in that arrays of individual dislocations were observed. The association of porosity and dislocations were observed. The association of porosity and dislocations is indicated by the arrows.

C) Kinetics of Grain and Void Growth

The average grain, GS, and void diameters, VS, are listed in Tables XI and XII for the different times studied and for many areas of each specimen.

The overall mean for each oxidation time is given with a 95% confidence interval determined by the Students "t" distribution. The standard deviation, S, of an individual measurement is listed and summarized in the pooled standard deviation for each oxidation time. The standard deviations are large with respect to the means ($\sim$one half) because of the wide range of values measured within any given micrograph. However, the standard error of the mean, $S/\sqrt{N}$, is actually quite small (less than one-tenth of the mean values) due to the large number of total observations.

The depth beneath the oxide-gas interface was approximated as one-half the total thickness for the 0.1 hr and 1.0 hr scales which were ion thinned equal times on both sides. Also listed is the data for the 20 hr specimen produced near the oxide-gas interface.

The total oxide thicknesses were estimated from the previously quoted k_p for these alloys (0.002 $mg^2/cm^4 \cdot hr$ or 0.57 $\mu m^2/hr$). The three levels are all within 0.1 μm of each other; therefore plotting these grain and void sizes vs. time is a good description of the coarsening kinetics for the structues near the oxide-gas interface. Because the oxide-gas surface consists of the first oxide formed, these kinetics do represent coarsening phenomena and not new oxide structures.

1) Grain Growth

This coarsening data is plotted as log-log curves in Figure 102. Grain growth models generally describe the grain size by $GS^n - GS_o^n = k_G t$, where n is an integer, GS_o is the original grain size, and k_G is a constant. Linear plots of grain size vs. time were used to determine $GS_o \approx 0.130$ μm. Values of k_G were determined from $GS_{0.1}$ and $GS_{1.0}$. The remainder of the curve was then generated for n = 2,3. The generated curve for n = 3 coincides with the experimental data, whereas the curve for n = 2 predicts grain growth rates larger than those observed. It should be noted that because GS_o is of the same order as the actual data, one is not permitted to find n simply from the slope of the log-log plot. The slope of the log-log curve is 0.18 which overestimates n considerably, (n = 5). SEM studies of grain size of Al_2O_3 scales formed on NiAl at 1100°C have also shown n ≈ 5 as determined only from the slope of the log-log plot.[15] Recently grain growth of Al_2O_3 scales on NiAl were shown to have growth exponents of 2 at 1200° and 1300°C.[48] The reason for these kinetic differences is not clear.

Theoretically, n = 2 for a pure system where grain growth is uninhibited. The observed n = 3 indicates grain growth inhibition. Pores are not believed to be directly responsible because in large part they were not observed on grain boundaries in the mature oxides. Impurity segregation at grain boundaries is a possible retarding force, since nickel containing oxides were formed during the transient period, and nickel is always available at the oxide-metal interface.

The value of n = 3 is in agreement with those found in a sintering study of bulk Al_2O_3.[49] In that study n was found to be 2.8 at 1675°C, 2.6 at 1550°C, 2.7 at 1480°C, and 3.2 at 1450°C. In another sintering study n was found to be 3 at 1700-1800°C.[50] Both of these studies found no change in n with MgO additives until exaggerated grain growth became significant in the undoped Al_2O_3 samples. The occurrence of $n \approx 3$ for Al_2O_3 grain growth appears to be a general observation.

Since the primary transport mode is by oxygen grain boundary diffusion, it follows that the scale thickening rate will be reduced as grain growth occurs and the total volume of grain boundaries is reduced. By using the approximations that $k_p \approx D_{eff} \approx \frac{2\delta D_{GB}}{GS}$ and $GS^n = k_G \cdot t$ it follows that the oxide thickness is: *

$$x^2 = \frac{2\delta D_{GB}}{k_G} \cdot \frac{t^{(1-1/n)}}{(1-1/n)}$$ where δD_{GB} = grain boundary diffusivity product

k_G = grain growth rate

n = grain growth exponent

*A more detailed discussion of grain boundary diffusion equations is given in Section D.

Thus, modifications to the parabolic growth rates will occur due to the grain growth rate. The following summarizes the effect of the grain growth exponent, n, on the slope, m, of log x vs. log t plots:

n	m
2	0.250
3	0.333
4	0.375
5	0.400
∞	0.500 (parabolic)

The observation of less than parabolic kinetics is commonly observed for Al_2O_3 scales, for example m = 0.4 for Al_2O_3 growth on NiAl.[15] This corresponds to a grain growth exponent of 5, which was observed in that study. Although this agreement is encouraging, the consideration of GS_o and the variation of grain growth through the scale thickness will be needed for a more precise model.

The grain size distribution curves for typical areas of the various scales examined are summarized in Figure 103. It is immediately clear that even the most extreme curves have a finite region of overlap. Nevertheless, the coarsening trends with oxidation time (curves a→b→c) and with depth in the scale (curves $c_1 \rightarrow c_2 \rightarrow c_3$) are apparent. The 0.1 and 1.0 hr distributions are the most similar; the 1.0 hr curve has more distribution skewed towards larger grain sizes. The c_2 curve for the 20 hr scale midsection also shows much intensity skewed towards larger grain sizes. The distribution did not indicate a true bimodal microstructure which would have indicated exaggerated grain growth. However, it was common that

the maximum grain size in a given micrograph was an order of magnitude greater than the minimum size.

2) Void Growth

The kinetics of void growth are compared in Figure 102 to model curves for n = 1,2,3 where $VS^n - VS_o^n = k_v t$. VS_o was estimated to be 0.010 μm from linear plots of VS against time. The average VS data fit the n = 1 model best. However, the data for the 20 hr scale is believed to be biased towards the larger voids at the immediate oxide-gas surface. This is because voids smaller than $0.5\xi_g$ ($\sim$.03 μm) are obscurred by the absorption effects in the thick portions of the foil, i.e., where the macrovoids were measured. Therefore, kinetic models for n = 2 or 3 may also be applicable.

The classic Ostwald ripening model predicts n = 3. This model assumes a constant total volume of precipitate (voidage) and predicts the growth of larger particles at the expense of smaller ones. The result is a reduction in the total number of particles and an increase in the average particle size. It is clear from the micrographs that the number of voids near the gas surface has decreased with time; only one macrovoid per grain was observed in many areas of the 20 hr scale. The constancy of total void volume was tested by point counting. Values of 0.06, 0.04, and 0.03 were obtained for 0.1, 1.0, and 20 hrs, respectively. These values are not completely accurate because point counting assumes a two-dimensional surface analysis. It can be shown that from geometric considerations the true volume fraction, f_v, is given by:

$$f_V = \frac{4/3r \cdot f_A}{\gamma}$$ where f_a = measured area function

r = particle radius

γ = foil thickness

Therefore the volume fractions are overestimated, especially for the finer void sizes. The corrected void volume fractions for $\gamma \approx$ 0.1 μm are 0.01, 0.01, 0.03. Some increase in total voidage appears to be real, but the accuracy of these values is uncertain. The main conclusion of the void growth kinetics is that considerable growth and coalescence has occurred. Exact modelling by a determination of the growth exponent, n, is not possible due to uncertainties in the 20 hr scale values.

The void size distributions are compared in Figure 104. The void growth with time (curves $a \rightarrow b \rightarrow c_1$) is clear, although some overlap exists for the 0.1 and 1.0 hr distributions. The decrease in void size with depth in the 20 hr scale (curves $c_1 \rightarrow c_2 \rightarrow c_3$) is also apparent. It is most interesting that the 0.1 hr and 20 hr metal distributions both contain the finest voids. This suggests that the age of the voids in the 20 hr scale near the metal is comparable to that of a 0.1 hr scale. This is consistent with accepted models of inward growth of Al_2O_3 scales, which state that fresh oxide is formed at the oxide-metal interface.[1,4]

D) Discussion of Mature Scales

1) A Mechanism of Void Formation

a) Qualitative equilibrium vacancy profiles. While void growth has been established as a simple particle coarsening phenomenon, the reason for void nucleation within the thickness of the scale is not at all obvious. The gradient in the amount of porosity through the scale, suggests that void precipitation is related to some property that also changes across the thickness of the scale. A likely candidate for this process would be the equilibrium vapor pressures of aluminum and oxygen across the scale: The equilibrium concentration of vacancies can be directly related to these pressures; the pressures dramatically change from the gas-oxide to the oxide-metal surface.

The following hypothetical reactions show the pressure-vacancy concentration dependencies (all reactions have been considered because of current uncertainty on the major equilibrium defect species in Al_2O_3 [51]).

$$1/2\ O_2\ (vap) + 2e' = O_i'' \qquad k_8 = \frac{[O_i'']}{(pO_2)^{1/2}\ e'^{\,2}} \qquad \text{Eqn. 8}$$

$$1/2\ O_2\ (vap) + V_o'' + 2e' = \phi \qquad k_9 = \frac{1}{(pO_2)^{1/2}\ [V_o'']\ [e']^2} \qquad \text{Eqn. 9}$$

$$Al\ (vap) = Al_i''' + 3e' \qquad k_{10} = \frac{[Al_i'''][e']^3}{(pAl)} \qquad \text{Eqn. 10}$$

$$Al\ (vap) + V_{Al}^{'''} = 3e' \qquad k_{11} = \frac{[e']^3}{(pAl)\ [V_{Al}^{'''}]} \qquad \text{Eqn. 11}$$

Reactions (8) and (9) state that higher oxygen pressures (i.e., the oxide-gas surface) will increase oxygen interstitials and decrease oxygen vacancies. The Frenkel oxygen defect relation states that oxygen vacancies and interstitials are inversely related:

$$[V_O^{\cdot\cdot}]\,[O_i^{''}] = k_{F,O} \qquad \text{Eqn. 12}$$

Thus, regardless of whether (8) or (9) predominates, fewer oxygen vacancies are at equilibrium at the high pO_2 gas surface than at the oxide-metal surface. From reactions (10) and (11), it can be seen that high aluminum equilibrium vapor pressures (i.e., at the oxide-metal interface) will increase aluminum interstitials or decrease aluminum vacancies. The Frenkel aluminum defect relation states that:

$$[V_{Al}^{'''}]\ [Al_i^{\cdot\cdot\cdot}] = k_{F,Al} \qquad \text{Eqn. 13}$$

Thus, regardless of whether (10) or (11) predominates, fewer aluminum vacancies will be in equilibrium at the oxide-metal interface than at the gas surface.

Finally, the oxygen and aluminum vacancies are inversely related by Schottky equilibrium:

$$[V_{Al}^{'''}]^3\ [V_O^{\cdot\cdot}]^2 = k_S \qquad \text{Eqn. 14}$$

Irrespective of which defect equation predominates, oxygen vacancies will be greater at the oxide-metal surface and aluminum vacancies will be greater at the gas surface.

Gradients of equilibrium vacancy concentrations can be visualized as in Figure 105a. After further oxidation, the scale thickens by inward oxygen diffusion (Figure 105b), but the equilibrium vacancy concentrations at the two interfaces remain the same; they are governed only by the fixed pO_2 (gas) and a_{Al} (metal). This has the consequence that at position "X", the equilibrium concentration of oxygen vacancies has dropped, while that of aluminum vacancies has been raised. The precipitation of unstable oxygen vacancies into voids is thus possible for an inward growing scale. Furthermore, the amount of excess vacancies is less for deeper positions in the scale, as shown by the arrows at X_1, X_2, and X_3. This agrees qualitatively with the observation that the amount of porosity decreases towards the oxide-metal interface.

It is interesting to point out that because the equilibrium concentration of cation vacancies is being raised over the existing concentration, one would predict that no excess of cation vacancies ever exists for an inward growing scale. On the other hand, an outward growing scale controlled by cation diffusion would exhibit a continually decreasing equilibrium cation vacancy concentration at internal positions in the scale. Thus a situation completely analogous to that in Figure 105 can also be proposed for precipitation of excess cation vacancies in an outward growing scale. This version of the model may be applicable for outward growing metal-deficient scales, such as $Fe_{1-x}O$, $Ni_{1-x}O$, and $Co_{1-x}O$. Such cases will be discussed in part e of this section.

The above analysis is purely qualitative and is meant to provide a framework for discussing a possible source of porosity. Two quantitative factors are required to fully justify the model:

1) The excess vacancies cannot be annihilated immediately as the equilibrium concentration curve is lowered. (A significant non-equilibrium excess must be allowed to accumulate.)
2) The magnitude of $[V_O^{\cdot\cdot}]$ at the oxide metal interface, and ultimately $[V_O^{\cdot\cdot}]_{ex}$ must be large enough to account for the observed porosity.

Wagner has discussed the possibility of non-equilibrium defects for the case of scales with cation Frenkel defects.[52] He has made the assumptions that $[M_i]_{\text{oxide-metal}} = [V_m]_{\text{gas-oxide}}$, that $[Mi]_{\text{gas-oxide}} = [V_m]_{\text{oxide-metal}} = 0$, and that $D_v = D_i = D$ in order to simplify the calculations. The degree of deviation from equilibrium was then dependent on the magnitude of scale growth rate relative to the defect annihilation rate due to recombination of interstitials and vacancies. He concluded that non-equilibrium defects could be possible only in high purity compounds, with low defect concentrations. This analysis is not believed to be applicable to the present case of Al_2O_3 scales because of the restrictions concerning the symmetry of defect concentrations and diffusivities and the mechanism of defect annihilation. For example, Al_2O_3 has often been suggested to have primarily Schottky vacancy defects.[53,54] In such a case the annihilation of oxygen vacancies by the vacancy/interstitial recombination mode would appear to be minimal. Furthermore, the primary scale growth mechanism is by

oxygen grain boundary diffusion. Thus, the coupling of the primary defect flux giving rise to scale growth with diffusivities in the lattice cannot be made, as Wagner did. Thus, another representation of vacancy annihilation is presented below using assumptions more appropriate for Al_2O_3.

b) Semi-quantitative treatment of non-equilibrium vacancy profiles. A model is proposed here to describe the distribution of excess oxygen vacancies resulting from the two competing processes of a decreasing tolerance for equilibrium vacancies (as the scale grows inward, Figure 105) and the annihilation of vacancies at grain boundaries. The following major assumptions were used to construct the model:

1. The scale is inward growing with parabolic kinetics.
2. The equilibrium vacancy concentration is approximated as a linear function of position in the scale.
3. D_{Vo} is considered to be constant across the scale thickness.
4. Grain boundaries are the primary locations for vacancy annihilation and are perfect vacancy sinks.

The details of the analysis can be found in Appendix B. It was found that the net relative amount of excess oxygen vacancies remaining at a position "1" in the scale after total oxidation time "2" is: (equation B6)

$$\frac{\Delta V_{ex}}{(V_m - V_g)} = (1 - \sqrt{t_1/t_2}) \quad (1 - {}^{\Delta V_{GB}}/_{\Delta V_T})$$

where ΔV_{ex} = concentration of excess non-equilibrium oxygen vacancies

V_m = equilibrium oxygen vacancy concentration at the oxide-metal interface, i.e., $[V_o]_m$

V_g = equilibrium oxygen vacancy concentration at the gas-oxide interface, i.e., $[V_o]_g$

ΔV_{GB} = amount of vacancies able to diffuse to grain boundaries in time t_2-t_1.

V_T = total amount of excess vacancies assuming no annihilation at grain boundaries or other sinks.

$\Delta V_{GB}/\Delta V_T$ is given by the analytical function of $\sqrt{\frac{4D_{Vo}\ (t_2-t_1)}{(GS)^2}}$ described in Appendix B.

The vacancies are assumed to precipitate at the dispersed voids much faster than at the grain boundaries because of the greatly reduced diffusion distances. Thus, the calculated values of ΔV_{ex} in effect represent the amount of excess vacancies which can precipitate as voids. Profiles of the relative excess vacancy concentration are plotted in Figure 106 for the three times of oxidation studied: 0.1, 1.0, and 20 hrs. A constant grain size of 0.5 μm was used to allow direct comparison between the three curves. A value of 0.002 $mg^2/cm^4 \cdot hr$ (or $1.58 \times 10^{-13} cm^2/sec$) was used for k_p.

Also, a defect diffusion constant D_{Vo}, of $\sim 10^{-14}$ cm^2/sec was used as an upper limit. (Typical values of D_L^o obtained by extrapolation of data published for bulk Al_2O_3 are much lower, i.e., 10^{-21}-10^{-16} cm^2/sec at 1100°C.) In Figure 106a the relative excess vacancy concentration at the gas surface is near the maximum of unity, i.e., $\Delta V_{ex} = V_m - V_g$. The excess concentration decreases with

increasing distance and reaches zero at the oxide-metal interface. At longer times, 1.0 hr in Figure 106b, the profile has flattened considerably and the value at the gas surface has dropped to less than 0.4. A slight inflection point in the curve has also developed. And after 20 hours the entire curve has dropped orders of magnitude, the inflection point has evolved a maximum very near the oxide-metal interface, but this maximum is only $\sim$0.01.

The continual decrease in the amount of excess vacancies at the gas surface is shown in Figure 106 for various values of $\frac{\sqrt{D_{Vo}.}}{GS}$ For very low values of D, the decay by annihilation at grain boundaries is very slow; the maximum amount of excess may be continually maintained if $D_{Vo} \leq 10^{-20}$ cm^2/sec (for typical grain sizes of $\sim$0.5 μm). For the upper limit of 10^{-14} cm^2/sec used previously, the curve labeled $5x10^{-3}$ $sec^{-1/2}$ is appropriate; here the decay of excess vacancies is complete after 5-10 hours.

Thus, the following points summarize the discussion of non-equilibrium vacancy concentration and annihilation:

1. At very short times few vacancies can be annihilated at grain boundaries and more ΔV_{ex} are available for precipitation into voids observed in the 0.1 hr scale.
2. The amount of ΔV_{ex} available for precipitation into voids at the gas surface is constantly decreasing and is negligible for a 20 hr scale. This agrees with the prior conclusion that the total amount of porosity near the gas-oxide surface has not increased appreciably with time, e.g., 0.01, 0.01, and 0.03 void fractions for 0.1, 1, and 20 hr scales, respectively.

3. At long times, even the maximum in $\Delta V_{ex}/(V_m-V_g)$ is very small. This agrees with the observation that few new voids are precipitated near the oxide-metal interface in the 20 hr scale.

Since the actual value of D_{Vo} is not known, the effect of different assumed values of D_{Vo} on the excess vacancy profiles was also determined. Two families of curves resulted as shown in Figure 108 for a 20 hr scale and a 0.5 μm grain size. For $D_{Vo} \leq 10^{-15}$ cm^2/sec, Figure 108a, nearly linear, monotonically decreasing curves were obtained. At $D_{Vo} \leq 10^{-20}$ cm_2/sec, diffusion is so slow that no annihilation at grain boundaries would be possible. Thus, from equation B6, $\frac{\Delta V_{ex}}{(V_m-V_g)} = (1 - \sqrt{t_1/t_2})$. When plotted against distance for a parabolic scale this becomes a straight line. For higher values of D, the maximum excess (at the gas-oxide surface) continually decreases.

For D_{Vo} in the range of 10^{-15}-10^{-14} cm^2/sec, the concentration at the gas surface falls more rapidly than the rest of the curve, resul ing in a small maximum near the metal interface. The low ΔV_{ex} profiles in this range of D's are consistent with a relatively constant total amount of porosity at any given position in the scale.

The oxygen diffusion coefficient, D_L^o, was estimated to be $\sim 10^{-15}$ cm^2/sec from the relation for defect diffusion, $D_L^o = D_{Vo}[Vo]$, (from the kinetics of Ostwald ripening of voids, section 2, part a, below). Since $[Vo] << 1$ for a stoichiometric oxide such as α-Al_2O_3, then $D_{Vo} >> 10^{-15}$ cm^2/sec. This indicates that the lower curves in Figure 108 should apply. Thus the value of

$D_{Vo} = 10^{-14} \frac{cm^2}{sec}$ used in Figure 106 can be viewed as consistent with the Ostwald ripening value, or as a lower limit. Higher values will cause more rapid annihilation and lower ΔV_{ex} profiles.

The initial assumption of a linear gradient of equilibrium oxygen vacancies across the oxide in Appendix B was only a first approximation. The true $[V_o]_{eq}$ gradient may deviate appreciably from linearity, and this would cause dramatic changes in the excess vacancy profiles. Consider the extreme case where $V = V_g$ all through the scale, except for a very thin transition layer at the immediate oxide-metal interface. The working equation B8, developed in Appendix B is then:

$$\frac{\Delta V_{ex}}{(V_M - V_g)} = (1 - \frac{\Delta V_{GB}}{\Delta V_T}$$

where again $\frac{\Delta V_{GB}}{\Delta V_T}$ = an analytical function of $\sqrt{\frac{4 D_{V_o} (t_2 - t_1)}{GS^2}}$

The effect of this extreme equilibrium vacancy profile on the excess vacancy profile is shown in Figure 109 for a 1.0 hr scale. The basic form is that the maximum excess occurs just before the transition layer at the oxide-metal interface and is always at the maximum relative value of 1.0. The minimum value is at the oxide-gas surface and is always identical to that for the linear gradient case. The implications are that void precipitation close to the oxide-metal should occur, at least to the same extent that annihilation at grain boundaries is allowed (both processes are dependent on the rate of volume diffusion). This is contrary to the structural

observations. It is concluded that some finite gradient of equilibrium oxygen vacancies across the scale represents a more realistic view of the scale. The true equilibrium pO_2 gradient, and hence the V_{eq} gradient, can be calculated if the variation of ionic conductivity and transport number are known.[89] However, such data are not available for Al_2O_3 over the entire pO_2 range required or at 1100°C.

c) Absolute magnitude of ΔV_{ex} and observed void concentrations. The remaining requirement of the excess vacancy precipitation model is to assure that a sufficiently high excess vacancy concentration can be generated to account for the observed porosity. The maximum excess, possible at the gas interface for short times (Figure 106), is $\sim(V_m - V_g)$. This should be on the same order of magnitude as the maximum in void concentration. It can be shown* that the volume fraction of voids, fv, resulting from an excess vacancy concentration, ΔV_{ex}, is given by:

$$fv = .77\ \Delta V_{ex}$$

$$\therefore fv(max) = .77\ (V_m - V_g) \approx .77\ V_m \text{ since } V_m >> V_g$$

---

* $$fv = \left(\frac{\text{no. vacancies}}{\text{no. oxygen sites}}\right) \times (\text{volume per vacancy}) \times \left(\frac{\text{no. oxygen sites per mole } Al_2O_3}{\text{vol } Al_2O_3 \text{ per mole } Al_2O_3}\right) = \frac{\text{total vacancy volume}}{\text{vol } Al_2O_3}$$

$$fv = \frac{V \times 4/3\pi r_v^3 \times 3\ N_{Av.}}{\Omega_{Al_2O_3}} = \sim .77\ V$$

where: V = mole fraction of vacancies

r_v = radius of oxygen vacancy (1.374 Å)

N_{Av} = Avagadro's number (6.023×10^{23})

$\Omega_{Al_2O_3}$ = molar volume of Al_2O_3 ($25.56\ cm^3$)

Values for the maximum observed porosity ranged from about 0.01 to 0.03, giving $\Delta V_{ex}=V_m$ = 0.013 and 0.039, respectively. The existence of vacancy concentrations of 1-4% are considered to be very high for a stoichiometric oxide such as Al_2O_3. These values can be combined with the Ostwald ripening D_L^o values and the relation for defect diffusion, $D_L^o = D_{Vo}[Vo]$, to estimate D_{Vo}. The calculated values ranged from $1x10^{-14}$ to $4x10^{-13}$ cm^2/sec, which are consistent with the profiles in Figure 106.

d) Contribution of the oxygen vacancy flux. The non-equilibrium vacancies discussed above resulted by default; that is, new vacancies were not really created, but the equilibrium level was merely lowered by a decreasing pO_2 gradient. Vacancies may also be incorporated into the grains by diffusion due to the vacancy gradient across the scale. If the vacancy distribution is slightly above the equilibrium profile, then void precipitation is thermodynamically possible. In the vacancy flux model presented below, it is assumed that a vacancy lost to a precipitation process can be immediately replaced by the continual flux of vacancies flowing from an infinite source at the oxide-metal interface. It is this key assumption that allows for accumulation of vacancies into voids to values greater than 1.0 (V_m-V_g), which was the maximum excess vacancy concentration developed in part b.

Two cases of vacancy distributions are considered in Appendix C. In case A, the vacancy concentration was assumed to be linear from the gas to the metal. In case B, only an outer layer of scale (X_1)

was equilibrated with the gas; the rest of the scale (X_2) maintained a constant vacancy concentration, $V=V_m$. The following table gives the vacancy accumulation for both cases if $t_2 = 20$ and $t_1 = 0.1$ hr (i.e., the accumulation in the outer layer of the scale after 20 hr):

TYPE	EQUATION	f_v
A)	$\frac{2D}{k_p}(V_m-V_g)\ (1+\ln\sqrt{t_2/t_1})$	$7.3\ \frac{D}{k_p}(V_m-V_g)$
B)	$\frac{2D}{k_p}(V_m-V_g)\ (\sqrt{t_2/t_1})$	$23.3\ \frac{D}{k_p}(V_m-V_g)$

If $D_{Vo} > k_p$, then these models for vacancy accumulation allow values greater than (V_m-V_g). Recall that the excess vacancy model allowed a maximum of only 1.0 (V_m-V_g). Thus, the contribution of the oxygen vacancy flux could be of importance if some mechanism of continual replenishment operates. The maximum values, however, are still within two orders of magnitude of V_m, and the rationalization of 1% porosity thus requires $V_m \geq 10^{-4}$.

e) Void precipitation in other oxide systems. The occurrence of voids in oxide scales formed on metals is not a new phenomenon, although void occurrence in Al_2O_3 scales is not widely known because of the extremely small void sizes here. Voids have been easily observed in scales formed on Ni, Fe, and Co based alloys by standard optical metallography. The mechanisms of void formation which have been proposed for these alloys generally require the "injection" of cation vacancies to the oxide-metal interface whereupon eventual precipitation occurs. Thus, the key difference between these mechanisms and the excess vacancy model presented in parts a, b, and

c above is in the location of the precipitation event.

Gibbs described the production of voids in the inner layer of a duplex Fe_3O_4 scale formed on pure Fe in CO_2 at 500°C.[55] An elaborate theoretical treatment was presented which was based on the following sequence for a cation outward growing scale:

1. Inward cation vacancy diffusion
2. Precipitation of interface voids
3. Dissociation of scale over voided regions and the formation of a microchannel connected to the gas surface
4. Inward growth of a highly porous inner scale by metal recession plus molecular transport of the gas. The molecular transport takes place through the microchannels in the outer scale and interconnected porosity in the inner scale.

Since the heavily voided layer is inward growing, it is impossible to distinguish voids which may have been precipitated at the original metal interface from those which may have precipitated within the scale. But, because it is inward growing, the excess oxygen vacancy model presented for Al_2O_3 can be invoked as before in part a. Furthermore, the cation outward version of the excess vacancy model can be used to explain the voids in the outer scale -- a microstructural feature not discussed by Gibbs. Also, the proposed system of microchannels, theorized to be 0.2 μm wide, could not be resolved or verified in the optical micrographs presented. Finally, some of the micrographs presented show a low enough amount of porosity in the inner scale to preclude gaseous transport by interconnected pores in this region. Thus, the proof of an interface

void mechanism, as opposed to void precipitation with the scale, appears to be lacking.

Another study of pure Fe, oxidized in 1 atm air at 700-900°C, documented the existence of porosity throughout an outward growing FeO scale.[56] Again, only the pores at the oxide-metal interface were discussed, and again as a cation vacancy injection mechanism. The presence of a large amount of dispersed porosity in the bulk of the scale was not discussed.

A TEM study of oxides formed on pure Fe at 600°C in 10 torr O_2 has shown very fine pores in the Fe_2O_3 and Fe_3O_4 outer layers of the scale.[44] Since these layers are not in proximity to the oxide-metal interface, the cation vacancy injection model cannot account for them. The position of the voids within an oxide layer again suggests a bulk precipitation phenomenon as opposed to an interface void mechanism.

In the case of NiO scales formed on pure Ni, Rhines and Wolf have observed pores at NiO grain boundaries throughout the scale.[57] They have speculated, but not proven, that these pores resulted from gain boundary sliding caused by growth stresses in the scale. More recently the pores were thought to be "foreign matter" precipitates left from an unclean specimen surface or impurities in the nickel substrate.[58] However, a study of various purities of nickel (30, 200 and 4000 ppm) has shown little correlation between porosity in the scale and nickel purity.[59] Thus, the voids were probably not artifacts and their production has not been adequately explained. This then is another example where void precipitation throughout

the scale may provide the most direct mechanism and most satisfactory explanation of the observed distributions.

Impressive evidence of the power of a change in the pO_2 gradient, or of the pO_2 gradient itself, to produce vast amounts of porosity in an oxide was presented by Yurek and Schmalzried.[60] They annealed single crystal CoO in 1 atm air at 1200°C for 12 hours. This was then subjected to 1 atm air (pO_2=0.2 atm) on one side of the crystal and to a CO/CO_2=0.10 gas mixture (pO_2=1.1x10^{-9} atm) on the other side. After 1.5 hr at 1200°C the crystal developed approximately 5 volume percent of porosity; after 42.5 hr the crystal was well above 50% porous. For short times, a distinct increase in pore size with distance from the low pO_2 side was observed.

The authors described the pore formation process as the result of V_{Co} diffusion from the high pO_2 side ($[V_{Co}]_{eq} \approx 10^{-2}$) and precipitation at the low pO_2 gas-oxide interface ($[V_{Co}]_{eq} \approx 10^{-4}$). The distribution of pores throughout the crystal was explained as the result of pore migration counter to the vacancy flux (toward the high pO_2 side) and coalescence of these migrating pores with increasing distance traveled. Interface pore marker movement in MgO-CoO diffusion couples was presented as the experimental evidence of pore movement counter to a flow of vacancies. (Here V (pure MgO) = 10^{-4} V (pure CoO) at 1400°C.) However, it appears that this pore motion towards the CoO side could have simply resulted from faster diffusion of Co into MgO than Mg into CoO. Indeed, the edges of Pt markers were also seen to move away from the MgO toward

the CoO side of the couple. Thus, more matter accumulated into the MgO side, causing displacement of interface debris into the CoO side.

The pore distribution in the CoO single crystal subjected to a pO_2 gradient will now be discussed as a bulk precipitation process (as opposed to a gas-oxide interface precipitation followed by pore migration and coalescence). The low pO_2 environment requires a much smaller cation vacancy concentration for equilibrium than the initial pre-annealing treatment in 1 atm air. As a result, the initial high equilibrium value now becomes in excess of equilibrium. This provides a driving force for pore precipitation, ΔG_p. From the relation for critical stable nuclei, $r_e=2\gamma/\Delta G_p$, a qualitative distribution of pore sizes vs. supersaturation can be put forth. The direction of ΔG_p can be estimated from the volume free energy change associated with precipitating a given fraction of vacancies. From the usual vacancy configurational entropy term in a crystal[61] it can be shown that $\Delta G_p=N_v RT \ln (N_v/N_{v,eq.})$, where N_v is the mole fraction of vacancies in the supersaturated state and $N_{v,eq.}$ is that in the equilibrium state (i.e., after pore precipitation).

Yurek and Schmalzried estimated $N_{v,eq}$ to be 10^{-4} at the low pO_2 side and 10^{-2} at the high pO_2 side. Thus, the maximum N_v at the low pO_2 side before any defect relaxation process occurs is 10^{-2}. From the above equation this produces a maximum ΔG_p of 565 J/mole at the low pO_2 side and an r_e of $\sim$400 Å (a typical value of 1.0 J/m^2 for γ was assumed). If $N_{v,eq}$ can be determined as a function of position across the crystal, r_e could then be calculated

for various positions across the scale.

This exercise was performed by first assuming a linear relationship of $N_{v,eq}$ across the scale, as shown in Figure 110. The resultant r_e is compared to the actual r_p (from the micrograph of CoO at 1200°C, 1.5 hr by Yurek and Schmalzried). The parallelism of the two curves is exceptional. (The error bars represent ± 1σ.) The curves are not meant to agree quantitatively, since the critical pore size only gives an indication of how large the pores must have been to be stable. No account of how large these nuclei may have grown has been attempted. But, if it is assumed that there should be some correlation between initial and final pore size (or, equivalently, initial and final number of pores), then Figure 110 gives testimony to the possibility of pore nucleation in the bulk. Therefore, it is again proposed that voids nucleate and grow in the bulk of oxide specimens or scales when subjected to a change in pO_2 gradient. The role of the pO_2 gradient appears not only to produce a vacancy gradient and flux, but also to create an unstable supersaturation of vacancies. Admittedly, after continued exposure the vacancy flux must command an increasing role in the growth of voids. This is concluded because the porosity in CoO was seen to increase from the 1.5 hr to the 42.5 hr exposure. Thus, pore growth continued even after the equilibrium vacancy concentration should have been reached.

As a final note, a transitory stage in the conductivity of NiO subjected to a pO_2 change has been suggested as a non-equilibrium effect.[62,63] It was found that NiO, equilibrated at 10^{-5} torr O_2,

exhibited a sharp rise in conductivity as the pO_2 was instantaneously raised. After some time the conductivity abruptly returned to the initial value. This time interval substantially increased with pO_2 and decreased with temperature. This behavior was modeled by means of an equivalent electrical circuit. The results supported a mechanism of mixed kinetics whereby the pO_2 increase first caused an instantaneous rise in $[V_{Ni}]$ at the oxide-gas surface, which then decayed as though the oxide was a discharging condenser. The authors thus believed the transitory effect to be due to a non-equilibrium defect concentration created by a change in pO_2 environment. It is precisely this effect which is being proposed as the cause of voids in bulk oxides and oxide scales subjected to a changing pO_2 gradient.

2) Diffusion Processes in Al_2O_3 Scales

a) Void growth and Ostwald ripening. The dramatic increase in void diameter with time and decrease in the number of overall voids discussed in Section C indicated that the voids were growing, at least in part, by an Ostwald ripening process. According to this model the surface of a precipitate (void in this case) builds up a higher concentration of solute (vacancies) than the bulk material. The degree of supersaturation is inversely proportional to the particle radius as given by the Gibbs-Thompson equation:

$$RT\ln {C_r}/{C_\infty} = \frac{2\gamma M}{r\rho}$$ Eqn. 16

where C_r, C_∞ are concentrations at the particle surface and in the bulk

γ = surface energy
M = molecular weight
r = particle radius
ρ = density of particle

A solute gradient and flux is set up from small particles to larger ones. By taking account of the flux from various sized particles it was shown by Greenwood[91] that the average particle diameter can be approximated by:

$$r^3 - r_o^3 = \left(\frac{6DC_\infty M\gamma}{RT\rho^2}\right)t \qquad \text{Eqn. 17}$$

From the appropriate constants and from the void growth data, values of DC_∞ can be obtained. It will be recalled that cubic growth laws were not observed, so that only approximations of the growth rate could be obtained. These attempts produced DC_∞ in the range of $4.4\text{x}10^{-16}$ to $5.5\text{x}10^{-15}$ $\frac{cm^2}{sec}$. Since C is really the concentration of vacancies in the scale and D is the vacancy diffusivity, then DC_∞ is equivalent to the self-diffusion coefficient from $D_L^O = D_{Vo}[Vo]$. If the voids were caused by an excess of oxygen vacancies, as discussed in part 1, then DC_∞ should reflect oxygen diffusivity. It will be seen in the following discussion that this value (Fig.111) is much higher than measured oxygen lattice diffusivities in bulk Al_2O_3.

b) Grain boundary diffusivity, scale growth, and grain growth.

Ideally the growth of an oxide scale by volume diffusion controlled processes can be described by the Wagner equation. This relates the parabolic growth constant to an integral of conductivity (or diffusivity) over the range of the equilibrium oxygen potential across the scale thickness. However, for these fine grained Al_2O_3 scales, the contribution of grain boundary diffusion of oxygen is generally accepted to be of primary importance. The equivalent of the Wagner equation has not been developed for the case of scale growth by

combined grain boundary and volume diffusion. Furthermore, the pressure dependence of diffusivity is not known for bulk Al_2O_3. Thus, the classic treatment of scale growth by comparison of measured and calculated k_p's has not been performed for Al_2O_3 scales.

Although this situation precludes modeling of the transport processes in the scale, it is useful to perform some calculations based on a simplified growth model. For this purpose the scale is envisioned as a moving boundary of fixed composition. Such phase boundary motion generally follows a parabolic law, and the approximation is made that:

$$x^2 \approx D_{eff}\, t \approx k_p t \qquad \text{Eqn. 18}$$

$$\text{i.e., } D_{eff} \approx k_p$$

Furthermore, if grain boundaries represent the major short circuit diffusion path, then

$$D_{eff} \approx (1-f)D_L + f\, D_{GB} \qquad \text{Eqn. 19}$$

where D_{eff} = effective diffusion coefficient

D_L = lattice diffusion coefficient

D_{GB} = grain boundary coefficient

f = effective volume fraction of grain boundaries

For columnar grains it can be shown that,

$$f = \frac{2\delta}{GS} \qquad \text{Eqn. 20}$$

where δ = grain boundary width

GS = grain size

Thus, for $\delta \approx 100$ Å, and GS$\sim$2000Å, then $f \sim 0.1$ and $D_{eff} \approx 0.9 D_L + 0.1 D_{GB}$. Since it has been shown that $D_{GB} >> D_L$ for oxygen transport in bulk Al_2O_3[64], the following approximation is valid:

$$k_p \approx D_{eff} \approx f D_{GB}$$

or Eqn. 21

$$\delta D_{GB} = k_p \cdot \frac{GS}{2}$$

From the discussion of microstructures, it was clear that the grain size was on the order of 2000 Å at the gas surface; and from studies on Al_2O_3 scale growth on NiCrAl alloys[39] it was found that $k_p \approx 0.002$ mg^2/cm^4 · hr, corresponding to $D_{eff} = 1.6 \times 10^{-13} \frac{cm^2}{sec}$.

The separation of the terms in δD_{GB} has been discussed (Mistler and Coble) in a review of grain boundary diffusion processes.[65] The product can be obtained by diffusion studies giving D_{eff} and D_L. This analysis is essentially what was attempted above. The quotient of $\frac{D_{GB}}{\delta}$ is then obtained by an analysis of grain growth rates. Since this data was also available from the microscopy study, it will be possible to separate δ and D_{GB} and compare these values to those determined for bulk oxides.

From Mistler and Coble:

$$\frac{D_{GB}}{\delta} = \left(\frac{GS^2 - GS_o^2}{t}\right) \frac{RT}{4\Omega\sigma}$$ Eqn. 22

or:
$$\frac{D_{GB}}{\delta} = \left(\frac{GS^2 - GS_o^2}{t}\right) \; 7.12\times10^6 \text{ cm}^{-1}$$

where Ω = molar volume of Al_2O_3 = 25.56 cm^3/mole

σ = grain boundary energy $\approx$ 540 ergs/cm^{2*}

RT = gas constant X temperature

t = time

Although a parabolic grain growth law was not observed, it was still possible to determine a range of slopes from a plot of $GS^2 - GS_o^2$ against time. Table XIII shows the values of δ and D_{GB} calculated from the Mistler and Coble equation with $\delta D_{GB} = 1.58\times10^{-18}$ cm^3/sec from the k_p data. The range of D_{GB} and δ resulting from the different initial and final grain growth rates was not too large.

c) Comparison to grain boundary diffusion in bulk Al_2O_3. In the discussion to follow, an attempt will be made to compare values of δ and D_{GB} inferred from the oxidation studies to those determined from bulk Al_2O_3 diffusion studies. In order to do so some manipulation of the published data is required.

The major studies of oxygen grain boundary diffusion in bulk Al_2O_3 were by Reddy[67] and by Mistler and Coble's analysis[65] of Oishi and Kingery's data[64]. Oishi and Kingery showed a low and high temperature branch to their diffusivity data and this is shown in Figure 111. This occurred for their polycrystalline samples as well as for some single crystal samples. The high diffusivities of

---

*Estimated as one-half the surface energy at 1100°C.[27,66]

the low temperature branch appeared to be associated with samples which had not been pre-annealed like the others in 1 atm air at 1900°C.

The data for the polycrystalline material is representative of D_{eff} and that of the single crystal samples reflects D_L. Thus, as originally determined by Mistler and Coble, δD_{GB} can be calculated from the equation for effective diffusion coefficient (as in part b). Table XIV lists the relations for D_{eff}, D_L and δD_{GB} for Oishi and Kingery's data. Relations for δD_{GB} vs T were determined from an Arhhenius plot of values calculated at specific temperatures. Mistler and Coble calculated δD_{GB} (high temp) = $515\ \delta \exp\left(\frac{-108\ kcal}{RT}\right)$. This is the same as that in Table XIV if $\delta \approx 250$ Å. Also shown for comparison are values for D_L and D_{GB} from Reddy. Here δD_{GB} was measured directly from ^{18}O profiles in polycrystalline samples determined by proton activation techniques.

All the δD_{GB} relations are shown in Figure 112. It is apparent that the calculated high temperature branch agrees well with Reddy's direct measurement. This result supports the validity of using the D_{eff} concept for estimating δD_{GB}. The low temperature branch shows a significant departure from Reddy's data. But there is good agreement between this calculated low temperature branch and the value obtained in part b from the oxide growth data at 1100°C.

Values for D_{GB} in the bulk can be separated from δD_{GB} if the grain boundary width is known. Plots of D_{GB} vs. 1/T are shown in Figure 113 for various assumed values of δ. Also shown is the value for Al_2O_3 scales formed on the Ni-Cr-Al alloy (from Table XIII).

It is encouraging that the NiCrAl oxidation data again agrees with the low temperature, bulk Al_2O_3 data for δ in the range of 100-500 Å. Recall that δ of 450-800 Å had been estimated for the Al_2O_3 scales in Table XIII.

Reddy determined δD_{GB} and δ from an analysis of ^{18}O levels and profiles in polycrystalline Al_2O_3.[67] His δD_{GB} was shown in Figure 112. Values of δ calculated by Reddy and values for D_{GB} which were inferred from δ, are shown in TAble XV. The grain boundary widths ranged from 160-500 Å for pure hot pressed Al_2O_3 and from 1600-2700 Å for MgO-doped Lucalox.

Thus, the Al_2O_3 scale values of 450-770 Å are in basic agreement with Reddy's data for pure Al_2O_3. Mistler and Coble calculated δ from various grain growth and diffusion data and obtained values between 70-150 Å.[65] More recently, grain boundary widths were measured directly for a synthetically produced tilt boundary in a pure Al_2O_3 bicrystal (< 50 ppm total impurities).[68] They determined δ by back-extrapolating optically determined grain boundary groove widths vs. chemical etching time. They found boundary widths at zero etching time to be 500-550 Å. Also depth-profiling with an ion microprobe revealed an impurity segregation layer of 600-800 Å for these reasonably pure samples.

In summary, the Al_2O_3 scales possess an effective grain boundary width in accord with values determined on bulk Al_2O_3 of reasonable purity. Some impurity effect is to be expected due to probable Ni and Cr dopant elements from the alloy. Of more importance is the agreement of δD_{GB} and D_{GB} with the low temperature branch calculated

from the data of Oishi and Kingery. Comparison with an extrapolation of the high temperature branch shows the δD_{GB} and D_{GB} for the scales to be more than two orders of magnitude too high. Thus, the following section will discuss the possible causes of the low temperature branch and its significance to the transport processes in the scale.

d) Non-equilibrium defects in Al_2O_3. Oishi and Kingery originally interpreted the low temperature branch of their data as an extrinsic effect due to impurities. (See Figure 112.) This was later interpreted by Reddy as non-equilibrium effects caused by the lack of pre-annealing the samples in a pO_2 comparable to the ^{18}O exchange pressure.[67] For example, Oishi's samples which were pre-annealed in 1 atm air at 1900°C exhibited diffusivities lower by a factor of 2 (at 1600°C) and lower by a factor of 12 (at 1500°C) than comparable unannealed samples. The unannealed samples thus exhibited high diffusivities in the low temperature region because of a high concentration of defects, presumably $V_O^{\cdot\cdot}$. These defects remained from the low pO_2 environment during crystal growth or sintering. This argument becomes more convincing when the annealing effects observed by Reddy are examined.

Reddy's O^{18} profiles on unannealed single crystals showed deviation in the form of long "tails" extending into the crystal. The following findings were crticial to his final conclusions:

1. The tails were largest in samples which were manufactured at the lowest pO_2 ($\sim 10^{-4}$ torr).

2. The tails were eliminated by a 1 atm air or O_2 pre-anneal for times longer than the subsequent diffusion test.
3. Vacuum pre-annealing at 10^{-2}-10^{-3} torr did not eliminate the tails.
4. Diffusion tests made at low pressure did not exhibit the tails.
5. The magnitude of the tails was not increased with the number of short-circuit paths, i.e., dislocations.

These observations were all consistent with his suggestion that the deep penetrations were due to defects produced by a low pO_2 manufacturing process. Equilibration with the high pO_2 of the diffusion exposure occurred too slowly to fully eliminate these defects during a test, especially at lower temperatures. However, a long pre-anneal in air did allow equilibration to occur. One further experiment exhibited somewhat of an anomaly, in that the tails did not reappear in samples first annealed in air then in vacuum. Whether the vacuum was not low enough or whether a true irreversible effect existed was not decided.

From Reddy's own experiments and from his interpretation of Oishi and Kingery's low temperature branch, it appears that oxygen diffusion can be dramatically enhanced by a low pO_2 environment or perhaps a large pO_2 gradient. Thus, agreement between the low temperature branches of δD_{GB}, D_{GB}, and δ with the values estimated for the Al_2O_3 scale (in part c), suggests that a low pO_2 or non-equilibrium effect is important in the scales. It is precisely the hypothesis of non-equilibrium [Vo] or a high Vo flux, that was used in section 1 to account for the void formation. Thus a

consistent model of scale growth exists based on enhanced grain boundary diffusion and non-equilibrium oxygen vacancies due to the extremely low pO_2 at the oxide-metal interface.

While these diffusion studies presented an interpretation consistent with the oxidation model, low pO_2 effects on electrical conductivity were more difficult to interpret in detail. Nevertheless, it is useful to review some of these results to both assess the credibility of the oxidation model as well as to gain an appreciation for the many other Al_2O_3 growth processes and scale morphologies which might occur.

Table XVI summarizes trends in ionic conductivity with pO_2. It is clear that in both pure and doped Al_2O_3, the ionic conductivity has been found to increase, decrease, or remain relatively constant over the range of pO_2 studied. Samples which showed a 1-2 order of magnitude increase in σ_i with decreasing pO_2 suggest that ionic diffusivities may also increase with low pressures. From the diffusion data in Figure 111 and 113, the low temperature branch showed a 10^4 enhancement in D_L and 10^2 in D_{GB} (data extrapolated to 1100^oC). Since these were explained as a non-equilibrium low pO_2 effect, the high electrical conductivities at low pO_2's could support such an argument. Of course, no quantitative comparison can be made unless both conductivity and diffusion studies are performed on identical samples. The unpredictable behavior of these conductivity relations with low levels of dopants and prior heat treatment suggest that any minor changes in Al_2O_3 scale composition could significantly influence transport properties in the lattice and

scale morphology. For example, aluminum interstitials could be the major defect species in a doped Al_2O_3 scale. Then the pO_2 gradient would not necessarily result in oxygen vacancies and void formation. Recall that the occurrence of void-free grains was also noted in the prior discussions of scale morphologies.

The effect of hold time in these conductivity tests provided some additional relevant information. For pure Al_2O_3 at 1500°C, the instantaneous conductivity was recorded as the pO_2 was decreased. This reading was about 2/3 of the value obtained a few hours later when equilibration had occurred.

In another study the change in total conductivity of polycrystalline Al_2O_3 was recorded as a function of time after a discontinuous change in the oxygen partial pressure.[72] By decreasing the pO_2 from 1 atm to $< 10^{-5}$ atm the conductivity was observed to decrease about one order of magnitude over a period of a few hours at 1100°C. This relaxation time reflected the change of equilibrium defect concentration from the surface to the bulk of the sample, until total equilibration is reached. The conductivity experiments do indicate that finite equilibration times are required for bulk Al_2O_3 when a change in pO_2 is imposed. Alumina scales also exhibited conductivity transients following a pO_2 change.[73] These transients lasted 1/2-2 hours at 1100°C.

It would also be instructive to examine the microstructural changes in bulk Al_2O_3 after a change in pO_2 or in an imposed pO_2 gradient. Such an experiment could give convincing evidence to the hypotheses presented above concerning the precipitation of non-

equilibrium vacancies into voids. The literature dealing with this type of study is generally directed towards gas permeability in Al_2O_3 tubes. In these studies the internal and external gases are controlled (usually low pO_2 and high pO_2, respectively). The low pO_2 side is monitored for leaks after high temperature exposure. Explanations are then put forth based on microstructural examination of the deteriorated tubes.

A summary of these experiments is given in Table XVII. In all cases polycrystalline sintered Al_2O_3 tubes were used. After high temperature exposure, interconnected grain boundary porosity was observed to form, especially at the low pO_2 side of the tube. Prior to complete channeling through the entire tube thickness, appreciable rises in the oxygen content inside the tubes were measured. These were often consistent with a solid state diffusion porocess through an impermeable skin of large grains where no interconnected porosity was observed. In the study of hydrogen permeability no interconnected porosity was observed, but a slight increase in the total amount of porosity did occur.[78]

Thus, all these studies do confirm the production of porosity in bulk Al_2O_3 subjected to a low pO_2 environment. However, the explanation put forth did not deal with the production of oxygen vacancies due to the low oxygen pressures. Rather, the reduction and volatilization of SiO_2, CaO, or Na_2O impurities was suggested as the reason for the porosity increase. (All the materials contained $\sim$0.1% impurities.) In the hydrogen study, H_2 bubble formation or "bloating" was suggested as the reason for the

density decrease. These complications do not allow a definitive statement from the permeability studies regarding the low pO_2 effect on vacancy formation. A critical experiment involving higher purity Al_2O_3 would be required. Such a test was referred to for single crystal Al_2O_3.[75] No high permeabilities were found, but no mention of microstructural changes or pore formation was made. The observed effects of low oxygen pressures on bulk Al_2O_3 porosity remains to be an interesting but poorly understood phenomenon which may have direct impact on pore formation in Al_2O_3 scales. The possibility of pore precipitation due to non-equilibrium oxygen vacancies resulting from a pO_2 gradient has not been dealt with. It is the author's opinion that such a mechanism remains to be a viable explanation in light of the experiments performed to date on bulk Al_2O_3.

3) Subgrains, Texture, and Deformation Processes

The clusters of subgrains in the 20 hr scale present a new and interesting feature to the subject of scale microstructures. The subgrain boundaries appear to be the prime location for individually resolved dislocations and thus are important to a discussion of deformation by dislocation glide or climb. The large number of subgrains in a cluster and the apparent frequency of these clusters indicate that they may reflect a widespread preferred orientation of the scale.

The orientations of the clusters, $\langle 10\bar{1}1\rangle$ and $\langle 20\bar{2}1\rangle$, suggest that the overall texture of the scale may be close to these

directions. Some preliminary X-ray diffraction studies performed on NiCrAl+Y and NiCrAl+Zr oxidized for 20 hours at 1100°C indicated that the plane of oxidation contained a weak basal (0001) texture.[79] Similar work was also performed on TD-NiCrAlY and FeCrAl (HOSKINS 875) oxidized at 1200°C for 500 hr and 100 hr, respectively. Here stronger (0001) textures were apparent. Ratios of relative intensities from inverse pole figures of the (0006) peak were ∿5 for these alloys, as compared to unity for a perfectly random structure. It was concluded that the clusters of subgrains observed in the 20 hr scale contributed, on the average, to a weak (0001) texture. The angles which the $[10\bar{1}1]$ and $[20\bar{2}1]$ directions make with [0001] are 32.4° and 51.8°, respectively. Thus, the TEM information alone does not reflect the average texture, which is still in a rather weak state of development.

There are a number of possible causes of the texture, which are related to the anisotropy of the α-Al_2O_3 crystal structure. They are: a) deformation texture, b) surface energy texture, c) diffusional growth texture, and d) elastic strain energy texture. Experimental evidence of the first two phenomena is available and will be discussed in detail.

a) Deformation texture and creep models. The occurrence of a deformation texture in polycrystalline Al_2O_3 has been widely observed.[45,46,80,81] Although clusters of subgrains have not been specifically reported in the microstructural studies of these works, subgrain boundaries have been the primary location of dislocations observed. This similarity to the scale structure suggests that

texture and subgrain boundaries may have common related origins in bulk Al_2O_3 and in thin scales.

The bulk Al_2O_3 studies all report a moderate (0001) fiber texture parallel to the compression axis for uniaxial compression; that is, the basal plane is parallel to the compression surface. Ratios of relative intensities of the (0006) peak from inverse pole figures ranged from 3-20, and were greatest for high temperature and strains. It is generally believed that this texture results from the occurrence of basal slip and the rotation of the slip planes perpendicular to the compression axis. Although the geometry of this texture appears similar to that of the scales, i.e., (0001) is rotating into the plane of oxidation, the stress situation is different. The growth stress on the scales is primarily of biaxial compression in the plane of oxidation, as caused by the volume expansion during conversion of metallic aluminum to Al_2O_3. One would predict that such a stress state should rotate the (0001) planes perpendicular to the compression axes, resulting in (0001) planes perpendicular to the plane of oxidation. Thus, the predicted deformation texture would be of the type (hki0) and is diametrically opposed to the observed (0001) oxidation texture.

It is discouraging that the oxidation texture cannot be described by a basal slip deformation texture. However, since diffusional creep is also considered to be of prime importance to the deformtion of polycrystalline Al_2O_3, it is useful to relate the scale structures to diffusional processes as well.

The compressive creep mechanisms in fine-grained (~15 μm) Al_2O_3 have been recently investigated and the primary process has been identified as interface-controlled diffusional creep.[82] That is, conventional Nabarro-Herring volume diffusion or Coble boundary diffusion mechanisms account for most of the deformation, but the overall creep rate is determined by the rate at which vacancies can be absorbed or emitted at grain boundaries. The critical process in interface-controlled creep has been theorized to be the climb of grain boundary dislocations having a component of the Burgers vector normal to the boundary.[83] Thus, it is believed that the most important structural features in fine-grained Al_2O_3 are the dislocations observed in high angle grain boundaries; these both control vacancy absorption/emission and the generation of lattice dislocations which produce a limited amount of basal slip.

It is a curious fact, however, that no observations of lattice-glide dislocations in basal slip bands were observed. The most common occurrence of lattice dislocations in fine grained Al_2O_3 was in the arrays of low angle boundaries. The question arises as to the detectability of glide dislocations; they may simply be emitted and absorbed by grain boundaries in such a rapid fashion that they are never retained after stress removal for post-test examination. Thermally activated recovery can also serve to lower the dislocation density as observed by annealing heavily deformed Al_2O_3 at 1200 and 1500°C.[45,84] Here uniformly distributed dislocations were annihilated or rearranged into low angle boundaries during annealing. Thus, the commonly observed low angle

boundaries may be due to recovery of glide dislocations.

From these studies on bulk Al_2O_3, the following implications arise for the Al_2O_3 scales: interface-controlled diffusional creep, more important for finer grain sizes, ought to control deformation in the Al_2O_3 scales, where grain sizes from 0.1 to 1.0 μm were common. The role of dislocation glide is somewhat problematic in that glide dislocations may not be observable for these extremely fine grained scales. The occurrence of numerous subgrain boundaries may reflect the prior interaction of glide dislocations. However, the exact relationship of glide dislocations and subgrain boundaries is not clear even for bulk Al_2O_3. Certainly the observed scale textures do not support the occurrence of (0001) $\langle 1\bar{2}10\rangle$ glide. However, since diffusional creep is expected to predominate, the role of subgrain boundary dislocations in the scales may be to serve as additional climb sources for Nabarro-Herring Creep, as described below.

An array of edge dislocations in a low angle boundary is shown schematically in Figure 114. The horizontal solid lines are high angle grain boundaries parallel to the surface of oxidation. Under the action of a compressive stress, σ, the dislocations will absorb vacancies by climbing from A to B. This is done most efficiently if $\vec{b}$ is perpendicular to $\vec{\sigma}$; that is, the rate of climb is proportional to the reduction in strain energy due to climb, $\sigma b\cos\theta$. The counterflux of atoms and vacancies is such that the grain grows vertically.

For Al_2O_3, basal $\langle 1\bar{2}10 \rangle$ dislocations are the most energetically favored to exist. Thus, the perpendicular direction of climb, $\bar{c}$, will most often be [0001]. Thus, grains oriented such that [0001] is normal to $\bar{\sigma}$ will exhibit the fastest rate of climb-assisted growth. This model qualitatively supports the occurrence of moderate (0001) textures in the scales. It emphasizes the role of dislocation climb, in accord with expected diffusional creep processes, over that of dislocation glide. While addressing the development of (0001) fiber textures, it does not necessarily explain the existence of subgrains in highly aligned clusters.

b) Surface energy texture. The occurrence of (0001) textures in thin tape-cast Al_2O_3 provides another mechanism which may account for both the scale texture and the existence of subgrain clusters. Bellosi and Vincenzini observed (0001) texturing of tape-cast Al_2O_3 powders, with a (10·10) normalized intensity ratio increasing from 1.2 in the as-dried condition to 3.4 after three hours at 1600°C.[85] Nakada and Schock observed the (0006) intensity ratio to increase from 4.4 as-dried to 75 after sintering at 1700°C for four hours.[86] They also observed that vacuum and hydrogen atmospheres were less conducive to texturing than was air. Although some texturing was caused by the (0001) plate-shaped particles in the unfired slurry, both studies attributed the more dramatic effects caused by sintering to the enhanced growth of grains having a low surface energy plane exposed to the atmosphere, i.e., (0001). They presented hexagonal surface steps produced by thermal faceting as evidence of the low surface energy of the (0001) planes. They also related these

phenomena to a commercial process of texture control in thin Fe-Si transformer sheet, where different atmospheres changed the relative surface energies and resulted in different sheet textures.

The application of this phenomenon to the Al_2O_3 scales is attractive because the scales are usually only a few grains thick, so that the influence of the surface grains is emphasized. It is also encouraging that the tape-cast studies proposed that accentuated grain growth occurred for (0001) grains. If such a process occurred for the Al_2O_3 scales, then the large grains so produced may segment under the influence of the growth stress into many subgrains retaining for the most part the orientation of the parent grain. It should also be pointed out that exaggerated grain growth is common for pure bulk Al_2O_3 and that this process could also account for large parent grains.

In retrospect, the surface energy mechanism predicts the observed scale textures, whereas the basal glide mechanism does not. Stress-assisted climb of the subgrain dislocations could accelerate vertical growth of (0001) grains, but could not account for the extent of subgrain clusters. Some mechanism to account for the clusters, such as prior exaggerated grain growth, is also required. The relationship of the subgrain boundaries to active glide dislocations is not clear, although there is evidence in bulk Al_2O_3 that recovery of glide dislocations into low energy arrays does occur.

SUMMARY AND CONCLUDING REMARKS

The transmission electron microscopy study of oxide scales formed on oxidation-resistant NiCrAl engineering alloys has revealed a wealth of previously unobserved structures. The initial oxidation process was characterized by oriented scales of α-$(Al,Cr)_2O_3$, α-Al_2O_3, and $Ni(Al,Cr)_2O_4$. The orientation effect probably resulted from an initial epitaxial growth on the metal substrate. The eventual development of a randomly oriented, stable, pure α-Al_2O_3 scale was observed at the immediate oxide-metal interface. The many features found in the oriented scales, such as aligned precipitates, Moire' patterns, and anti-phase domain boundaries, were interpreted as transition effects from the Ni,Cr-containing scales to pure Al_2O_3. They can be viewed as variations in the cation chemistry and stacking periodicity in a close-packed oxygen lattice. The scale structures were similar for pure, Y-doped, and Zr-doped NiCrAl, with perhaps a higher degree of orientation for the doped alloys. A significant amount of grain boundary porosity was also observed for the scales on the Y-doped alloy.

The random α-Al_2O_3 structure was dominated by dispersed porosity which was most prevalent at the oxide-gas interface. The voids were seen to coarsen by an Ostwald ripening process until many grains exhibited only one large void after 20 hours of oxidation. The occurrence of porosity in the form of fine voids in the midsection of the scale indicated that void precipitation occurred

continually in this inward growing scale. The distribution of porosity was consistent with a model of oxygen vacancy precipitation based on a decreasing pO_2 gradient and a decreasing equilibrium level of oxygen vacancies as a function of oxide thickness. Vacancy precipitation into a uniform distribution of voids occurred in preference to annihilation at sinks such as grain boundaries because of the shorter diffusion distances required. The large amount of porosity could not totally be accounted for by this model; thus, an outward flux of vacancies from the oxide-metal interface may have also operated. The effect of the voids on the oxidation process was not clear; however, the surface energy stresses calculated for $\leq$200 Å voids was $\sim$100 MPa; high enough to exert attractive forces on dislocations.

Diffusional analyses based on void growth, grain growth, and scale thickening rates yielded oxygen lattice and grain boundary diffusivities much higher than values extrapolated from reported data for annealed bulk Al_2O_3. Agreement was obtained, however, with grain boundary diffusivities calculated for unannealed material, which was believed to contain nonequilibrium oxygen vacancies remaining from low pO_2 processing during crystal growth. The postulate of nonequilibrium oxygen vacancies to account for high diffusivities in the scale is consistent with the aforementioned model of void precipitation in the scale.

Free dislocations or precipitates were generally absent from the random Al_2O_3 scales. Occasionally small dark spheres, probably $NiAl_2O_4$, were associated with fine pores. Clusters of subgrains of

<$10\bar{1}1$> or <$20\bar{2}1$> orientations were readily found in the 20 hr scale at all levels in the scale. Individual dislocations and Moire' patterns were frequently imaged in the subgrain boundaries which represented a slight 1-5° misfit between adjoining subgrains.

These subgrain clusters were thought to be the beginnings of a moderate (0001) texture, possibly caused by anisotropic surface energies in α-Al_2O_3 in conjunction with abnormal grain growth. Deformation textures predicted for basal slip processes could not account for the observed scale textures; however, stress-assisted climb of basal dislocations in the boundaries did offer another possible texture mechanism. Theories of deformation in fine-grained Al_2O_3 predict interface-controlled diffusional creep to be the dominant deformation mechanism in submicron Al_2O_3 scales; it was also noted that stable glide dislocations may simply not be observable in fine-grained Al_2O_3.

The implication of this work on the field of oxidation should be considered from both a fundamental and applied perspective. From a basic standpoint, it has been useful to show that transient oriented (epitaxial) scales are comprised of fine substructural detail due to the very changing nature of their composition and crystal structure, while the stable α-Al_2O_3 grains are relatively free from defects other than voids. The transition from the oriented mosaic of subgrains to a polycrystalline scale is an interesting phenomenon worthy of further study. The production of an oriented stable α-Al_2O_3 scale would result in reduced short-circuit grain boundary diffusion and reduced scale growth rates.

This benefit might also be realized by encouraging the texturing found in the mature α-Al_2O_3 scales where high angle boundaries would be replaced by low angle subgrain boundaries.

The proposition that nonequilibrium vacancies are produced and precipitated in oxide scales offers a different approach to void formation and transport in scales. Generally, void formation is assumed to occur at the oxide-metal interface only. Nonequilibrium defects have been previously discounted in models of scale growth by lattice transport. However, the predominant grain boundary transport occurring in these fine Al_2O_3 scales can allow the scale to grow without necessarily relaxing the lattice vacancy concentrations. Certainly the copious void precipitation with the scale emphasizes the role of excess vacancies.

Finally, the features which were originally thought to be the most important, based on previous theories of scale adherence, simply failed to materialize. No evidence of selective vacancy accommodation in the doped NiCrAl metals or oxides thereof was found, as might be expected from the vacancy sink model. Nor were numerous dislocations found in the scale, to serve as short-circuit paths for aluminum diffusion, as suggested by the growth stress theory. Although most of the structural evidence obtained by TEM has not supported these oxide adherence theories, it is acknowledged that little work has been done on the mature adherent scale structures and that this should be an important area for future work.

Appendix A d-spacings of Various Oxides Formed on NiCrAl Alloys

Al_2O_3 [a]	α-Cr_2O_3 [b]	γ-Al_2O_3 [c]	$NiAl_2O_4$ [d]	$NiCr_2O_4$ [e]	NiO [f]
				4.804(111)	
			4.650(111)		
	4.528(0003)[g]	4.566(111)			
4.320(0003)[g]					
	4.092(10$\bar{1}$1)[g]			4.160(200)	
			4.024(200)		
3.9?8(10$\bar{1}$1)[g]		3.954(200)			
	3.633(10$\bar{1}$2)				
3.479(10$\bar{1}$2)					
				2.942(220)	
		2.796(220)	2.846(220)		
	2.666(10$\bar{1}$4)				
2.552(10$\bar{1}$4)					
	2.480(11$\bar{2}$0)			2.509(311)	
		2.384(311)	2.427(311)		2.410(111
2.379(11$\bar{2}$0)				2.402(222)	
			2.322(222)		
	2.264(0006)	2.283(222)			
2.165(0006)					
	2.176(11$\bar{2}$3)				
2.085(11$\bar{2}$3)					2.088(200
	2.119(20$\bar{2}$1)[g]			2.080(400)	
	2.048(20$\bar{2}$2)				
2 .03(20$\bar{2}$1)[g]			2.013(400)		
1.964(20$\bar{2}$2)		1.977(400)			
	1.812(20$\bar{2}$4)		1.846(331)		
			1.800(420)		
1.740(20$\bar{2}$4)		1.768(420)			
	1.672(11$\bar{2}$6)			1.698(422)	
			1.641(422)		
1.601(11$\bar{2}$6)		1.614(422)		1.601(333)	
1.546(21$\bar{3}$1)	1.579(12$\bar{3}$2)		1.549(333)		
1.514(21$\bar{3}$2)		1.522(333)			
1.510(10$\bar{1}$8)	1.465(12$\bar{3}$4)			1.471(440)	1.476(220
1.404(21$\bar{3}$4)	1.431(30$\bar{3}$0)		1.423(440)		
1.374(30$\bar{3}$0)		1.398(440)		1.341(442)	

(a) Rhombohedral, a = 4.758Å, c = 12.991Å, ASTM Card #10-173

(b) Rhombohedral, a = 4.954Å, c = 13.584Å, ASTM Card # 6-0504

(c) Cubic , a_o = 7.908 Å, ASTM Card # 10-425

(d) Cubic , a_o = 8.048 Å, ASTM Card # 10-339

(e) Cubic , a_o = 8.320 Å, ASTM Card # 4-0763

(f) Cubic , a_o = 4.177 Å, ASTM Card # 4-0838

(g) Double diffraction spots

Appendix B

Development of Excess Oxygen Vacancy Model

1) Linear $[V_o]_{eq}$ Gradient

From the assumption of a linear vacancy concentration and the nomenclature of Figure B1, the equilibrium vacancy concentration, V_1, at any position, X_1, can be given in terms of the total thickness, X_2, by the relation:

$$V_1 = (V_m - V_g)(X_1/X_2) + V_g \qquad \text{EQN B1}$$

The total amount of excess vacancies possible is $(V_m - V_1)$ or:

$$\Delta V_{..} = (V_m - V_g)(1 - X_1/X_2) \qquad \text{EQN B2}$$

And, assuming parabolic oxide growth kinetics:

$$\Delta V_T = (V_m - V_g)(1 - \sqrt{t_1/t_2}) \qquad \text{EQN B3}$$

Since it is not generally accepted that the oxygen interstitial is a common defect in Al_2O_3, Wagner's proposed mechanism of vacancy/interstitial recombination cannot be used to account for the decay of oxygen vacancies. Vacancy sinks represent an alternative mechanism, and, of the typical candidates for vacancy sinks, grain boundaries were certainly the most prevalent in the Al_2O_3

(B1)

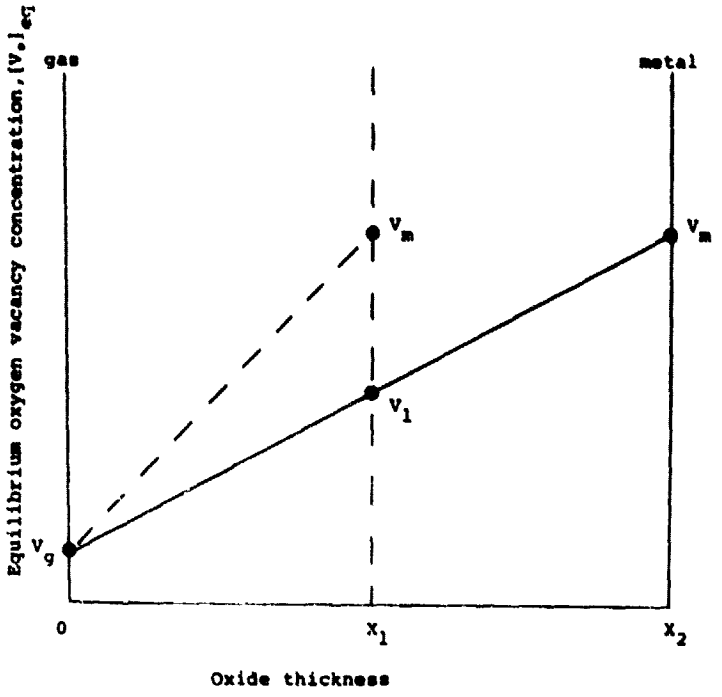

(B2)

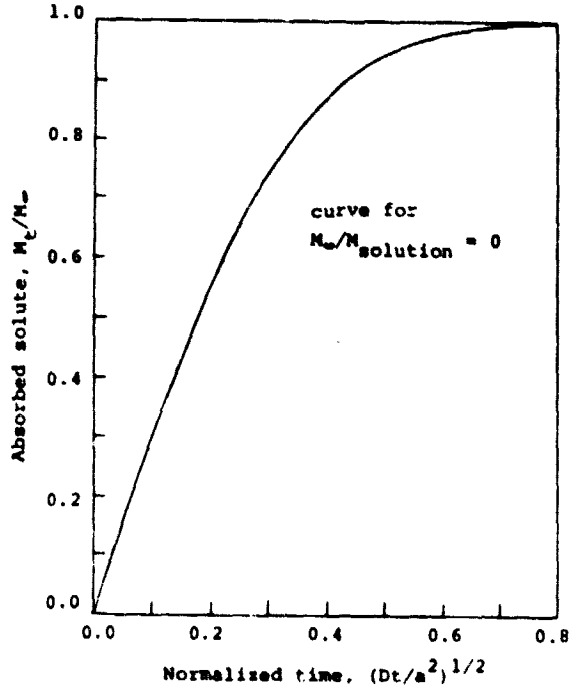

Figure B1. Schematic equilibrium oxygen vacancy concentration in a growing scale.

Figure B2. Relative amount of solute absorbed by a sphere from an infinite source, ref. 90.

scales. Thus the net excess quantity of vacancies available for forming voids is:

$$\Delta V_{ex} = \Delta V_T - \Delta V_{GB} \quad \text{EQN B4}$$

where ΔV_{GB} is the amount of vacancies annihilated by diffusion into grain boundary sinks.

The relative amount of vacancy loss to grain boundaries, $\Delta V_{GB}/\Delta V_T$, can be calculated from the solutions of Crank for uptake of a solute from a stirred solution by a sphere of radius 'a'.[90] The analogy is that the solute represents the vacancy concentration, the volume of solution represents the grain boundary sinks, and the uptake of solute by the sphere represents the egress of vacancies from the grain to the grain boundary. Thus the amount of vacancy annihilation, $\Delta V_{GB}/\Delta V_T$, equals the amount of absorbed solute at time t relative to the total amount of absorbed solute, M_t/M_∞. Curves of M_t/M_∞ vs Dt/a^2 are given in Crank for various $M_\infty/M_{solution}$, the amount of total uptake by the sphere relative to the total solute in the solution. Since the grain boundaries were assumed to be infinite sinks, $M_\infty/M_{solution} = 0$. This curve is shown in Figure B2. Thus for a given $D=D_{V_o}$, t=net time for annihilation=t_2-t_1, and a=½ grain size, the annihilated vacancies can be calculated. Thus from EQN B4:

$$\Delta V_{ex} = \Delta V_T - \Delta V_T(M_t/M_\infty) \quad \text{EQN B5}$$

and combining B3 and B5,

$$\Delta V_{ex} = (V_m - V_g)(1 - \sqrt{t_1/t_2})(1 - M_t/M_\infty) \qquad \text{EQN B6}$$

$$\text{or: } \Delta V_{ex}/(V_m - V_g) = (1 - \sqrt{t_1/t_2})(1 - \Delta V_{GB}/\Delta V_T) \qquad \text{EQN B6a}$$

where: $\Delta V_{GB}/\Delta V_T = M_t/M_\infty$ is the function of Dt/a^2 given in Figure B2.

2) Zero $[V_o]$ Gradient

The above treatment can be easily modified if a flat equilibrium vacancy profile is assumed:

let $V_1 = V_g$ for all X except X_2,

let $V_1 = V_m$ only at X_2,

then $\Delta V_T = V_m - V_1 = V_m - V_g$ for all X except X_2, EQN B7

and $\Delta V_{ex} = (V_m - V_g)(1 - \Delta V_{GB}/\Delta V_T)$ EQN B8

Appendix C

Estimate of Vacancy Accumulations

The mole fraction of accumulated vacancies can be approximated from Fick's first law:

$$df_v = \frac{JAdt}{V} = \frac{-D(dc/dx)dt}{X} \qquad \text{EQN C1}$$

where df_v = fractional accumulation of vacancies in a slab after time dt

J = flux of vacancies through area A

V = volume of a slab of material

X = thickness of slab

dc/dx = vacancy concentration gradient

$D=D_{V_O}$ = diffusion coefficient of oxygen vacancies

For the case of a linear gradient as in Figure C1, dc/dx is dependent on scale thickness. Up to time t_1, the accumulation of vacancies in the outer slab, X_1, can be approximated by:

$$f_{v,11} = \frac{\int_{t_o}^{t_1} D(V_m - V_g)/X \, dt}{X_1} = 2D(V_m - V_g)/k_p \qquad \text{EQN C2}$$

From t_1 to t_2 it is assumed that only a fraction of the flux, proportional to the thickness of the slab, X_1/X, can be accumulated in the slab. Thus:

(C1)

(C2)

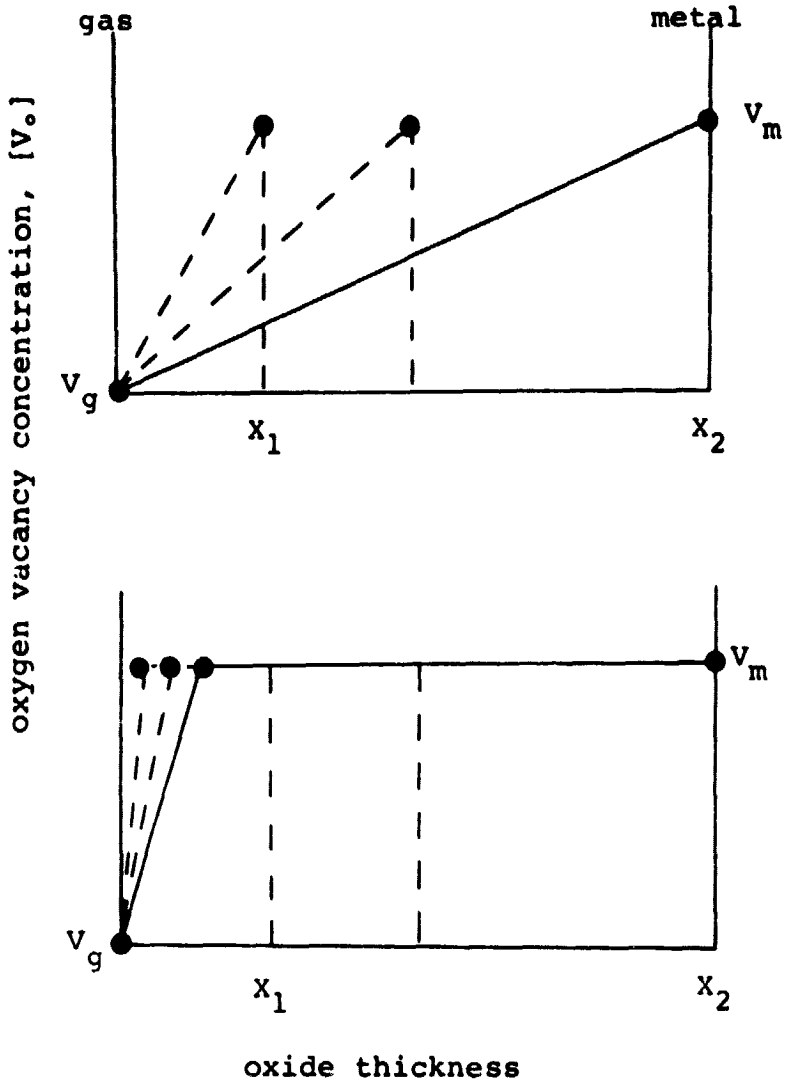

Figure C1. Linear vacancy profiles.

Figure C2. Vacancy profiles with extreme surface gradients.

$$f_{v,12} = \frac{\int_{t_1}^{t_2} (X_1/X)D(V_m-V_g)/X \, dt}{X_1} = \frac{D}{k_p}(V_m-V_g)(\ln(t_2/t_1)) \qquad \text{EQN C3}$$

And the total accumulation in the outer slab is:

$$f_{v,1} = f_{v,11} + f_{v,12} \qquad \text{EQN C4}$$

$$f_{v,1} = \frac{2D}{k_p}(V_m-V_g)(1+\ln(t_2/t_1)^{\frac{1}{2}})$$

Next consider the case where a steep gradient is maintained at the gas surface, as in Figure C2. This is closer to the situation where an equilibrium gradient is only slowly approached. Thus from t_0 to t_1:

$$f_{v,11} = \frac{\int_{t_o}^{t_1} \frac{D}{X}(V_m-V_g)\, dt}{X_1} = \frac{2D}{k_p}(V_m-V_g) \qquad \text{EQN C5}$$

and from t_1 to t_2:

$$f_{v,12} = \frac{\int_{t_1}^{t_2} \frac{X_1}{X}\frac{D}{X}(V_m-V_g)\, dt}{X_1} = \frac{2D}{k_p}(V_m-V_g)((t_2/t_1)^{\frac{1}{2}}-1) \qquad \text{EQN C6}$$

and totaled:

$$f_{v,1} = f_{v,11} + f_{v,12} \qquad \text{EQN C7}$$

$$f_{v,1} = \frac{2D}{k_p}(V_m-V_g)(t_2/t_1)^{\frac{1}{2}}$$

References

1. J.K. Tien, F.S. Pettit: "Mechanism of Oxide Adherence on Fe-25 Cr-4Al (Y or Sc) Alloys," Met. Trans., 3, p1587 (1972).

2. C.S. Giggins, F.S. Pettit: "Oxide Scale Adherence Mechanisms," ARL-TR-75-0234, (Pratt and Whitney Aircraft, PWA 5364), (1975).

3. E.J. Felten, F.S. Pettit: "Development, Growth, and Adhesion of Al_2O_3 on Platinum-Aluminum Alloys," Oxid. Met., 10, p189 (1976).

4. F.A. Golightly, F.H. Stott, G.C. Wood: "The Influence of Yttrium Additions on the Oxide-Scale Adhesion to an Iron-Chromium-Aluminum Alloy," Oxid. Met., 10, p163 (1976).

5. F.A. Golightly, F.H. Stott, G.C. Wood: "The Relationship Between Oxide Grain Morphology and Growth Mechanisms for Fe-Cr-Al and Fe-Cr-Al-Y Alloys," J. Electrochem. Soc., 126, p1035 (1979).

6. I.M. Allam, D.P. Whittle, J. Stringer: "The Oxidation Behavior of CoCrAl Systems Containing Active Element Additions," Oxid. Met., 12, p35 (1978).

7. I.M. Allam, D.P. Whittle, J. Stringer: "Improvements in Oxidation Resistance by Dispersed Oxide Additions: Al_2O_3-Forming Alloys," Oxid. Met., 13, p381 (1979).

8. D.P. Whittle, J. Stringer: "VIII. Improvement in Properties: Additives in Oxidation Resistance," Phil. Trans. R. Soc. Lond., A295, p309 (1980).

9. R.T. Phelps, E.A. Gulbransen, J.W. Hickman: "Electron Diffraction and Electron Microscope Study of Oxide Films Formed on Metals and Alloys at Moderate Temperatures," Ind. Eng. Chem., Analytical Edition, 18, p391 (1946).

10. G.M. Scamans, E.P. Butler: "In Situ Observations of Crystalline Oxide Formation During Aluminum and Aluminum Alloy Oxidation," Met. Trans, 6A, p1795 (1975).

11. R.I. Nazarova: "Electron Diffraction Study of the Oxidation Process of Thim Films of Intermetallic Compounds of the System Nickel-Aluminum," Izvestiya Akad. Nauk SSSR, 7, p1164 (1964).

12. G.C. Wood, B. Chattopadhyay: "Transient Oxidation of Ni-Base Alloys," Corr. Sci., 10, p471 (1970).

13. B.H. Kear, F.S. Pettit, D.E. Fornwalt, L.P. Lemaire: "On the Transient Oxidation of a Ni-15Cr-6Al Alloy," Oxid. Met., 3, p557 (1971).

14. E.F. Koch, G. Romeo: "Growth of Thin Oxide Scales for Electron Microscopy Studies," Metallography, 8, p509 (1975).

15. J.L. Smialek: "Oxide Morphology and Spalling Model for NiAl," Met. Trans., 9A, p309 (1978).

16. C.E. Lowell, D.L. Deadmore: "The Role of Thermal Shock in Cyclic Oxidation," Oxid. Met., 14, p325 (1980).

17. H.D. Karnthaler: "The Study of Glide on (001) Plane in F.C.C. Metals Deformed at Room Temperature," Phil. Mag., A38, p141 (1978).

18. P.B. Hirsch, et al.: Electron Microscopy of Thin Crystals, Plenum Press, New York, 1965.

19. K. Otsuka, C.M. Wayman, H. Kubo: "Diffuse Electron Scattering in Beta-Phase Alloys," Met. Trans., 9A, p1075 (1978).

20. A.J. Bradley, A. Taylor: "An X-Ray Analysis of the Ni-Al System," Proc. Roy. Soc., A159, p56 (1937).

21. K.R. Kinsman, H.I. Aaronson: "Structure of Crystalline Interfaces," Metallography, 7, p361 (1974).

22. J.W. Edington: Practical Electron Microscopy in Materials Science, Macmillan, Phillips Technical Library, Eindhoven, 1974.

23. H. Kubo, C.M. Wayman: "Spinodal Decomposition of Beta Brass," Met. Trans., 10A, p633 (1979).

24. W.J. Moore: Physical Chemistry, Prentice-Hall, Englewood Cliffs, N.J., 1955.

25. G.C. Kuczynski: "Theory of Solid State Sintering," in Powder Metallurgy, Conference Proceedings of TMS-AIME, New York, 1960, p11.

26. F. Kohl: NASA Lewis Research Center, unpublished research, 1978.

27. G. Achutaramayya, W.D. Scott: "Interfacial Energies of Coherent Twin Boundaries in Alumina," Acta Met., 23, p1469 (1975).

28. B.J. Pletka, T.E. Mitchell, A.H. Heuer: "Solid Solution Hardening of Sapphire," Phys. Stat. Sol., 39a, p301 (1977).

29. S. Timoshenko, J.N. Goodier: Theory of Elasticity, McGraw-Hill, New York, 1951.

30. G.E. Dieter, Jr.: Mechanical Metallurgy, McGraw-Hill, New York, 1961.

31. N. Soga, O.L. Anderson: "High Temperature Elastic Properties of Polycrystalline MgO and Al_2O_3," J. Am. Ceram. Soc., 49, p355 (1966).

32. D. Hull: Introduction to Dislocations, Pergamon Press, New York, 1965, p76.

33. K. Heinemann, H. Poppa: In Situ Metal-Gas Reaction Studies, Proceedings of Thirty-First EMSA Meeting, 1973.

34. A.H. Heuer, T.E. Mitchell: "Precipitation in Ceramics," in Precipitation Processes in Solids, TMS-AIME Symposium, 1978, p222.

35. C.J.P. Steiner, D.P.H. Hasselman, R.M. Spriggs, "Kinetics of the Gamma-to-Alpha Alumina Phase Transformation," J. Am. Ceram. Soc., 54, p412 (1971).

36. O. Kubaschewski, B.E. Hopkins: Oxidation of Metals and Alloys, Butterworths, London, 1967, p53.

37. H.M. Flower, P.R. Swann: "An in Situ Study of Titanium Oxidation by High Voltage Electron Microscopy," Acta Met., 22, p1339 (1974).

38. V.R. Howes: "The Early Growth of Oxide on a Fe-Cr Alloy," Corr. Sci., 7, p735 (1967).

39. A.S. Khan, C.E.Lowell, C.A. Barrett: "The Effect of Zirconium on the Isothermal Oxidation of Nominal Ni-14Cr-24Al Alloys," J. Electrochem. Soc., 127, p670 (1980).

40. K. Fueki, H. Ishibashi: "Oxidation Studies on Ni-Al Alloys," J. Electrochem Soc., 108, p306, (1961).

41. F.S. Pettit: "Oxidation Mechanisms for Nickel-Aluminum Alloys at Temperatures Between 900-1300°C," Trans. TMS-AIME, 239, p1296 (1967).

42. G.J. Santoro, D.L. Deadmore, C.E. Lowell: "Oxidation of Alloys in Nickel-Aluminum System with Third-Element Additions of Chromium, Silicon, and Titanium at 1100°C," NASA TN D-6414, 1971.

43. C.E. Lowell, G.J. Santoro: "The 1200°C Cyclic Oxidation Behavior of Two Nickel-Aluminum Alloys (Ni_3Al and NiAl) with Additions of Chromium, Silicon, and Titanium," NASA TN D-6838, 1972.

44. D. Voss: "Microstructure of Oxides Scales Formed on Iron," M.S. Thesis, Case Western Reserve University, Cleveland, Ohio, 1979.

45. J.D. Snow: "High Temperature Plastic Deformation of Polycrystalline Aluminum Oxide," M.S. Thesis, Case Western Reserve University, Cleveland, Ohio, 1972.

46. A.H. Heuer, N.J. Tighe, R.M. Cannon: "Plastic Deformation of Fine-Grained Alumina (Al_2O_3): II, Basal Slip and Nonaccommodated Grain Boundary Sliding," J. Am. Ceram. Soc., 63, p53 (1980).

47. A.R. Tholen: "On the Ambiguity Between Moire Fringes and the Electron Diffraction Contrast From Closely Spaced Dislocations," Phys. Stat. Sol., 2, p537 (1970).

48. H.M. Hindam, W.W. Smeltzer: "Growth and Microstructure of Alpha-Al_2O_3 on Beta-NiAl," J. Electrochem. Soc., 127, p1630 (1980).

49. R.L. Coble: "Sintering Crystalline Solids. II. Experimental Test of Diffusion Models in Powder Compacts," J. Appl. Phys., 32, p793 (1961).

50. A. Mocellin, W.D. Kingery: "Microstructural Changes During Heat Treatment of Sintered Al_2O_3," J. Am. Ceram. Soc., 56, p309 (1973).

51. S.K. Mohapatra, S.K. Tiku, F.A. Kroger: "The Defect Structure of Unintentionally Doped Alpha-Al_2O_3 Crystals," J. Am. Ceram. Soc., 62, p50 (1979).

52 C. Wagner: "Deviations from Internal Equilibrium in Scales Growing on Metals in Corroding Gases," Ber. Bunsenges. physik. Chem., 78, p611 (1974).

53. G.J. Dienes, et al.: "Shell-model calculation of some point-defect properties in Alpha-Al_2O_3," Phys. Rev. B, 11, p3060 (1975).

54. S.K. Mohapatra, F.A. Kroger: "The Dominant Type of Atomic Disorder in Alpha-Al_2O_3," J. Am. Ceram. Soc., 61, p106 (1978).

55. a.) G.B. Gibbs: "A Model for Mild Steel Oxidation in CO_2," Oxid. Met., 7, p173 (1973), b.) G.B. Gibbs, M.R Wooton, W.R. Rice, K.E. Hodgson: "Scale Streses During Protective and Breakaway Corrosion of Iron and Rimming Steel in CO_2," Oxid. Met., 7, p185 (1973).

56. S. Tanigchi, D.L. Carpenter: "The Influence of Scale/Metal Interface Characterizacion on the Oxidation Behavior of Iron at Elevated Temperatures," Corr. Sci., 19, p15 (1979).

57. F.N. Rhines, J.S. Wolf: "The Role of Oxide Microstructure and Growth Stresses in the High Temperature Scaling of Nickel," Met. Trans., 1, p1701 (1970).

58. F.N. Rhines, R.G. Connell, Jr., M.S. Choi: "Microstructural Evolution of the Inner Layer of the High Temperature Oxide Scale on Nickel," J. Electrochem. Soc., 126, p1061 (1979).

59. C.E. Lowell, S.J Grisaffe, D.L. Deadmore: "Oxidation of TD Nickel at 1050 and 1200°C as Compared to Three Grades of Nickel of Different Purity," Oxid. Met., 4, p91 (1972).

60. G.J. Yurek, H. Schmalzried: "Deviations from Local Thermodynamic Equilibrium During Interdiffusion of CoO-MgO and CoO-NiO," Ber. Bunsenges, physik. Chem., 79, p255 (1975).

61. R.A. Swalin: Thermodynamics of Solids, New York, 1962, p219.

62. R.L. Lalauze, J.H. Meunier: "Experimental Study of NiO Electrical Conductivity Changes Under Low Oxygen Pressures," Oxid. Met., 12, p183 (1978).

63. R.L. Lalauze, J.H. Meunier: "Kinetics Interpretation of NiO Electrical Conductivity Under Low Oxygen Pressures," Oxid. Met., 13, p301 (1979).

64. Y. Oishi, W.D. Kingery: "Self-Diffusion of Oxygen in Single Crystal and Polycrystalline Aluminum Oxide," J. Chem. Phys., 33, p480 (1960).

65. R.E. Mistler, R.L. Coble: "Grain-boundary diffusion and boundary widths in metals and ceramics," J. Appl. Phys., 45, p1507 (1974).

66. J.F. Schakelford, W.D. Scott: "Relative Energies of (1100) Tilt Boundaries in Aluminum Oxide," J. Am. Ceram. Soc., 51, p688 (1968).

67. K.P.R. Reddy: "Oxygen Diffusion in Close Packed Oxides," Ph.D. Thesis, Case Western Reserve University, Cleveland, Ohio, 1979.

68. O. Maryuama, W. Komatsu: "Observation on Grain-Boundary of the Al_2O_3 Bicrystal," Ceramurgia International, 5, p51 (1979).

69. S.K. Mohapatra, S.K. Tiku, F.A. Kroger: "The Defect Structure of Unintentionally Doped Alpha-Al_2O_3 Crystals," J. Am. Ceram. Soc., 62, p50 (1979).

70. B.V. Dutt, J.P. Hurrell, F.A. Kroger: "High-Temperature Defect Structure of Cobalt-Doped Alpha-Alumina," J. Am. Ceram. Soc., 58, p420 (1975).

71. B.V. Dutt, F.A. Kroger: "High Temperature Defect Structure of Iron-Doped Alpha-Alumina," J. Am. Ceram. Soc., 58, p474 (1975).

72. K. Kitazawa, R.L. Coble: "Electrical Conduction in Single-Crystal and Polycrystalline Al_2O_3 at High Temperatures," J. Am. Ceram. Soc., 57, p245 (1974).

73. J.S. Sheasby, D.B. Jory: "Electrical Properties of Growing Alumina Scales," Oxid. Met., 12, p527 (1978).

74. D. Hayes, E.W. Roberts, J.P. Roberts: "Development of Connected Porosity in Dense Sintered Oxides at High Temperature," in Science of Ceramics, ed. G. H. Stewart, Academic Press, London, 1965.

75. J. P. Roberts: "Microstructural Consideration in Gas Permeation," in Ceramic Microstructures, ed. R.M. Fulrath, J.A. Pask, John Wiley & Sons, New York, 1968, p509.

76. D. Hayes, D.W. Budworth, J.P. Roberts: "Permeability of Sintered Alumina Materials to Gases at High Temperatures," Trans. Brit. Ceram. Soc., 62, p507 (1963).

77. B.C.H. Steele, M.A. Williams: "Deterioration of impermeable alumina tubes in inert atmospheres at elevated temperatures," J. Mat. Sci., 8, p427 (1973).

78. R.M. Roberts, et al.: "Hydrogen Permeability of Sintered Aluminum Oxide," J. Am. Ceram. Soc., 62, p496 (1979).

79. J.L. Smialek: NASA Lewis Research Center, unpublished research, 1980.

80. A.H. Heuer, D.J. Sellers, W.H. Rhodes: "Hot-Working of Aluminum Oxide: I, Primary Recrystallization and Texture," J. Am. Ceram. Soc., 52, p468 (1969).

81. W.H. Rhodes, D.J. Sellers, T. Vasilos: "Hot-Working of Aluminum Oxide: II, Optical Properties," J. Am. Ceram. Soc., 58, p31 (1975).

82. R.M. Cannon, W.H. Rhodes, A.H. Heuer: "Plastic Deformation of Fine-Grained Alumina (Al_2O_3): I, Interface-Controlled Diffusional Creep," J. Am. Ceram. Soc., 63, p46 (1980).

83. B. Burton: "Interface Reaction Controlled Diffusional Creep: A Consideration of Grain Boundary Dislocation Climb Sources," Mat. Sci. and Eng., 10, p9 (1972).

84. B.J. Hockey: "Observations by Transmission Electromicroscopy on the Subsurface Damage Produced in Aluminum Oxide by Mechanical Polishing and Grinding," Proc. Brit. Ceram. Soc., 20, p95, (1972).

85. A. Bellosi, P. Vincenzini: "Microstructural Observations on Sintered Alpha Alumina," Mat. Chem., 4, p721 (1979).

86. Y. Nakada, T.L. Schock: "Surface Texture Formation in Al_2O_3 Substrates," J. Am. Ceram. Soc., 58, p409 (1975).

87. A. Boyde, P.G.T. Howell: "Taking, Presenting, and Treating Stereo Data from the SEM," Scanning Electron Microscopy, I, p571 (1977).

88. R. Hutchings, M.H. Loretto: "Compositional Dependence of Oxidation Rates of NiAl and CoAl," Metal Science, 12, p503 (1978).

89. N.S. Choudhury, J.W. Patterson: "Steady-State Chemical Potential Profiles in Solid Electrolytes," J. Electrochem Soc., 117, p1384 (1970).

90. J. Crank: The Mathematics of Diffusion, Oxford Press, London, 1956, p90.

91. G.W. Greenwood: "The Growth of Dispersed Precipitates in Solutions," Acta Met., 4, p243 (1956).

Tables

TABLE I

COMPARISON OF OXIDE RING PATTERN (Fig. 16) AND α-Al_2O_3 d-SPACINGS.

INTENSITY	d (MEASURED), Å	d (α-Al_2O_3)* Å		I/I_0 (X-RAY)*
W	3.542	3.479	$(01\bar{1}2)$	75
M	2.510	2.552	$(10\bar{1}4)$	90
S	2.379	2.379	$(11\bar{2}0)$	40
-	-----	2.165	(0006)	<1
S	2.098	2.085	$(11\bar{2}3)$	100
W	1.967	1.964	$(20\bar{2}2)$	2
M	1.751	1.740	$(02\bar{2}4)$	45
M	1.610	1.601	$(11\bar{2}6)$	80
M	1.552	1.546	$(21\bar{3}1)$	4
M	1.516	1.514	$(12\bar{3}2)$	6
-	-----	1.510	$(01\bar{1}8)$	8
S	1.413	1.404	$(12\bar{3}4)$	30
S	1.377	1.374	$(03\bar{3}0)$	50

*ASTM FILE #10-173

CS-80-4049

TABLE II

COMPARISON OF MEASURED AND CALCULATED

MOIRE´ FRINGE SPACINGS IN γ-Al_2O_3

ORIENTATION	MEASURED (Fig. 47)	CALCULATED FROM $1/\Delta\vec{g}$ (Fig. 47)
$[0\bar{1}1]$	15.0 ± 1.0 Å	15.3 ± 0.9 Å
[101]	14.4 ± 1.9 Å	16.7 ± 2.0 Å
[110]	14.8 ± 3.6 Å	17.1 ± 1.1 Å

TABLE III

SUMMARY OF AVERAGE GRAIN SIZES AND AVERAGE VOID SIZES FOR RANDOM AND ORIENTED SCALES.

	GRAIN DIAMETER, μm		VOID DIAMETER, Å	
	RANDOM	ORIENTED	RANDOM	ORIENTED
NiCrAl	0.14	0.10	100	110
NiCrAl + Y	.11	.05	65	110
NiCrAl + Zr	.09	.10	100	185

CS-80-4050

TABLE IV

SUMMARY OF ORIENTED OXIDE MORPHOLOGY

	OXIDE PHASE	MOIRE' FRINGE SPACING, Å	PRECIPITATES
NiCrAl	α-$(Al, Cr)_2O_3$	55	
NiCrAl + Y	α-$(Al, Cr)_2O_3$; $Ni(Al, Cr)_2O_4$	25	50 Å, $\langle 10\bar{1}0\rangle_\alpha$
NiCrAl + Zr	γ-Al_2O_3	25, 15	10-15 Å, $\langle 110\rangle_\gamma$ 150 Å, $\langle 110\rangle_\gamma$

CS-80-4052

TABLE V. SUMMARY OF GRAIN AND VOID SIZES IN A 1 HR Al_2O_3 SCALE

	AVG. GRAIN SIZE ± 1σ (μm)	AVG. VOID SIZE ± 1σ (Å)
1)	0.12 ± 0.04 (γ/γ′)	100 ± 50
2)	0.17 ± 0.05 (β)	80 ± 50
3)	0.16 ± 0.09	———
4)	0.17 ± 0.05	160 ± 110
5)	0.20 ± 0.07	130 ± 70
6)	0.20 ± 0.09	210 ± 140
7)	0.20 ± 0.06	190 ± 180
8)	0.22 ± 0.07	160 ± 50
	0.18 ± .07 μm	150 ± 90 Å

TABLE VI. ANALYSIS OF α-Al_2O_3 SPOT AND FCC RING PATTERNS FROM FIGURE 71

SPOT PATTERN	α-Al_2O_3	RING PATTERN	a_o(FCC) = 3.595
d_1 = 3.476 Å	3.479 Å $(10\bar{1}2)$	d_1 = 2.076 Å	2.076 (111)
d_2 = 1.597	1.601 $(11\bar{2}\bar{6})$	d_2 = 1.803	1.797 (200)
d_3 = 1.387	1.404 $(21\bar{3}\bar{4})$	d_3 = 1.266	1.271 (220)
d_4 = 1.500	1.514 $(01\bar{1}\bar{8})$	d_4 = 1.084	1.084 (311)

$\bar{g}_1 + \bar{g}_2 = \bar{g}_3$

$\bar{g}_2 - \bar{g}_1 = \bar{g}_4$

TABLE VII. GRAIN AND VOID SIZES AT VARIOUS LEVELS IN THE SCALE. (INDIVIDUAL MEANS, WEIGHTED MEANS, INDIVIDUAL AND POOLED STANDARD DEVIATIONS).

DEPTH (μm)	PLATE NO.	AVG. GRAIN SIZE (μm)	S (μm)	N	AVG. VOID SIZE (μm)	S (μm)	N
0.00 μm	(SEM)				0.188	0.088	18
0.17 μm	6796	0.310	0.124	29	0.129	0.066	31
	6817	0.440	0.187	19	0.033	0.023	38
	6807	0.350	0.140	27	0.121	0.077	7
	16078	0.336	0.195	67	NONE		
		0.347	0.175	142	0.083	0.050	76
0.50 μm	6750	0.370	0.168	127	0.011	0.005	70
	6762	0.314	0.133	148	0.132	0.057	30
	6746	0.518	0.212	10	0.016	0.008	50
	6731	0.491	0.232	112	NONE		
		0.387	0.179	397	0.037	0.041	150
0.72 μm	6828,32,40	0.466	0.217	42	NONE		
	6894	0.588	0.221	21	0.016	0.010	36
	6859	0.560	0.260	32	NONE		
	6870,79,81. 88,6906	0.464	0.184	40	0.016	0.009	74
		0.507	0.221	135	0.016	0.010	110
1.00 μm	(SEM)	0.620	0.252	27	NONE		

TABLE VIII. ANALYSIS OF RING PATTERN IN FIGURE 90 AS RANDOMLY ORIENTED α-Al_2O_3

MEASURED d-SPACING (λL = 6.0 cm·Å)	α-Al_2O_3 SPACINGS (ASTM CARD #10-173)	(hkil)
———	4.320*	0003
3.935	3.928*	$10\bar{1}1$
3.504	3.479	$10\bar{1}2$
2.559	2.552	$10\bar{1}4$
2.386	2.379	$11\bar{2}0$
2.162	2.165	0006
2.084	2.085	$11\bar{2}3$
———	2.030*	$20\bar{2}1$
1.967	1.964	$20\bar{2}2$
1.739	1.740	$20\bar{2}4$
1.600	1.601	$11\bar{2}6$
1.543	1.546	$21\bar{3}1$
———	1.514	$21\bar{3}2$
1.506	1.510	$10\bar{1}8$
1.404	1.404	$21\bar{3}4$
1.367	1.374	$30\bar{3}0$

*Double Diffraction

TABLE IX. DATA FOR [10$\bar{1}\bar{1}$] PATTERNS IN FIGURE 92.

PATTERN	GRAINS SAMPLED	SELECTED AREA APERTURE DIAMETER	SPECIMEN TILT AND ROTATION SETTINGS	GRAIN-TO-GRAIN ROTATIONAL MISMATCH IN PATTERNS
a	A1,A2,A3	0.75 μm	$18.7^{o}/-1.2^{o}$	1.5^{o}
b	B5	0.75 μm	$18.7^{o}/-1.2^{o}$	5^{o}
c	C4	0.75 μm	$12.1^{o}/-1.2^{o}$	——
d	F1,F2,F3,F4	1.35 μm	$9.9^{o}/-1.2^{o}$	3.5^{o}

TABLE X. RELATION OF SUBGRAIN BOUNDARY MOIRE' FRINGE AND DISLOCATION ARRAY SPACING TO ROTATIONAL MISMATCH

FEATURE	SPACING, D	$D_{calc.}$	ROTATION, θ	$\theta_{calc.}$	$g_{(hkl)}$	$d_{(hkl)}$	$D/\xi g$
Moire Pattern at C2-C3 S.G.B.	62 Å	58 Å (M) 118 Å (⊥)	2.3°	2.2° (M) 4.4° (⊥)	$(\bar{1}2\bar{1}0)$	2.379 Å	0.050
Tight Array at A4-B5 S.G.B.	91 Å	124 Å (M) 273 Å (⊥)	1.0°	1.4° (M) 3.0° (⊥)	$(\bar{2}11\bar{3})$	2.165 Å	0.100
Loose Dislocation Array at A2-A3 S.G.B.	216 Å	248 Å (⊥) 90 Å (M)	1 1°	1.3° (⊥) 0.5° (M)	$(\bar{2}02\bar{4})$	1.740 Å	0.23
Tight Array at F3-F4 S.G.B.	50 Å	47 Å (M) 128 Å (⊥)	2.1°	2.0° (M) 5.5° (⊥)	$(20\bar{2}4)$	1.740 Å	0.054

D = Measured Spacing

$D_{calc.}$ = Spacing Calculated from θ

θ = Measured Diffraction Pattern Rotation

$\theta_{calc.}$ = Rotation Calculated from D

$$D_{(M)} = \frac{d_{(hkl)}}{\theta}$$

$$D_{(\perp)} = \frac{b}{\theta} \quad ; \; b = a/3\,[1\bar{2}10] = 4.758 \text{ Å}$$

TABLE XI. GRAIN SIZES NEAR THE OXIDE-GAS SURFACE AS A FUNCTION OF TIME. (AVERAGE GRAIN SIZES FROM INDIVIDUAL MICROGRAPHS, WEIGHTED MEANS AND 95% CONFIDENCE LIMITS, INDIVIDUAL AND POOLED STANDARD DEVIATIONS).

Time	Approximate Level	GS(μm)	S	N
0.1 hr	(>0.04 μm)	0.173	0.045	20
		0.102	0.035	14
		0.087	0.024	28
		0.162	0.053	28
		0.139	0.031	19
		0.170	0.057	20
		0.129	0.047	76
		0.135 ± 0.006	0.044	205
1.0 hr	(0.12 μm)	0.101	0.047	65
		0.123	0.035	30
		0.168	0.052	62
		0.188	0.060	30
		0.163	0.089	25
		0.166	0.051	41
		0.195	0.074	30
		0.198	0.092	26
		0.202	0.061	35
		0.216	0.065	34
		0.166 ± 0.006	0.060	378
20.0 hr	(0.17 μm)	0.310	0.124	29
		0.440	0.187	19
		0.350	0.140	27
		0.336	0.195	67
		0.347 ± 0.029	0.175	142

TABLE XII. VOID SIZES NEAR THE OXIDE-GAS SURFACE AS A FUNCTION OF TIME. (AVERAGE VOID SIZES FROM INDIVIDUAL MICROGRAPHS; WEIGHTED MEANS AND 95% CONFIDENCE LIMITS; INDIVIDUAL AND POOLED STANDARD DEVIATIONS)

Time	Approximate Level	VS(μm)	S	N
0.1 hr	(0.04 μm)	0.0119	0.0071	49
		0.0074	0.0039	23
		0.0132	0.0055	47
		0.0112	0.0064	58
		0.0138	0.0090	23
		0.0080	0.0057	23
		0.0069	0.0029	17
		0.0074	0.0039	23
		0.0106 ± 0.0007	0.0059	286
1.0 hr	(0.12 μm)	0.0101	0.0047	34
		0.0083	0.0046	32
		0.0163	0.0108	26
		0.0131	0.0071	37
		0.0209	0.0138	38
		0.0189	0.0182	33
		0.0159	0.0049	38
		0.0149 ± 0.0031	0.0103	238
20.0 hr	(0.17 μm)	0.129	0.066	31
		0.033	0.023	38
		0.121	0.077	7
		0.083 ± 0.011	0.050	76

TABLE XIII CALCULATED 1100°C GRAIN BOUNDARY DIFFUSION COEFFICIENT AND WIDTH IN Al_2O_3 SCALE

($\delta D_{GB} \approx 1.58 \times 10^{-18}$ cm^3/sec)

	$\frac{GS^2 - GS_o^2}{t}$ $(\frac{cm^2}{sec})$	$\frac{D_{GB}}{\delta}$ $(\frac{cm}{sec})$	D_{GB} $(\frac{cm^2}{sec})$	δ (Å)
1 hr data	3.72×10^{-14}	7.89×10^{-8}	3.53×10^{-13}	447
20 hr data	1.25×10^{-14}	2.66×10^{-8}	2.05×10^{-13}	770

TABLE XIV GRAIN BOUNDARY DIFFUSIVITIES FROM BULK Al_2O_3 STUDIES

	D_l (cm^2/sec)	D_{eff}, 25μm (cm^2/sec)	δD_{GB} (cm^3/sec)
Oishi & Kingery (64)			
a) High Temp.	$1.9X10^{3}$ exp $\frac{-152\ KCAL}{RT}$	2.0 exp $(\frac{-110\ KCAL}{RT})$	$1.36X10^{-3}$ exp $(\frac{-109.7\ KCAL}{RT})$
b) Low Temp.	$6.3X10^{-8}$ exp $\frac{-57.6\ KCAL}{RT}$	1.76 exp $(\frac{-32.9\ KCAL}{RT})$	$4.0X10^{-14}$ exp $(\frac{-29.7\ KCAL}{RT})$
Reddy (67) (High Temp. Only)	$2.66X10^{2}$ exp $(\frac{-147\ KCAL}{RT})$	———	8.15 exp $(\frac{-142\ KCAL}{RT})$

TABLE XV

D_{GB} and δ Determined From ^{18}O Tracer Diffusion in Al_2O_3*

Sample	T(^{o}C)	D_{GB}(cm^2/sec)	δ (Å)
Pure	1350	$2.11X10^{-13}$	161
	1400	$1.6X10^{-13}$	500
	1500	$2.21X10^{-12}$	403
	"	$3.67X10^{-12}$	449
	"	$21.36X10^{-12}$	449
Lucalox	1500	$5.51X10^{-13}$	1623
	1582	$8.08X10^{-12}$	2723

*K. P. Reddy, 1979, (From Tables 17, 18, 19 in ref. 67).

TABLE XVI CHANGES IN IONIC CONDUCTIVITY WITH pO_2 IN SINGLE CRYSTAL Al_2O_3 ($T=1600^oC$, pO_2 range 10^{-8} to 10^o atm.)

Sample	σ_i range $(ohm\text{-}cm)^{-1}$	pO_2 dependence
undoped, ref. 69		
crystal I	10^{-7} to 3×10^{-7}	constant
crystal II	10^{-8} to 2×10^{-6}	$V_{Al}'''\alpha\ p^{+3/16}$
crystal II, annealed	10^{-8} to 9×10^{-7}	$V_o^{\cdot\cdot}\ \alpha\ p^{-1/6}$
Co-doped, ref. 70	10^{-6} to 7×10^{-8}	$Al_i^{\cdot\cdot\cdot}\ \alpha\ p^{-1/4}$
Fe-doped, ref. 71	10^{-6} to 2×10^{-5}	$Al_i^{\cdot\cdot\cdot}\ \alpha\ p^{-1/5}$

TABLE XI Gas Permeability of Sintered Al_2O_3 Tubes

STUDY	MATERIAL	ATMOSPHERE I	ATMOSPHERE II	TEMPERATURE	RESULTS
1,2	100% dense	1 atm O_2	Vacuum ($pO_2 \sim 10^{-8}$ atm)	1700°C	Extensive connected grain boundary porosity at vacuum side of tube. Some channels at 1 atm side of tube.
2,3	92% dense, closed pores	1 atm O_2	Vacuum ($pO_2 \sim 10^{-8}$ atm)	1700°C	Interconnected grain boundary porosity. Impermeable large grain outer skin only.
4	92% dense, closed pores	1 atm air	Purified argon ($pO_2 = 10^{-18}$ atm)	1300°C	Interconnected porosity at argon side only.
5	98% dense, closed pores	He ($pO_2 \sim 10^{-6}$ atm)	H_2 ($pO_2 \sim 10^{-13}$ atm)	1200-1450°C	0.17% decrease in density, no interconnected porosity apparent.

1) D. Hayes, E. W. Roberts, J. P. Roberts, 1965 (ref. 74)

2) J. P. Roberts, 1966 (ref. 75).

3) D. Hayes, D. W. Budworth, J. P. Roberts, 1963 (ref. 76).

4) B. C. H. Steele, M. A. Williams, 1973 (ref. 77).

5) R. M. Roberts, T. S. Elleman, H. Palmour, Kuruvilla, 1979 (ref. 78).

Figures

Figure 1. Overview of oxidized γ/γ' and β phases (undoped NiCrAl, 0.1 hr at 1100°C).

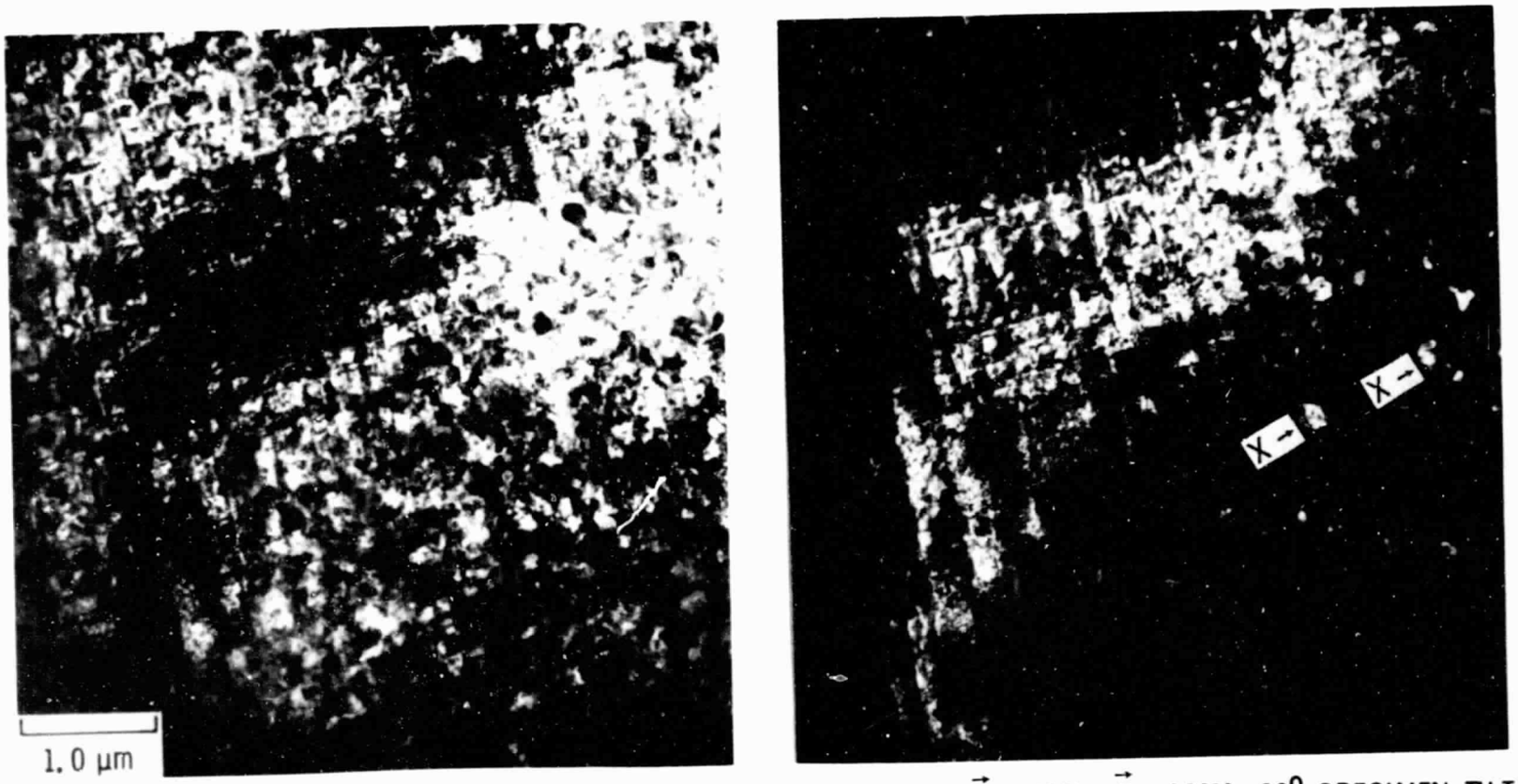

Figure 2. Dislocation arrays in the γ/γ' phase immediately adjacent to the oxide-metal interface.

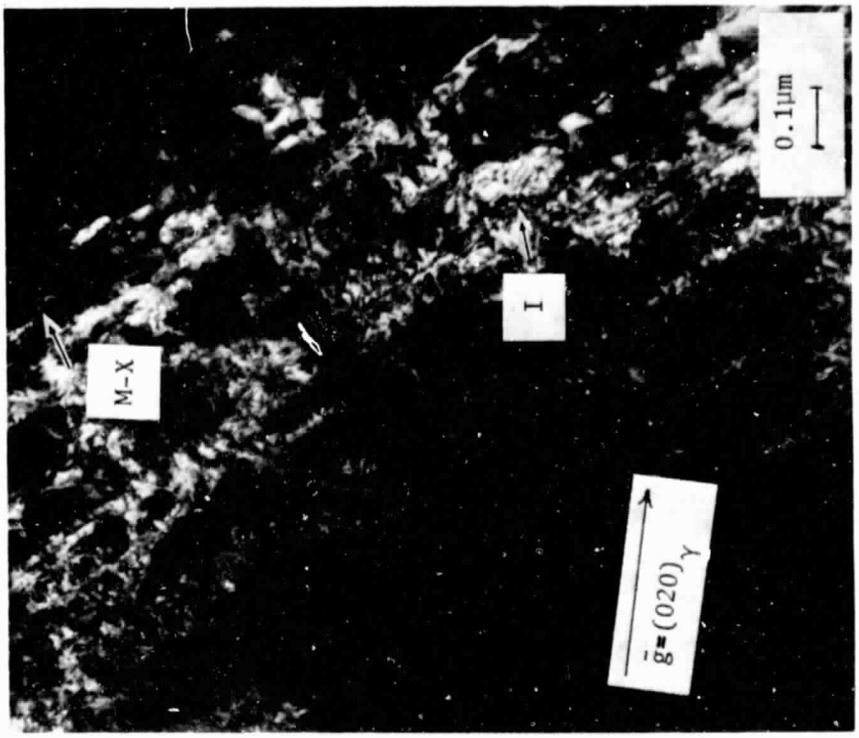

b) dark field, $\vec{g} = (020)\gamma$, $\vec{B} = [001]\gamma$

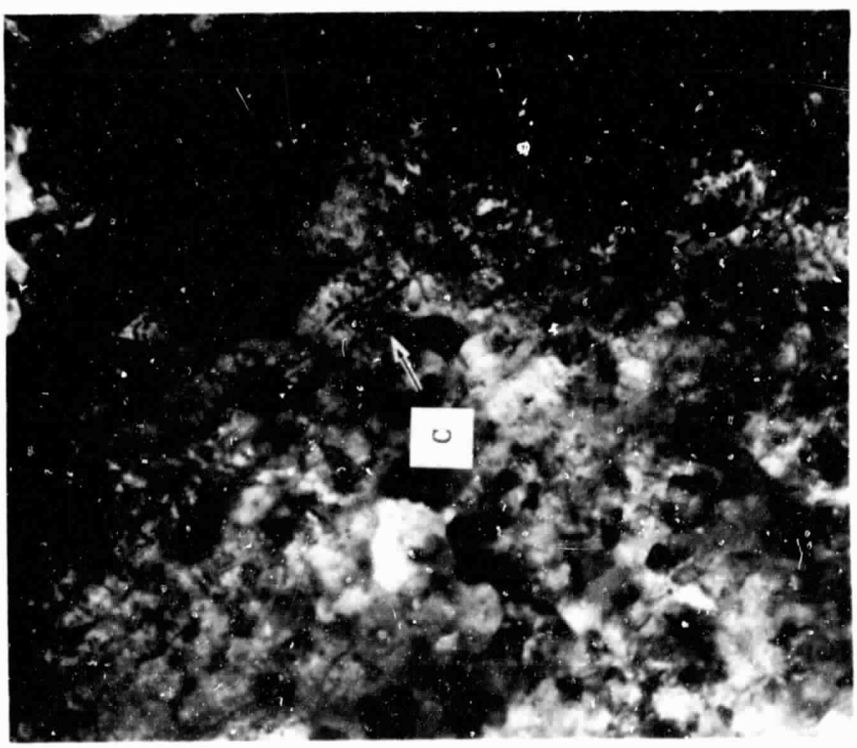

a) bright field

Figure 3. Interface structure of α-Al_2O_3 oxide grains and γ - Ni.

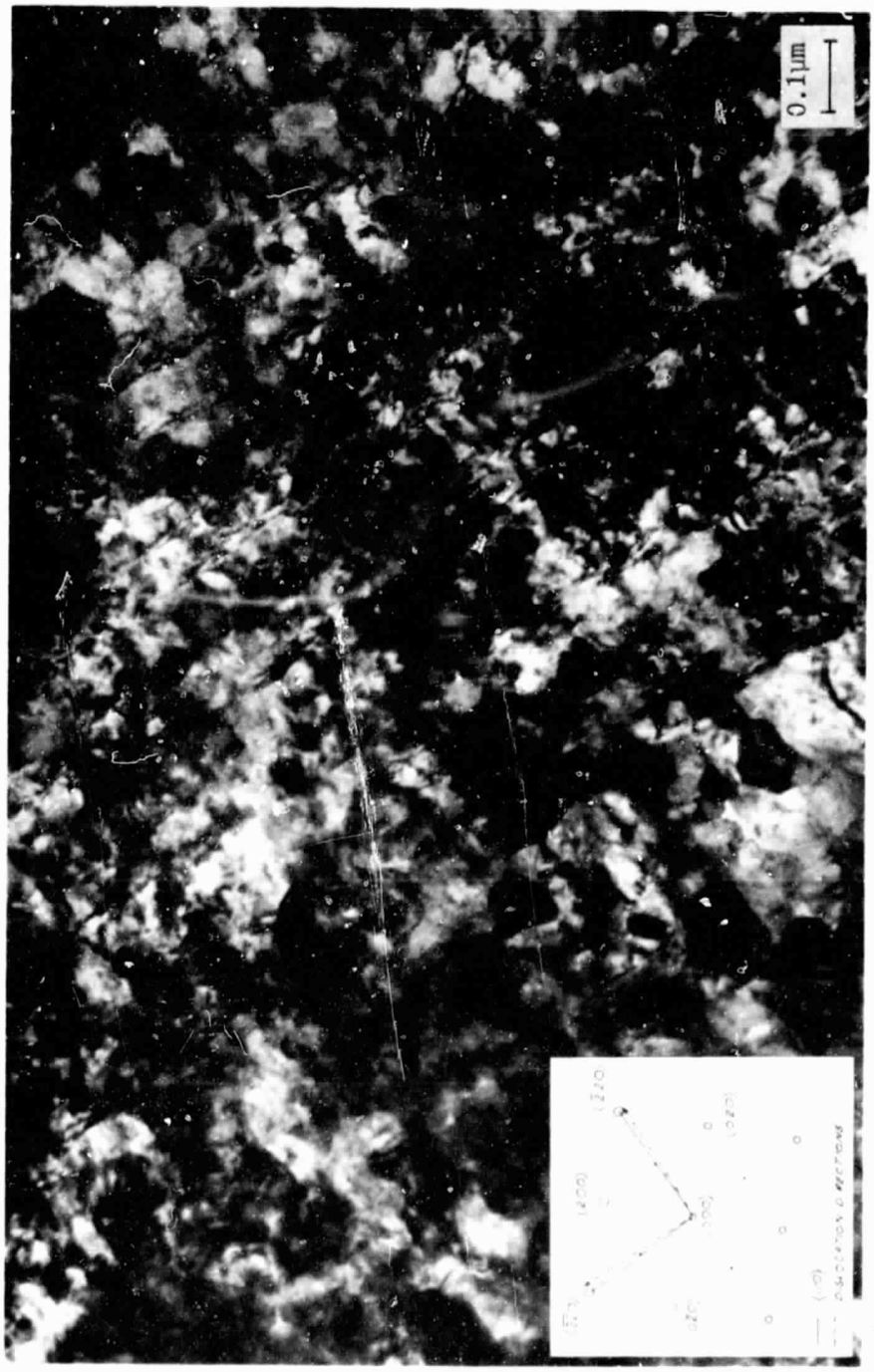

a) bright field of metal dislocations and α-Al_2O_3 grains

Figure 4. $\langle 110 \rangle$ Dislocation directions in oxidized γ/γ'.

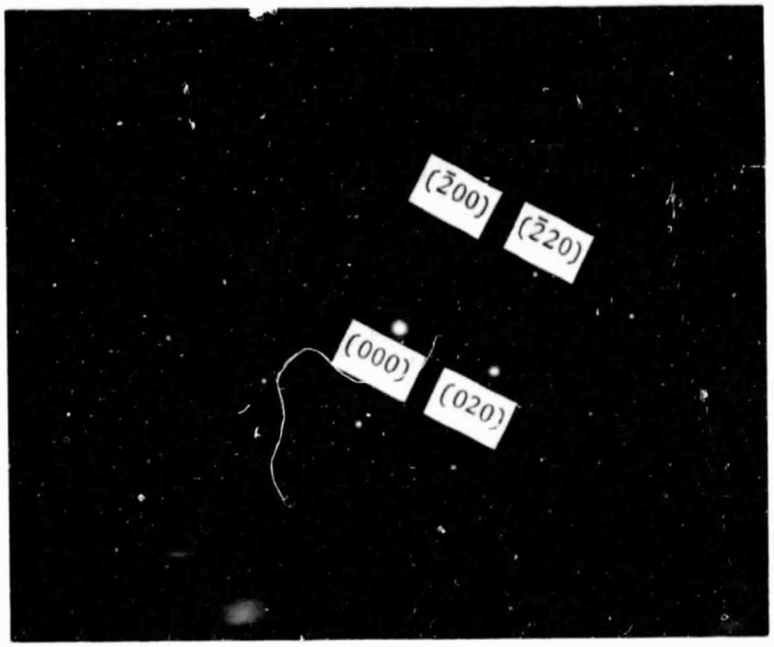

Figure 4b. [001] γ/γ' zone diffraction pattern

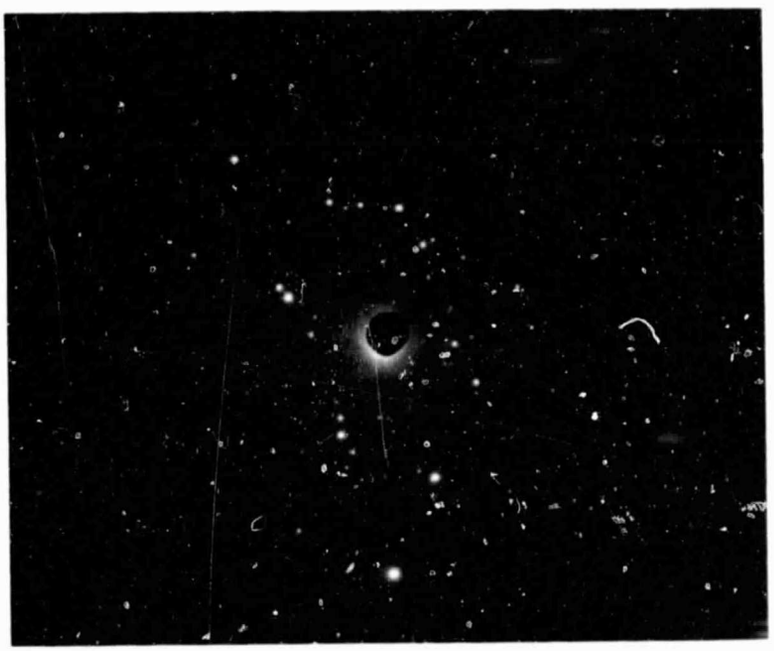

Figure 4c. [001] γ/γ' zone and α-Al_2O_3 rings

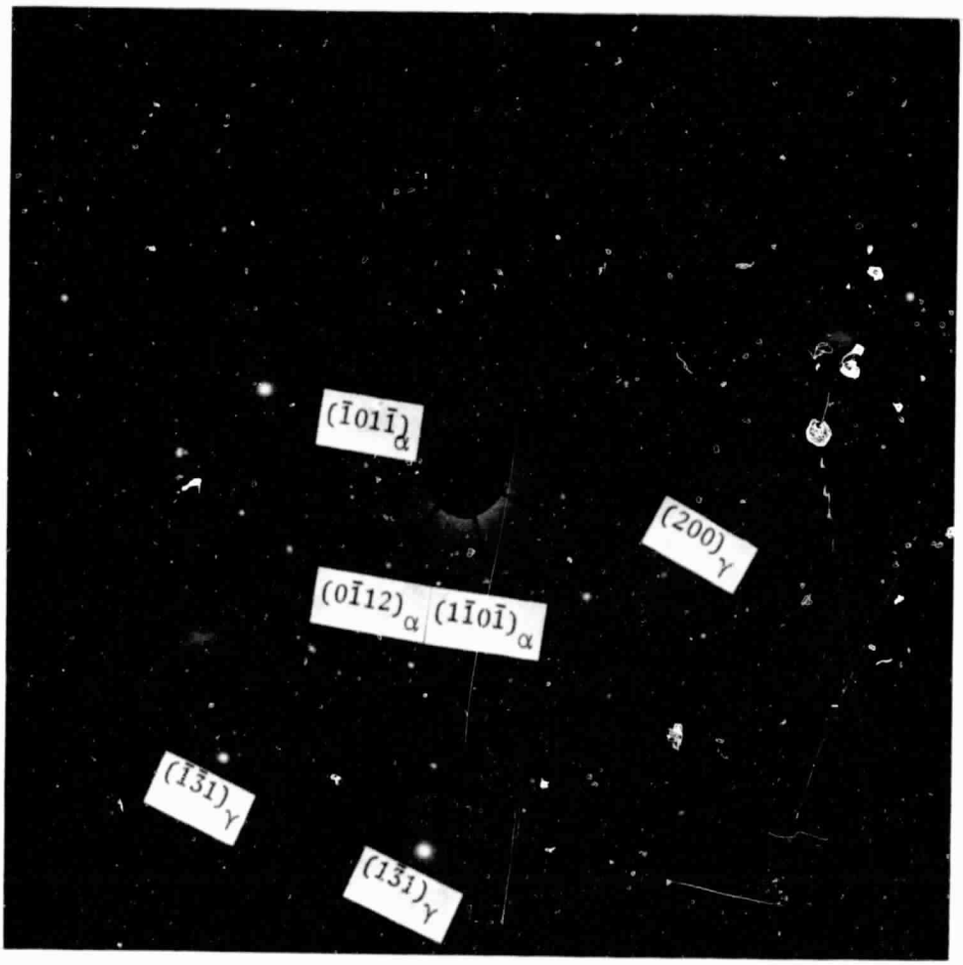

Figure 5. Superimposed γ-Ni and α-Al_2O_3 spot patterns, $\vec{B} = [013]\gamma$, $[0\bar{1}11]$ γ-Al_2O_3.

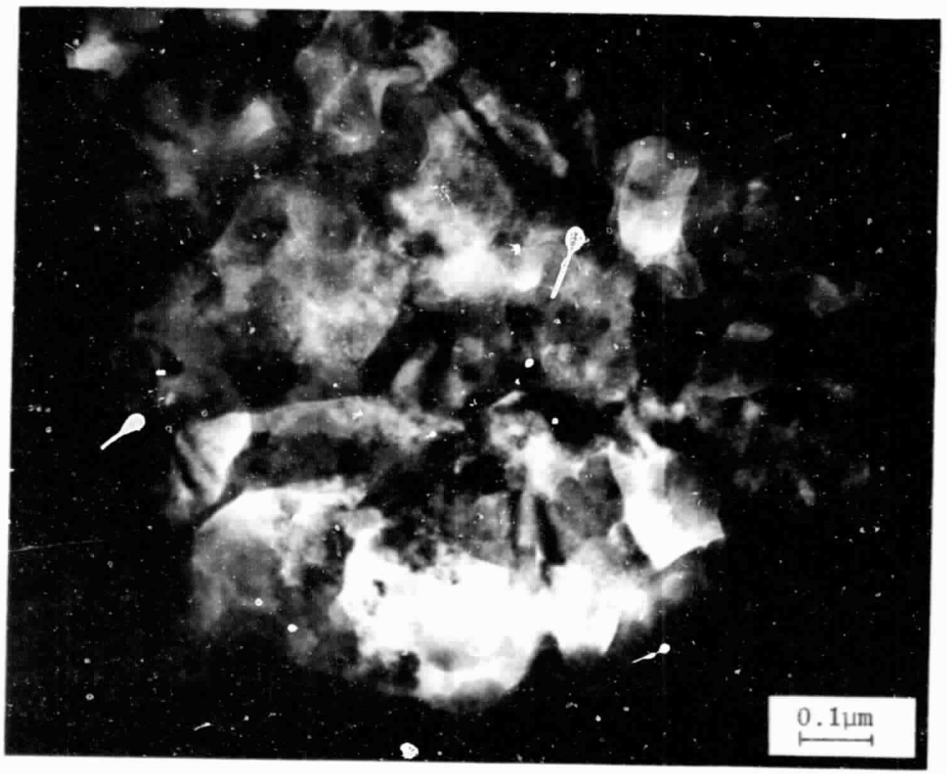

a) bright field

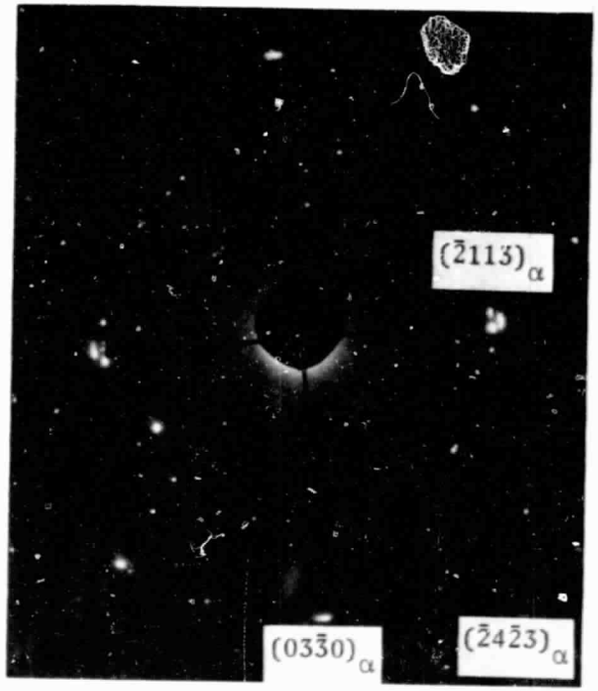

b) possible $[2\bar{1}\bar{1}2]$ Al_2O_3 zone pattern

Figure 6. α-Al_2O_3 grains over pits in β-NiAl phase.

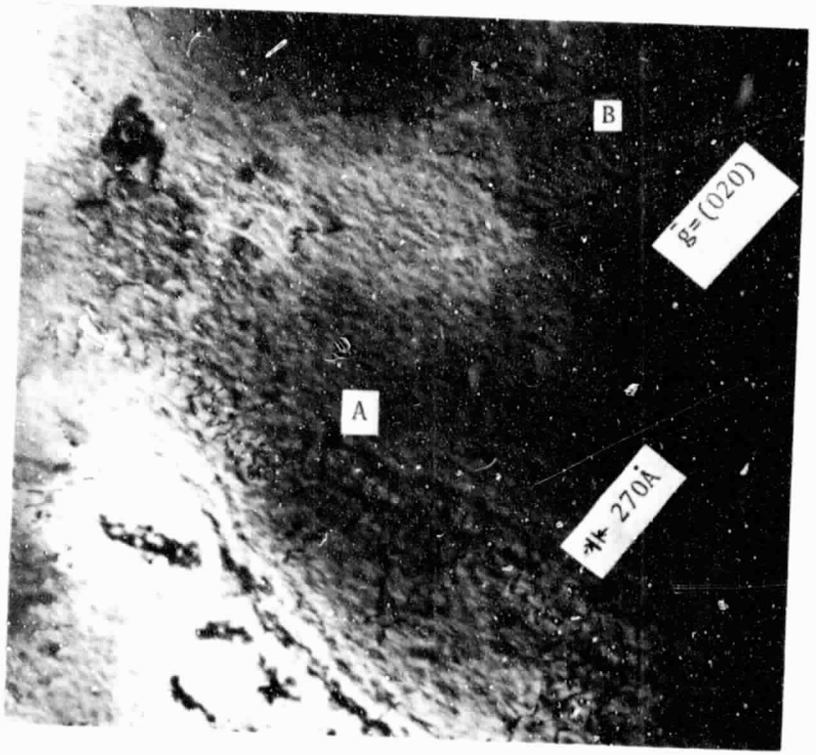

a) bright field

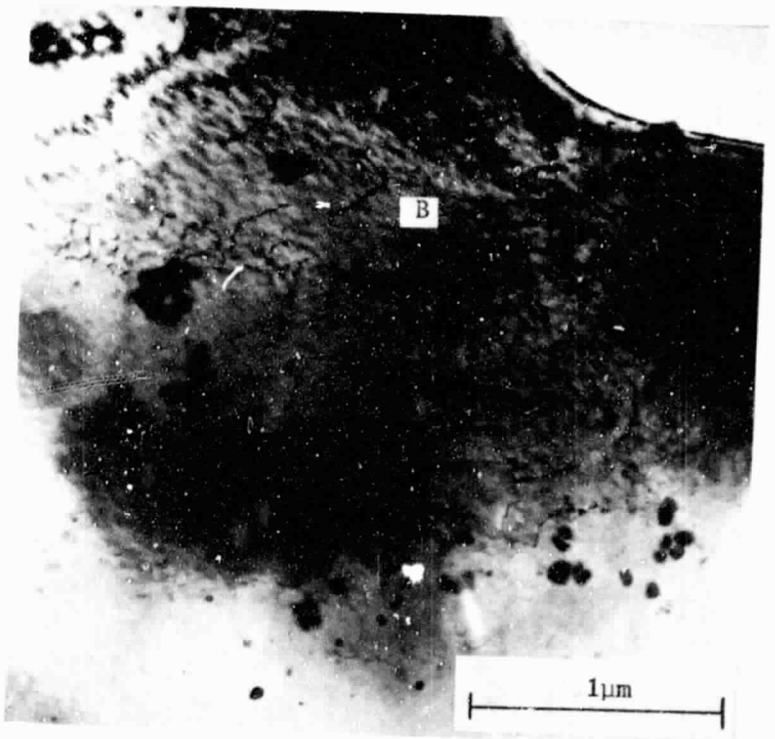

b) bright field

Figure 7. Straight and zigzag dislocation in γ/γ' phase below the oxide-metal interface.

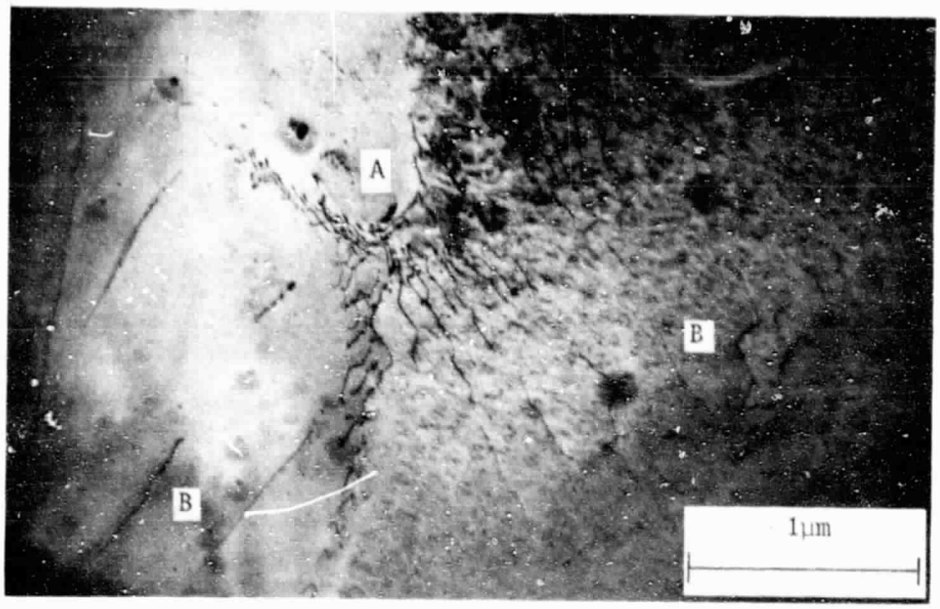

Figure 7c. bright field

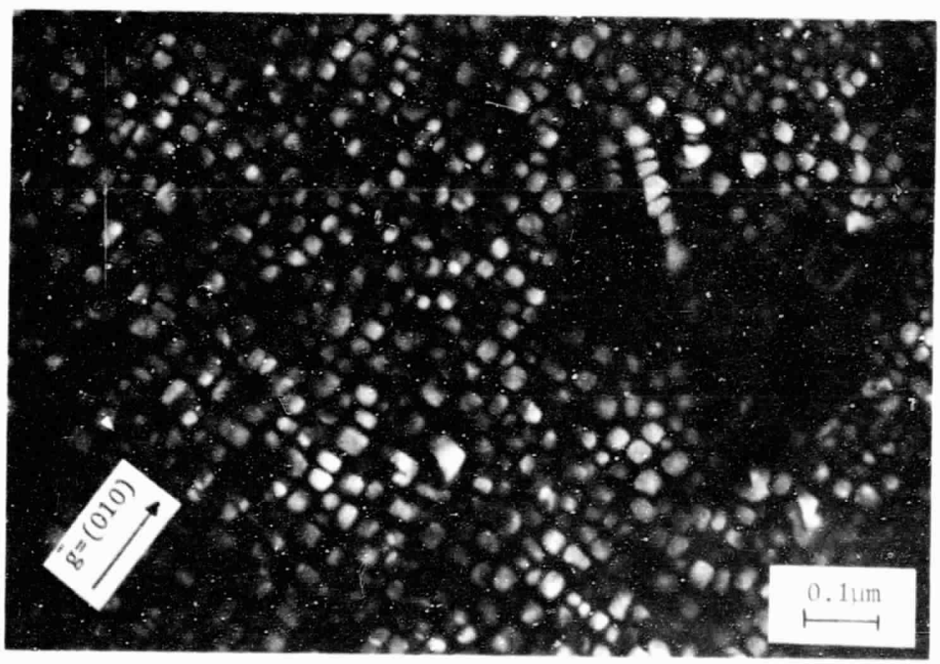

Figure 7d. (010)γ' dark field

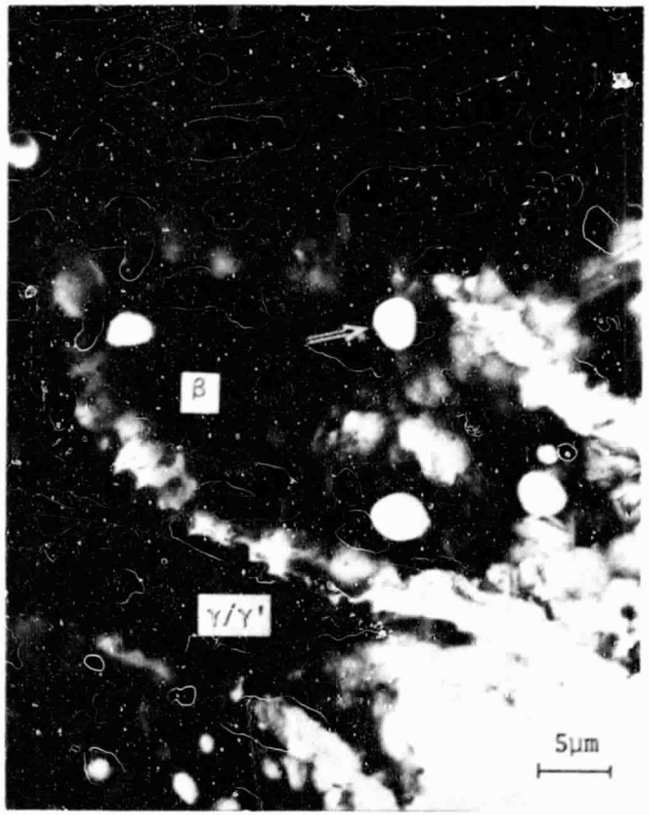

a) interface void formation

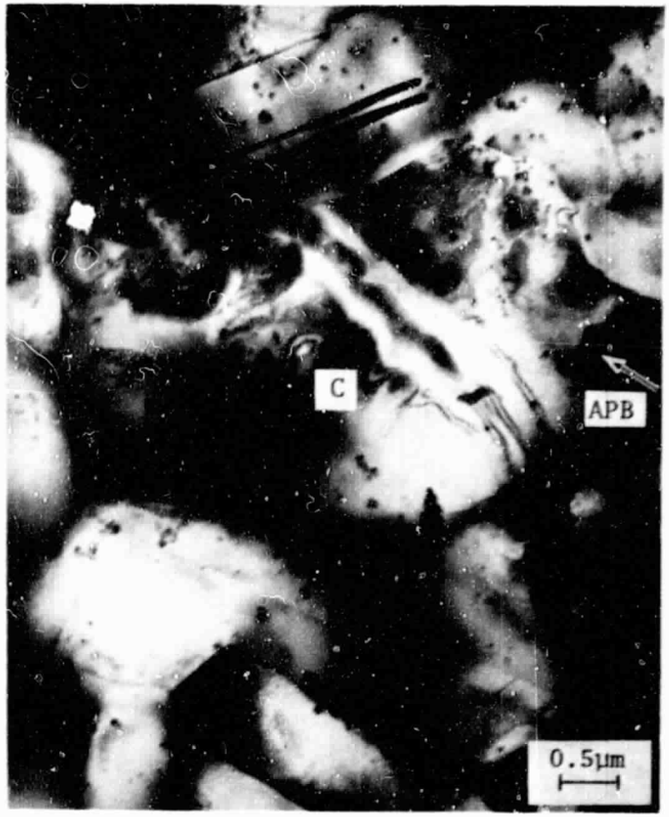

b) γ' subgrains, APB's, and fringe contours

Figure 8. Structure of depleted β phase near the oxide-metal interface.

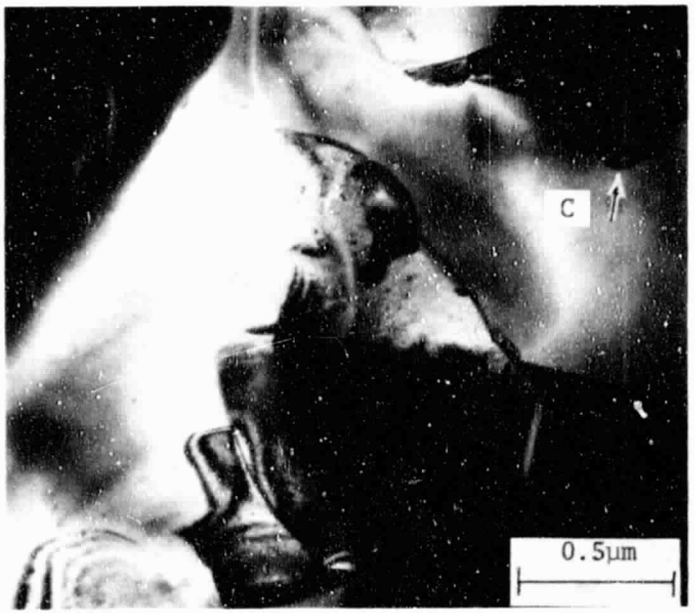

Figure 8c. γ' subgrains

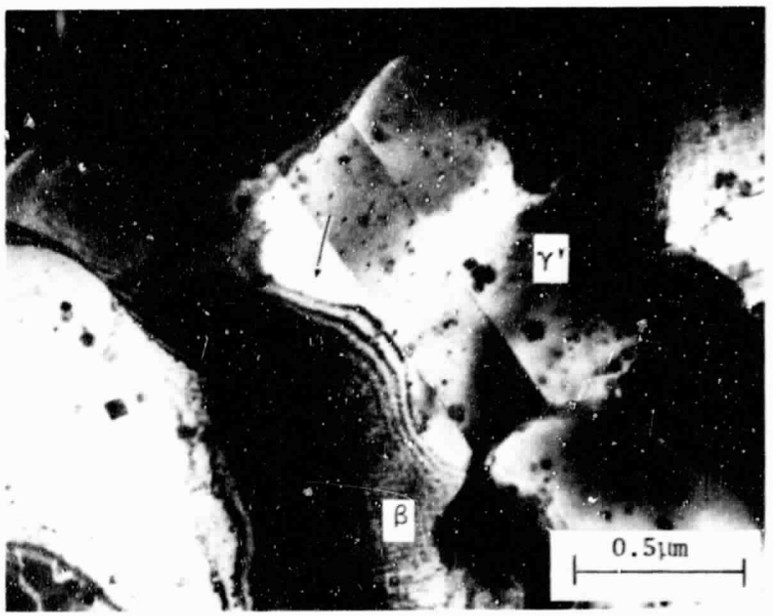

a) overview of a 1.5 μm wide γ' subgrain

Figure 9. Coherent γ'-Ni_3Al depletion layers formed upon β-NiAl

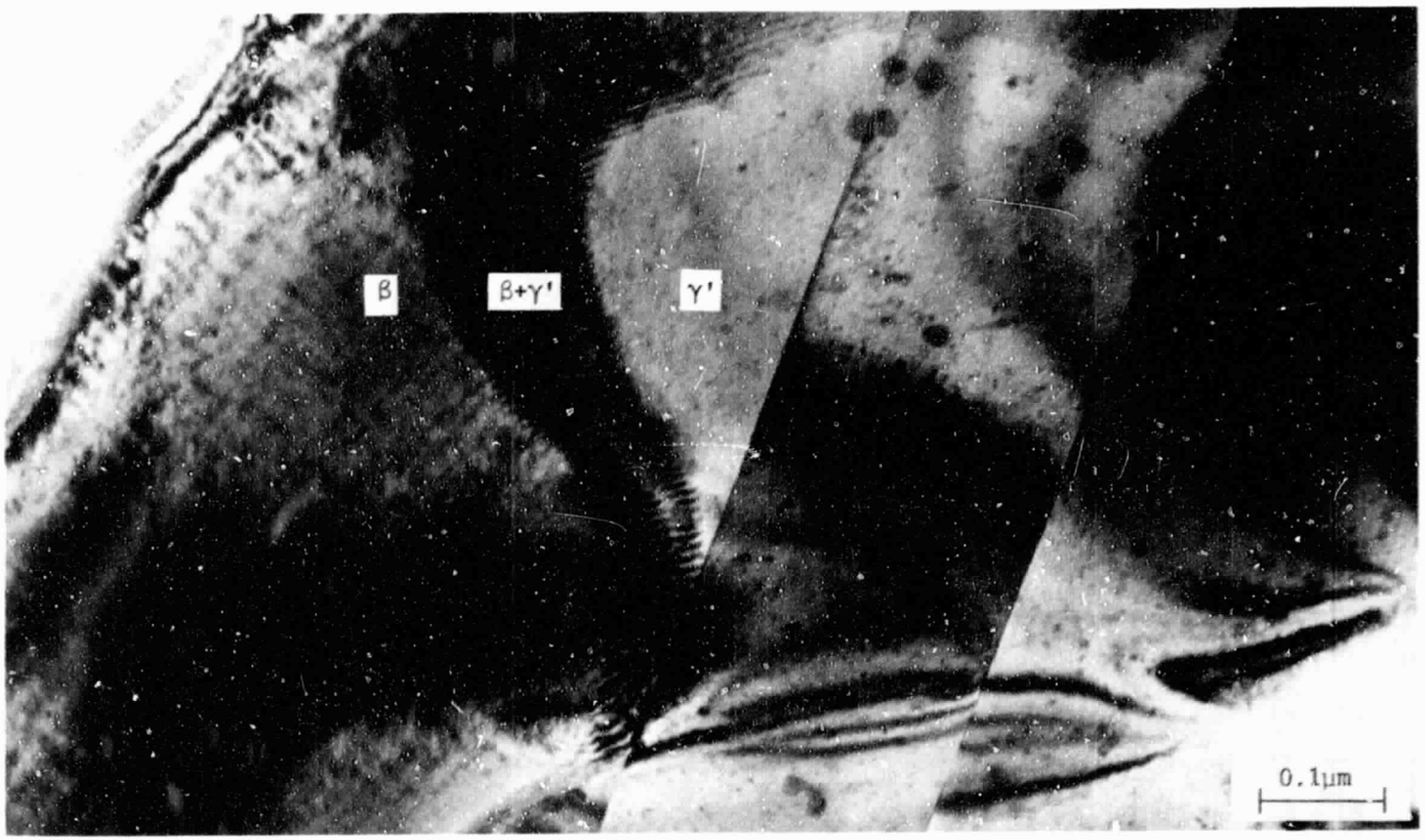

Figure 9b. Moire patterns at γ'-β interface region and crosshatched structure in β, bright field.

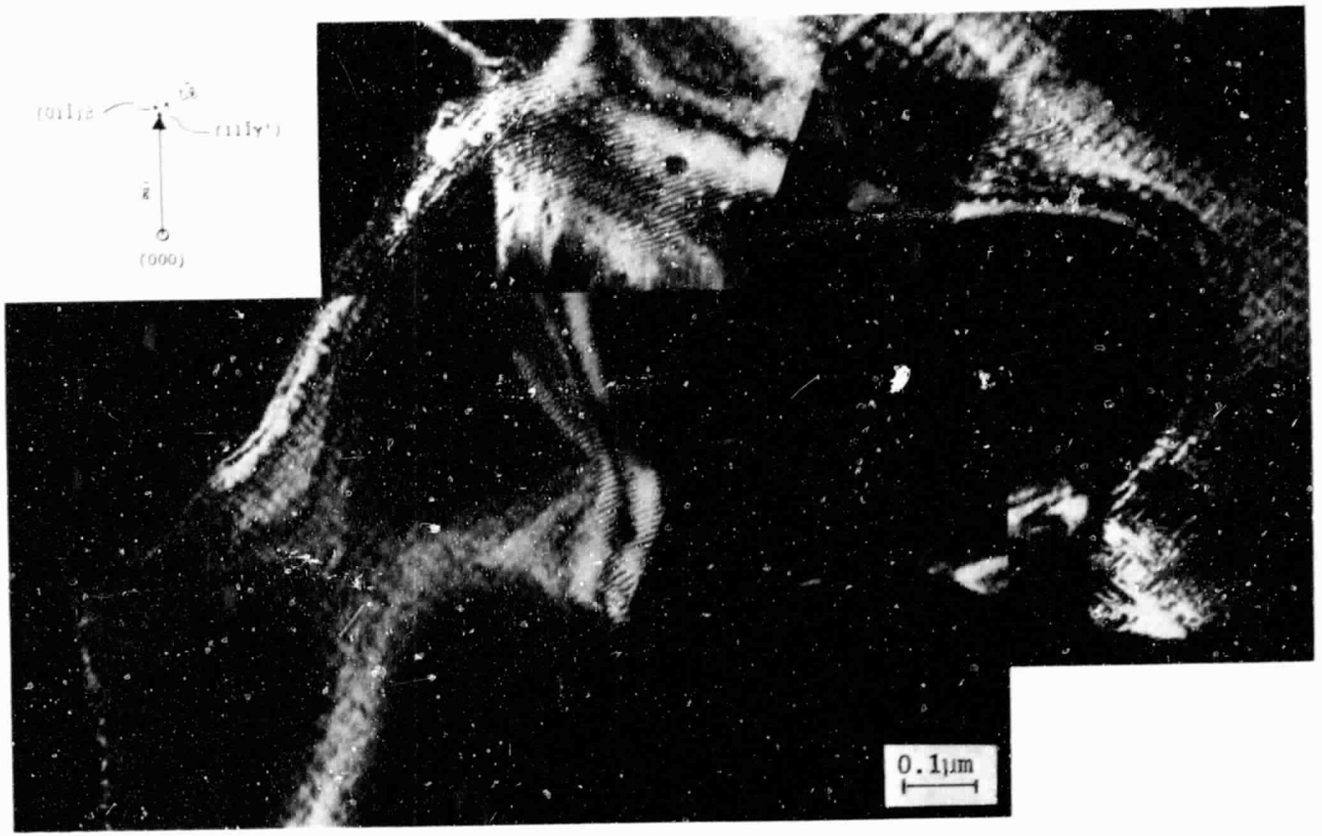

Figure 9c. dark field of (b); $\vec{g} = (01\bar{1})\beta, (11\bar{1})\gamma'$

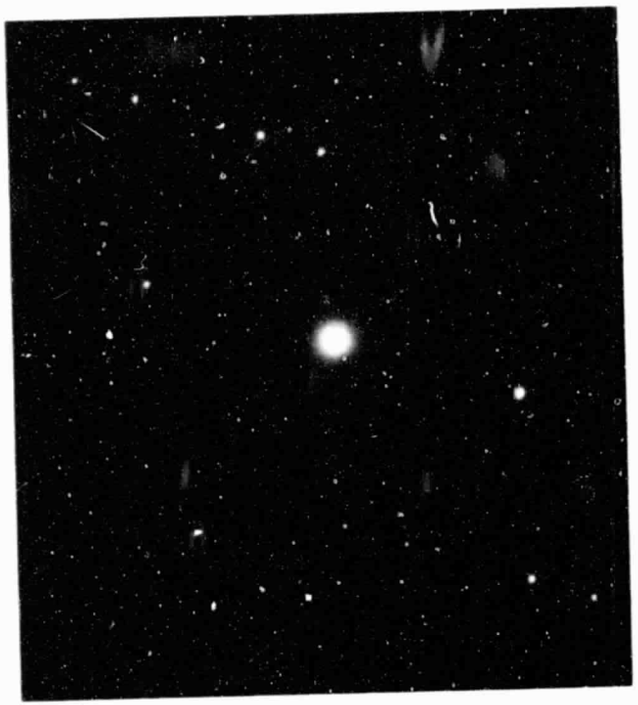

a) twin pattern for a $[1\bar{1}0]\gamma'$ zone

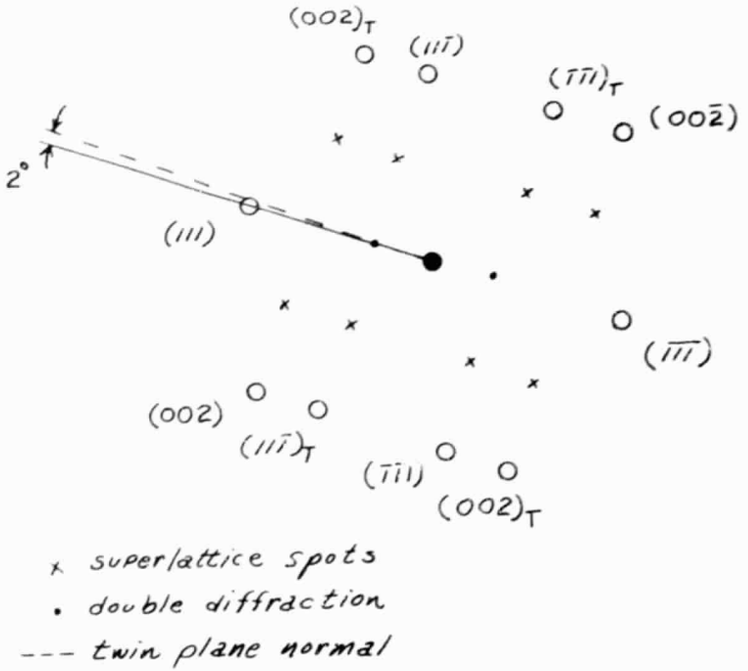

b) indexed pattern in (a)

Figure 10. Diffraction patterns from layered $\gamma'+\beta$ structure; foil tilted -5.5^{o} about $[111]\gamma'$.

Figure 10c. [100]β zone

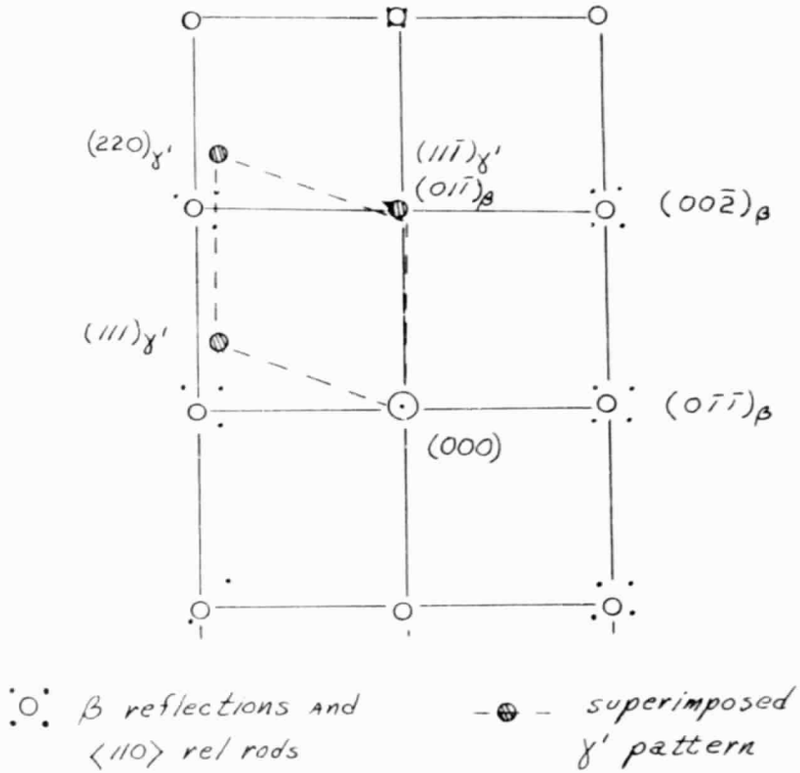

Figure 10d.
indexed pattern in (c) showing rel rods, superimposed γ'spots

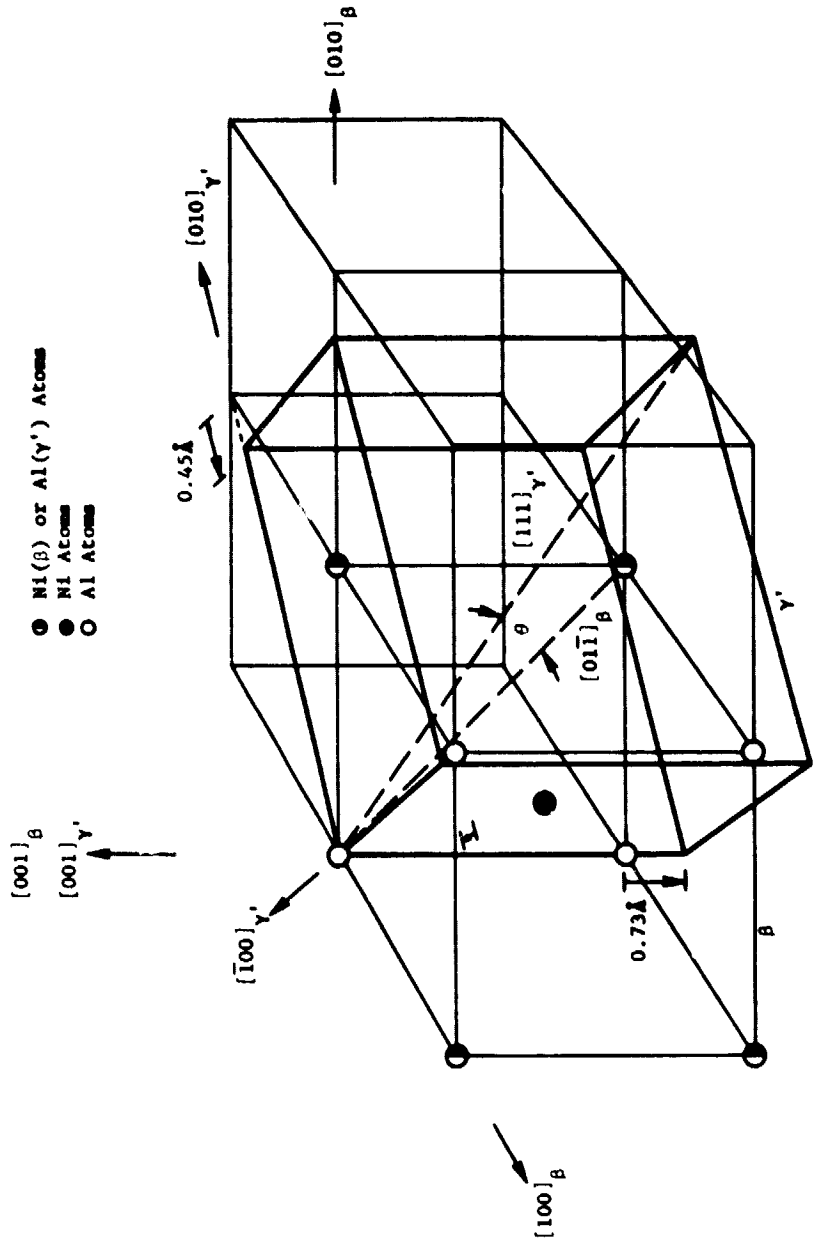

Figure 11. Derivation of FCC γ'-Ni_3Al cell (a_o=3.59 Å) from BCC β-NiAl cells (a_o=2.86 Å).

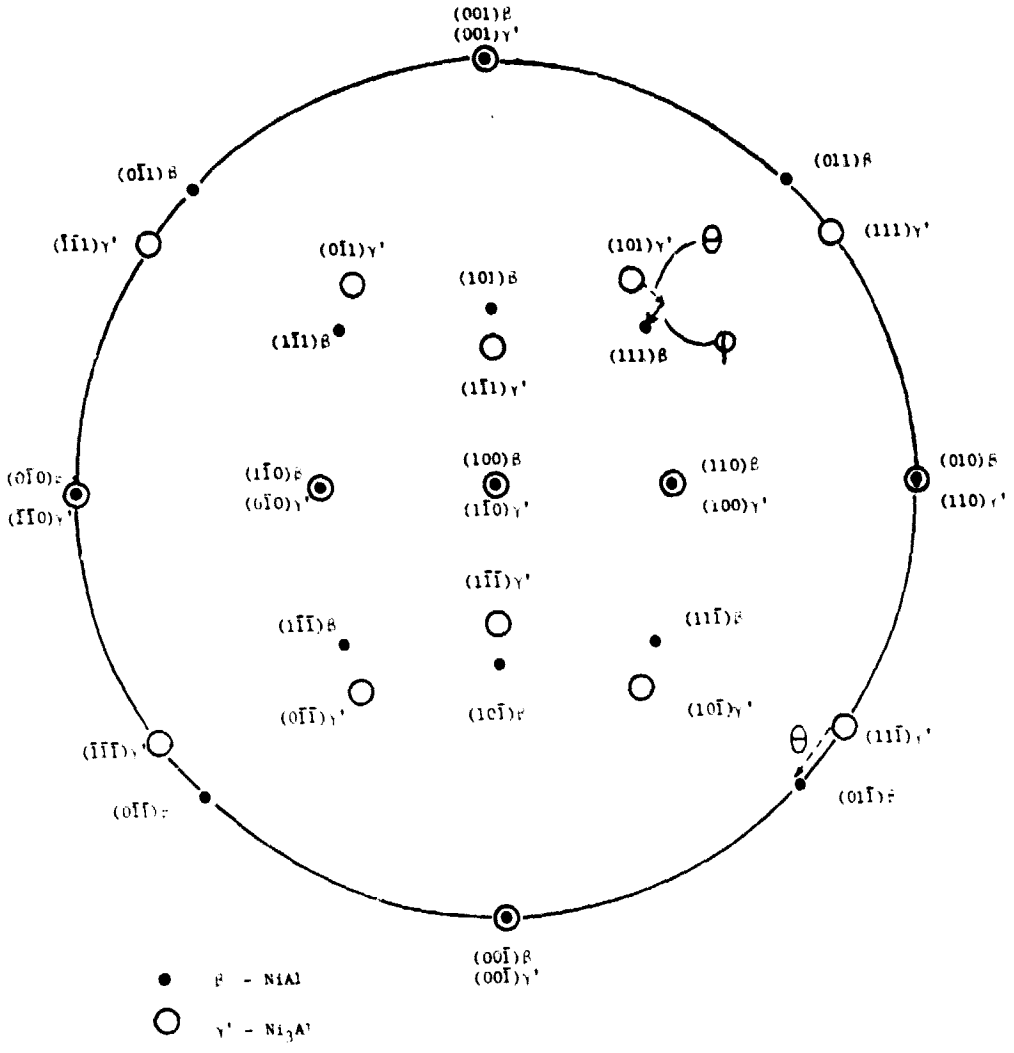

Figure 12. Stereographic projections of [100]β and [1$\bar{1}$0]γ' showing the production of a K-S or a N-W relationship between β and γ phases.

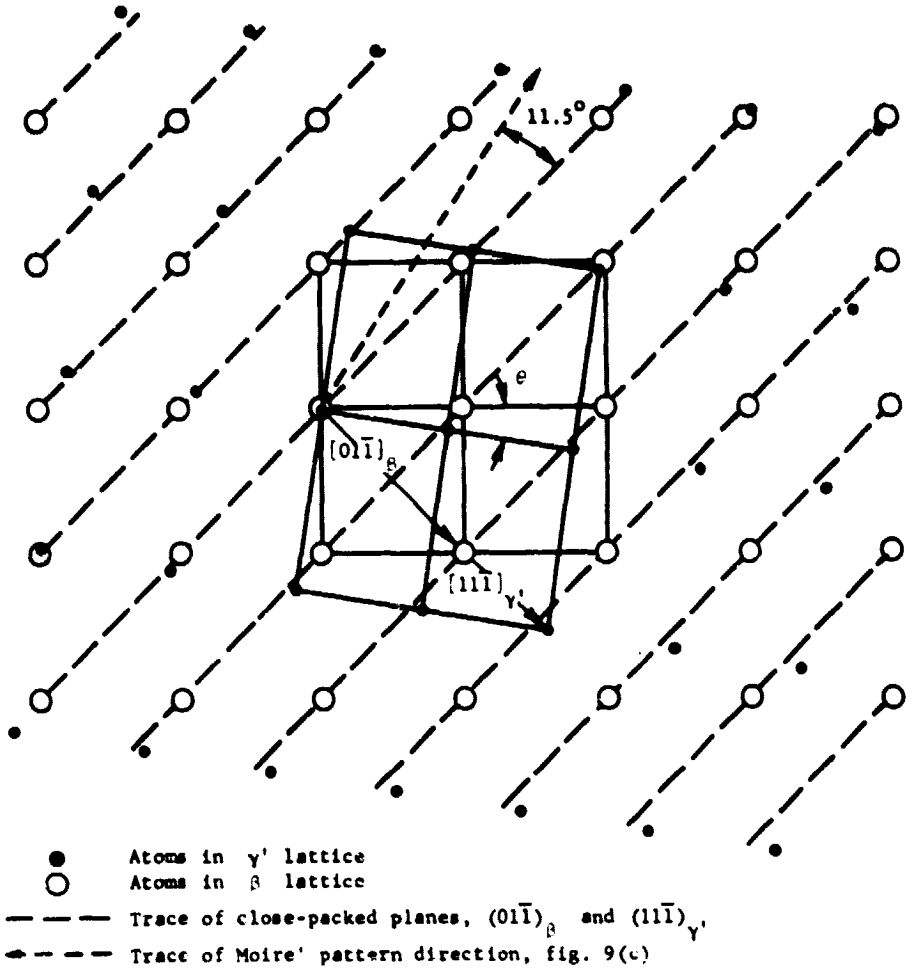

Figure 13. Atom site coincidence pattern for the $(100)\beta$ and $(1\bar{1}0)\gamma'$ planes having $[01\bar{1}]\beta \parallel [11\bar{1}]\gamma'$; these planes give rise to the Moire' patterns for Figure 9c.

a) bright field, $\vec{g} = (00\bar{2})$, $\vec{B}$ near [100]

b) new area, bright field, $\vec{g} = (01\bar{1})$, $\vec{B}$ near [100]

Figure 14. Modulated "tweed" structure of β-NiAl.

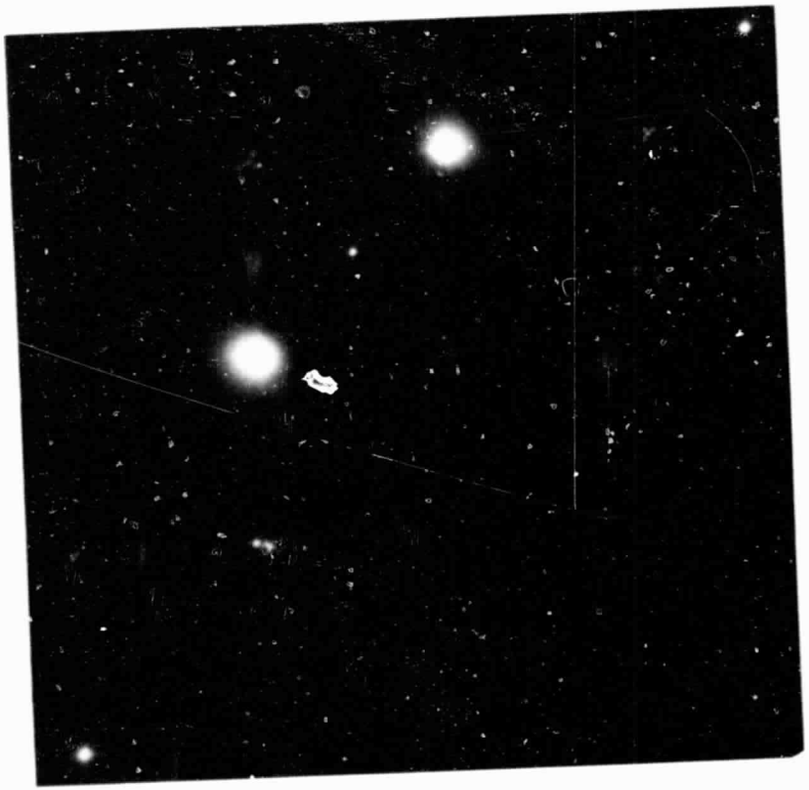

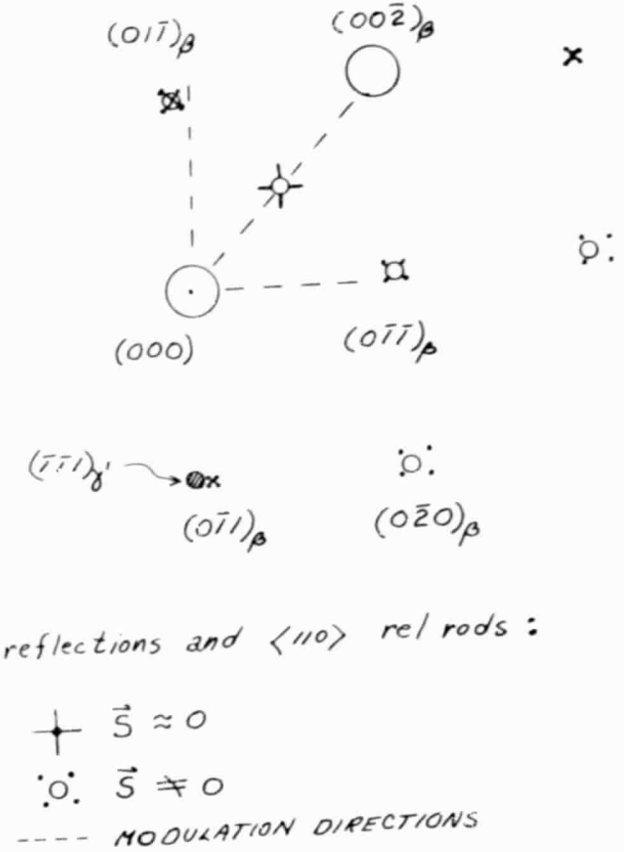

Figure 14c. [100] diffraction pattern showing directions of rel rods and tweed structure in 14a.

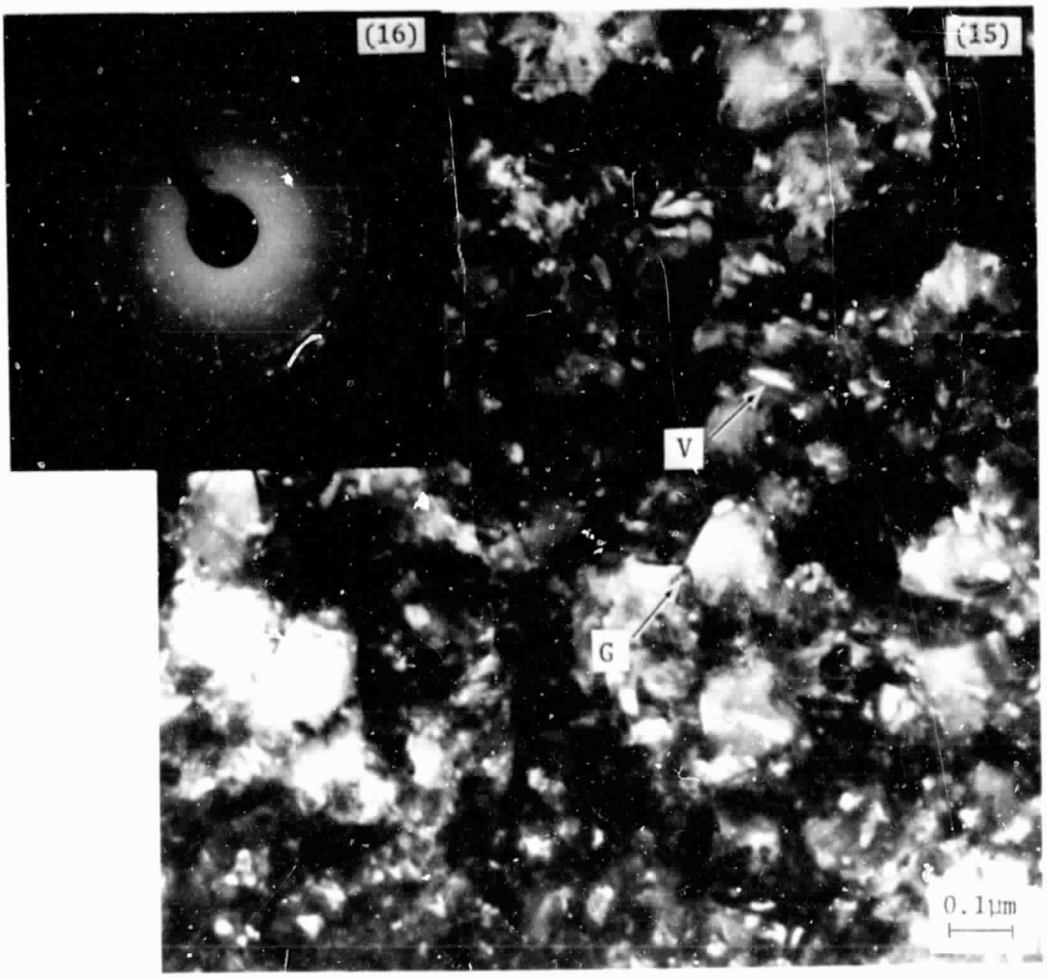

Figure 15. Large voids in random α-Al_2O_3 scale, ion thinned 8 minutes.

Figure 16. Random orientations of α-Al_2O_3 grains after ion thinning 90 minutes.

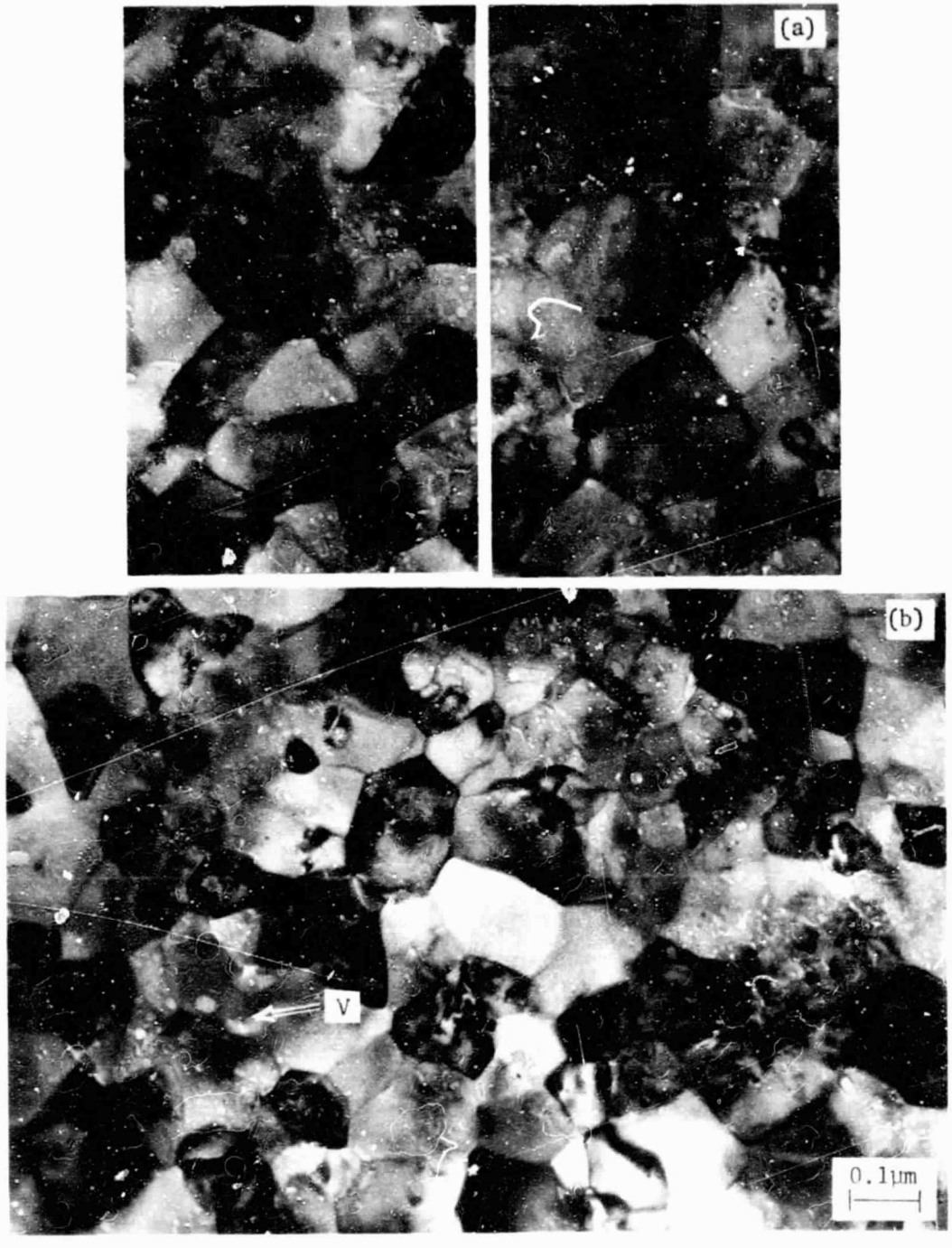

Figure 17. Grain and fine void morphology in the random α-Al_2O_3 scale after ion thinning 90 minutes.

a) stereopair (6.4° tilt difference) showing the intragranular distribution of voids.

b) adjacent field of view.

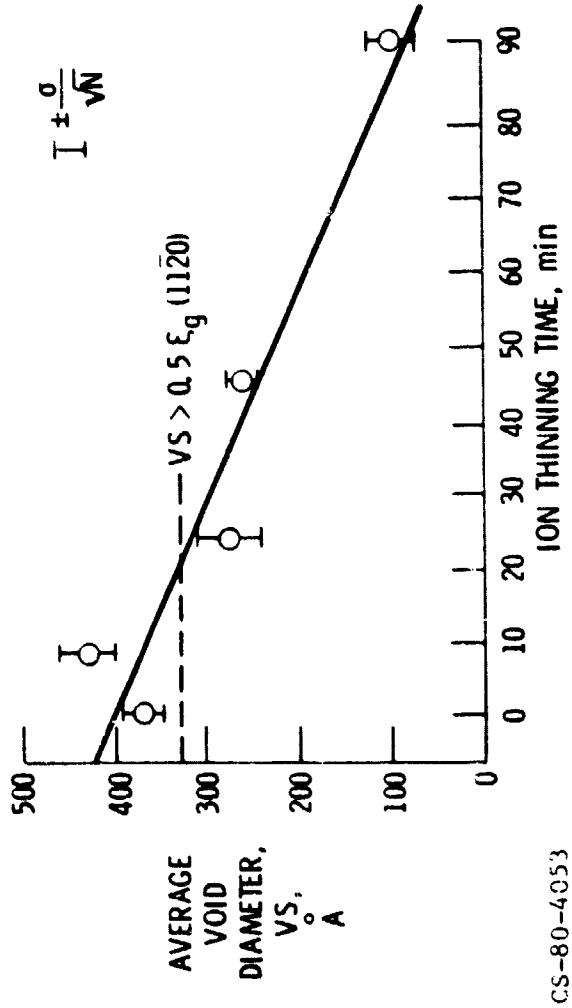

Figure 18. Decrease in measured void size with removal of oxide surface layers.

Figure 19. Strain contrast in Al_2O_3 grains.

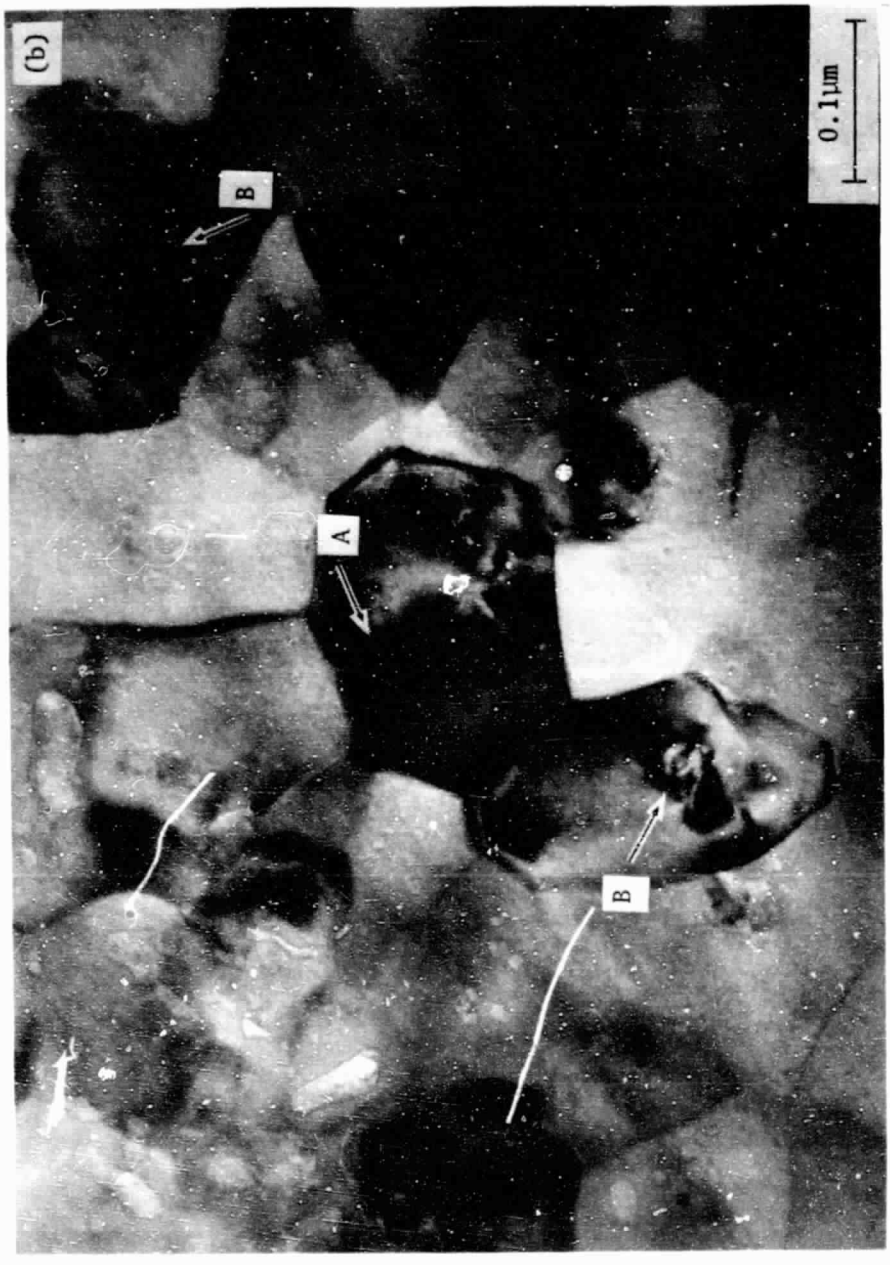

Figure 19b. Same area as Figure 19, tilted 6.4°.

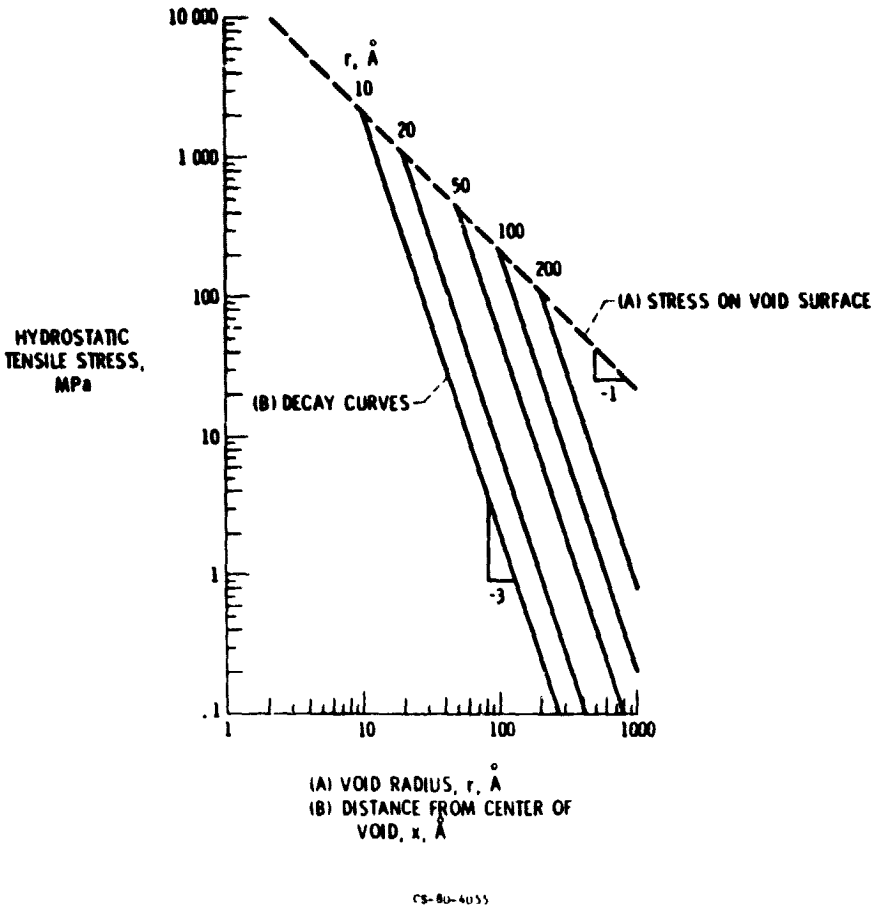

Figure 20. Calculated surface energy stresses (A) and decay curves (B) for varicus void sizes.

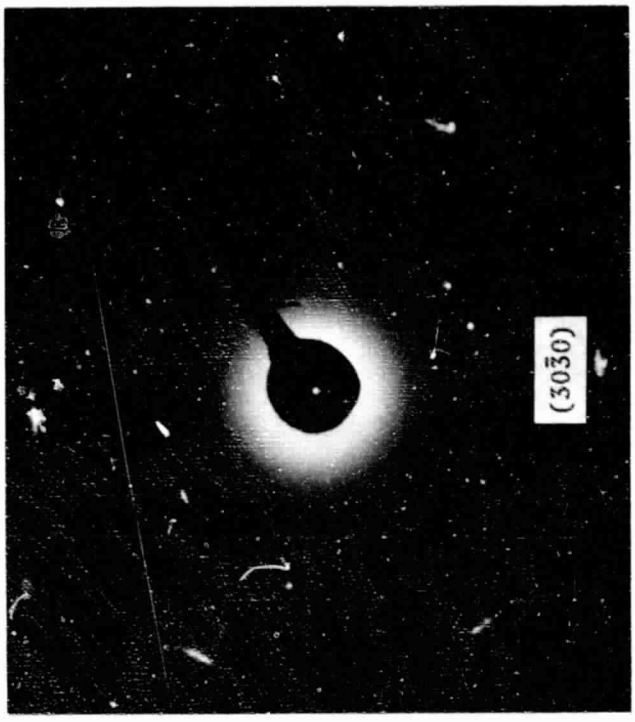

Figure 21. [0001] zone of oriented α-Al_2O_3.

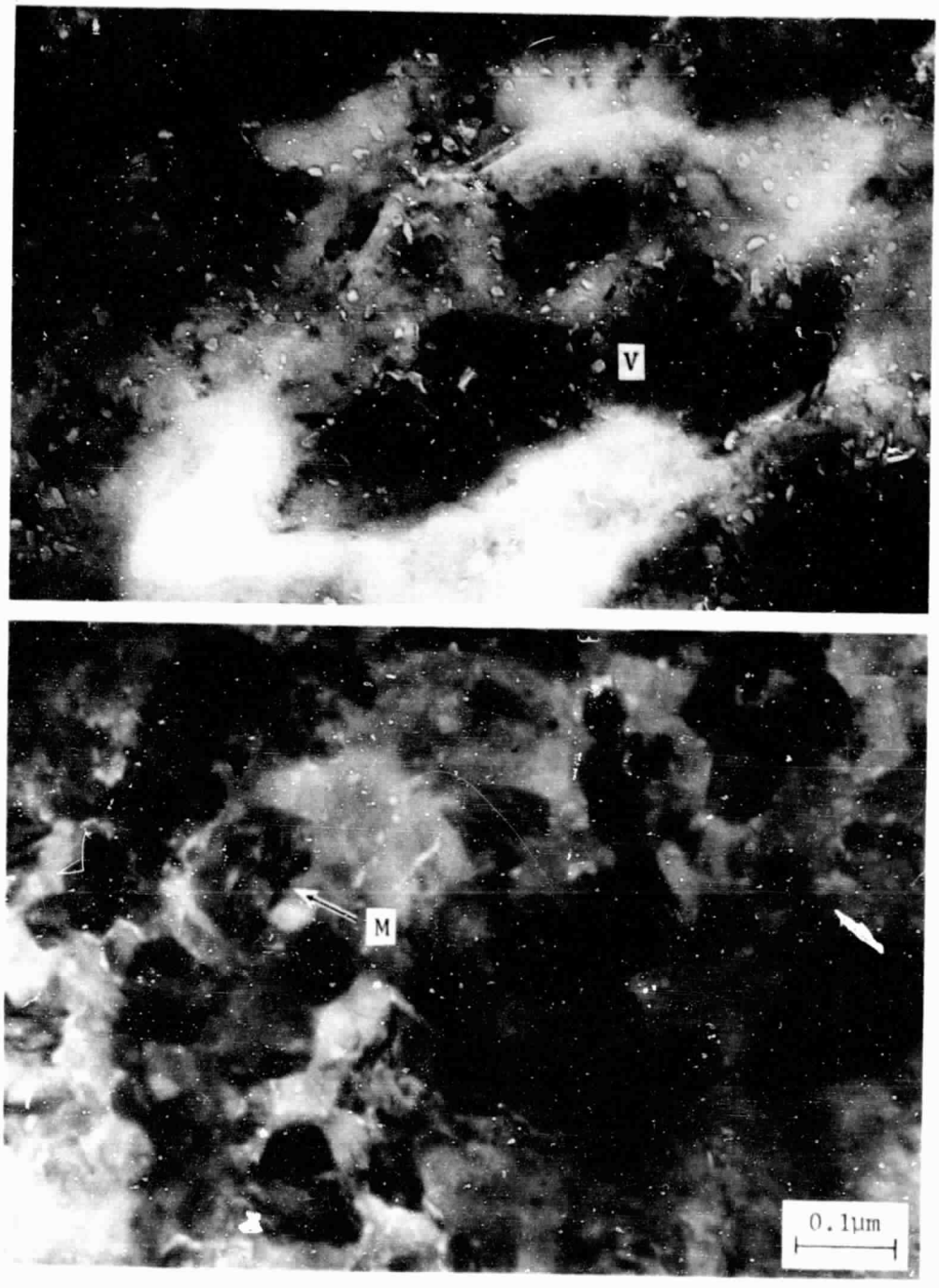

Figure 22. Structure of oriented oxide.

a) faceted voids, thin area.

b) distorted Moire' patterns, thick area.

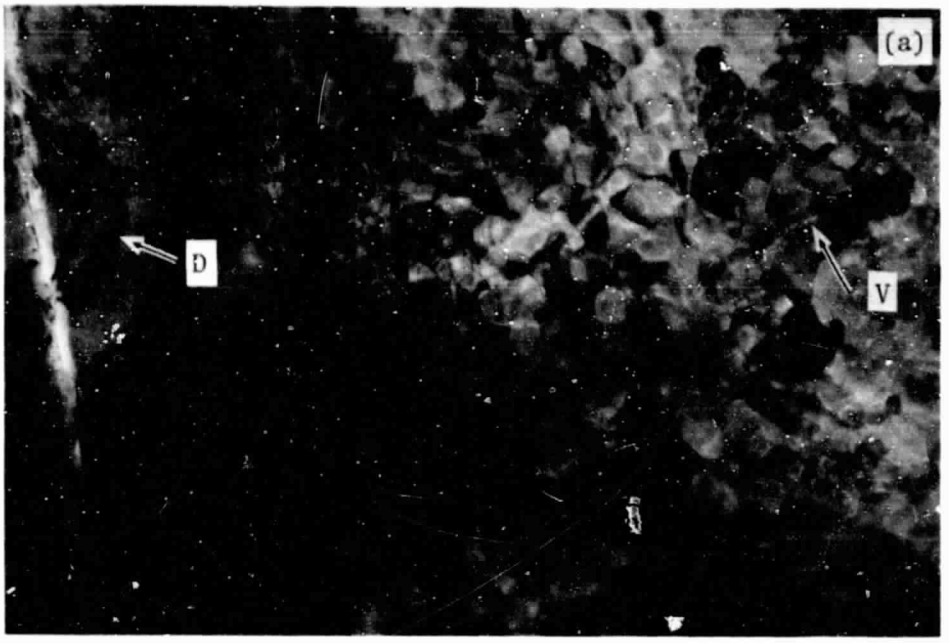

a) $\vec{B} \sim [001]\gamma$

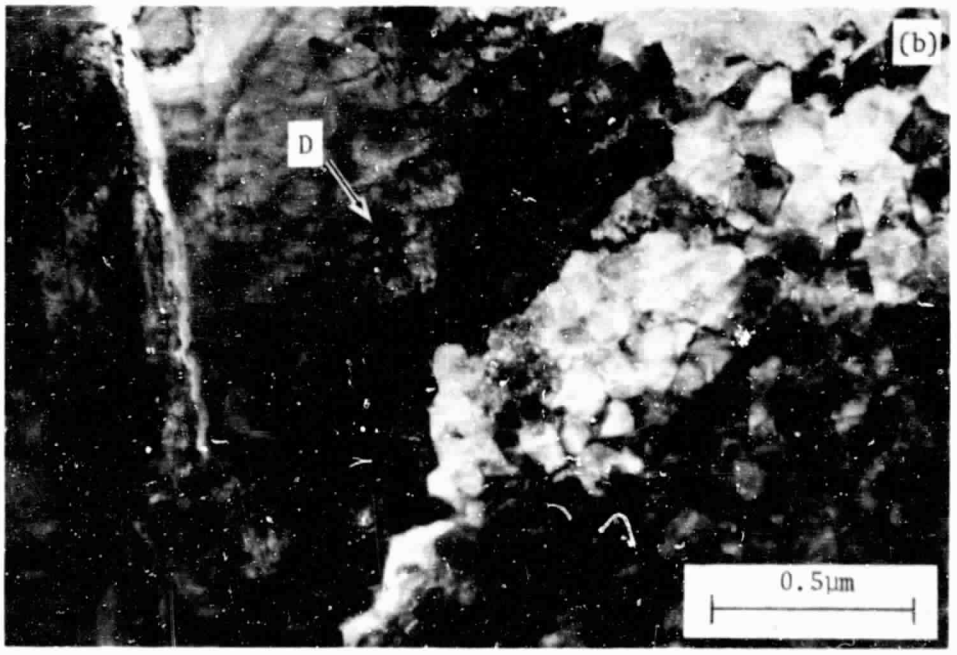

b) $\vec{B} \sim [0\bar{1}1]\gamma$

Figure 23. Random α-Al_2O_3 grains and γ-Ni at the oxide-metal interface; (NiCrAl+Y, 0.1hr at 1100°C).

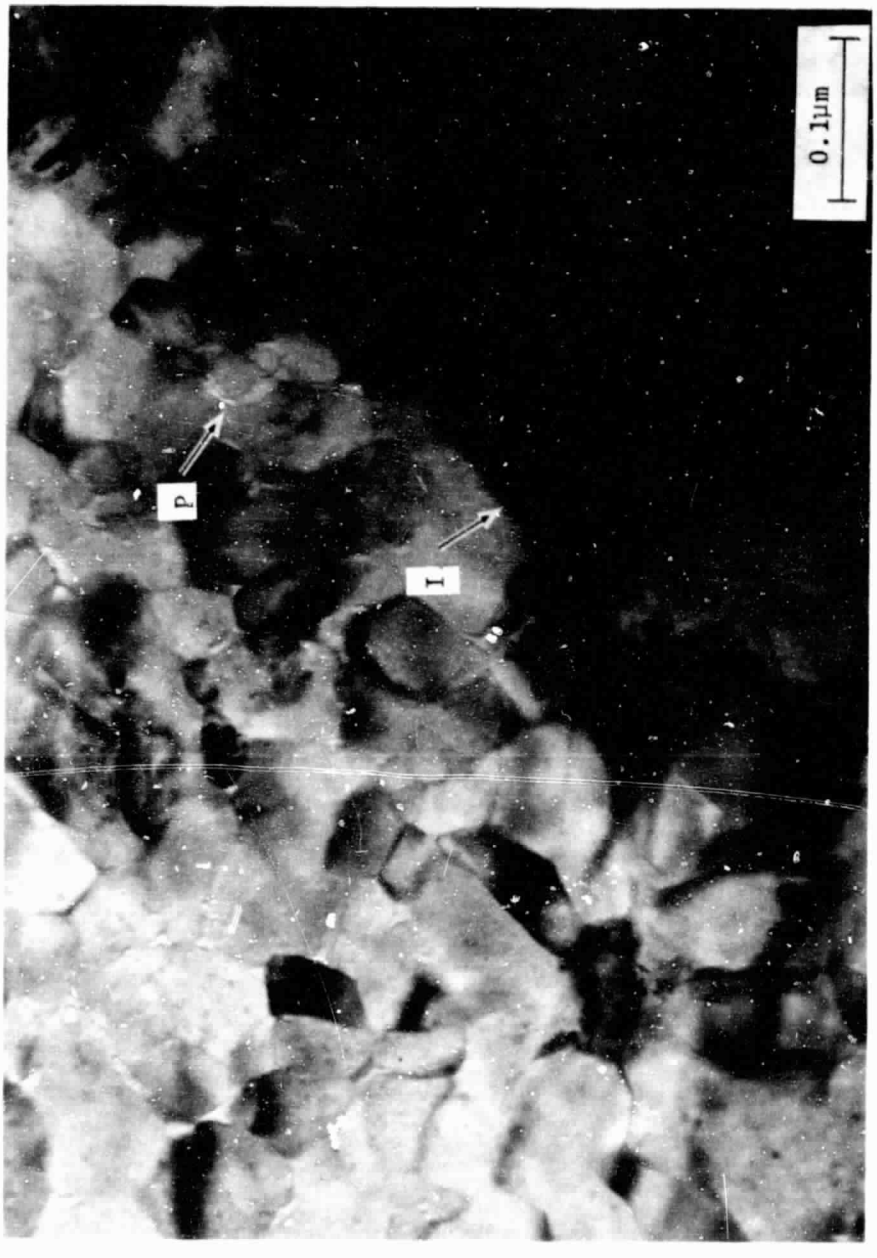

Figure 2 . Oxide-metal interface between α-Al_2O_3 and γ-Ni.

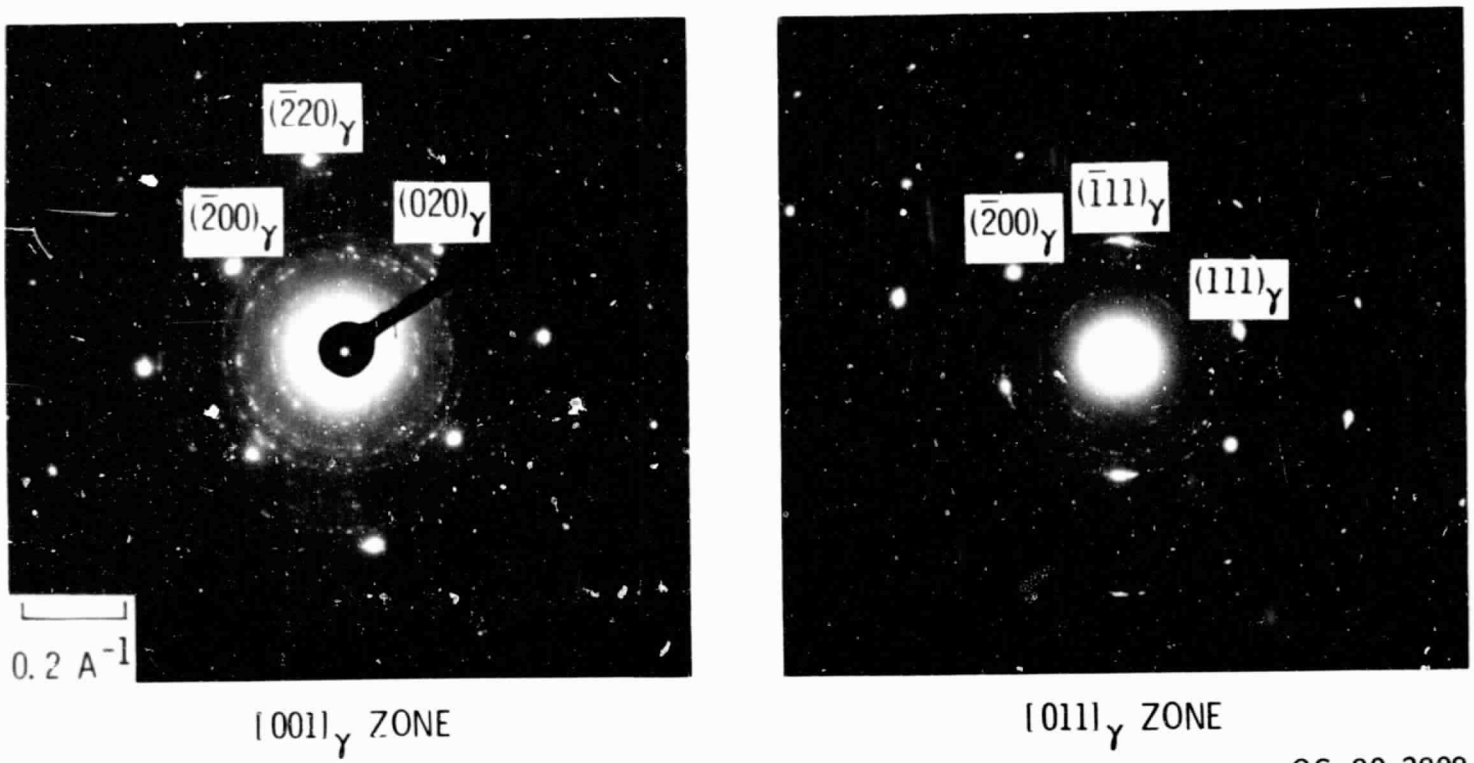

Figure 25. Superimposed γ-Ni spot pattern and α-Al_2O_3 ring pattern.

Figure 26. Dense dislocation arrays in γ-Ni.

Figure 27. γ'-Ni_3Al subgrains formation from β-NiAl near the oxidized surface. $\bar{g}=(1\bar{1}1)\gamma'$

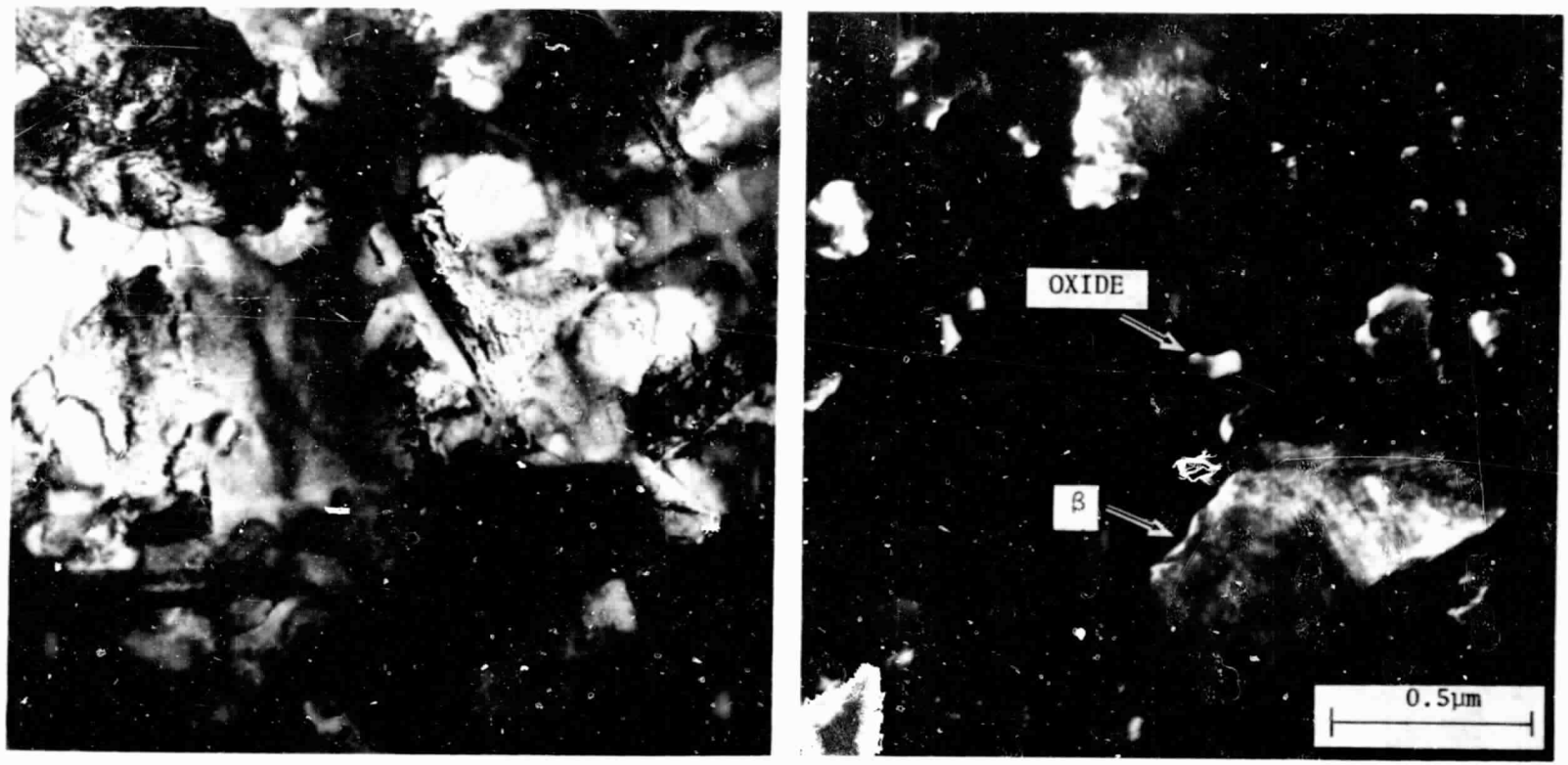

a) bright field

b) dark field, $\vec{g} = (200)\beta$

Figure 28. Complex layered structure arising from oxidation of β-NiAl phase.

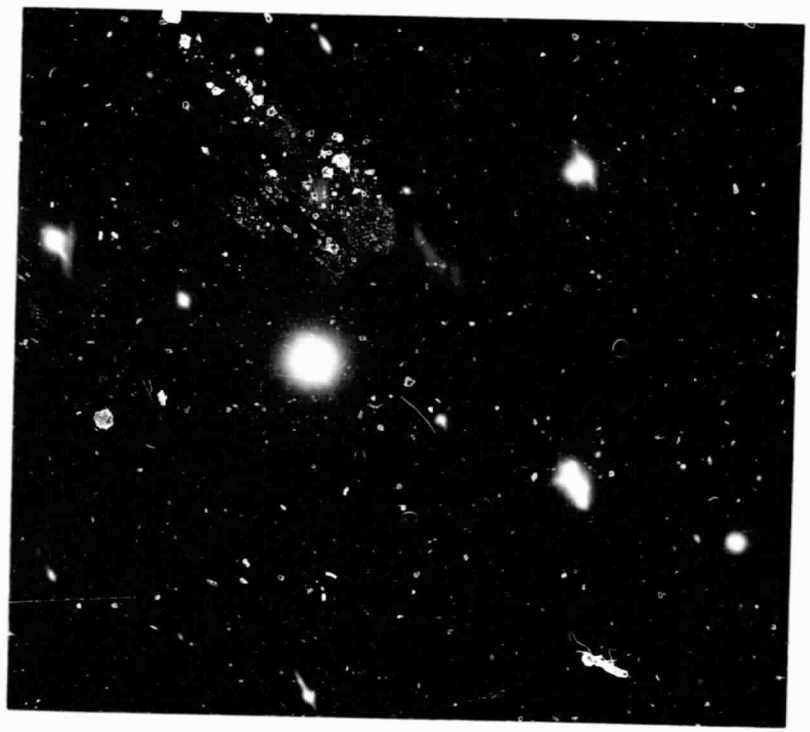

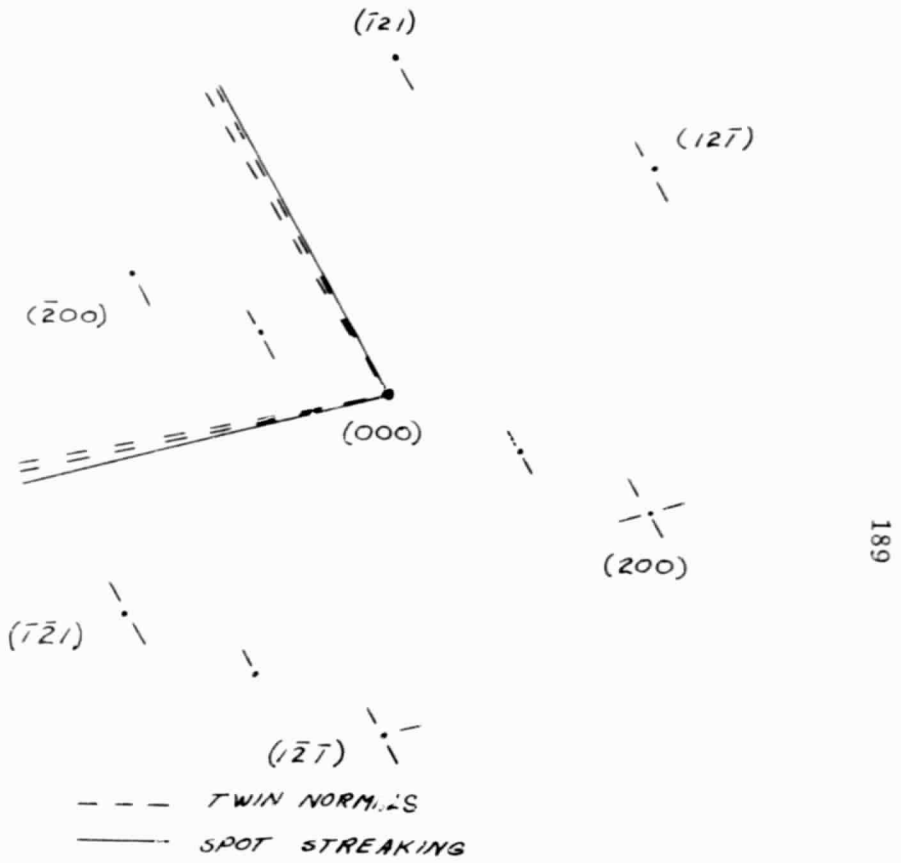

Figure 28c. spot streaking in β phase.

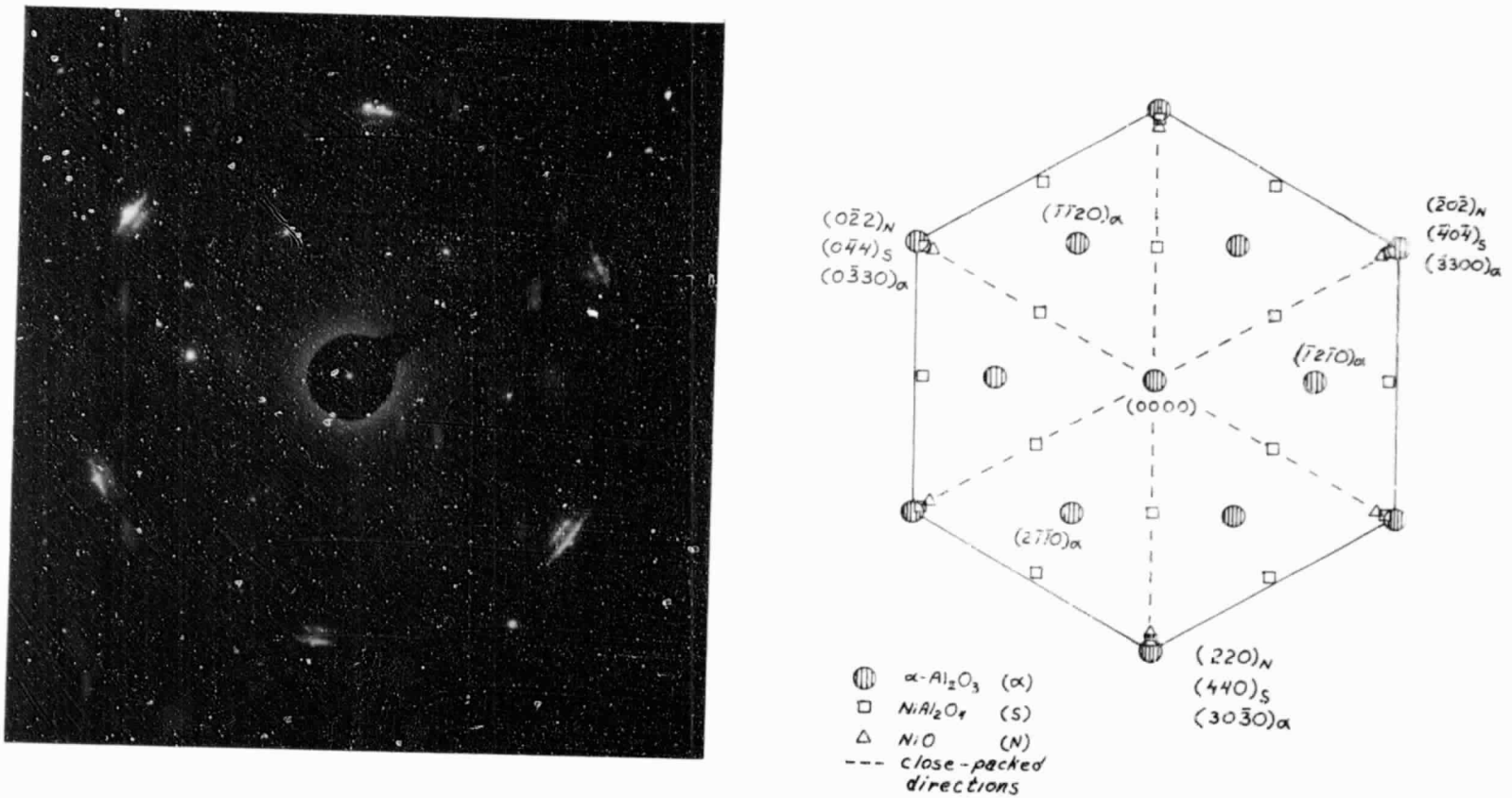

Figure 29. Oriented α-Al_2O_3, $\alpha(Al, Cr)_2O_3$, and $Ni(Al, Cr)_2O_4$ diffraction patterns; (0001) $\langle 10\bar{1}0 \rangle_\alpha$ || $(\bar{1}11)$ $\langle 110 \rangle_S$; foil tilted 19° from plane of oxidation.

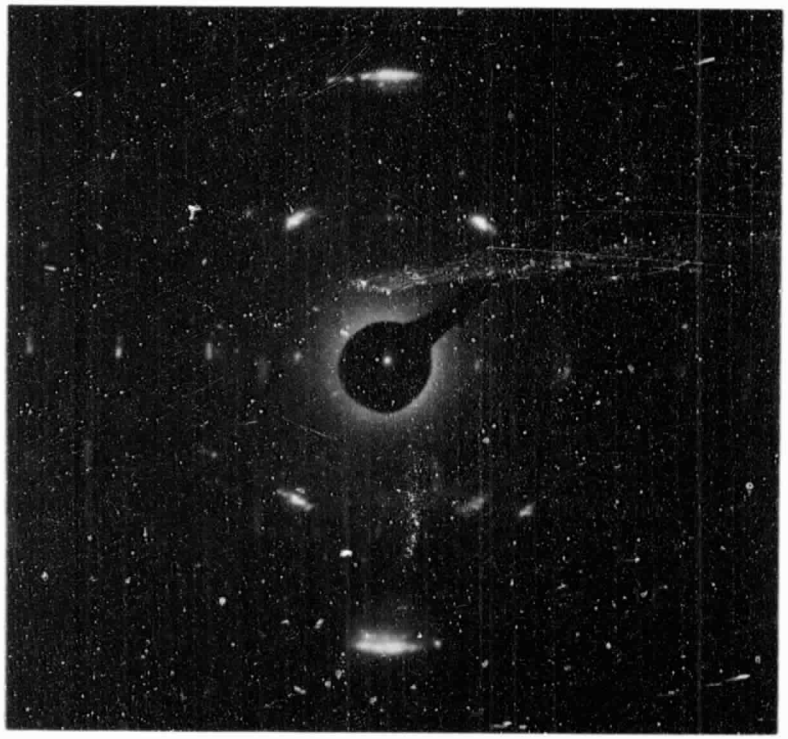

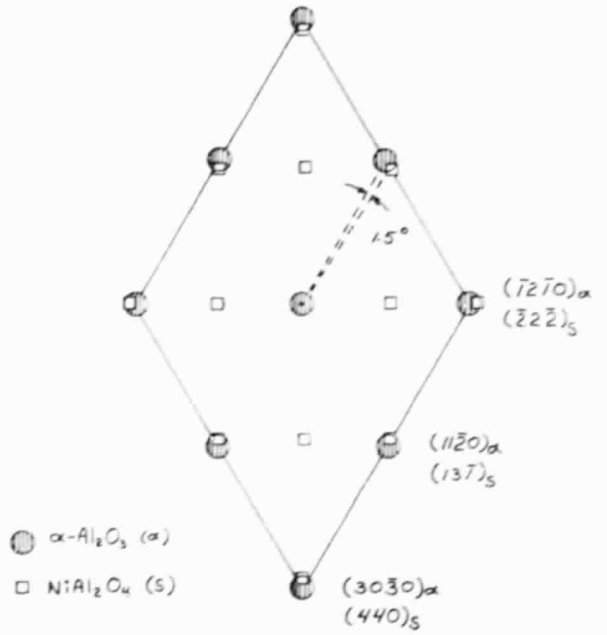

Figure 30. Oriented α-$(Al, Cr)_2O_3$ and Ni $(Al, Cr)_2O_4$ diffraction patterns; $(0001)_\alpha \parallel (\bar{1}12)_S$, $[10\bar{1}0]_\alpha \parallel [110]_S$, $[1120]_\alpha \parallel [13\bar{1}]_S$; foil tilted 3° from plane of oxidation.

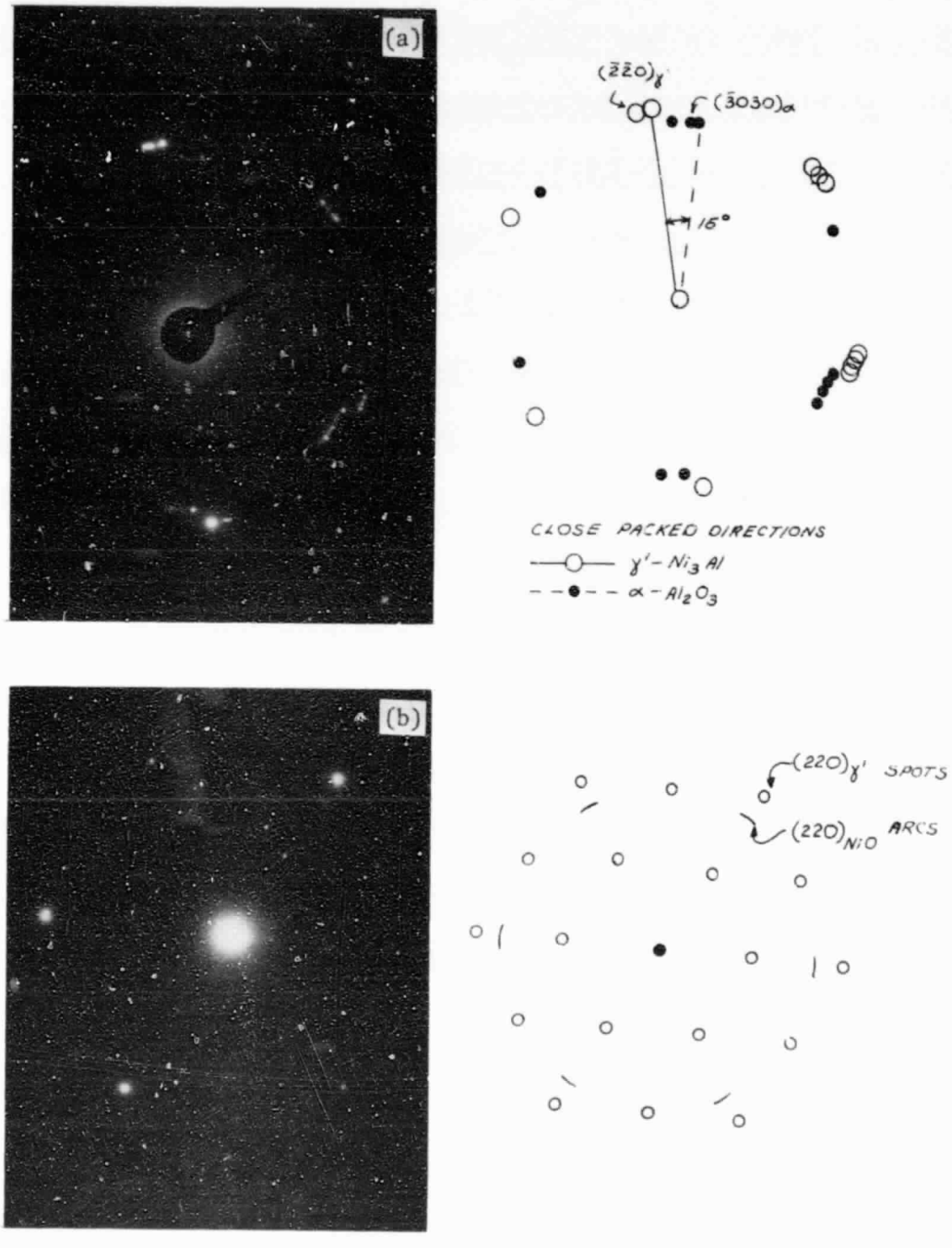

Figure 31. Possible epitaxy of oxides and metal in some areas.

a) coincident [0001]α -Al_2O_3 and [$\bar{1}$11] γ' patterns

b) coincident [$\bar{1}$11] zones and ⟨110⟩ directions of γ'-Ni_3Al and NiO.

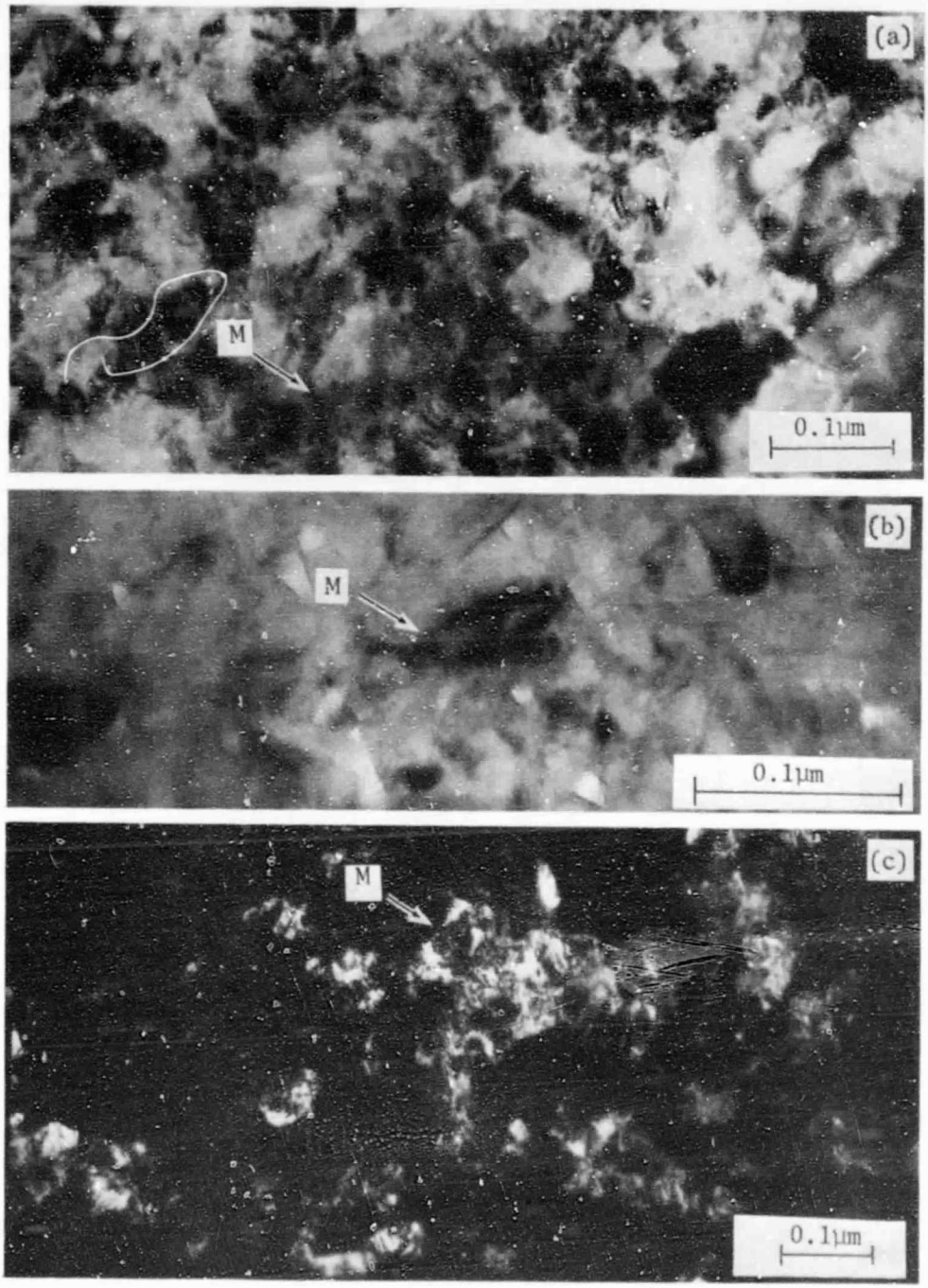

Figure 32. Colonies of Moire' patterns in the oriented scales.

a, b) bright field

c) dark field of a new area, $\vec{g} = (30\bar{3}0)_\alpha$

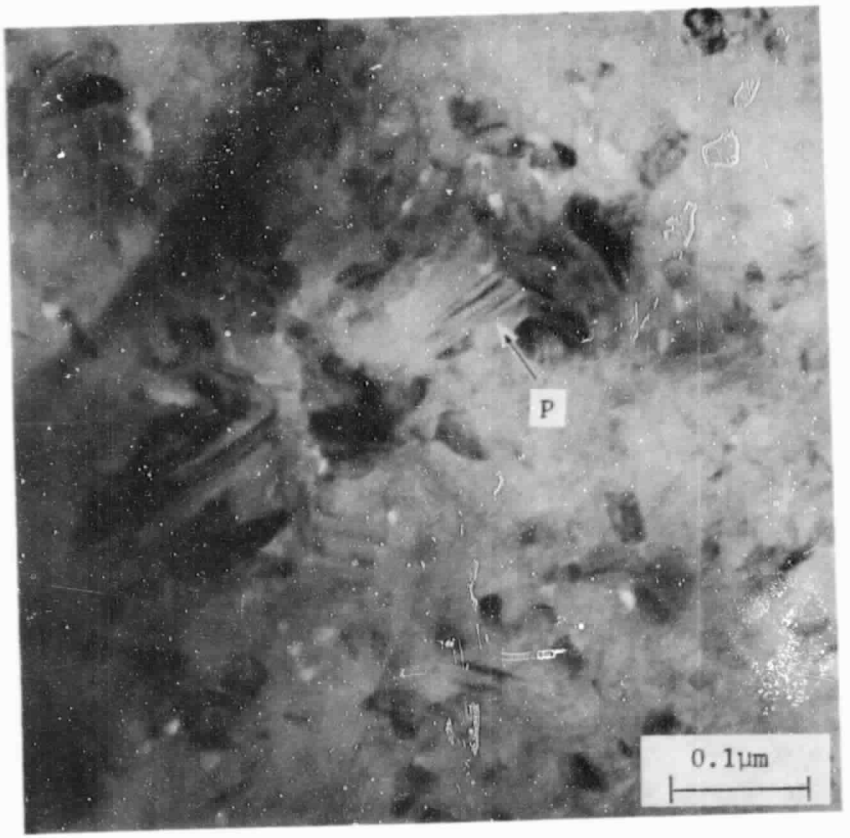

a) bright field

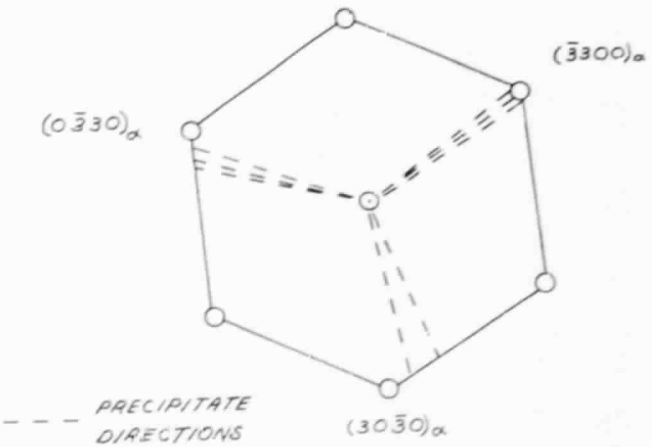

b) $\langle 10\bar{1}0\rangle$ precipitate directions in an [0001] α-Al_2O_3 zone

Figure 33. $\langle 10\bar{1}0\rangle$ precipitates in Al_2O_3.

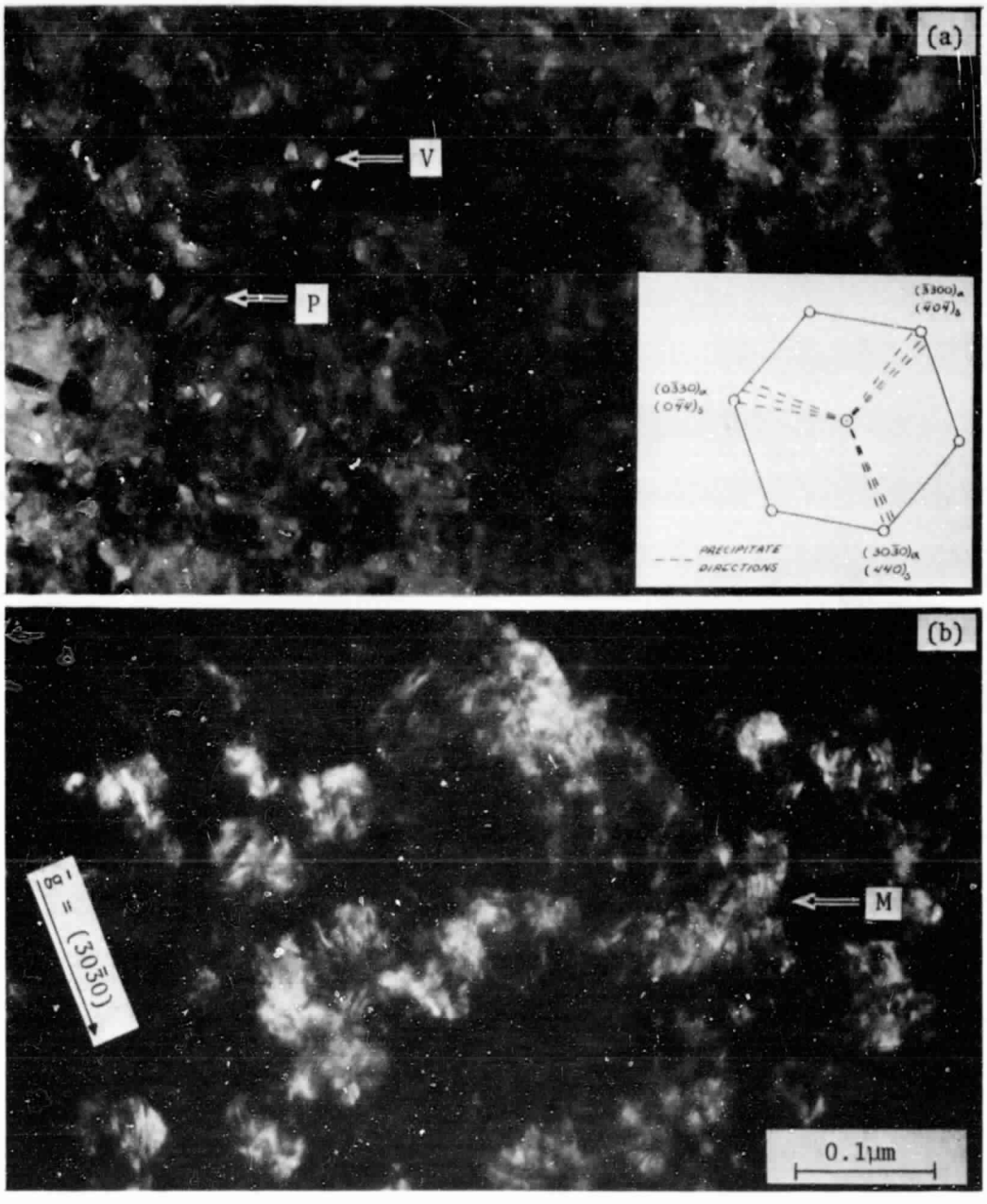

Figure 34. Precipitate directions, voids and Moire' patterns in the oriented α- $(Al, Cr)_2O_3$ scale.

a) bright field, precipitate directions

b) dark field, $\vec{g} = (30\bar{3}0)\alpha$; isolated subgrains resolved

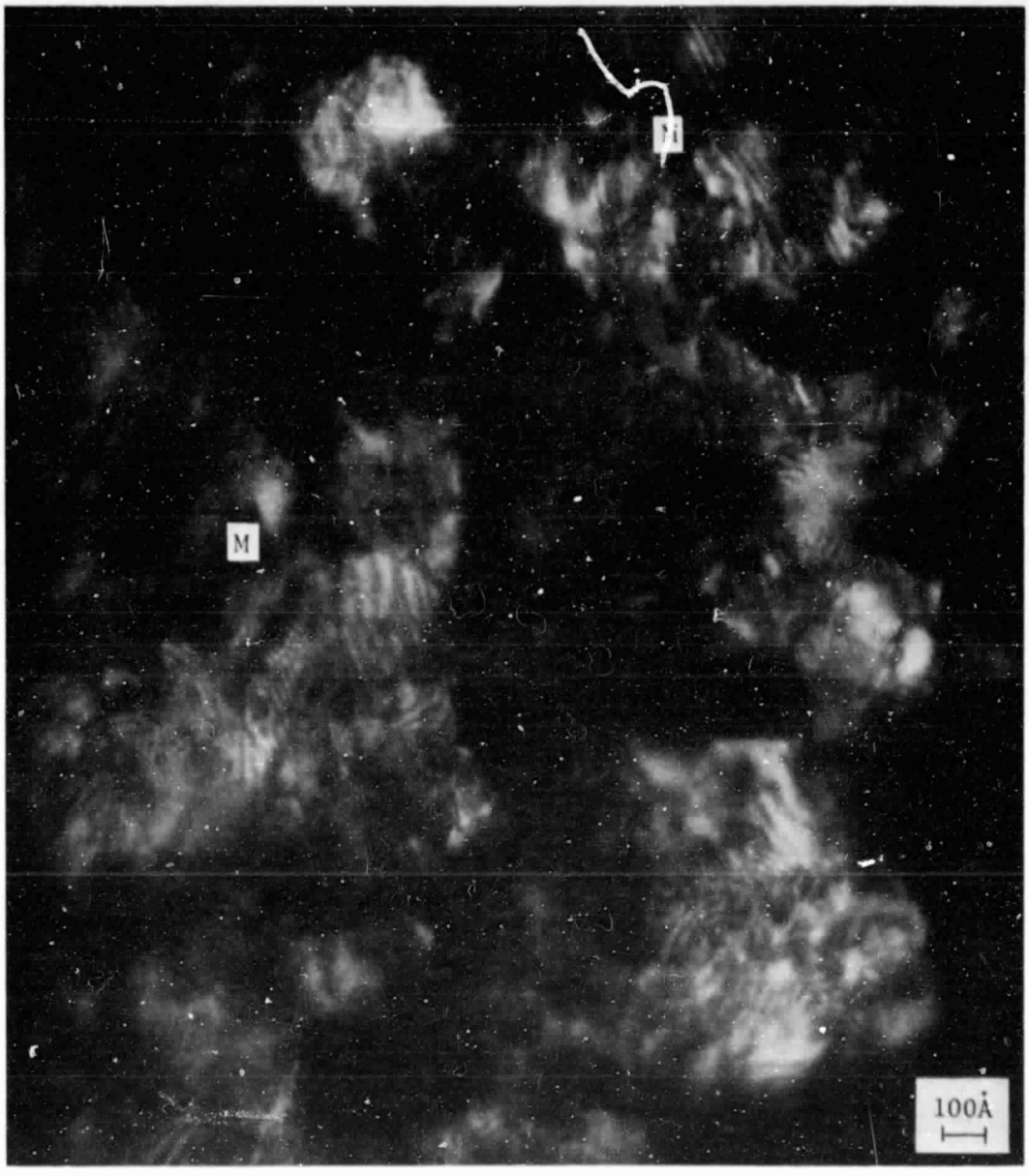

Figure 34c. fine Moire' patterns in α-$(Al, Cr)_2O_3$ subgrains; enlarged from Figure 34b.

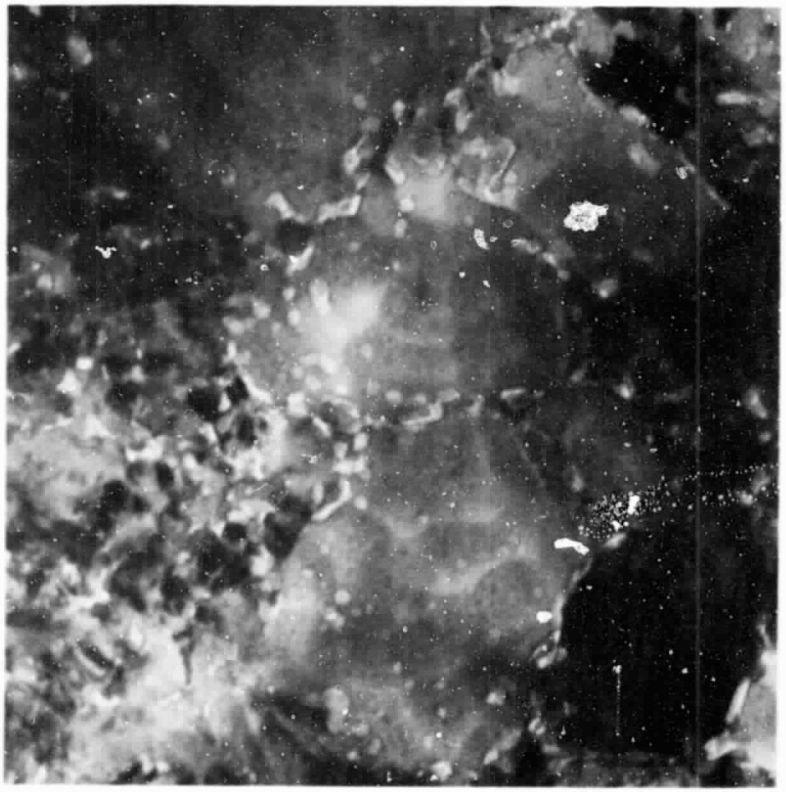

ORIENTED Al_2O_3

0.1 μm

Figure 35. Large grains and porosity in oriented Al_2O_3.

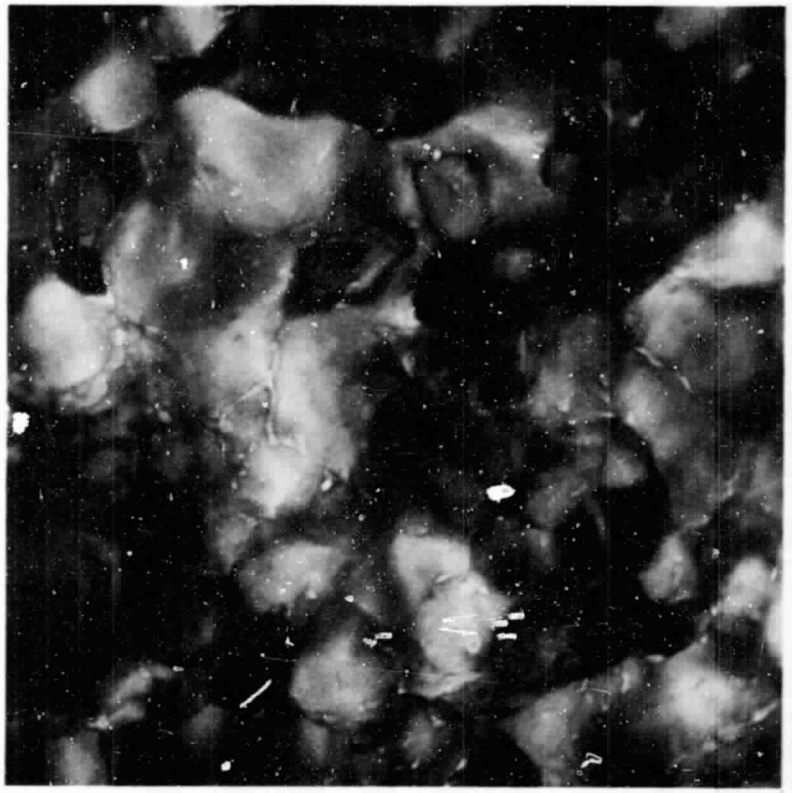

RANDOM Al_2O_3 CS-78-3809

Figure 36. Intergranular porosity in random Al_2O_3.

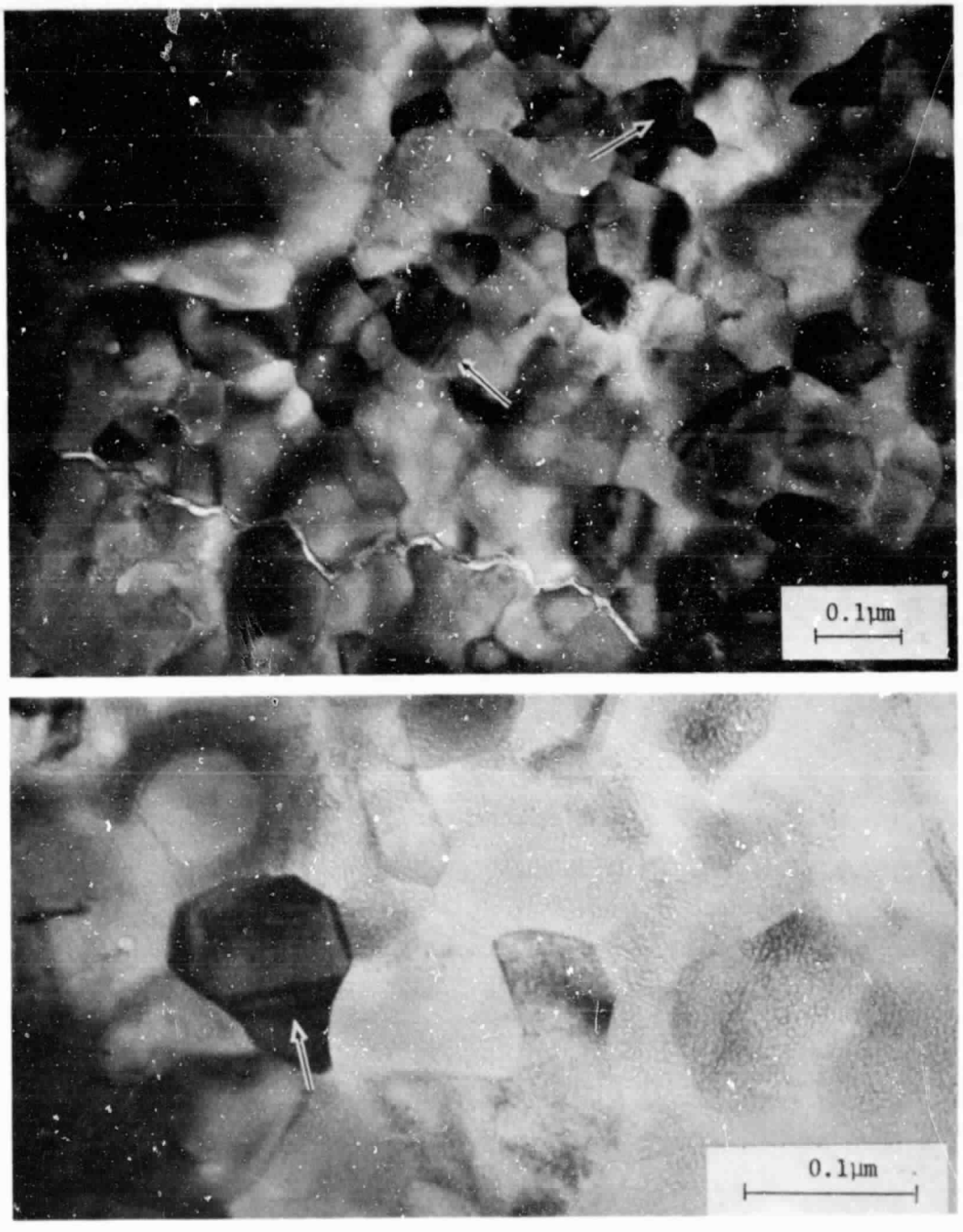

Figure 37. Lineal defects in random α-Al_2O_3 grains.

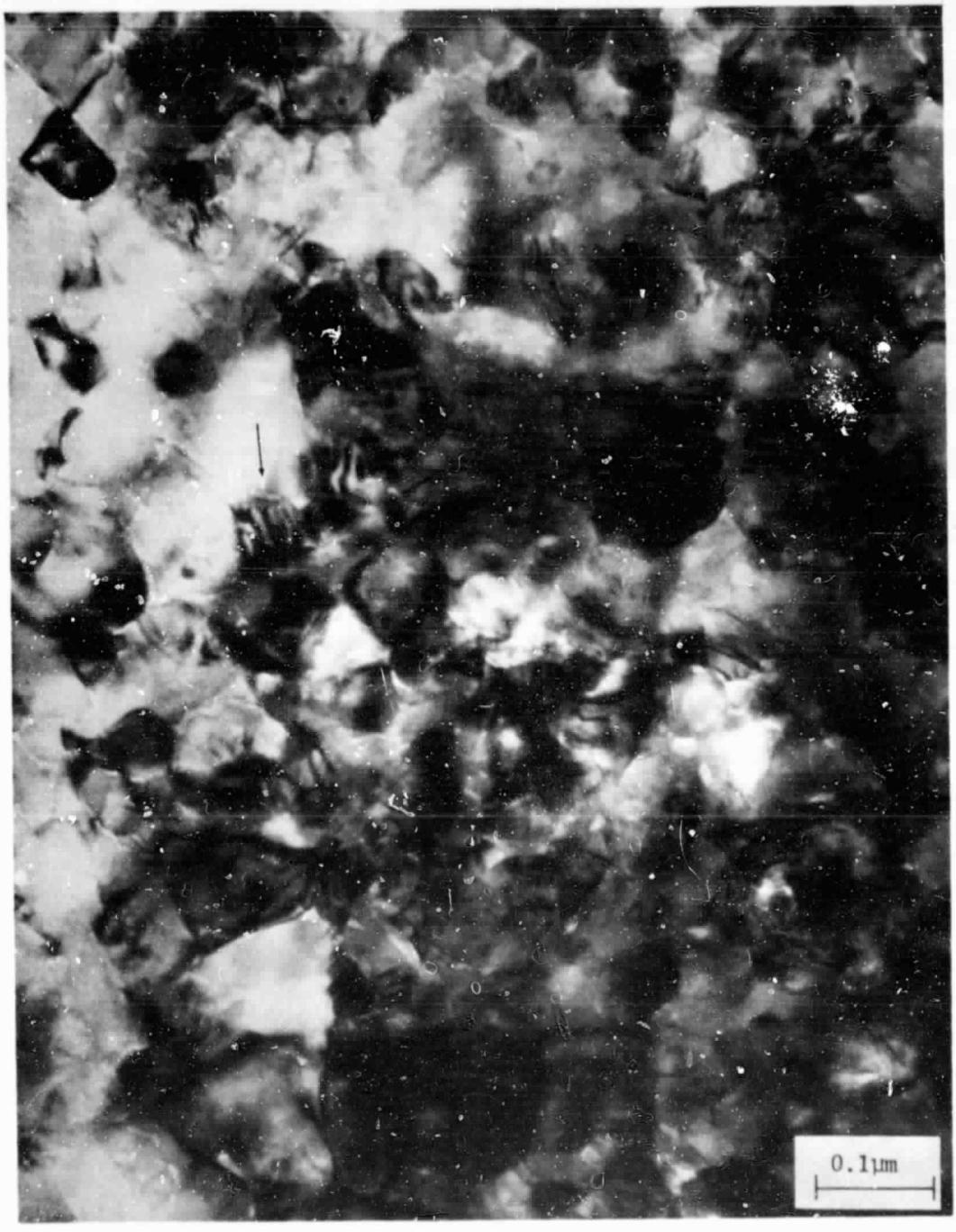

Figure 38. Moire' fringes (or strain patterns) in a thick area of the random α-Al_2O_3 scale.

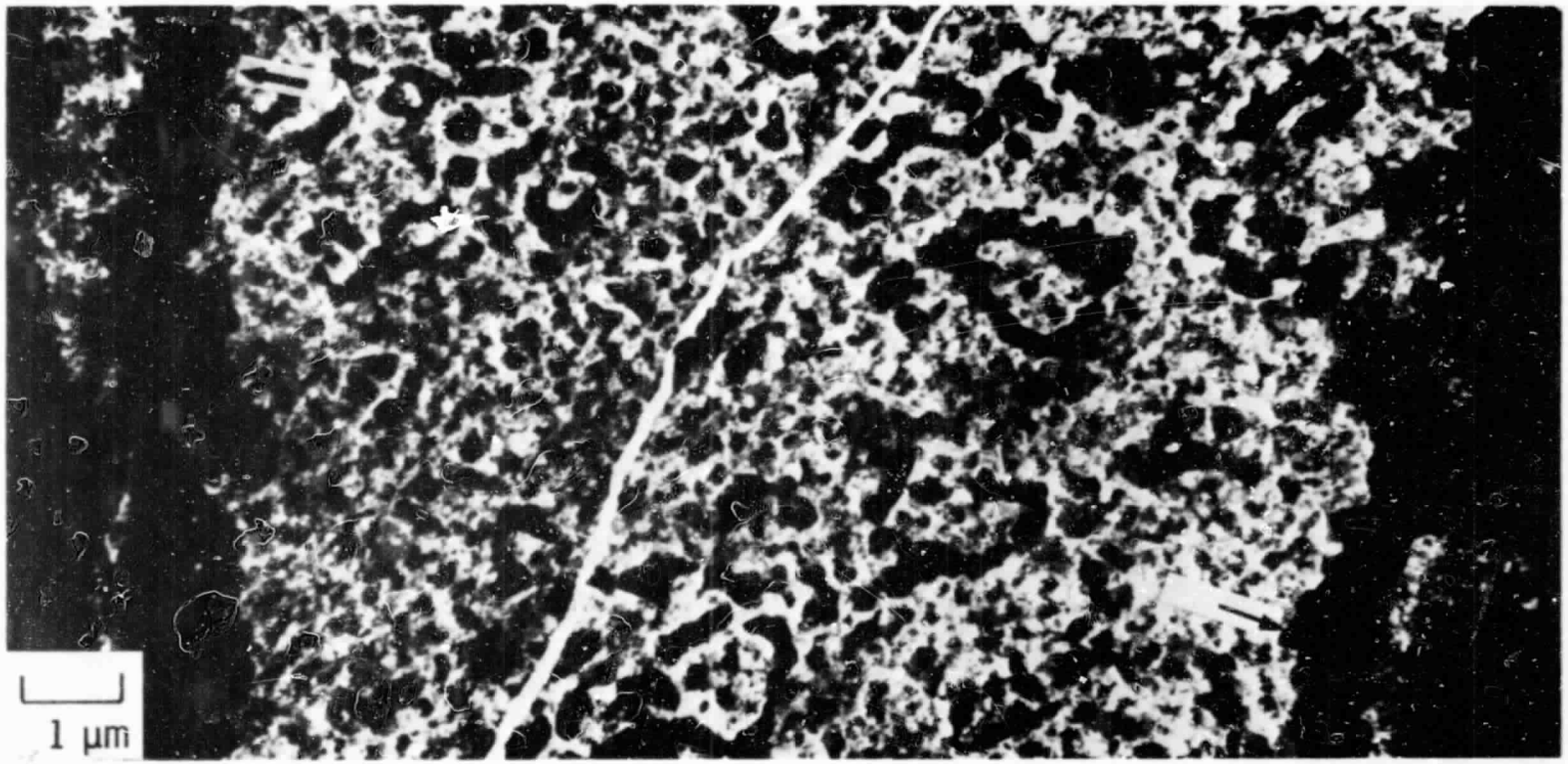

CS-78-3808

Figure 39. Irregular nature of the oriented scale formed on NiCrAl+Zr after 0.1 hr at 1100°C; as-electropolished.

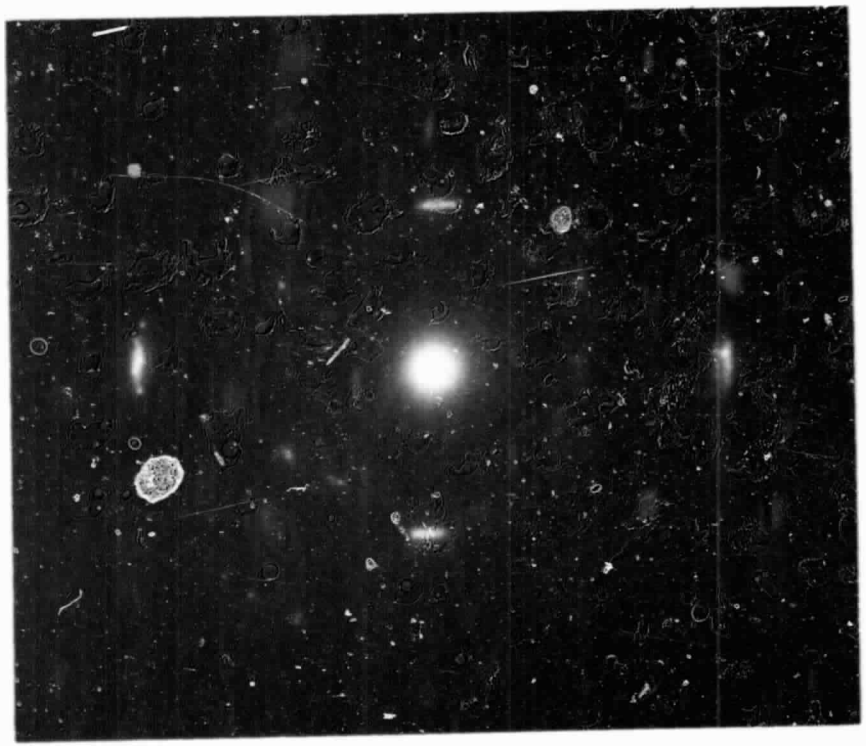

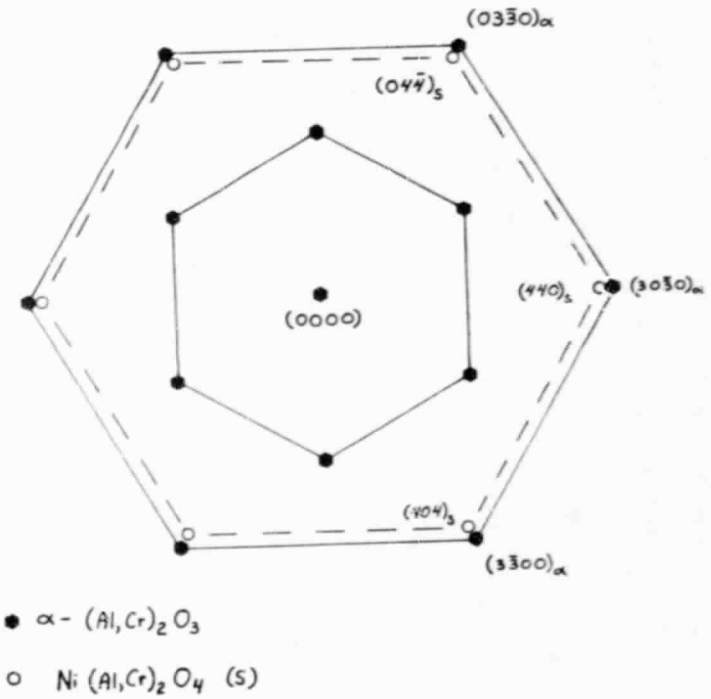

Figure 40. Phase identification in the oriented scale.

a) superimposed [0001] α-$(Al, Cr)_2O_3$ and [$\bar{1}$11] $Ni(Al, Cr)_2O_4$ zones; no ion thinning.

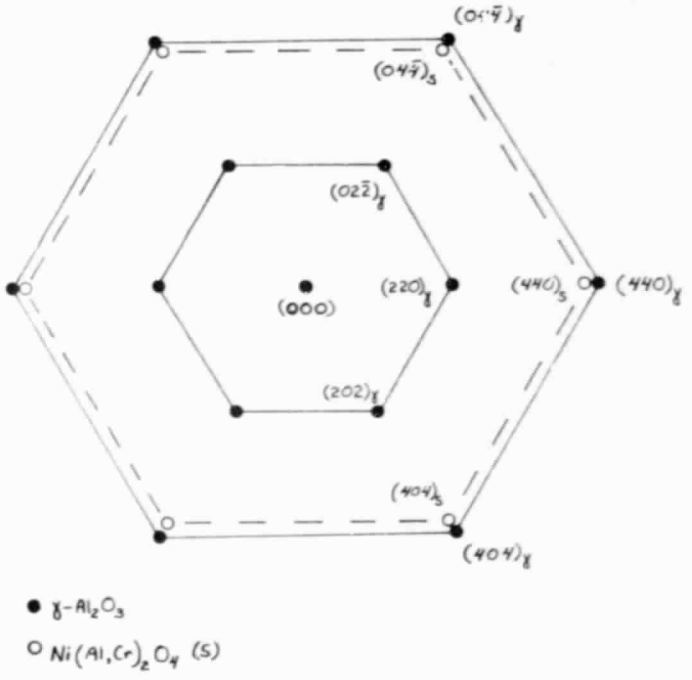

Figure 40b. superimposed $[\bar{1}11]$ γ-Al_2O_3 and $Ni(Al, Cr)_2O_4$ zones; ion thinned 10 minutes.

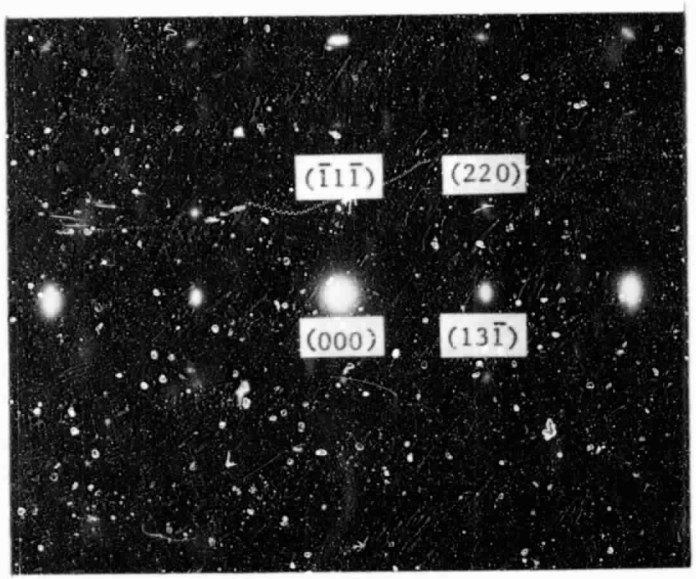

ion thinned 10 minutes

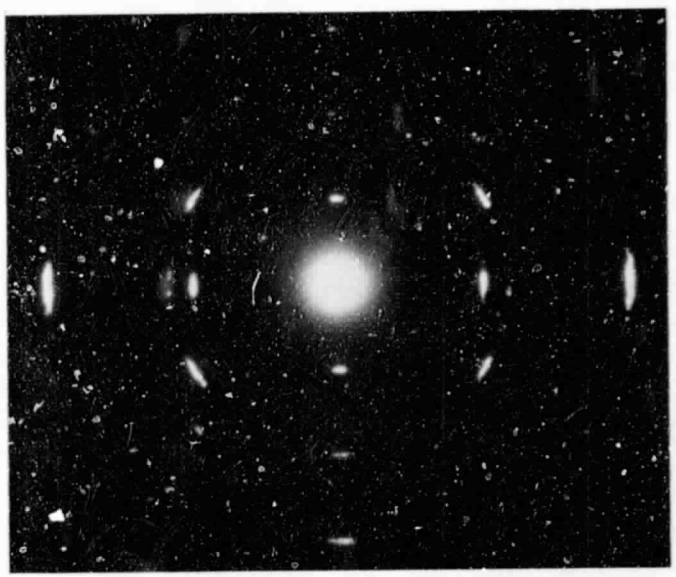

ion thinned 20 minutes

Figure 40c. [1̄12] γ-Al_2O_3 zone.

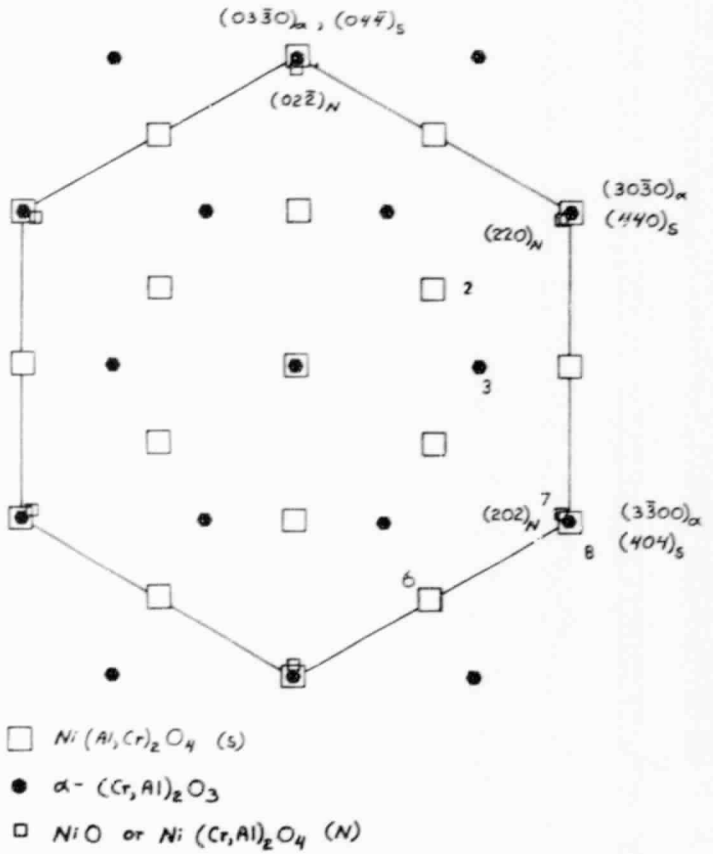

Figure 40d. [0001] rhombohedral and [$\bar{1}$11] cubic oxide zones for NiCrAl oxidized at 900°C, Ref 14.

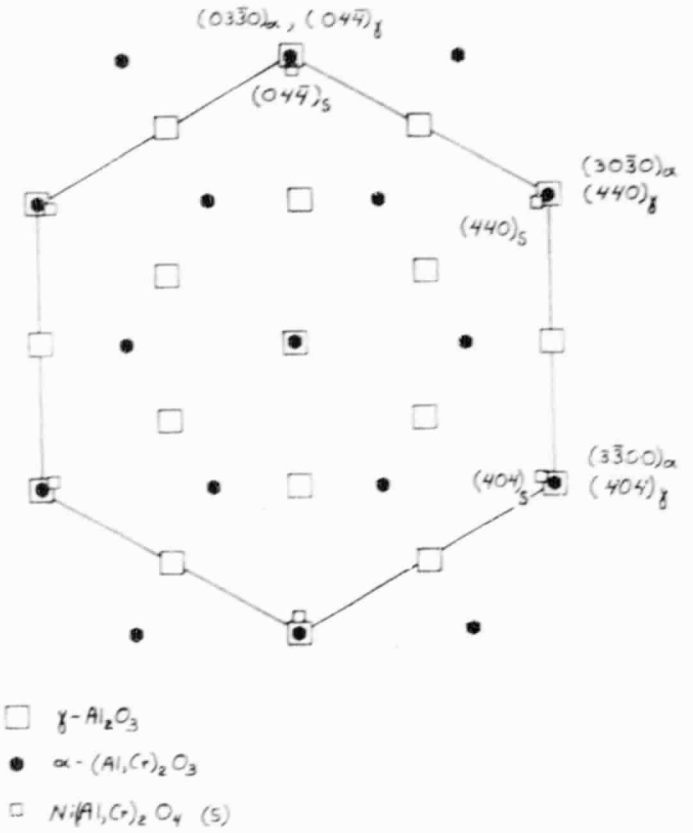

Figure 40e. combined patterns of (a) and (b) yield a composite of $[0001]_\alpha$, $[\bar{1}11]_S$, and $[\bar{1}11]_\gamma$ similar to the pattern in (d).

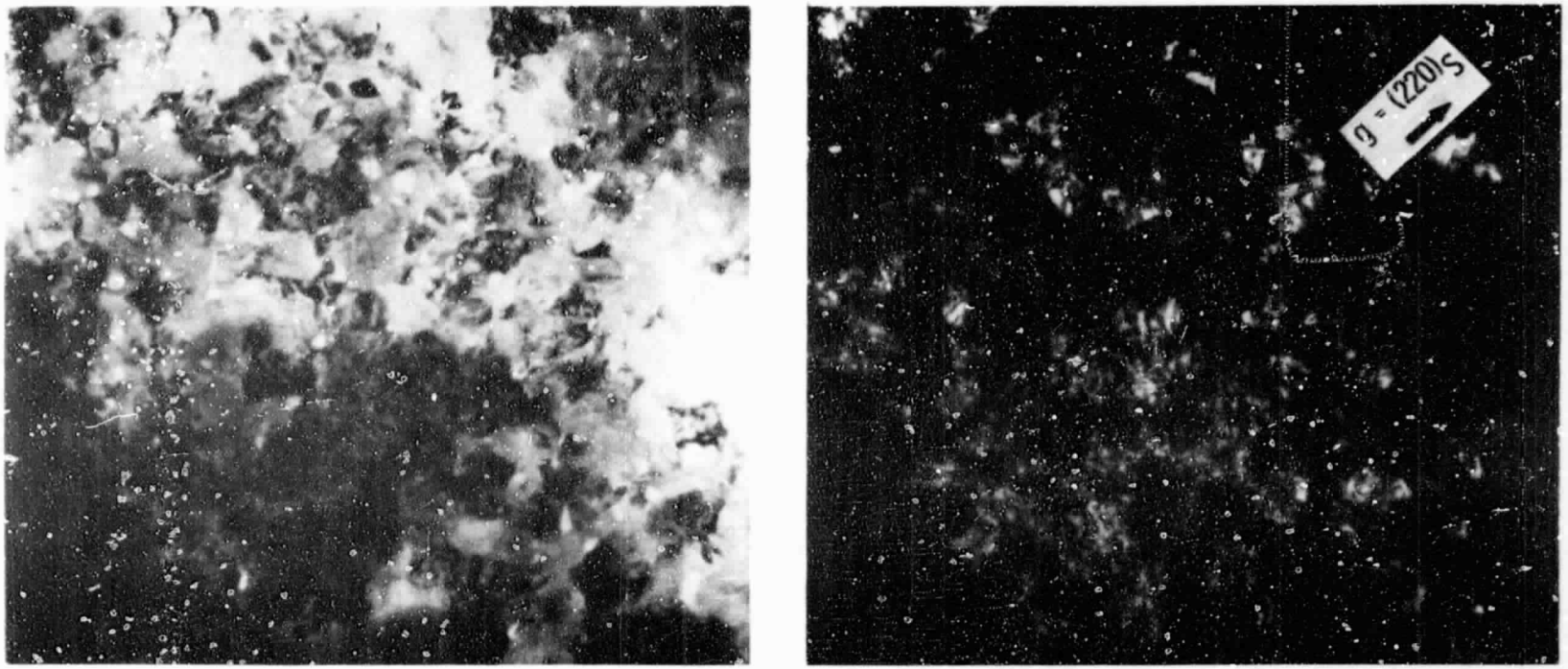

a) bright field

b) dark field, $\vec{g} = (220)$

Figure 41. Mosaic of fine subgrains in oriented γ-Al_2O_3 scale.

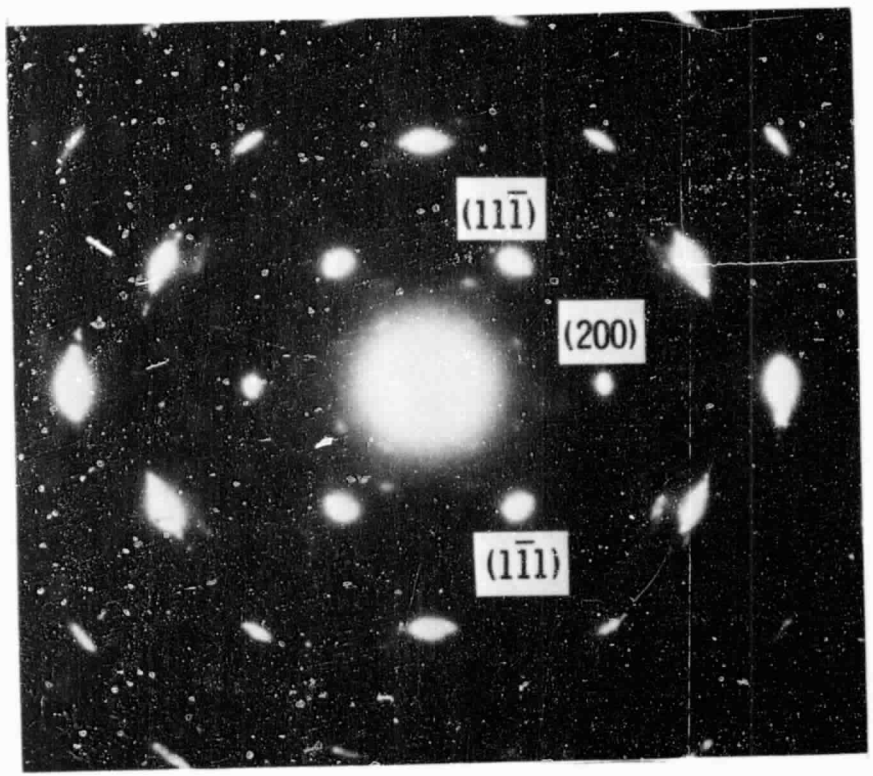

CS-80-3809

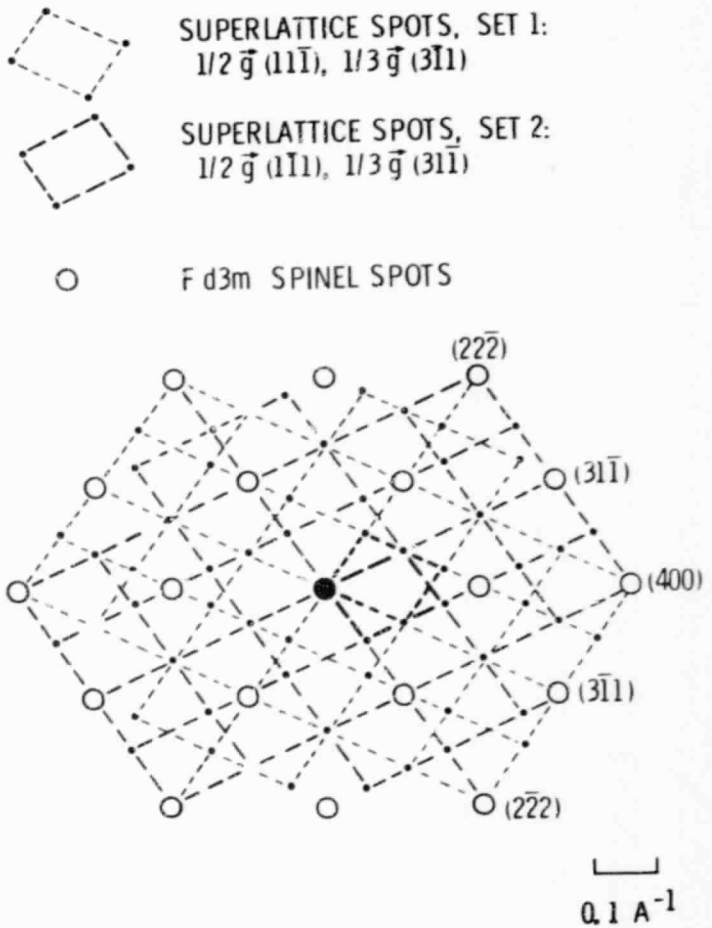

Figure 42. Superlattice reflections in an [011] γ-Al_2O_3 scale; foil tilted 5.8°.

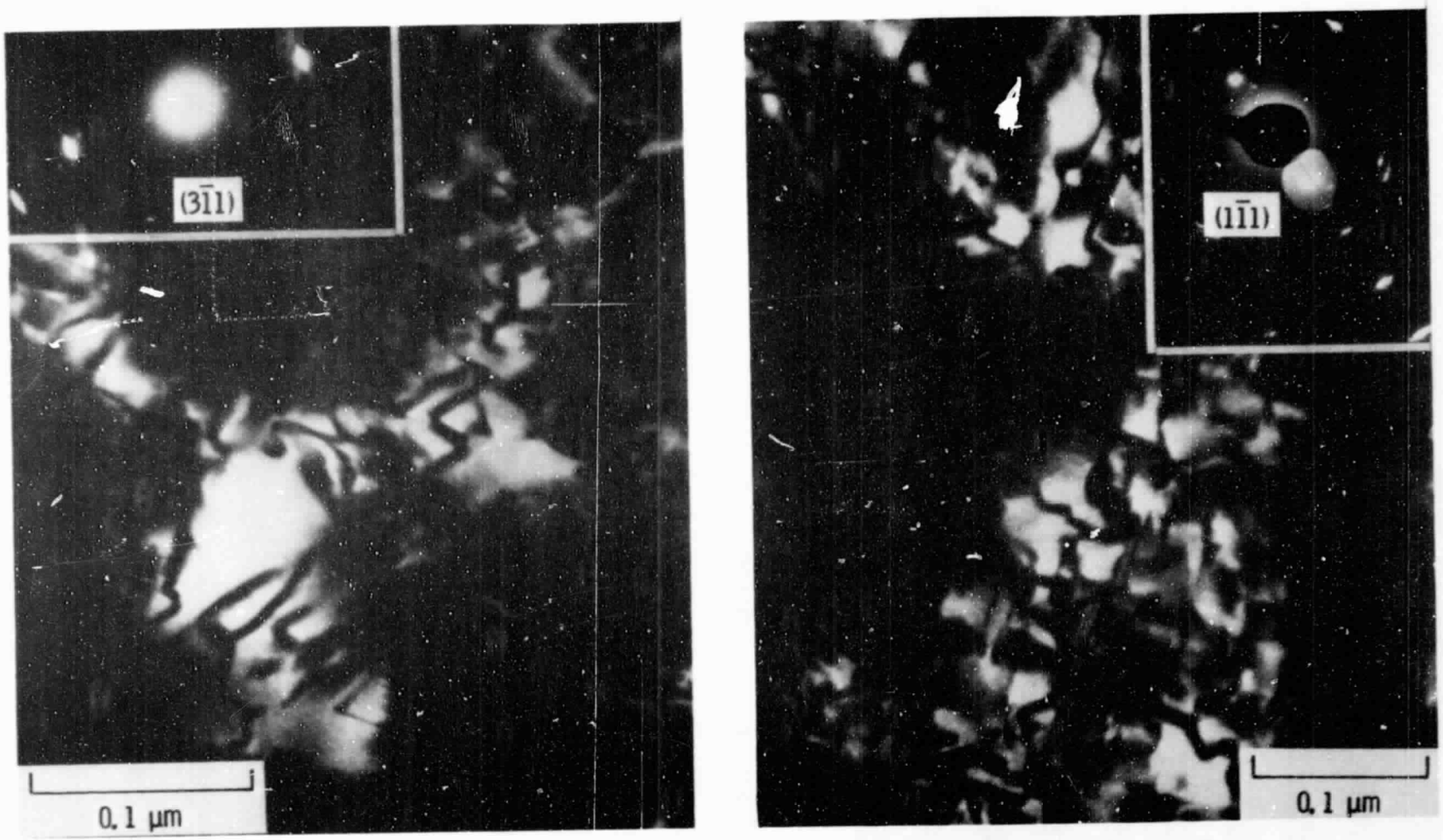

DARK FIELD, g = (3$\bar{1}$1) DARK FIELD, g = (1$\bar{1}$1) CS-78-3806

Figure 43. Antiphase domain boundaries in an [011] γ-Al_2O_3 scale.

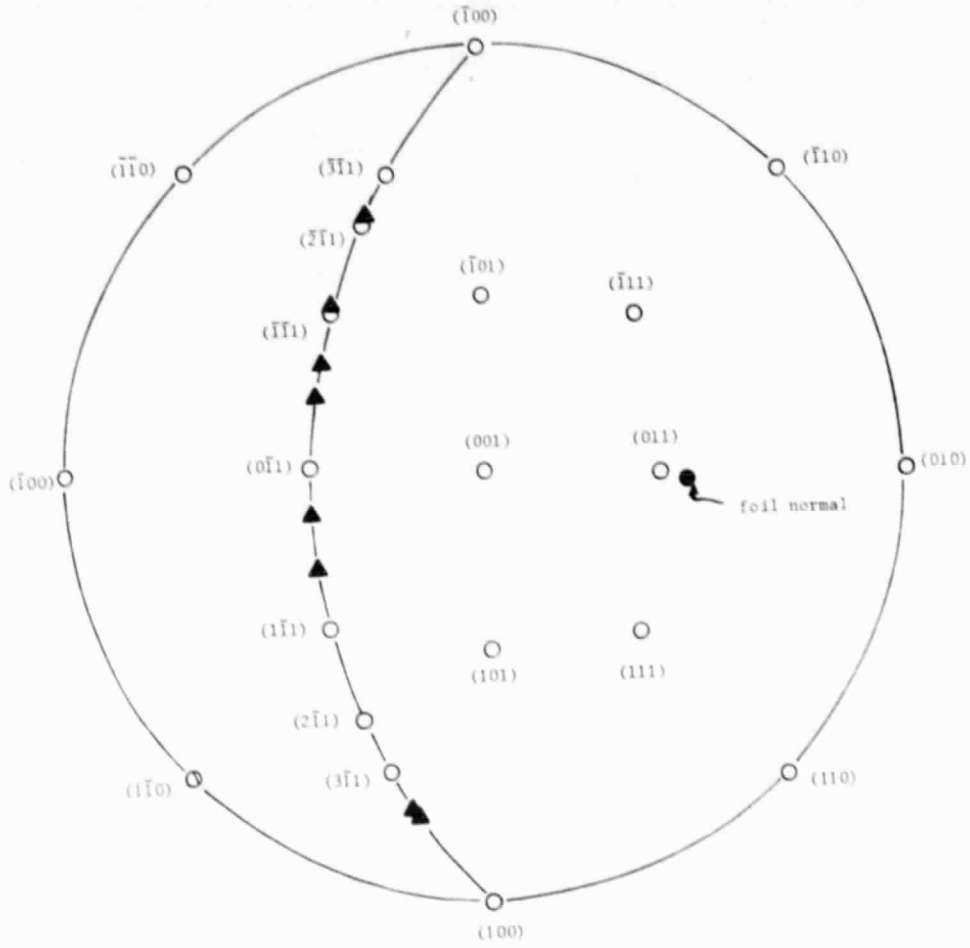

Figure 44. Projected directions of APB's (▲) in [011] oriented γ-Al_2O_3 scale (from Figure 43.)

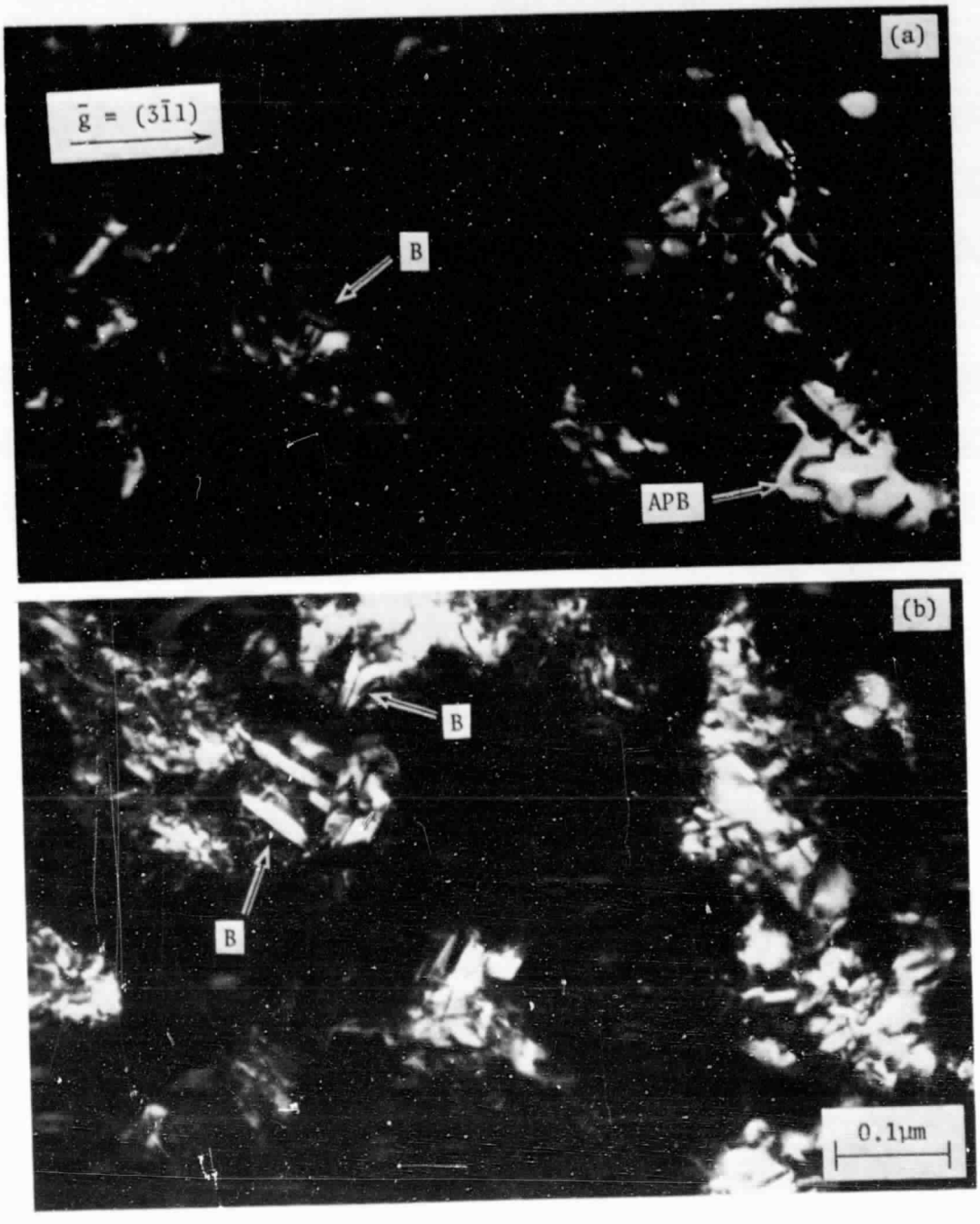

Figure 45. Planar deflects in [011] oriented γ-Al_2O_3; dark field, $\underset{\sim}{g} = (3\bar{1}1)$.

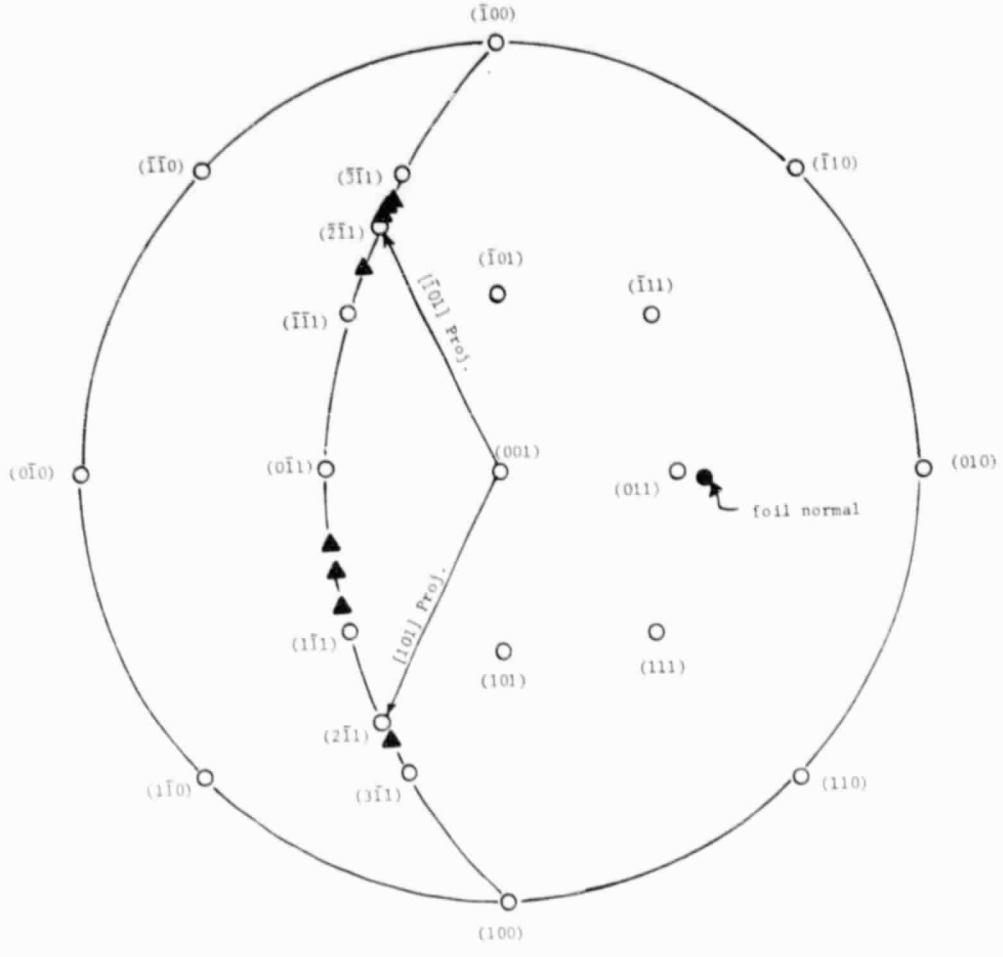

Figure 46. Projected precipitate directions (▲) in [011] oriented γ-Al_2O_3 scale (from Figure 45.)

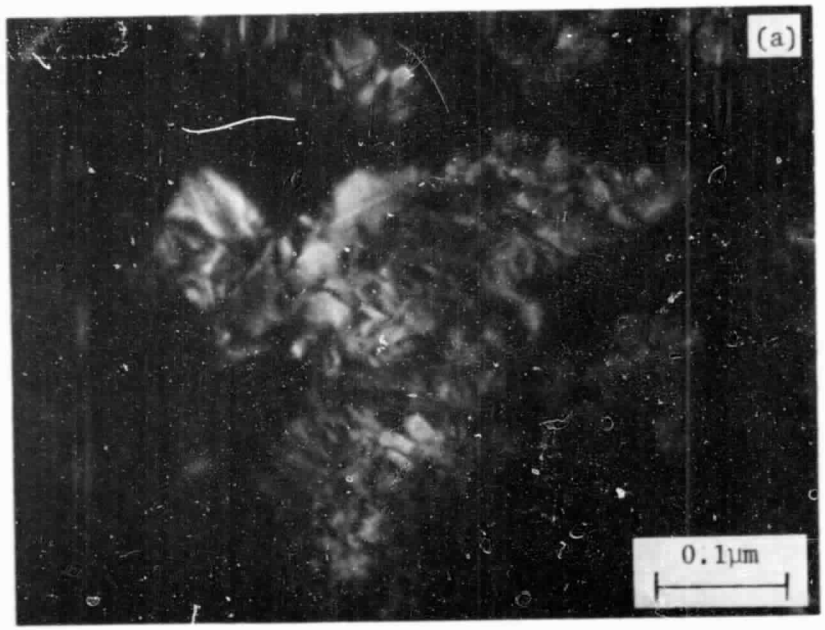

a) dark field, $\vec{g}$ = (220), $\vec{B} \sim [\bar{1}12]$.

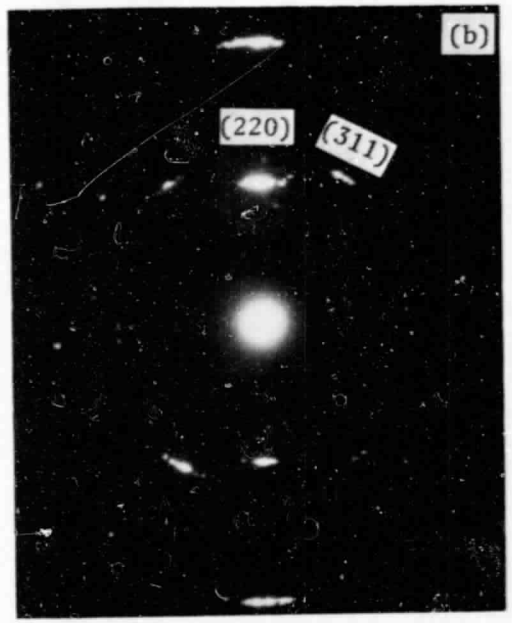

b) $[\bar{1}12]$ pattern showing extra spots around $\vec{g}$ = (220).

Figure 47. Parallel precipitates and Moire' fringes in a subgrain of $[\bar{1}12]$ oriented γ-Al_2O_3; foil tilted 0.2°.

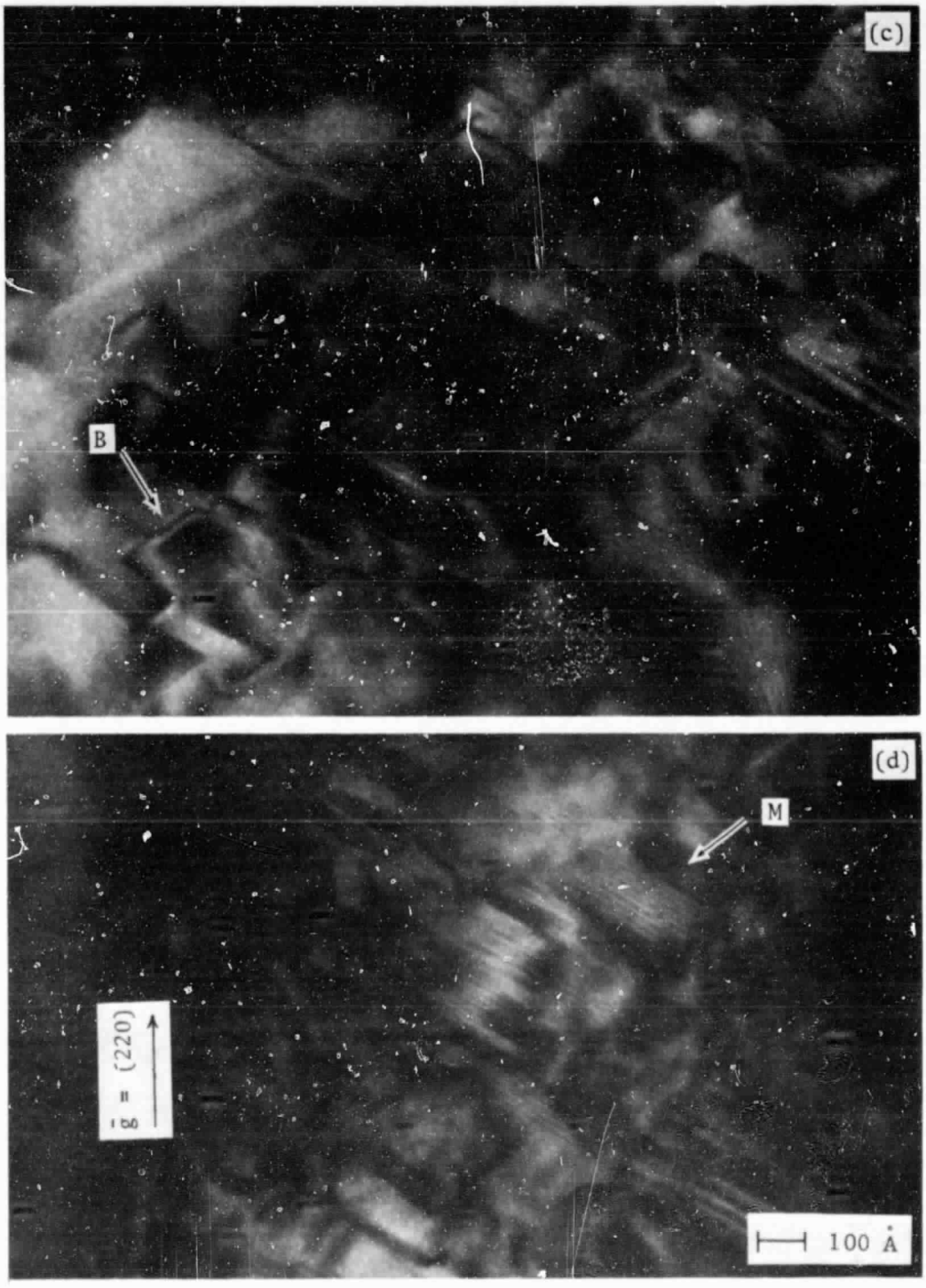

Figure 47c, 47d. enlargements of upper and lower portions of subgrain in (a), showing ~15Å precipitates and Moire' fringes.

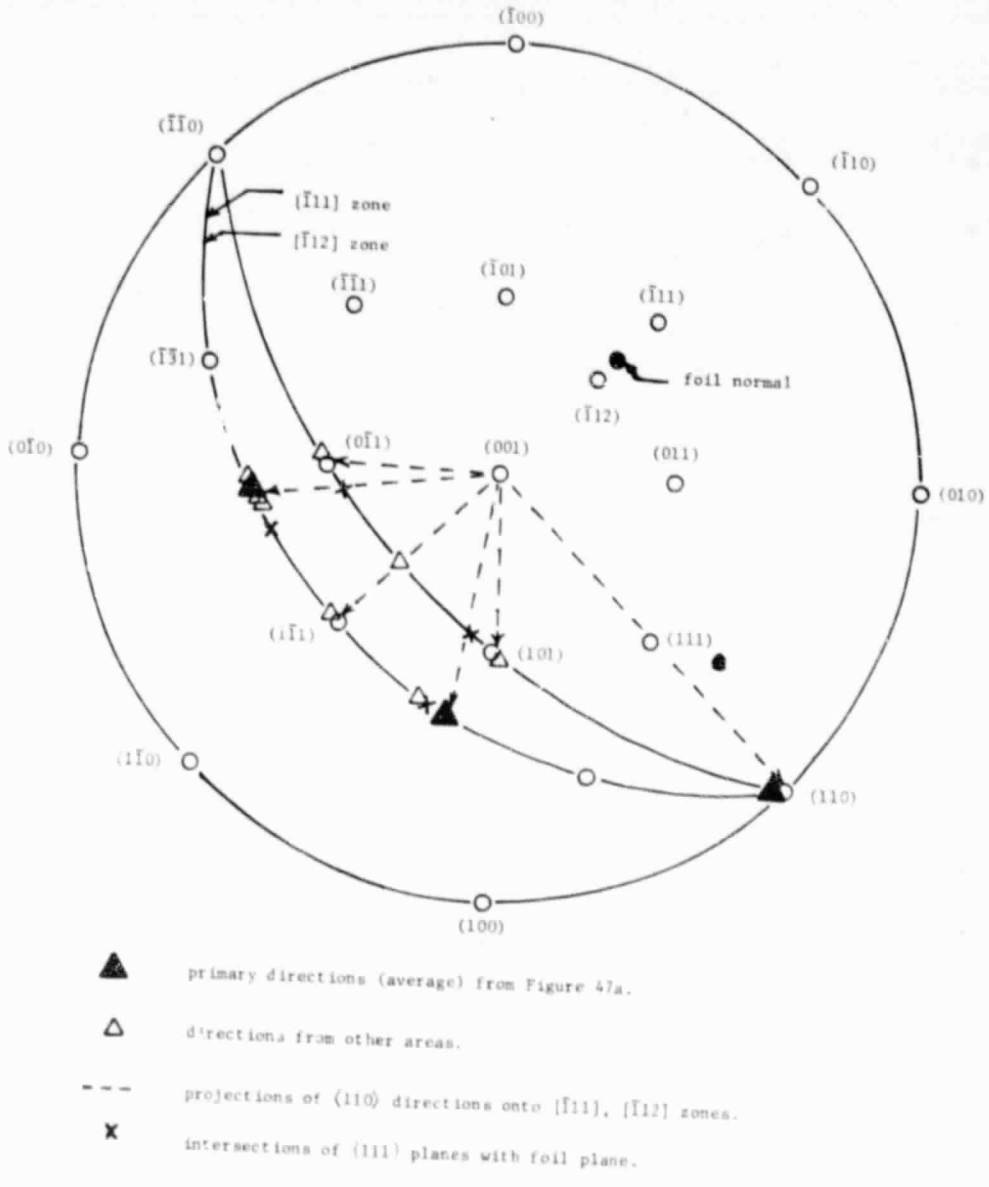

Figure 48. Projected directions of fine precipitates and Moire' fringes in [1̄12] oriented γ-Al_2O_3.

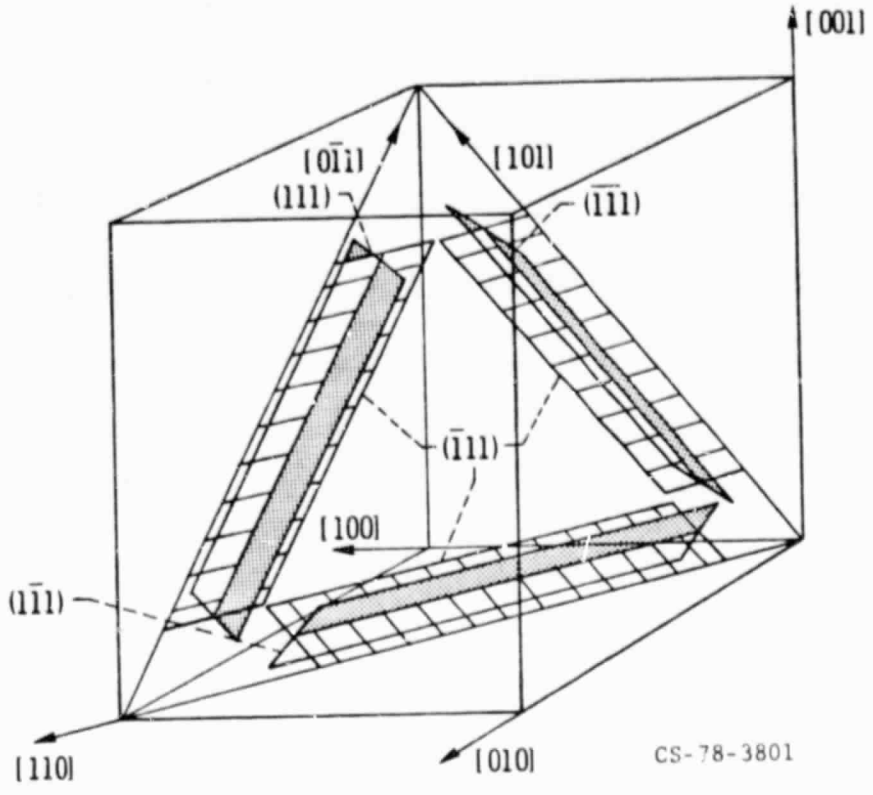

Figure 49. Proposed {111} ⟨110⟩ blade morphology for fine precipitates in γ-Al_2O_3 scale.

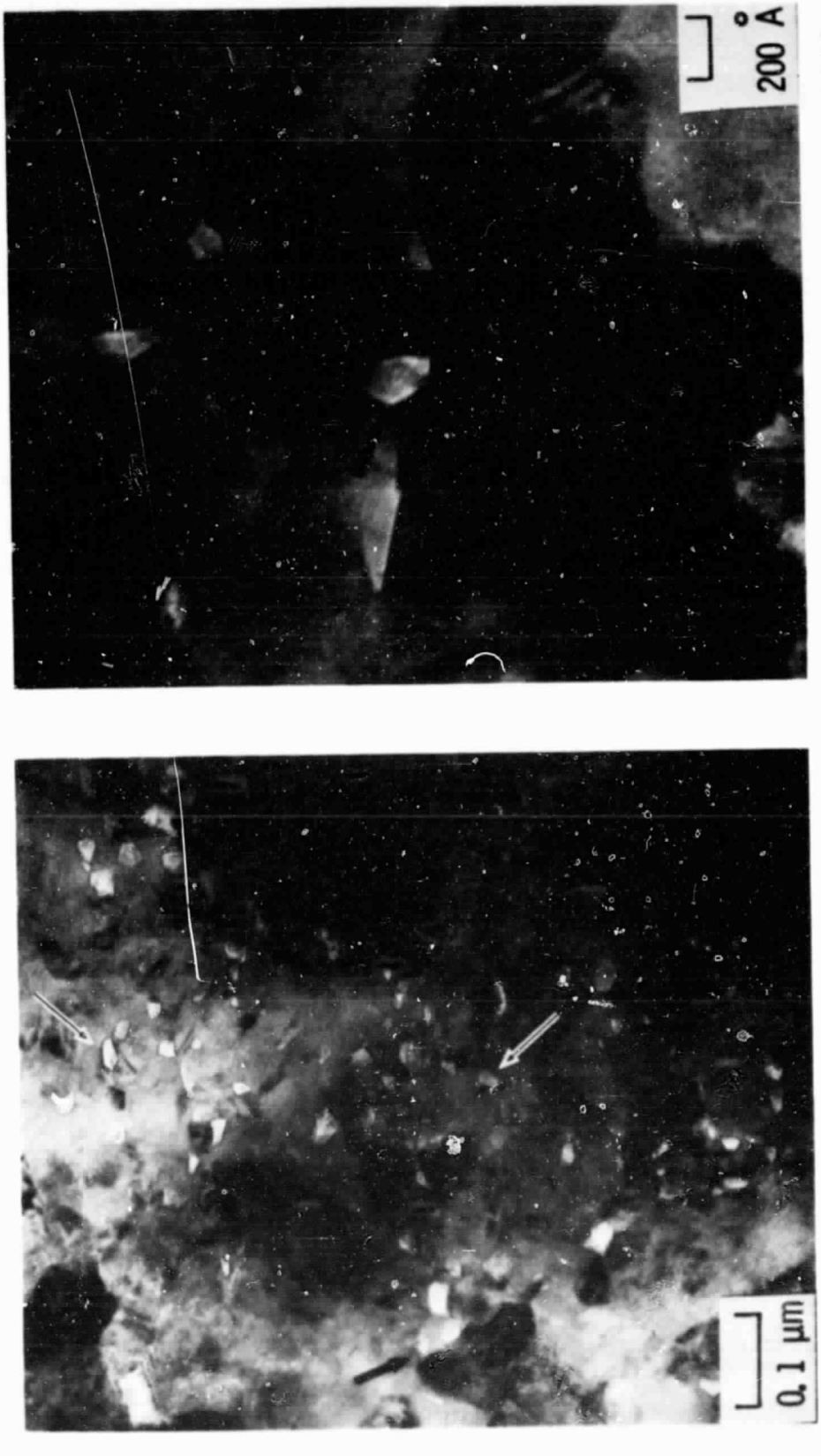

CS-78-3810

Figure 50. Faceted voids in [$\bar{1}12$] oriented γ-Al_2O_3

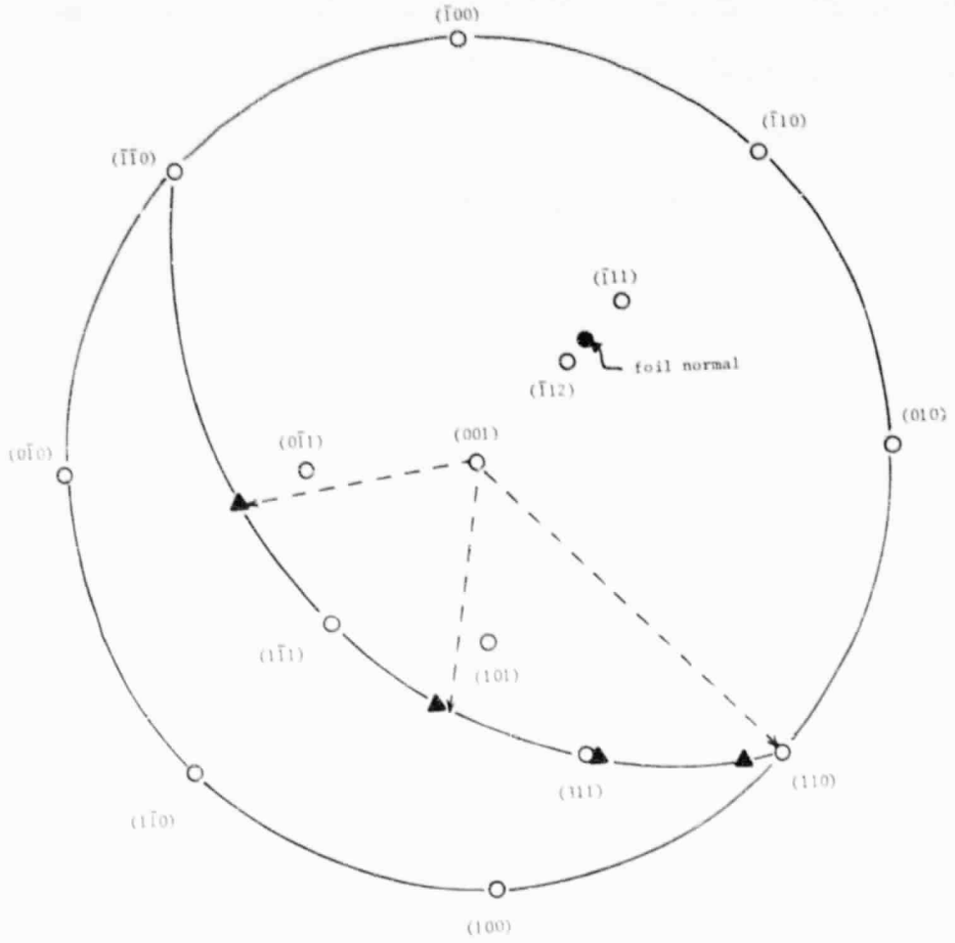

Figure 51. Projections of void facets in [$\bar{1}12$] oriented γ-Al_2O_3 (from Figure 50.).

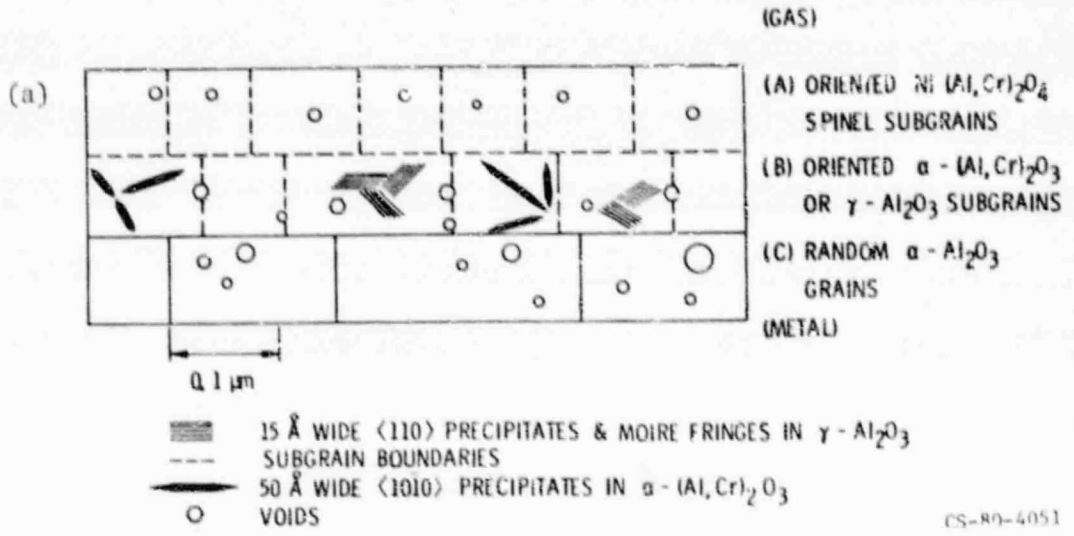

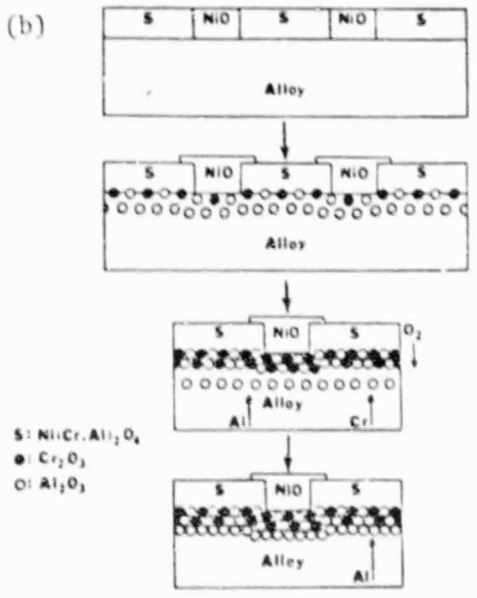

Figure 52. Schematic cross-sections of transient oxides on NiCrAl alloys.

a) various layers observed in this study
b) oxidation sequence according to ref. 13.

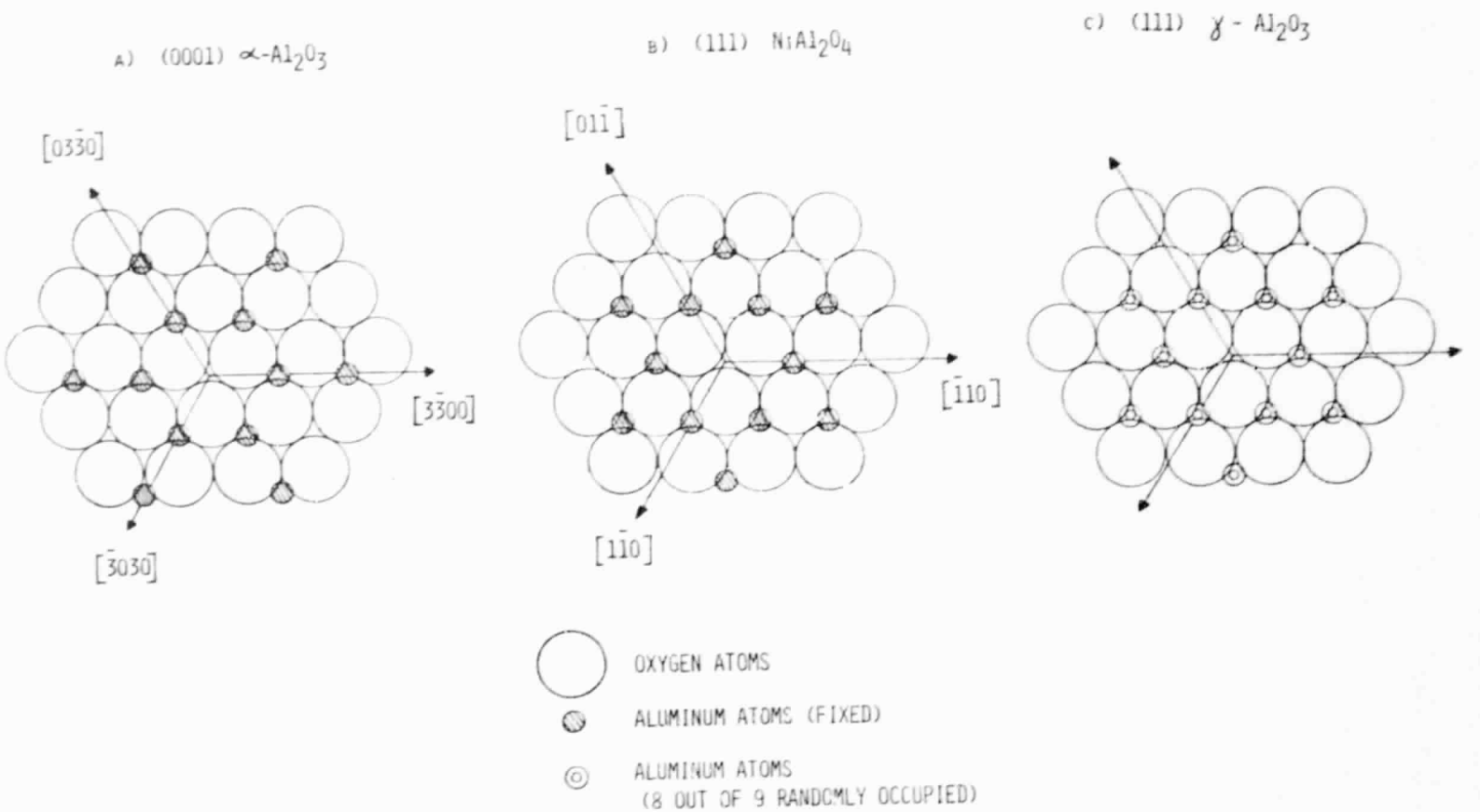

Figure 53. Comparison of close-packed planes of rhombohedral and cubic oxides of aluminum.

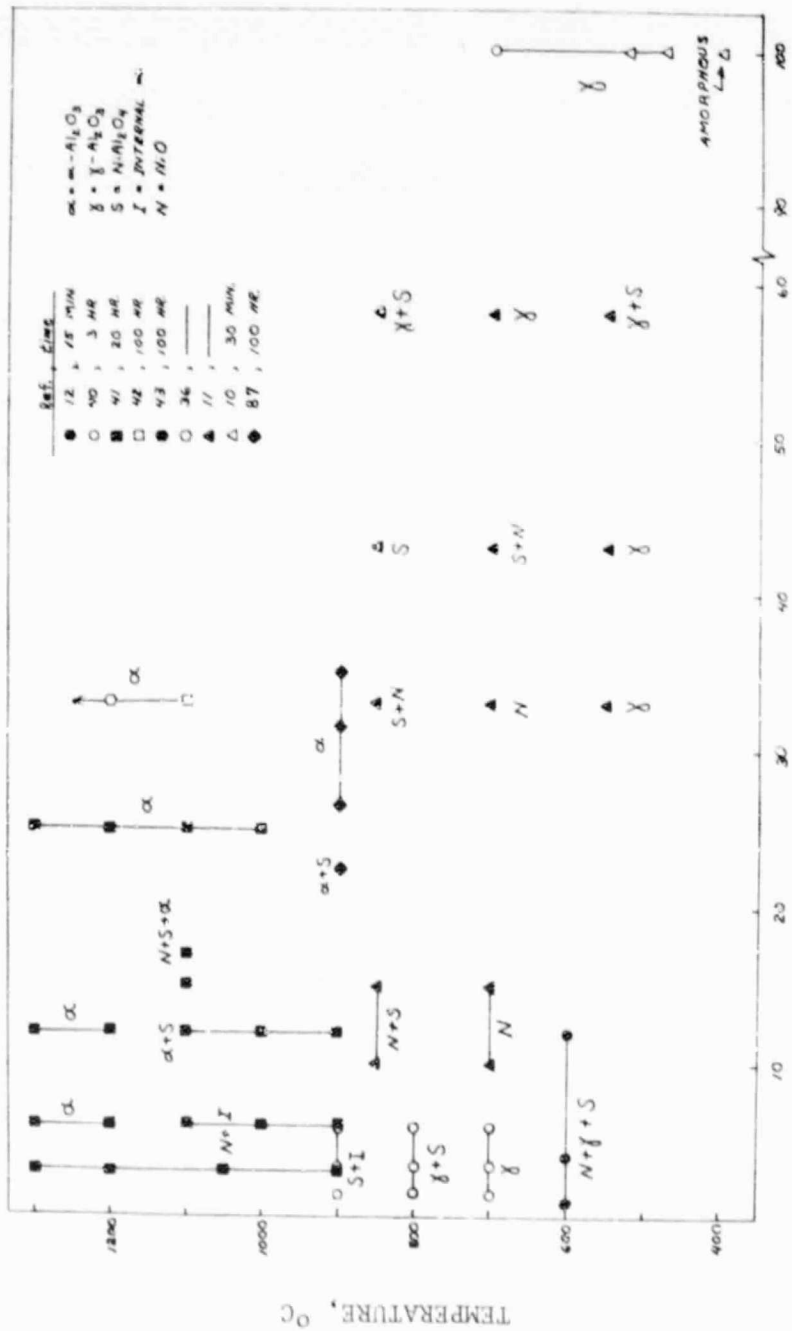

Figure 54. a) compilation of oxide phases observed on Ni-Al alloys.

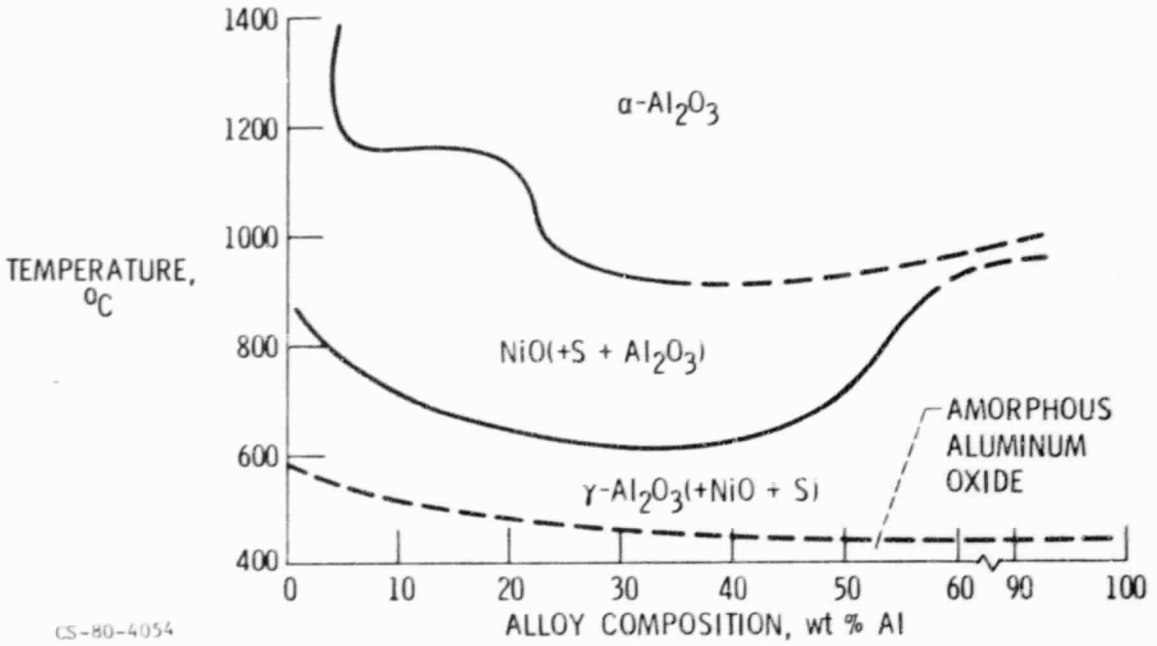

Figure 54b. Composite oxide map of the Ni-Al system based on the data in figure 54a.

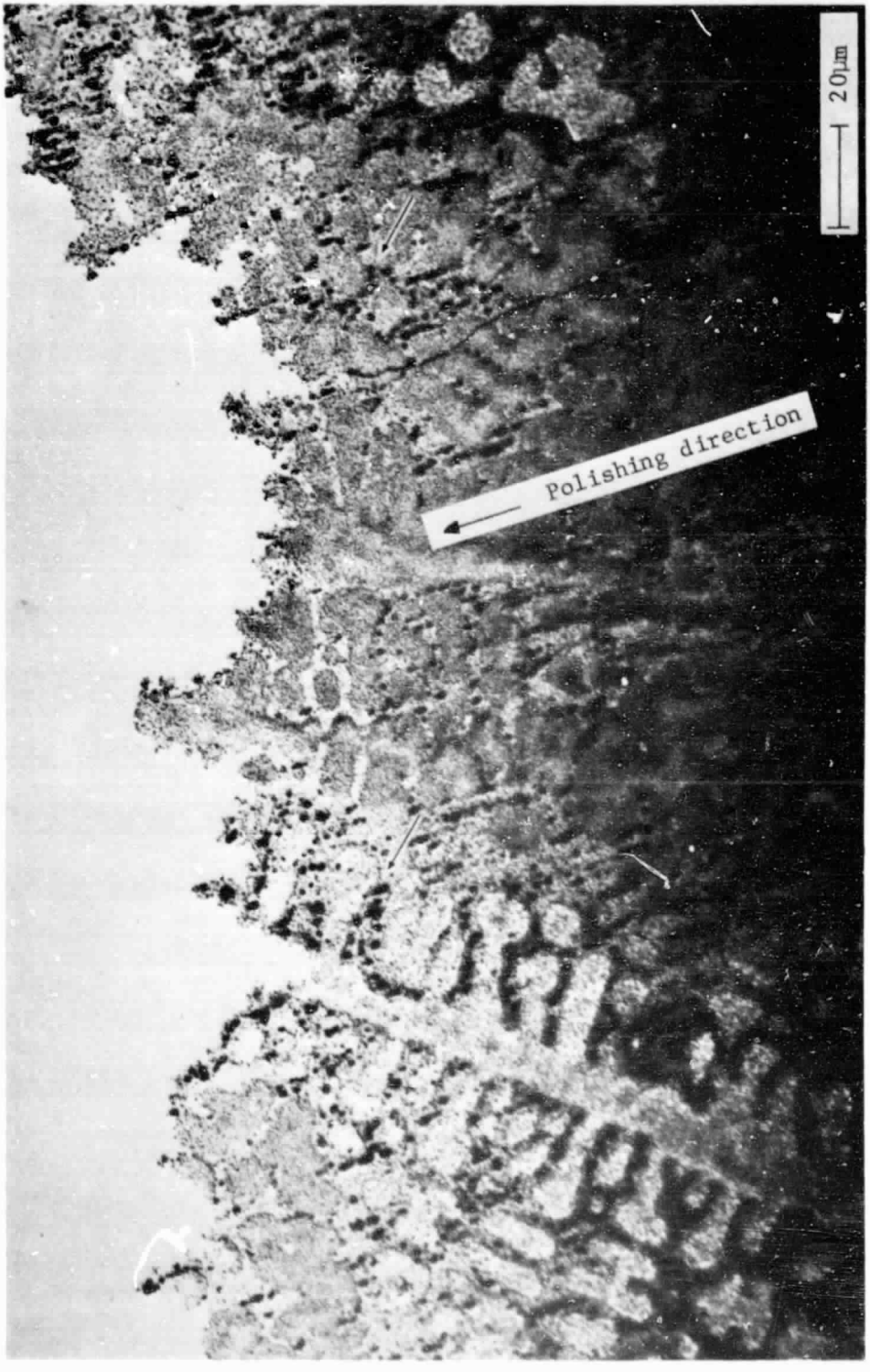

Figure 55. Overview of spalled oxide scale showing replication of dendritic structure and polishing scratches in the metal. (undoped NiCrAl, 1.0 hr., 1100°C)

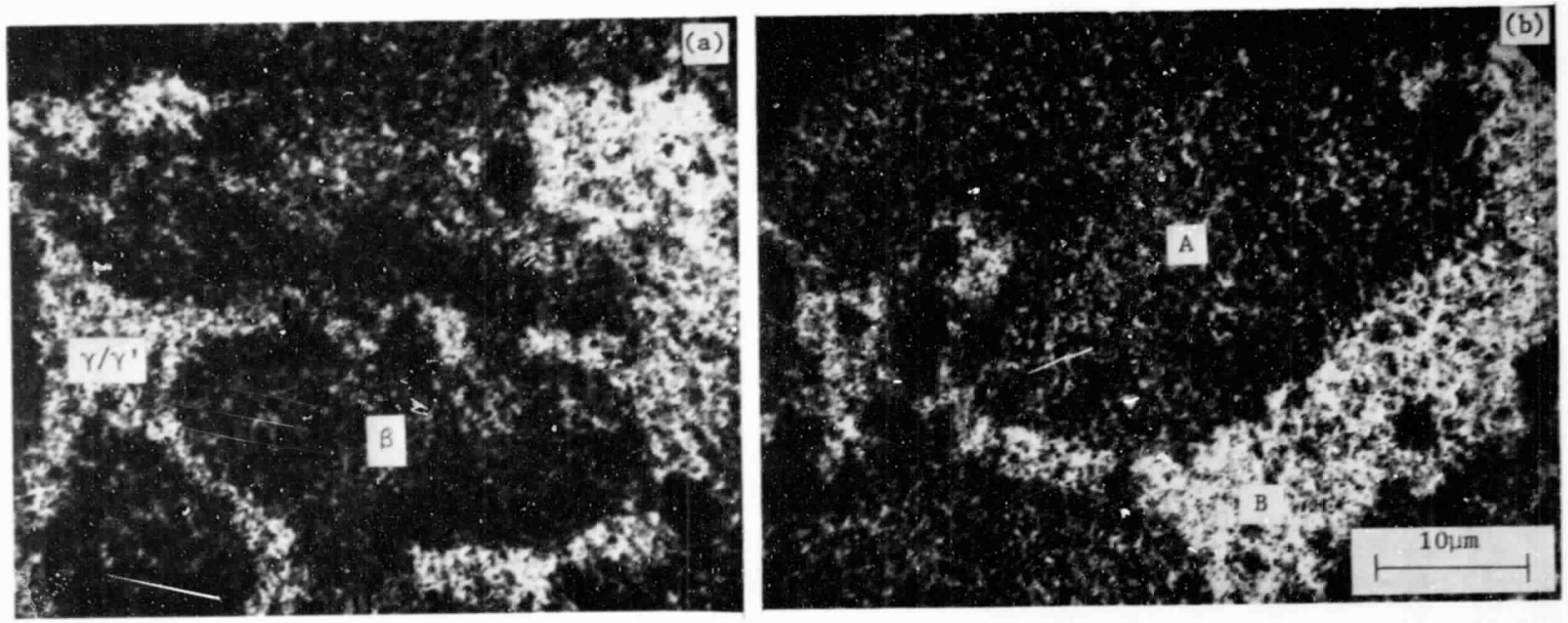

a, b) thick oxide over β-NiAl, thin oxide over γ/γ'.

Figure 56. Variations in oxide thickness.

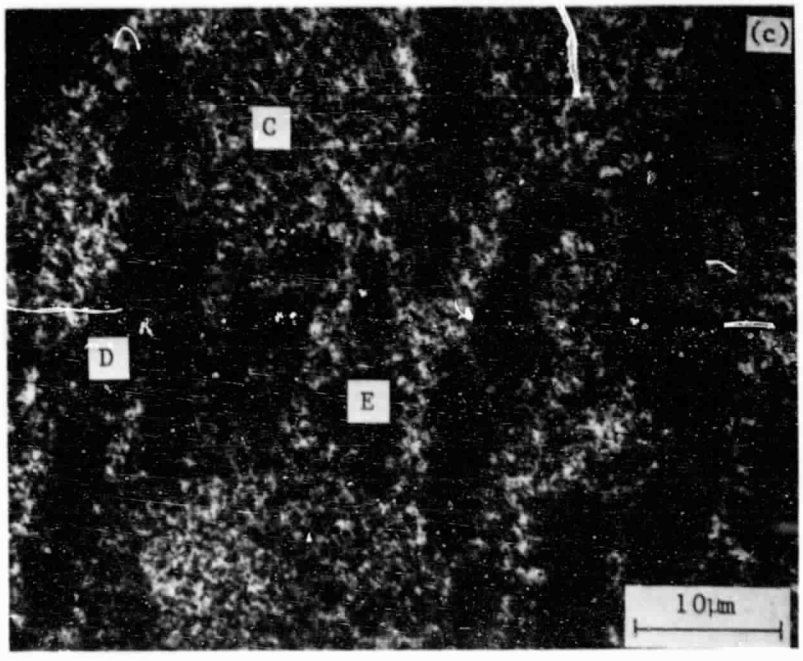

Figure 56c. thick oxide nodules in γ/γ' region.

Figure 57. α-Al_2O_3 diffraction patterns from the various morphologies shown in Figure 56.

a) light oxide over γ/γ', area "B"

b) dark oxide over β, area "A"

c) dark nodule, area "E"

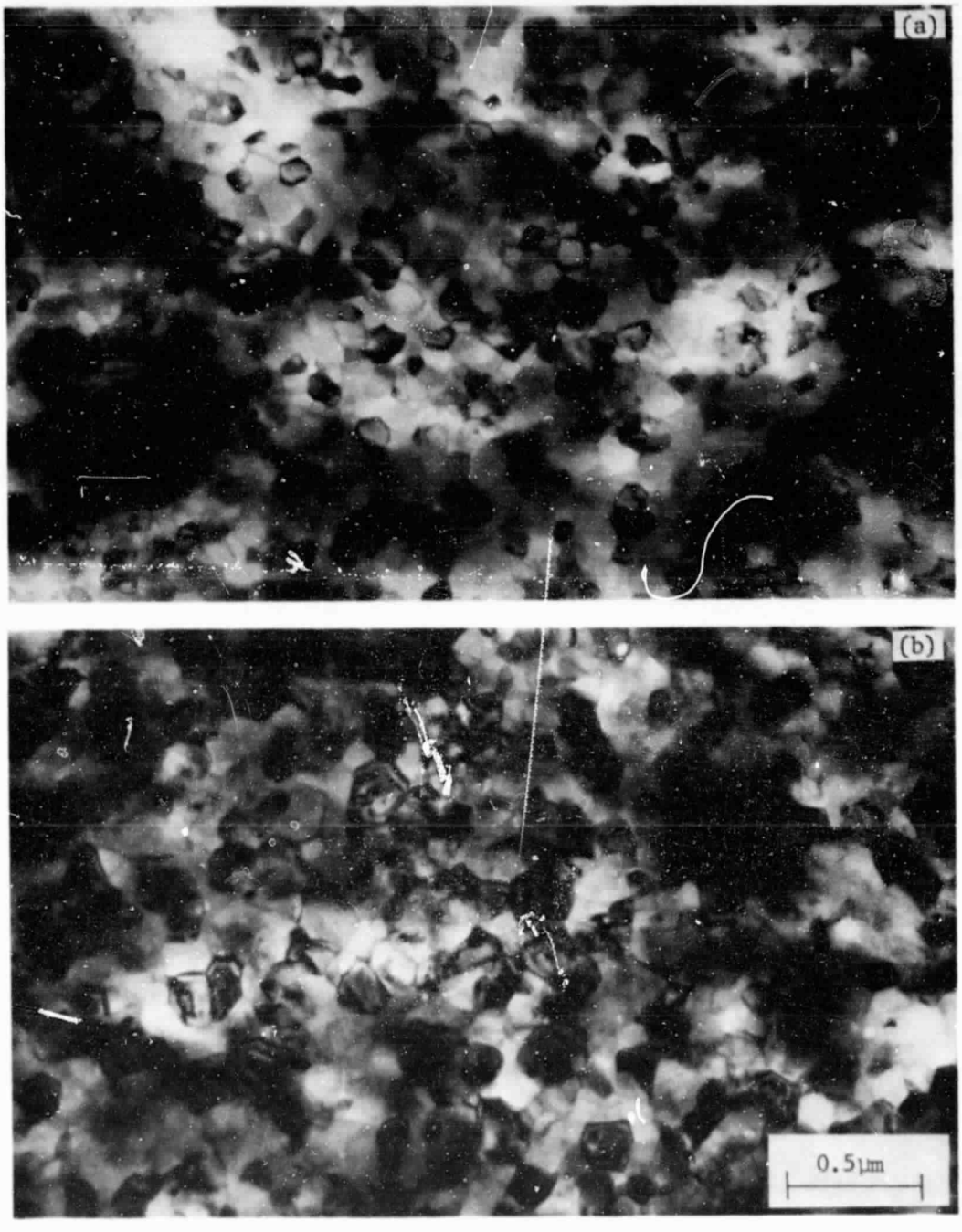

Figure 58. General microstructure of the areas in Figure 56.

a) light oxide over γ/γ', area "B"

b) dark oxide over β, area "A", showing more strain contrast and a larger grain size.

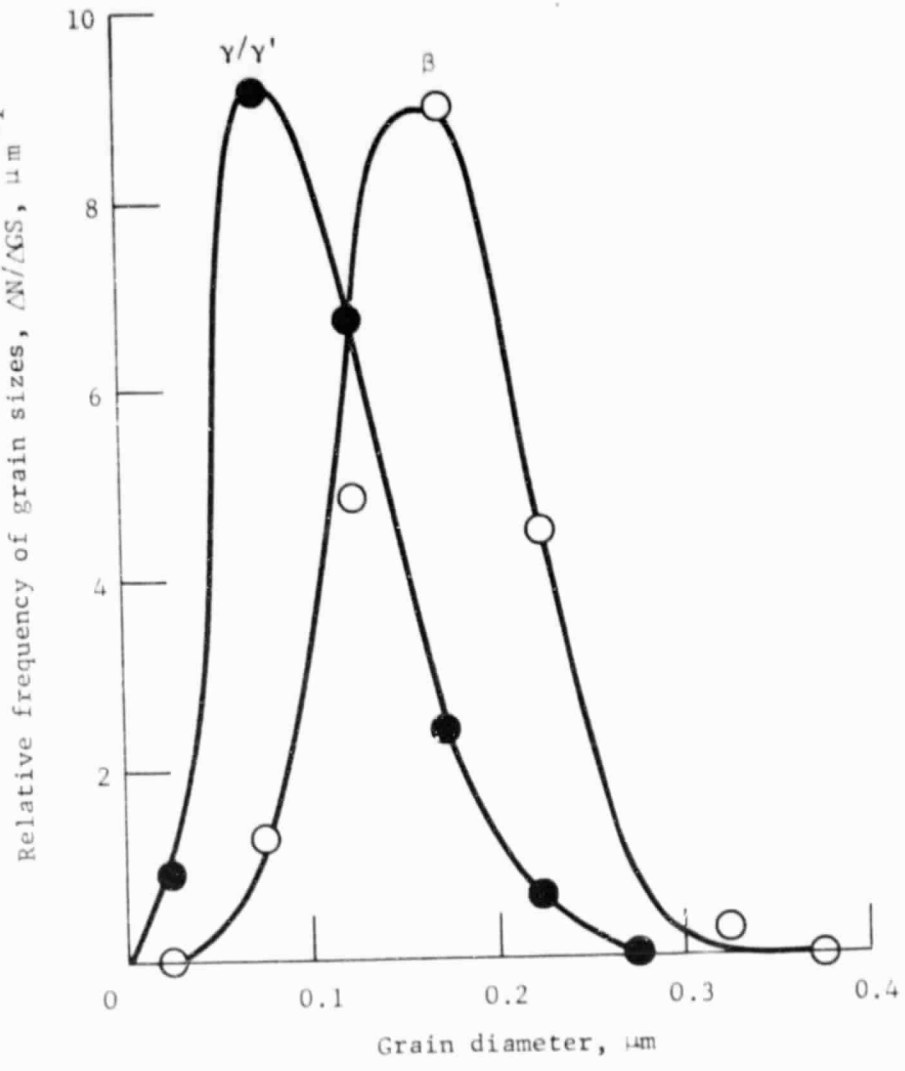

Figure 59. Grain size distribution over γ/γ' and β substrate phases (1 hr scale).

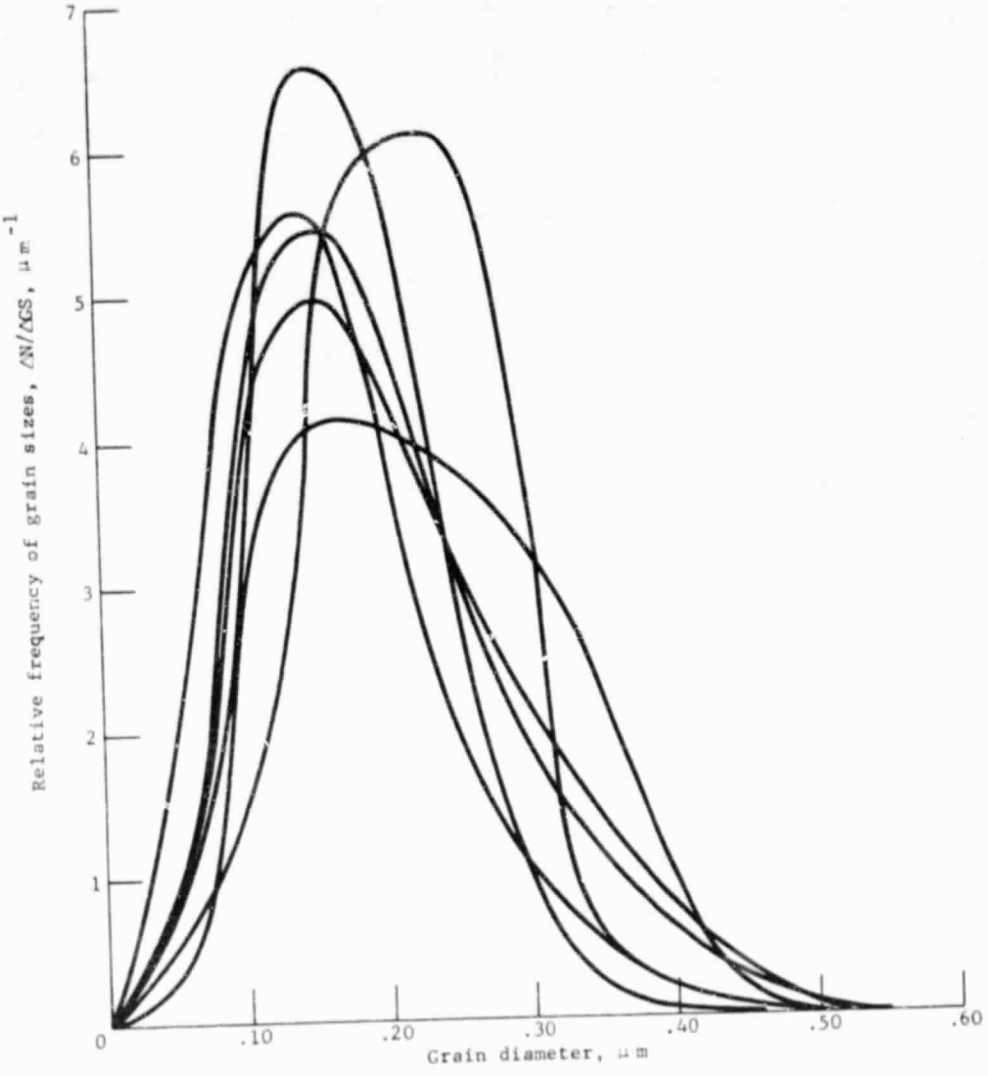

Figure 60. Grain size distribution at random locations in the 1 hr scale.

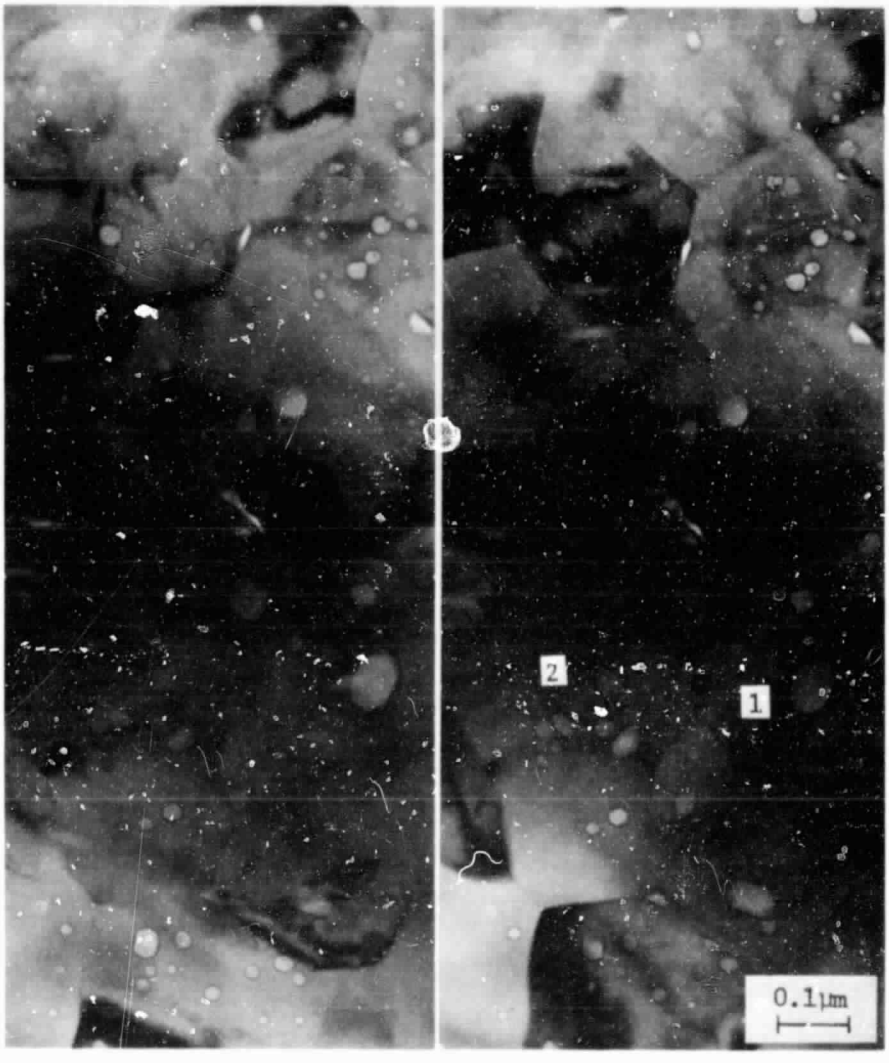

Figure 61. Stereopairs showing void distribution throughout the foil thickness; tilt -3.5°, 0.0° for left-right pair.

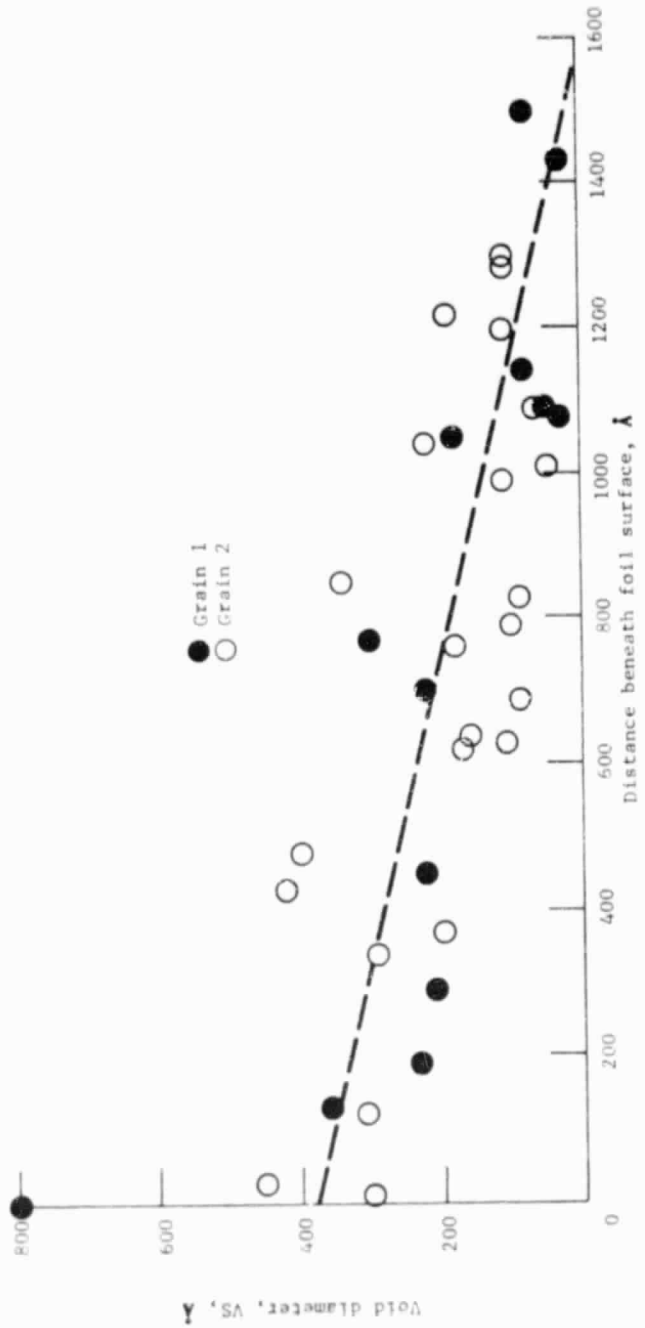

Figure 62. Variation of void size with depth into the scale for a 1 hr scale.

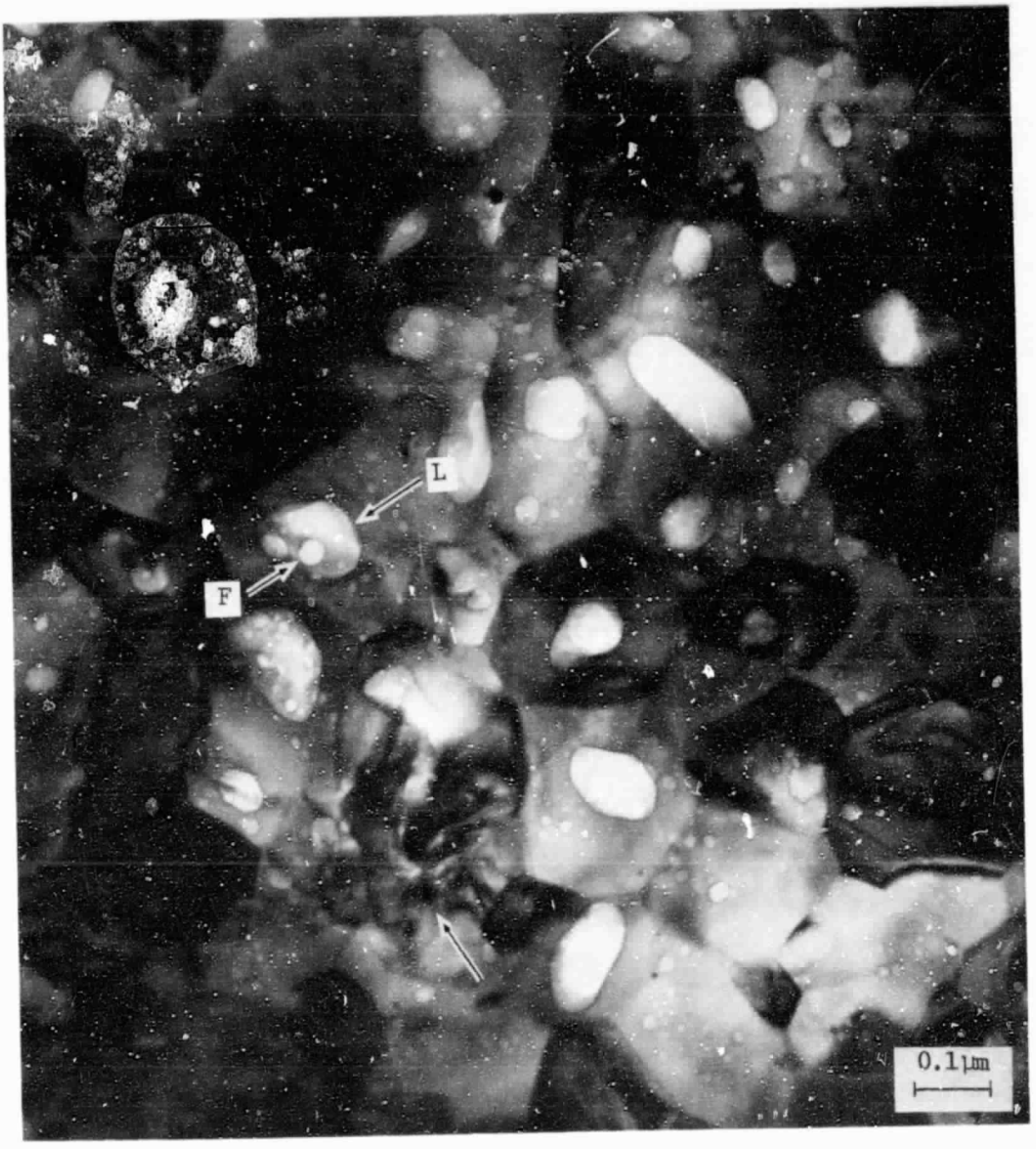

Figure 63. Large voids in the outer layer of a thick portion of the foil.

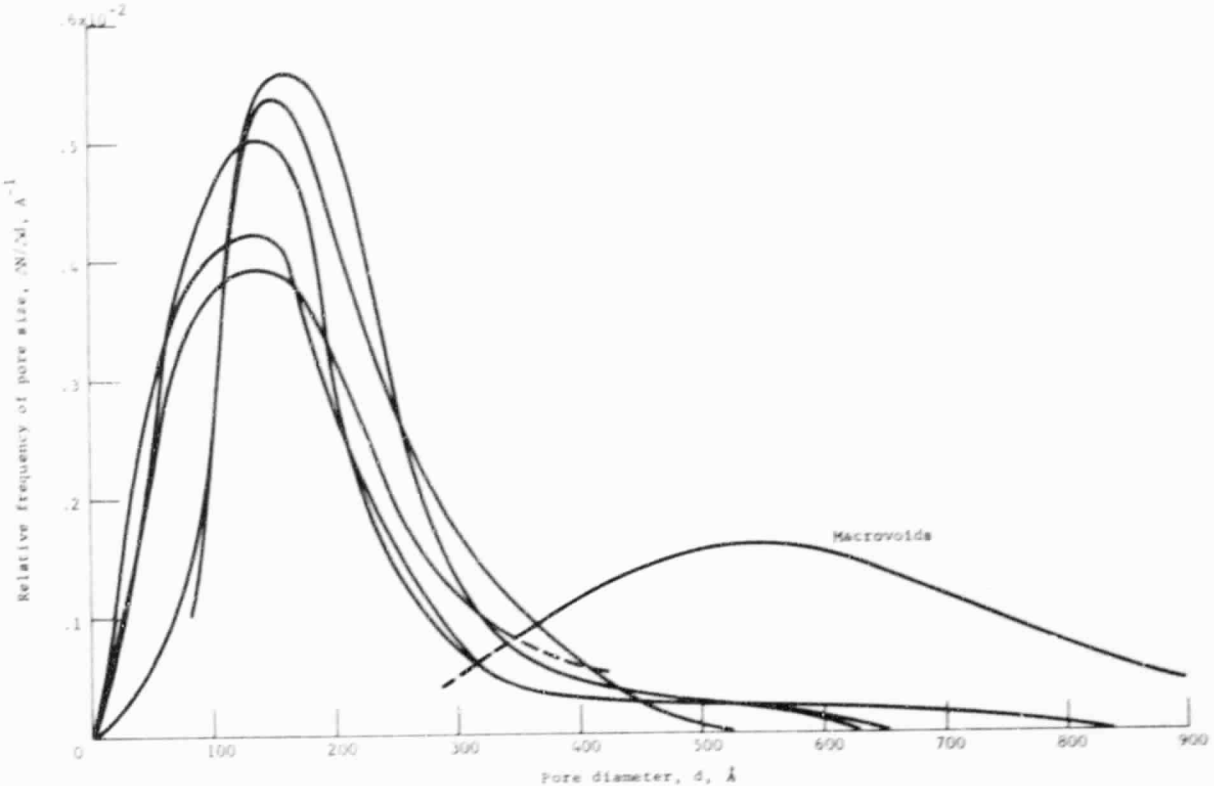

Figure 64. Void size distribution in the 1 hr scale.

Figure 65. Distorted α-Al_2O_3 grains; same area as in Figure 61.

Figure 66. Defects within oxide grains.

Figure 67. Defects and strongly diffracting grains.

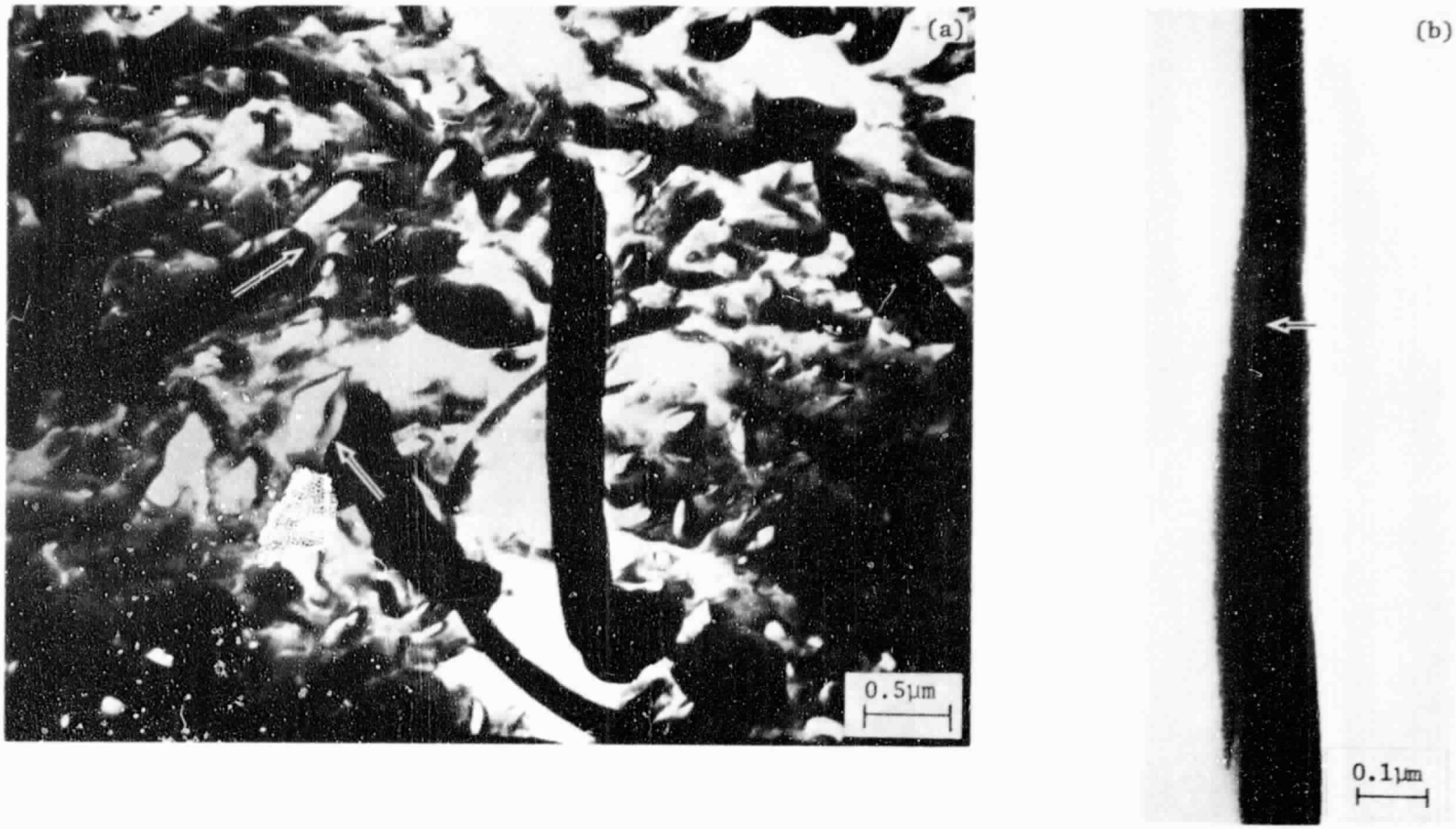

Figure 68. Whisker and void formation at the immediate oxide-gas interface; (undoped NiCrAl, 20 hr., 1100°C).

a) possible relation between whisker formation and macro-voids.
b) channel along whisker growth direction.

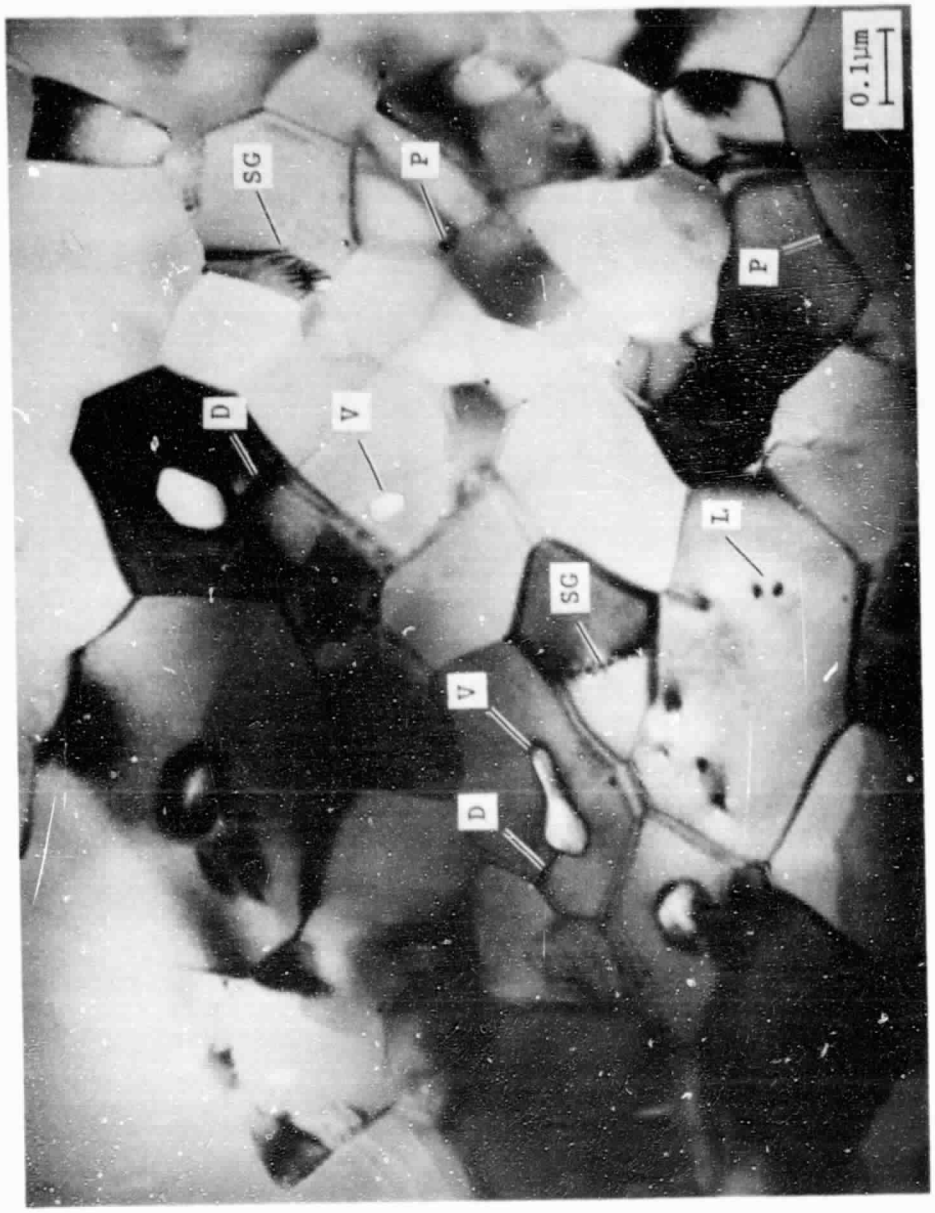

Figure 69. Typical microstructure near the oxide-gas interface. (P-precipitates, L-strain contrast lobes, V-voids, SG-subgrains, D-dislocation)

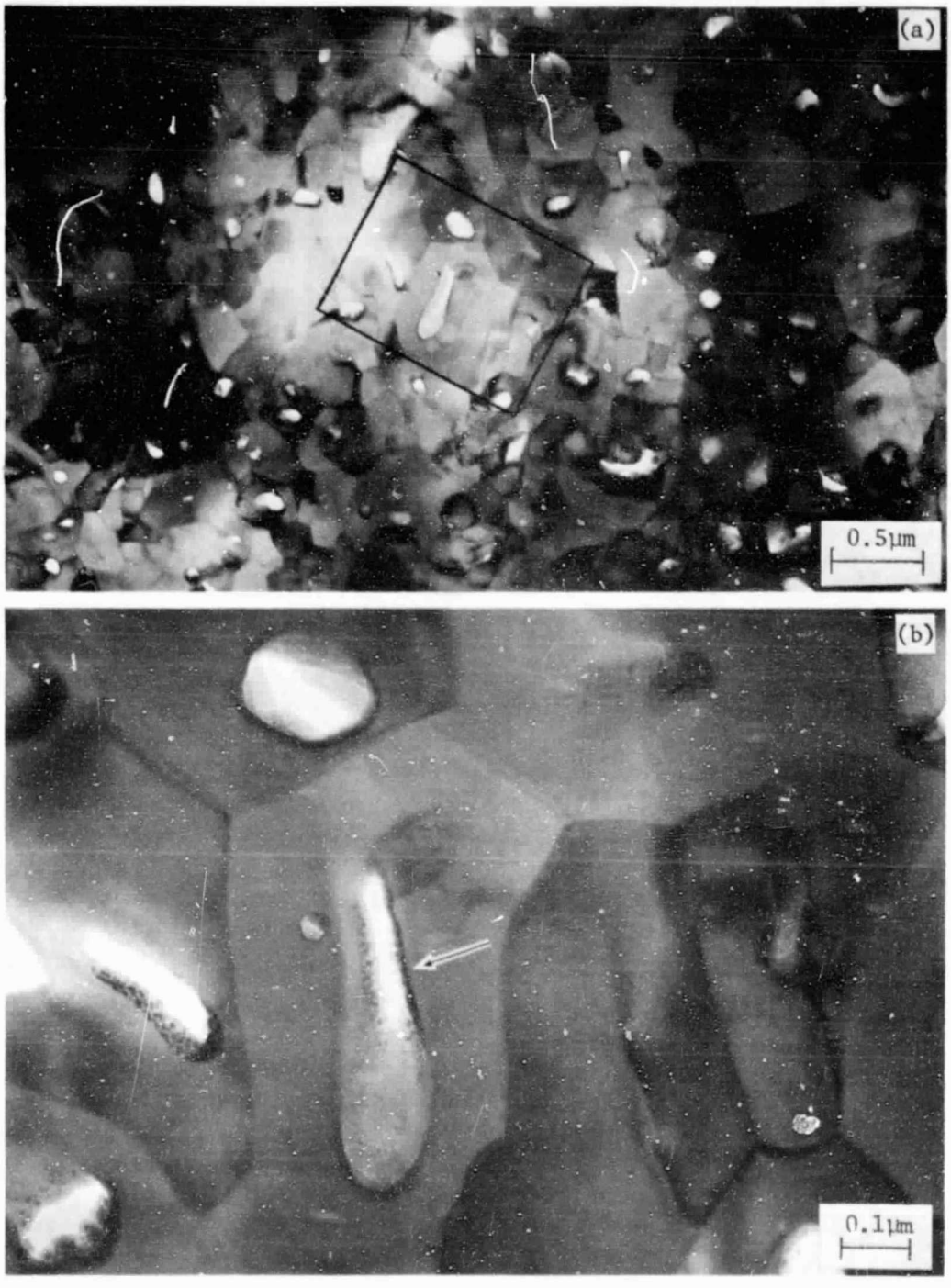

Figure 70. High density of intragranular voids typical of the oxide-gas surface.

a) nearly one macrovoid for each grain.

b) small crystallites at void surfaces.

Figure 71. Fine metal crystallites near the oxide-gas surface; FCC diffraction rings, single crystal $[\bar{4}6\bar{2}1]$ α-Al_2O_3 zone.

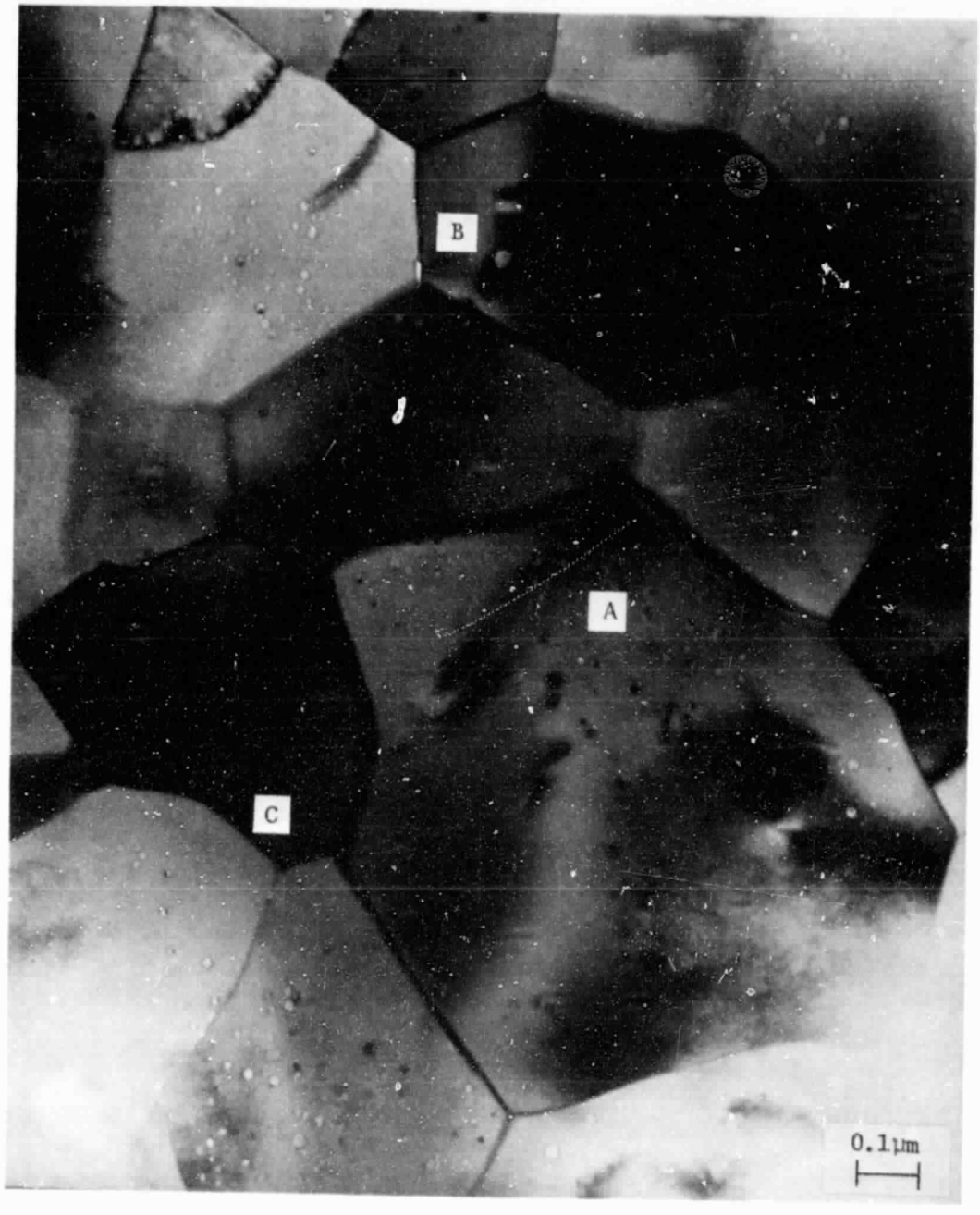

Figure 72. Dispersion of fine voids in grains >0.5 µm; a characteristic of the midsection of the scale.

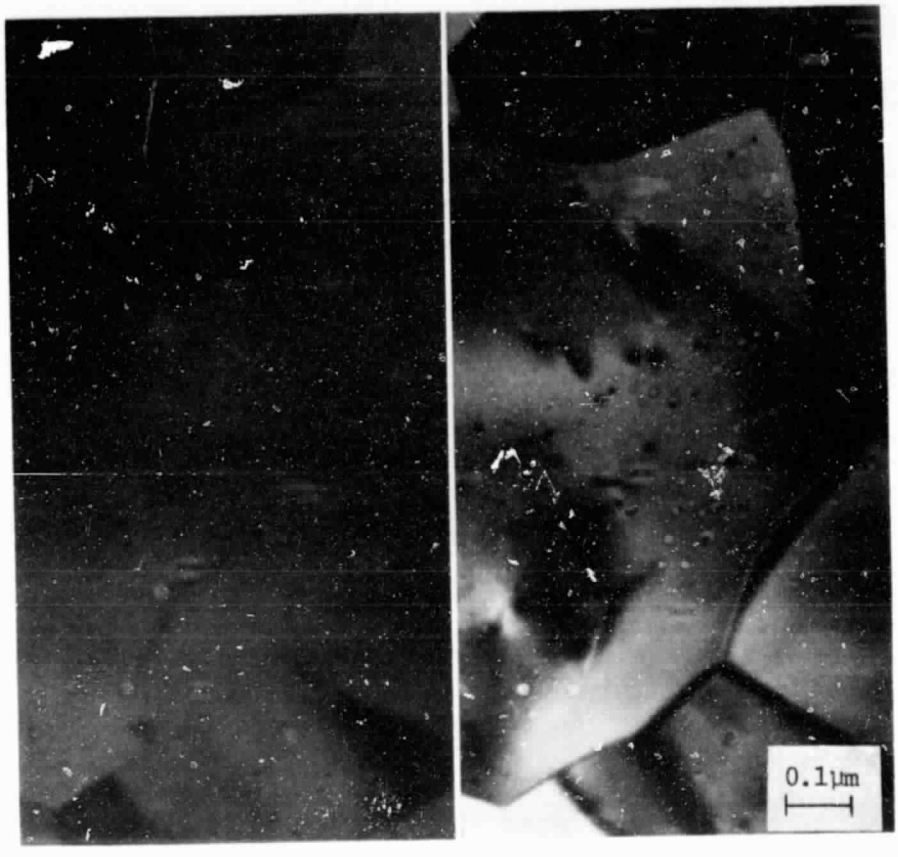

Figure 73. Stereopair showing the distribution of fine voids through the thickness of the foil; region "A" of Figure 72; 11° tilt difference.

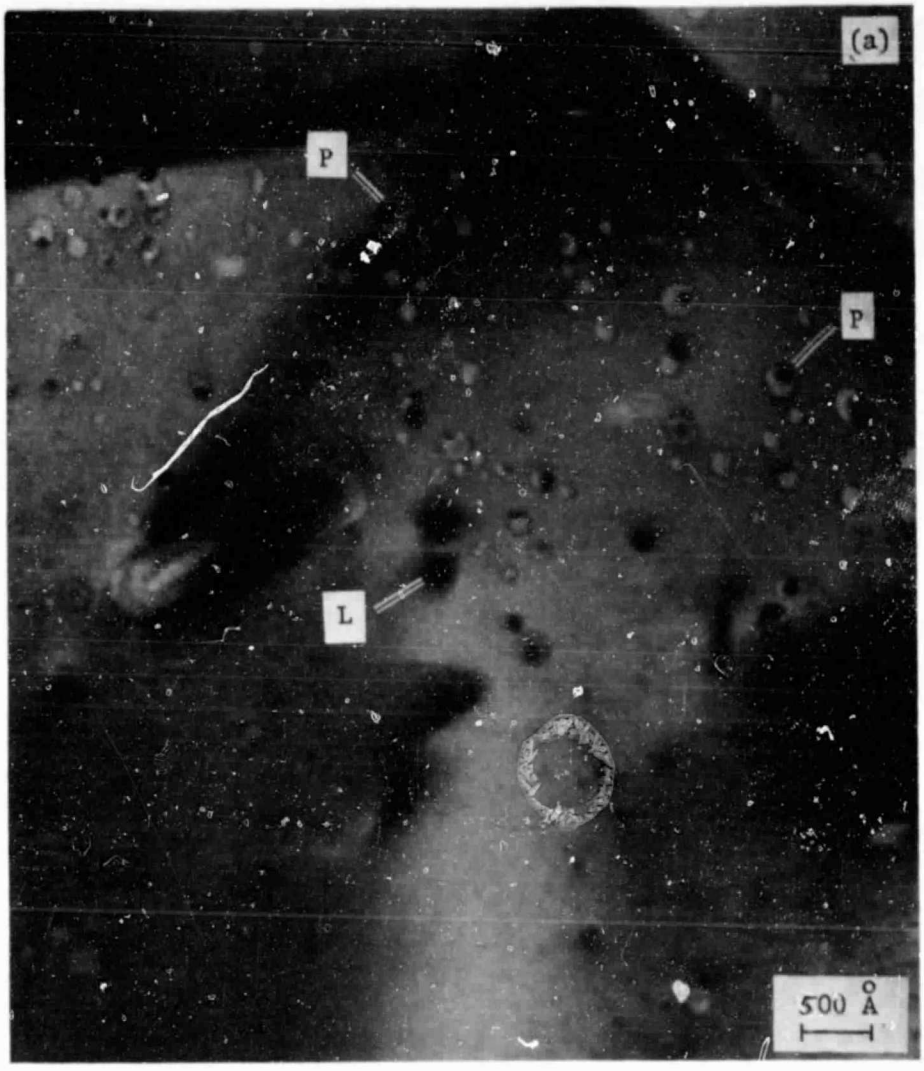

AREA "A"

Figure 74. Details of the dispersed porosity in the area of Figure 72. Dark precipitates, "P" associated with many of the voids; incompletely formed voids, "V", showing mottled structure; lobes, "L", of strain contrast.

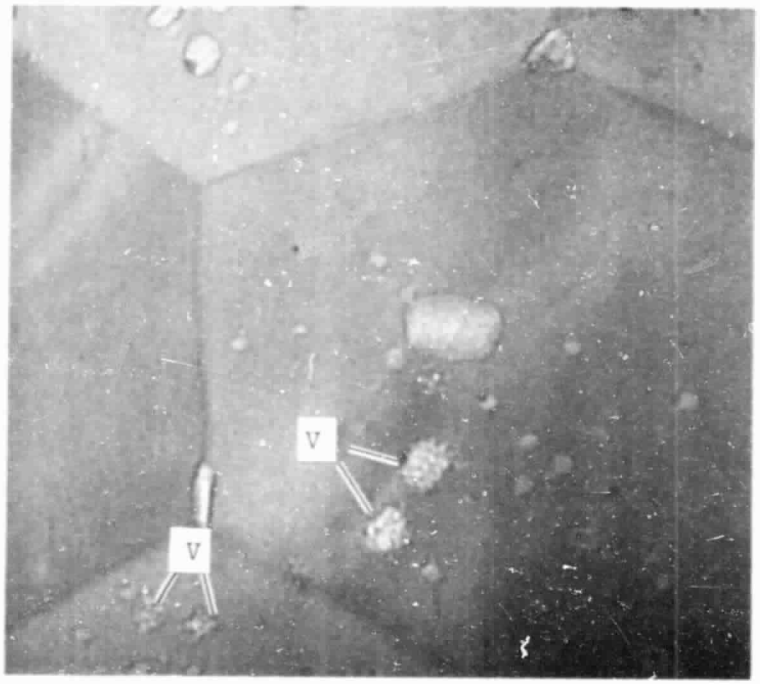

AREA "B"

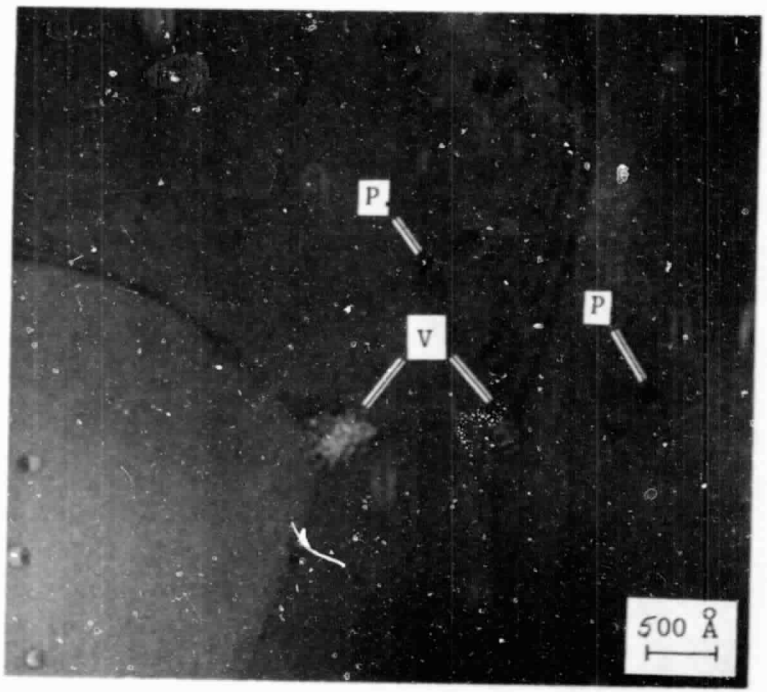

AREA "C"

Figure 74., continued

Figure 75. Fine voids and precipitate structure adjacent to a highly strained area, "S".

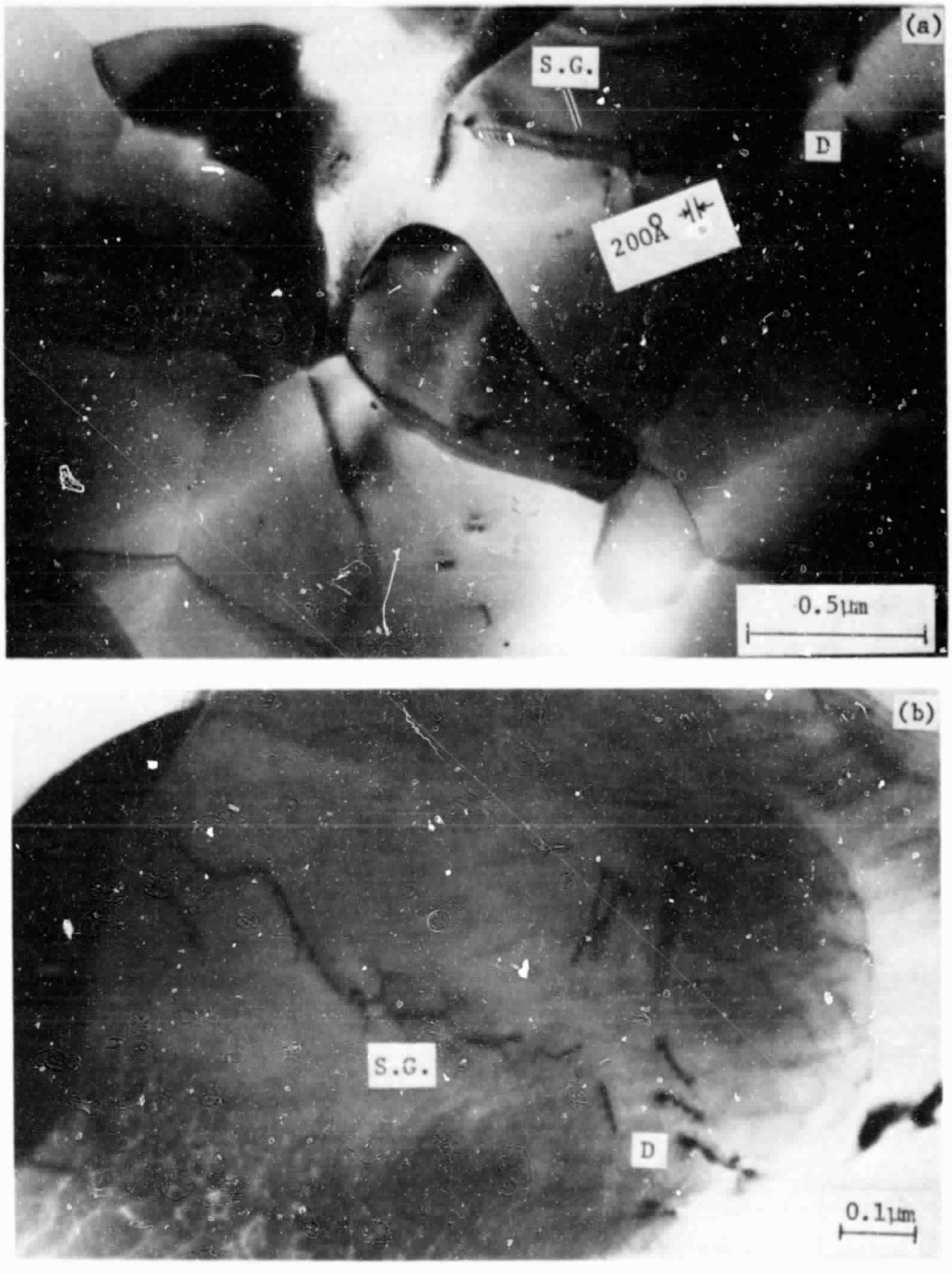

Figure 76. Individual dislocations, D, and subgrain arrays, SG, in large alumina grains.

Figure 77. Relatively void-free area more typical of the region near the oxide-metal interface.

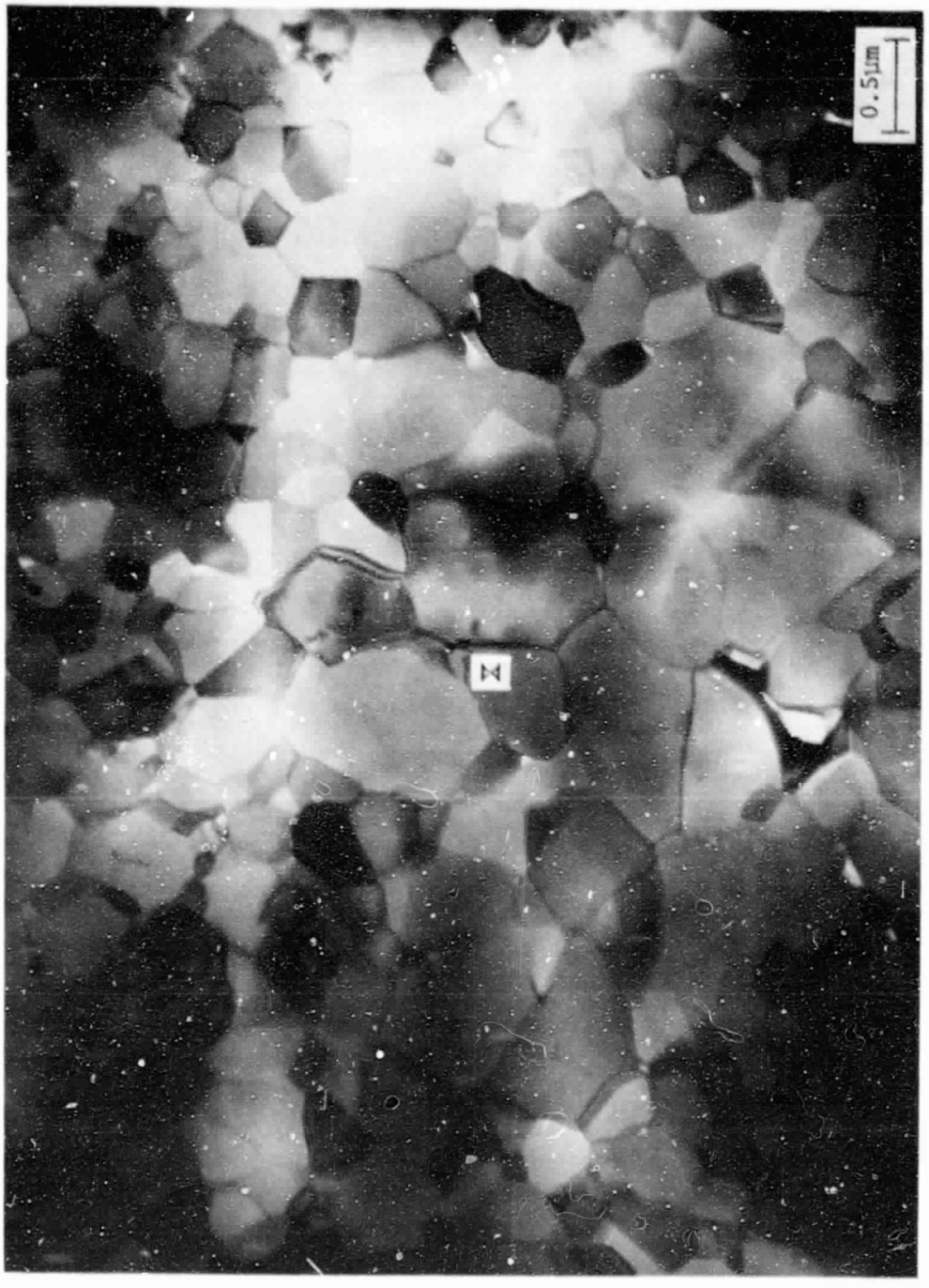

Figure 78. Decrease in grain size towards the thick periphery of this region.

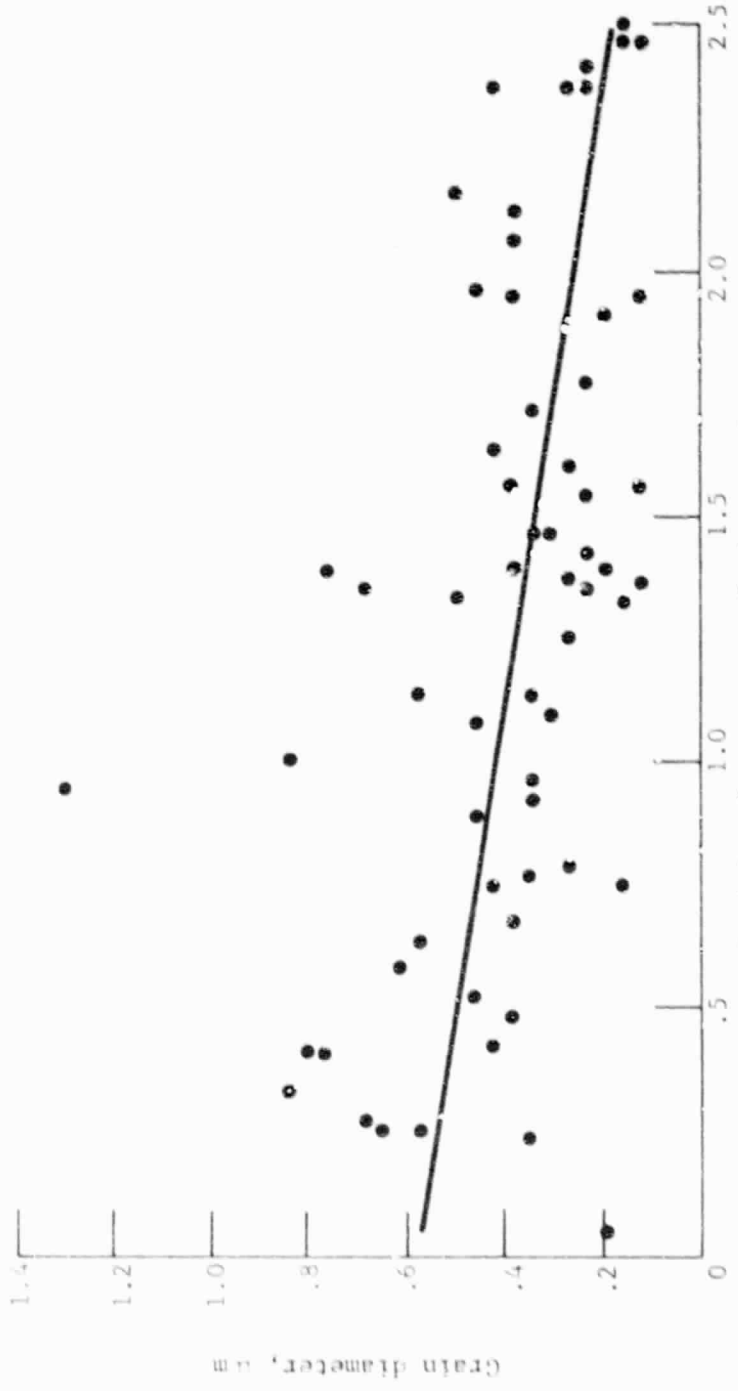

Figure 79. Decrease in grain size towards thicker region of the foil (Figure 78).

Figure 80. Dispersion of medium size (~150 Å) voids and precipitates (P) in a foil near the oxide-metal interface.

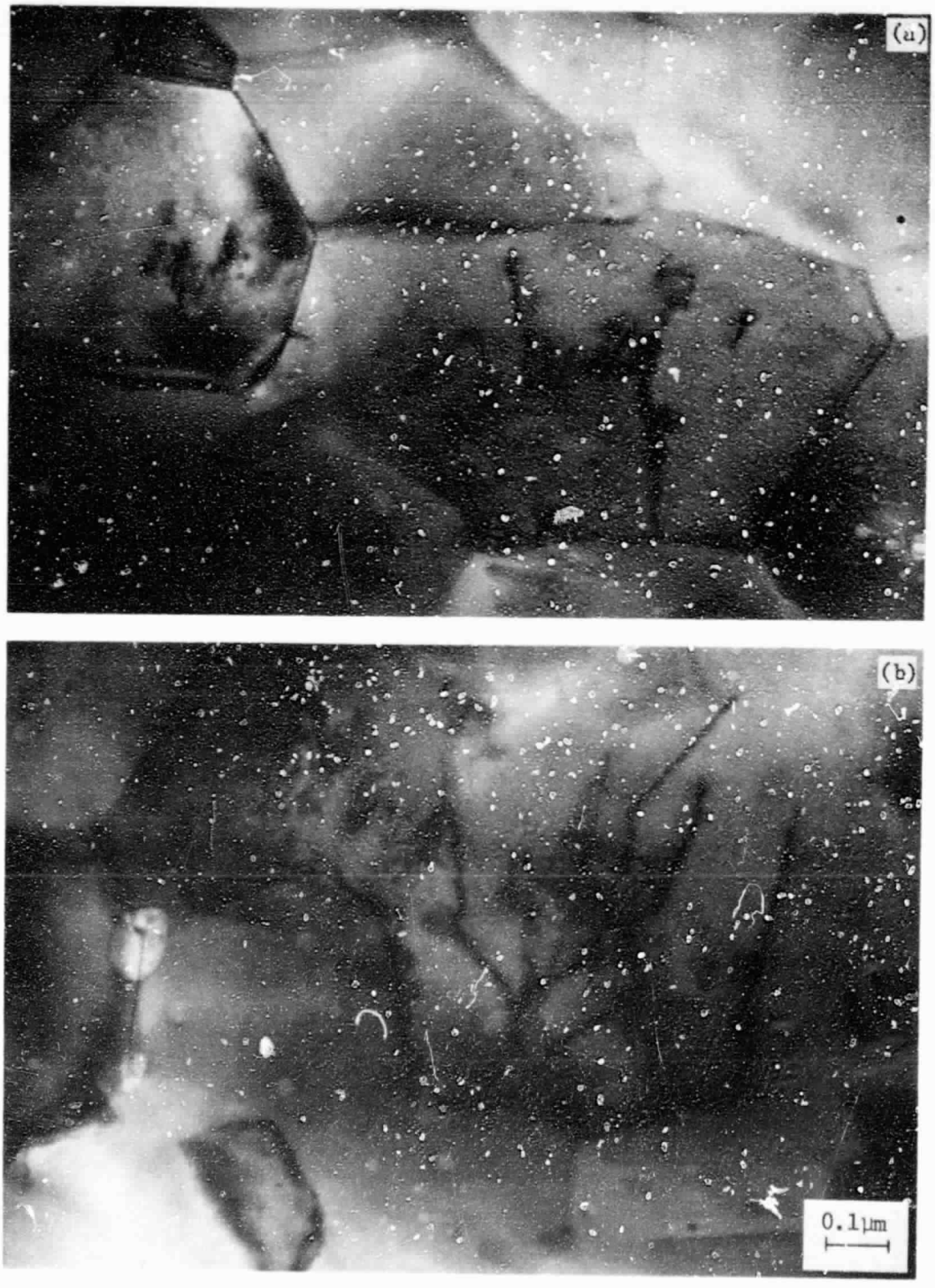

Figure 81. Individual dislocations in α-Al_2O_3 grains.

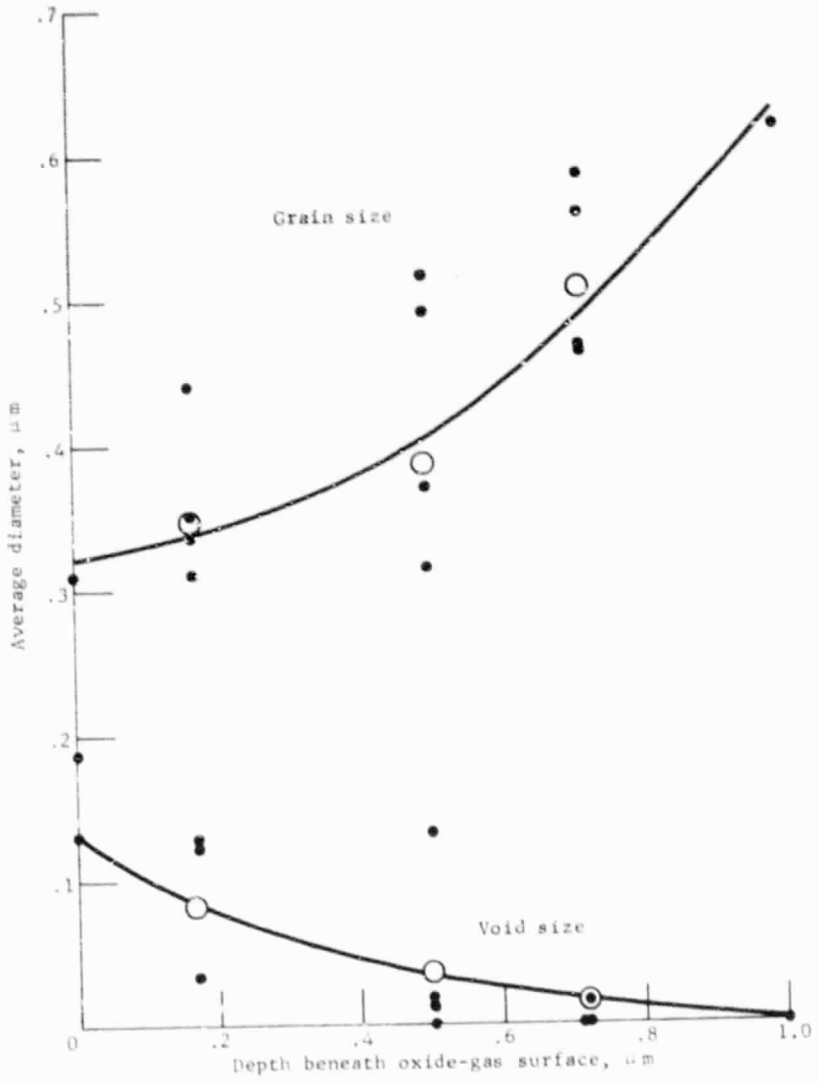

Figure 82. Variation of void and grain size through the thickness of the 20 hr scale. (Dots are average from single micrographs; open circles are weighted means.)

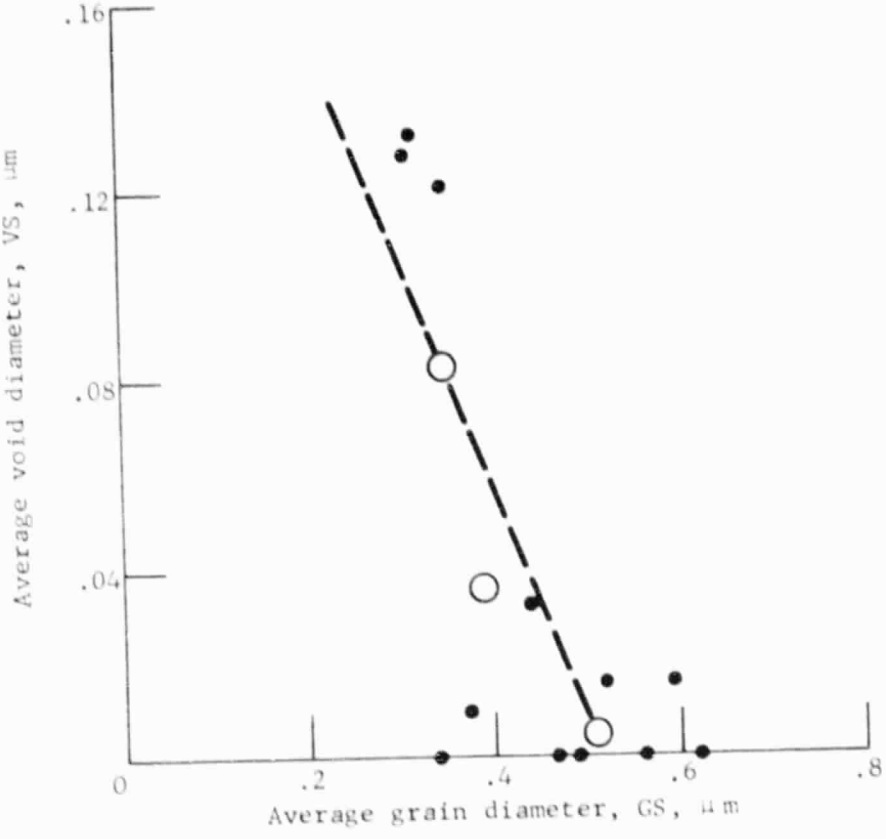

Figure 83. Inverse correlation of void size to grain size in the 20 hr scale. (Dots are averages from single micrographs; circles are weighted means.)

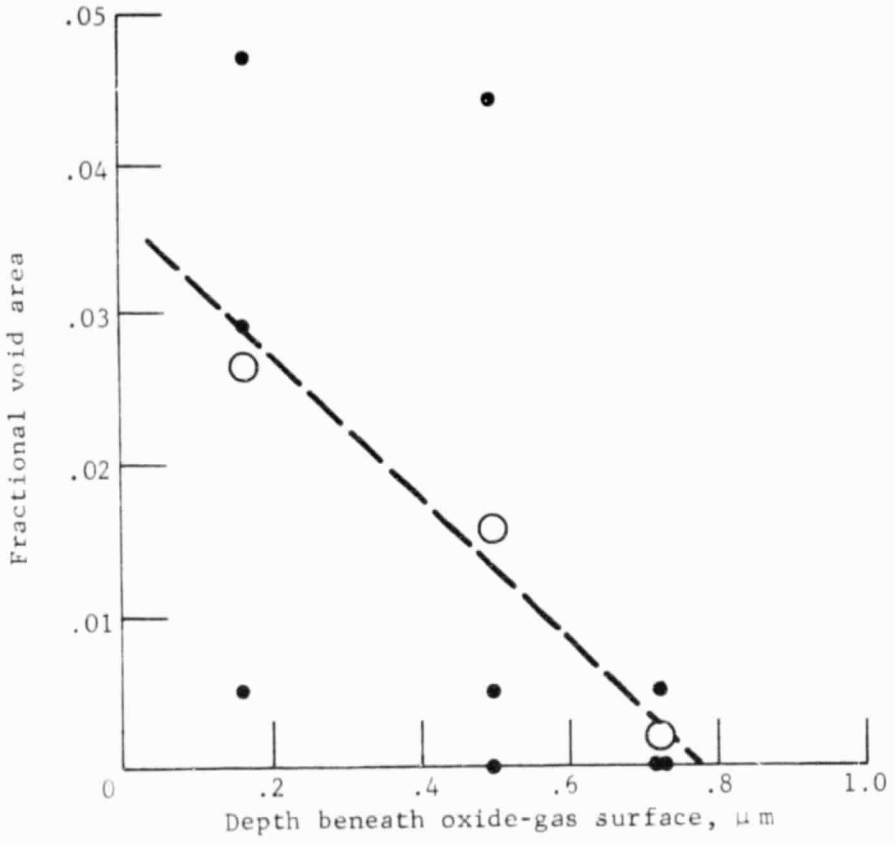

Figure 84. Decrease in estimated void concentration with position in the scale.

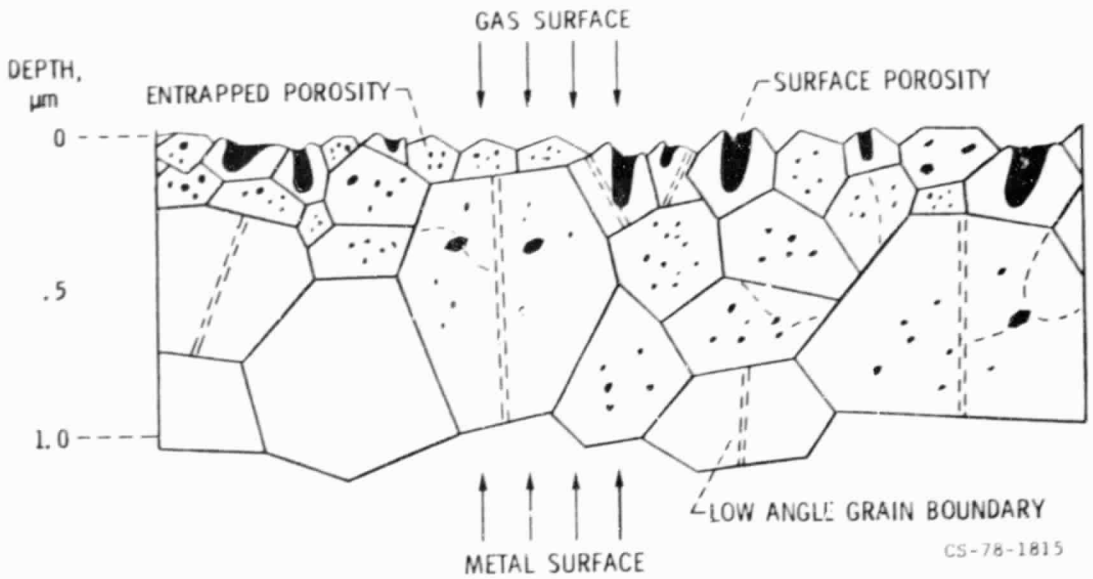

Figure 85. Schematic cross-section of α-Al_2O_3 scale formed on undoped NiCrAl after 20 hr. at 1100°C.